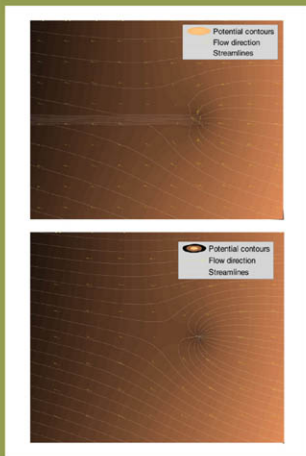


Geoenvironmental Engineering and Geotechnics

PROGRESS IN MODELING AND APPLICATIONS



Geotechnical Special Publication No. 204

Edited by

Qiang He
Shui-Long Shen

ASCE



**GEO-
INSTITUTE**

GEOTECHNICAL SPECIAL PUBLICATION NO. 204

GEOENVIRONMENTAL ENGINEERING AND GEOTECHNICS

PROGRESS IN MODELING AND APPLICATIONS

PROCEEDINGS OF SESSIONS OF GEOSHANGHAI 2010

June 3–5, 2010
Shanghai, China

HOSTED BY
Tongji University
Shanghai Society of Civil Engineering, China
Chinese Institution of Soil Mechanics and Geotechnical Engineering, China

IN COOPERATION WITH
Alaska University Transportation Center, USA
ASCE Geo-Institute, USA
Deep Foundation Institute, USA
East China Architectural Design & Research Institute Company, China
Georgia Institute of Technology, USA
Nagoya Institute of Technology, Japan
Transportation Research Board (TRB), USA
The University of Newcastle, Australia
The University of Illinois at Urbana-Champaign, USA
The University of Kansas, USA
The University of Tennessee, USA
Vienna University of Natural Resources and Applied Life Sciences, Austria

EDITED BY
Qiang He
Shui-Long Shen



Published by the American Society of Civil Engineers



Library of Congress Cataloging-in-Publication Data

Geoshanghai International Conference (2010)

Geoenvironmental engineering and geotechnics: proceedings of the GeoShanghai 2010 International Conference, June 3-5, 2010, Shanghai, China / edited by Qiang He, Shui-Long Shen.

p. cm. -- (Geotechnical special publication ; 204)

Includes bibliographical references and index.

ISBN 978-0-7844-1105-6

1. Engineering geology--Congresses. 2. Environmental geotechnology--Congresses. 3. Soil permeability--Congresses. I. He, Qiang, 1972- II. Shen, Shui-Long. III. American Society of Civil Engineers. IV. Title.

TA703.5.G4595 2010

624.1'51--dc22

2010012104

American Society of Civil Engineers

1801 Alexander Bell Drive

Reston, Virginia, 20191-4400

www.pubs.asce.org

Any statements expressed in these materials are those of the individual authors and do not necessarily represent the views of ASCE, which takes no responsibility for any statement made herein. No reference made in this publication to any specific method, product, process, or service constitutes or implies an endorsement, recommendation, or warranty thereof by ASCE. The materials are for general information only and do not represent a standard of ASCE, nor are they intended as a reference in purchase specifications, contracts, regulations, statutes, or any other legal document. ASCE makes no representation or warranty of any kind, whether express or implied, concerning the accuracy, completeness, suitability, or utility of any information, apparatus, product, or process discussed in this publication, and assumes no liability therefore. This information should not be used without first securing competent advice with respect to its suitability for any general or specific application. Anyone utilizing this information assumes all liability arising from such use, including but not limited to infringement of any patent or patents.

ASCE and American Society of Civil Engineers—Registered in U.S. Patent and Trademark Office.

Photocopies and reprints.

You can obtain instant permission to photocopy ASCE publications by using ASCE's online permission service (<http://pubs.asce.org/permissions/requests/>). Requests for 100 copies or more should be submitted to the Reprints Department, Publications Division, ASCE, (address above); email: permissions@asce.org. A reprint order form can be found at <http://pubs.asce.org/support/reprints/>.

Copyright © 2010 by the American Society of Civil Engineers.

All Rights Reserved.

ISBN 978-0-7844-1105-6

Manufactured in the United States of America.

Preface

Geoenvironmental Engineering and Geotechnics: Progress in Modeling and Applications selects 39 papers that represent the latest developments in the application of soil, rock, and groundwater mechanics in geotechnical engineering modeling and practice.

All the selected papers were presented at the GeoShanghai Conference, sponsored by the Geo-Institute of the American Society of Civil Engineers, held in Shanghai, China, June 3-5, 2010. The papers are selected from the following three technical sessions: *Geoenvironmental Engineering*; *Geotechnics*; and *Seepage and Porous Mechanics*. This conference provided a venue for both practitioners and researchers to showcase recent advances and discuss future directions in geotechnical engineering.

In the *Geoenvironmental Engineering* section of this GSP, studies on the engineering properties of reused waste materials in geotechnical application are presented, illustrating the close linkage between geotechnical engineering and sustainability. A number of papers provide insight into the impact of environmental contaminants on the geotechnical properties of geomaterials, demonstrating the importance of environmental factors in geotechnical applications. This section also highlights the latest understanding of groundwater contamination and remediation using cutting-edge interdisciplinary approaches integrating engineering modeling, biology, chemistry, and hydrogeology. The section of *Geotechnics* showcases new experimental evidence and theoretical developments in the strength and deformational behavior of soil. This section also presents development in a series of practical geotechnical problems such as stability analysis of slopes and risk analysis of landslides. Finally, the latest advances in the characterization and modeling of groundwater flow in geological formations of diverse geotechnical properties are highlighted in the section of *Seepage and Porous Mechanics*.

Each paper published in this ASCE Geotechnical Special Publication was evaluated by two or more reviewers and the editors. All published papers are eligible for discussion in the *Journal of Geotechnical and Geoenvironmental Engineering*, and are also eligible for ASCE awards.

We would like to acknowledge the quality and timely peer reviews provided by the reviewers listed below. Without their professional contributions, this publication would not be possible.

Heather J. Brown, Middle Tennessee State University, USA
Jun Chen, Shanghai Jiao-Tong University, China

Ren-Peng Chen, Zhejiang University, China
 Jin-Jian Chen, Shanghai Jiaotong University, China
 Chin-Min Cheng, Western Kentucky University, USA
 Yung-Ming Cheng, Hong Kong Polytechnic University, Hong Kong
 Yanjie Chu, California Environmental Protection Agency, USA
 Jian-Guo Dai, Hong Kong Polytechnic University, Hong Kong
 Joseph E. Dove, Virginia Polytechnic Institute and State University, USA
 Eric C. Drumm, University of Tennessee, USA
 Yan-Jun Du, Southeast University, China
 Gayathri Gopalakrishnan, Argonne National Laboratory, USA
 Ronald Green, Southwest Research Institute, USA
 Qiang He, University of Tennessee, USA
 Suksun Horpibulsuk, Suranaree University of Technology, Thailand
 Yu Huang, Tongji University, China
 Walter A. Illman, University of Waterloo, Canada
 Shigeyoshi Imaizumi, Utsunomiya University, Japan
 Ungtae Kim, University of Tennessee, USA
 Stanley A. Leake, U.S. Geological Survey, USA
 Eng-Choon Leong, Nanyang Technological University, Singapore
 Yanna Liang, Southern Illinois University, USA
 Fayun Liang, Shanghai Tongji University, China
 Cheng-Xian Lin, University of Tennessee, USA
 Chun-Yong Luo, Shanghai Jiao-Tong University, China
 Michael Lei Ma, Shanghai Jiao-Tong University, China
 Harry Moore, Tennessee Department of Transportation, USA
 M. Azizul Moqsud, Saga University, Japan
 Kiyoshi Omine, Kyushu University, Japan
 Andrea Panizzo, La Sapienza University of Rome, Italy
 Fang-Le Peng, Shanghai Tongji University, China
 Xiuchen Qiao, East China University of Science and Technology, China
 Steven A. Ripp, University of Tennessee, USA
 John Sanseverino, University of Tennessee, USA
 Jack Shui-Long Shen, Shanghai Jiao-Tong University, China
 Tatsuo Shimomura, Ebara Corporation, Japan
 Hong Sun, Shanghai Jiao-Tong University, China
 De-An Sun, Shanghai University, China
 Guoping Tang, Oak Ridge National Laboratory, USA
 Xiao-Wu Tang, Zhejiang University, China
 Stefano Tinti, University of Bologna, Italy
 George Veni, National Cave and Karst Research Institute, USA
 Baolin Wan, Marquette University, USA
 Louis Ngai-Yuen Wong, Nanyang Technological University, Singapore
 Kai-Sin Wong, Nanyang Technological University, Singapore
 Zhong Wu, Louisiana State University, USA
 Ming Xiao, California State University, Fresno, USA
 Ye-Shuang Xu, Shanghai Jiao-Tong University, China
 Zhifu Yang, Middle Tennessee State University, USA
 Guan-Lin Ye, Shanghai Jiao-Tong University, China

T.-C. Jim Yeh, University of Arizona, USA
Jian-Hua Yin, Hong Kong Polytechnic University, Hong Kong
Tae-Sup Yun, Yonsei University, Korea
Liang-Tong Zhan, Zhejiang University, China
Changyong Zhang, Pacific Northwest National Laboratory, USA
Lu-Lu Zhang, Shanghai Jiao-Tong University, China
Yongshuang Zhang, Chinese Academy of Geological Sciences, China
Guizhi Zhu, Swiss Federal Institute of Technology Zurich, Switzerland
Songye Zhu, Hong Kong Polytechnic University, Hong Kong

In producing this GSP, the editors would also like to acknowledge the assistance of Donna Dickert and Carol Bowers at ASCE Geo-Institute. In addition, the editors would like to extend their great appreciation to Professors Yongsheng Li, conference chair of GeoShanghai, Maosong Huang, Imad Al Qadi, and Baoshan Huang, who were instrumental in organizing the GeoShanghai Conference.

Qiang He

Assistant Professor, University of Tennessee, Knoxville, TN, USA

Jack Shui-Long Shen

Professor, Shanghai Jiao-Tong University, Shanghai, China

This page intentionally left blank

Contents

Geotechnics

Coupled Stability Analyses of Rainfall Induced Landslide: A Case Study in Taiwan Piedmont Area	1
Hung-Chieh Lo, Shih-Meng Hsu, Su-Yun Chi, and Cheng-Yu Ku	
Integrating Vegetation Role in Computer Simulation for Slope Stability: The Case Study of a Railway Embankment.....	9
Andrea Benedetto	
Optimal Design of Waste-Dump Slope of Open Pit Mine Based on Strength Reduction FEM	15
Jin-Sheng Lei, Da-Peng Zhu, Hui Peng, and Yue Li	
Risk Analysis of Individual Landslide in the Three Gorges Reservoir	21
Li-Xia Chen, Kun-Long Yin, and Yang Wang	
Back-Analysis of Water Waves Generated by the Dayantang Landslide	31
Yang Wang, Kunlong Yin, Li Zhou, and Juan Du	
Stochastic Durability Analysis of Under-Water Concrete Structure of Hangzhou Bay Bridge.....	39
Zhuo Zhao, Yan Zhang, and Changyong Ye	
Critical State Stress Analysis for Soil Body of Potential Heave	45
Jian-Min Yang and Gang Zheng	
Effect of Piping on Shear Strength of Levees	51
Ming Xiao and Jose Gomez	
Study on the New Deformation Characteristics of the Pumped Aquifers in Su-Xi-Chang Area, China	57
Fei Wang, Linchang Miao, and Weihua Lv	
Parametric Studies of Ground Deformation Induced by Pneumatic Caisson Construction in Soft Soils.....	63
Hailin Wang, Fangle Peng, Yong Tan, and Zhenliang Xu	
Simultaneous Modeling of Internal Erosion and Deformation of Soil Structures	71
Kazunori Fujisawa, Akira Murakami, and Shin-ichi Nishimura	
Closed-Form Solutions of the Homogeneous Isotropic Elastic Half Space Subjected to a Circular Plane Heat Source.....	79
John C.-C. Lu, Wei-Chih Lin, and Feng-Tsai Lin	
Golden Ratio in the Point Heat Source Induced Horizontal and Vertical Displacements of an Isotropic Elastic Half Space	87
Feng-Tsai Lin and John C.-C. Lu	

Geoenvironmental Engineering

Engineering Characteristics of Bottom Ash in Municipal Solid Waste Incinerators	95
Peng-Fei Fang, Xiang-Rong Zhu, Hong-Shui Chen, and Wei Chen	
Strength Comparison of Cement Solidified/Stabilized Soils Contaminated by Lead and Copper	103
Lei Chen, Song-Yu Liu, Yan-Jun Du, and Fei Jin	
Geotechnical Properties of Zinc/Lead Mine Tailings from Tara Mines, Ireland.....	111
Michael E. Quille and Brendan C. O’Kelly	
Experimental Study of Cemented Soil under Na₂SO₄ Corrosive Condition.....	118
Pengju Han and Xiaohong Bai	
Influence of Heavy Metal Contaminants on the Compressibility of Reconstituted Kaolinite	126
X. F. Liu, N. Saiyouri, and P. Y. Hicher	
Beneficial Reuse of Corrugated Board in Slurry Applications.....	132
James L. Hanson, Nazli Yesiller, Jagjit Singh, Greg M. Stone, and Adam Stephens	
Analysis on Tensile Force of Liner System with the Variation of Location of Roller Compactor in Landfill	140
Sifa Xu, Zhe Wang, and Hao Zhao	
pH Changes in Solidified Dredged Materials	146
Gan Zhao, Wei Zhu, Lei Li, and Chun-Lei Zhang	
Recent Developments in Modeling THCM Behaviour of Geoenvironmental Problems	153
Philip Vardon and Hywel Thomas	
Field Test of a Geothermal System in Hafen City, Hamburg.....	159
X. Ma and J. Grabe	
Bioremediation of Heavy Metals in Soil and Groundwater: Impact of Nitrate as an Inhibitor.....	167
Qiang He and Jizhong Zhou	
Simulation of Groundwater Composition Change Due to Deposition of Uranium Minerals in Dolomite Gravel Fill	181
Fan Zhang, Jack C. Parker, David B. Watson, Debra Phillips, and Philip M. Jardine	
“Kriging Assistant”: A Geostatistical Analysis and Evaluation Tool.....	188
Alessandro Mazzella and Antonio Mazzella	

Seepage and Porous Mechanics

The Wells Simulator: Analytical Solutions for Groundwater Flow Using Modified Streamfunction Contouring	194
Holzbecher Ekkehard and Sauter Martin	
Rapid Drawdown of Water Table in Layered Soil Column.....	202
Hong Yang, Harianto Rahardjo, and Daping Xiao	

The Effect of Clay Content on Filter-Cake Formation in Highly Permeable Gravel	210
Fan-Lu Min, Wei Zhu, Xiao-Rui Han, and Xiao-Chun Zhong	
Remote Sensing and GIS for Groundwater Mapping and Identification of Artificial Recharge Sites	216
Rajat C. Mishra, Biju Chandrasekhar, and Ranjitsinh D. Naik	
Development of Discharge Capacity Testing Apparatus and Numerical Analyses of Test Results	224
Nam-Jae Yoo, Dong-Gun Kim, Dong-Won Lee, and Sang-Hyun Jun	
An Aquifer Analogue Study of High Resolution Aquifer Characterization Based on Hydraulic Tomography	231
Rui Hu, Wei Zhao, and Ralf Brauchler	
A Mathematical Model for Determination of the Critical Hydraulic Gradient in Soil Piping	239
Jian Zhou, Yan-Feng Bai, and Zhi-Xiong Yao	
Application of Natural Element Method in Solving Seepage Problem	245
S. Shahrokhbadi, M. M. Toufigh, and R. Gholizadeh	
Spherical Discrete Element Simulation of Seepage Flow with Particle-Fluid Interaction Using Coupled Open Source Software	253
Feng Chen, Eric C. Drumm, and Georges Guiochon	
Seepage Failure and Erosion of Ground with Air Bubble Dynamics	261
Kenichi Maeda and Hirotaka Sakai	
A Proposed Calculation Method for Land Subsidence Caused by Groundwater Withdrawal in Jiangsu Province	267
Weihua Lv, Linchang Miao, and Chunlin Li	
Geotechnical Characterization of the Simsima Limestone (Doha, Qatar)	273
Ioannis Fourniadis	
Application of Microgravity Survey to Detect Underground Cavities in a Desert Karst Terrain	279
Hasan Kamal, Mahmoud Taha, and Shaikha Al-Sanad	

Indexes

Author Index	285
Subject Index	287

This page intentionally left blank

Coupled Stability Analyses of Rainfall Induced Landslide: A Case Study in Taiwan Piedmont Area

Hung-Chieh Lo¹, Shih-Meng Hsu², Su-Yun Chi³, Cheng-Yu Ku⁴

¹Research Engineer, Geotechnical engineering Research Center, Sinotech Engineering Consultants, Inc., Basement No. 7, Lane 26, Yat-Sen Road, Taipei City 110, Taiwan; jaylo@sinotech.org.tw

²Senior Research Engineer & Director of hydrogeology research group, Geotechnical engineering Research Center, Sinotech Engineering Consultants, Inc., Basement No. 7, Lane 26, Yat-Sen Road, Taipei City 110, Taiwan; shihmeng@sinotech.org.tw

³Manager, Geotechnical Engineering Research Center, Sinotech Engineering Consultants, Inc., Basement No. 7, Lane 26, Yat-Sen Road, Taipei 110, Taiwan; sychi@sinotech.org.tw

⁴Assistant Professor, Department of Harbor and River Engineering, National Taiwan Ocean University, No. 2, Beining Road, Keelung City 202, Taiwan; chkst26@mail.ntou.edu.tw

ABSTRACT: This study presents a 2D time-dependent infiltration-seepage-stability coupled hydrogeological model to simulate the seepage and slope stability of an active landslide site in northern Taiwan. The conceptual model and corresponding hydraulic and mechanical parameters applied in the model were based on a series of in-situ investigations and laboratory experimental results. A seepage analysis was conducted, and the model was calibrated and verified from the field monitoring data in order to minimize the difference between the computed pore pressures and the observed piezometric levels. A stability analysis coupled with the results of seepage analysis was performed to determine the slip potential of the landslide site under the rainfall brought up by two typhoon events. Various designed rainfall with different patterns, intensity and accumulated amount was then introduced in the model. The relationship between different rainfall characteristics and stability of the landslide site was identified and provided a good indication for the risk management under various rainfall conditions.

INTRODUCTION AND OBJECTIVES

Taiwan is an island located in an active collision zone between the Eurasian Plate and the Pacific Plate. In recent years, due to the abnormal climate change, typhoon events with high rainfall intensity frequently occurred during the summer and usually triggered severe damages such as landslides in piedmont areas. To better understand such an issue, using a numerical model to simulate rainfall infiltration and slope stability is fairly suitable. By integrating infiltration-seepage-stability to achieve a coupled time-dependent analysis, the factor of safety of the slope can be computed under various rainfall conditions and pore pressure distributions. Several studies performed coupled

analysis to simulate some actual landslide problems in these years (Gasmo et al., 2000; Rahardjo et al., 2001; Blatz et al., 2004; Casagli et al. 2006; Cascini et al., 2006; Calvello et al., 2008). In this study, a hydrogeological conceptual model was established to simulate seepage and slope stability at an active landslide site in northern Taiwan. Realization of the conceptual model and corresponding hydraulic and mechanical parameters applied in the model were based on a series of in-situ investigations and laboratory experimental results. The hydraulic parameters applied in the model were calibrated based on in-situ observed rainfall and piezometric levels. The precipitation data observed from two typhoon events, which took place in September of 2008, were adopted to verify the model. The stability analysis coupled with the result of seepage analysis was subsequently conducted to determine the slip potential of the slope during two typhoon events. Finally, various designed rainfall with different patterns, intensity and amount were introduced in the model, and the relationship between rainfall characteristics and the slope stability of the landslide site was established.

HYDROGEOLOGICAL INVESTIGATION OF THE LANDSLIDE SITE

The landslide site is located near the middle stream of the Da-Han River in northern Taiwan (Figure 1). In order to establish a precise hydrogeological conceptual model, four boreholes were drilled, and a series of investigation approaches including light detecting and ranging (LIDAR), ground resistivity image profiling (RIP), and borehole image scanning were conducted at the landslide site. According to the results, the elevation of the landslide site was identified (28 degree in slope angle), and the strata were divided into three layers, including colluvial cover, weathered bedrock, and bedrock. The in-situ double-ring infiltration test and packer isolated test were employed to obtain the hydraulic conductivity of three layers. The laboratory tests, such as physical properties test, pressure plate test, direct shear test, and triaxial test were conducted to acquire physical and mechanical parameters for each layer. Furthermore, the rain gage and piezometers were installed on the landslide site, and the observed data were collected to calibrate and verify the model.

MODELING OF SEEPAGE AND SLOPE STABILITY

An engineering tool GeoStudio, developed by the University of Calgary, was adopted to simulate seepage and slope stability of the landslide site in this study.

Seepage Analysis

A finite element analysis module SEEP/W was used to simulate the rainfall infiltration and groundwater flow in this study. Based on Darcy's law, the governing equation is given as:

$$\frac{\partial}{\partial x} \left(K_x \frac{\partial H}{\partial x} \right) + \frac{\partial}{\partial y} \left(K_y \frac{\partial H}{\partial y} \right) + Q = \frac{\partial \theta}{\partial t} \quad (1)$$

where H=total head; K_x =hydraulic conductivity in x-direction; K_y =hydraulic conductivity in y-direction; Q=applied boundary flux; θ =volumetric water content; and t=time. For the hydraulic boundary conditions applied in the model, the fixed head

was on the right and left while the zero flux was on the bottom. The observed rainfall data was applied as the recharge flux on slope surface. Both steady-state and transient analysis were performed. In transient analysis, the daily time step was applied. The transient hydraulic characteristics, such as flow field, distribution of pressure head and water content can be computed in SEEP/W. The 2D hydrogeological model of the landslide site was shown in Figure 1.

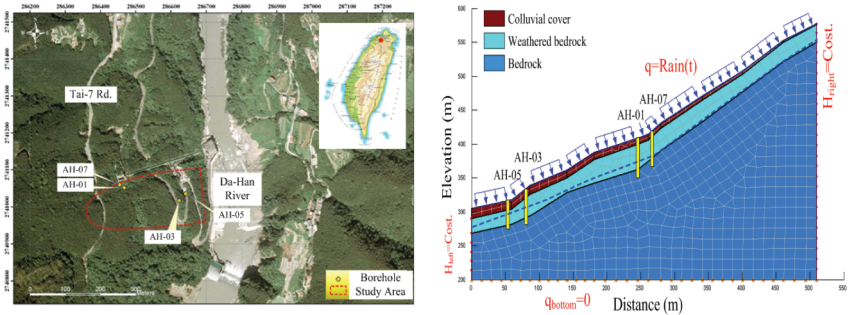


FIG. 1. The aerial photo of the landslide site (left); and the 2D hydrogeological conceptual model (right).

Calibration and Verification

In order to minimize the divergences between the computed results and real scenario, the calibration and verification of the model are crucial tasks. In this study, three borehole piezometric data observed from December 1, 2007 to August 1, 2008 were adopted to calibrate the hydraulic parameters. The calibrated results indicated that the average errors between simulated and observed groundwater levels of three boreholes are ranging from 1.82 to 2.28% as shown in Table 1. By comparing calibrated groundwater level with observed one, a similar trend in groundwater level movement was found as shown in Figure 2. Because the groundwater is mainly located in the fractured weathered bedrock, most rainfall may flow downward to the hillside through the fractures and hardly remained in the layer. Therefore, both groundwater levels showed small oscillation. Although a well calibration is achieved, the computed groundwater level is slightly higher than the observed groundwater level, namely, the numerical model still possessed some deviations and difficult to fully represent the complexity of real hydrogeological conditions. The calibrated parameters applied in the model were summarized in Table 2.

The rainfall data collected from Sinlerku and Jangmi typhoons, which occurred on September 11, 2008 and September 26, 2008, respectively, were introduced to the model to compute the pore water pressure during two typhoon events. The computed groundwater level was then compared with the observed piezometric level. The corresponding trends were found as shown in Figure 3. The average errors between simulated and observed groundwater levels are ranging from 1.50 to 2.58% for Sinlerku typhoon, and from 0.76 to 0.94% for Jangmi typhoon. It verified that the model is able to represent the real situation.

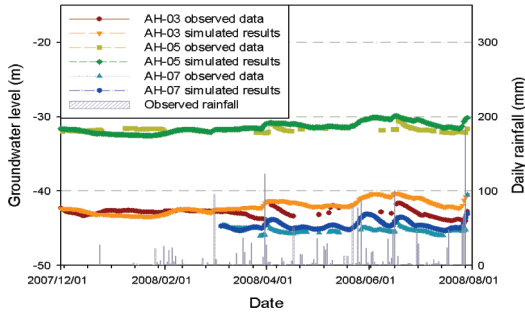


FIG. 2. Comparison of calibrated and observed groundwater level.

Table 1. The error between calibrated and observed groundwater level

Error (%)	Borehole No.	AH-03	AH-05	AH-07
Maximum error		7.40	5.71	3.70
Minimum error		0.08	0.05	0.01
Average error		2.02	2.28	1.82
Standard deviation		1.61	1.33	1.19

Table 2. The calibrated hydraulic parameters and applied mechanical parameters

Parameter	Layer	Colluvial cover	Weathered bedrock	Bedrock
Hydraulic conductivity, K (m/sec)		1.63×10^{-5}	7.94×10^{-5}	7.75×10^{-8}
Volumetric water content, ω (%)		23	22	20
Hydraulic conductivity anisotropy ratio, K_r		1	0.5	1
Unit weight, γ (kN/m ³)		16	22	26
Cohesion, c (kPa)		10	80	500
Friction angel, ϕ (deg)		29	32	42

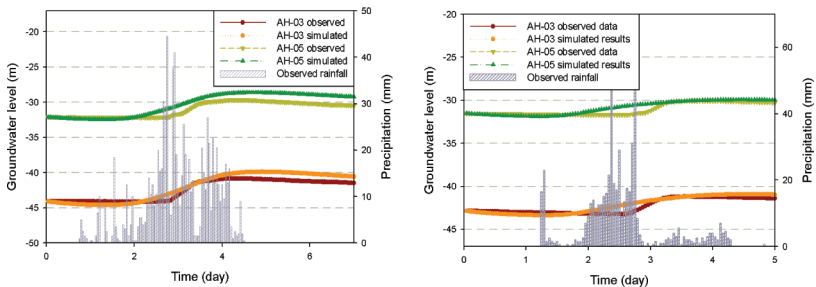


FIG. 3. Comparison of verified and observed groundwater level for Sinlerku typhoon event (left); and Jangmi typhoon event (right).

Slope Stability Analysis

A limit equilibrium method module SLOPE/W was used for the stability analysis. Three slip surfaces, located in the interface between weathered bedrock and bedrock, were recognized and specified to the model based on in-situ investigations including rock core drilling, ground resistivity profiling and borehole image scanning. Considering the unsaturated soil status, the factor of safety computed by SLOPE/W is based on Mohr-Coulomb modified equation suggested by Fredlund (1978). The computed factors of safety during Sinlerku and Jangmi typhoons were shown in Figure 4. Both trends demonstrated that the factor of safety decreased as the rainfall persisted. A more obvious drop in factor of safety, around 7.2~10.1%, was found in the Sinlerku typhoon event. Because the Jangmi typhoon had shorter rainfall duration and smaller rainfall amount, the factor of safety only decreased by 3.2~3.9%. Most results showed the factors of safety are greater than 1.5 at last stage, which implied the landslide site is stable under such rainfall condition. The mechanical parameters applied in SLOPE/W were shown in Table 2.

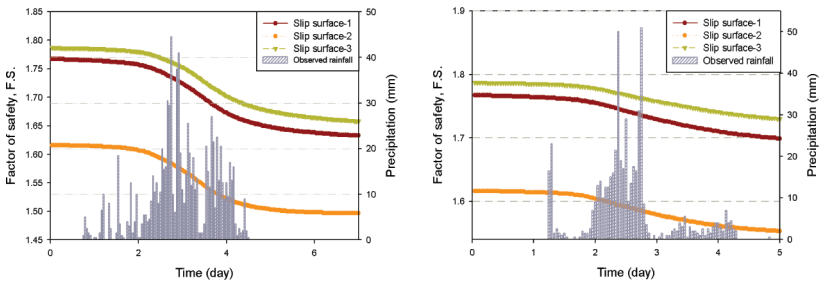


FIG. 4. The computed factor of safety during Sinlerku typhoon event (left); and Jangmi typhoon event (right).

THE RELATIONSHIP BETWEEN THE RAINFALL CHARACTERISTICS AND SLOPE STABILITY

In order to understand the stability of the landslide site under different rainfall characteristics, three types of deigned rainfall conditions, with different patterns, intensity and accumulated amount, were introduced in the model. The designed rainfall was based on the hydrological analysis from the precipitation observed in a rainfall station near the landslide site. The coupled stability analysis was then conducted to establish the relationship between the rainfall characteristics and slope stability.

Rainfall Pattern and Slope Stability

Five rainfall patterns with the same rainfall amount (824 mm) and duration (48 hours), but different precipitation distribution, as model inputs were introduced in the model to perform the stability analysis (Figure 5). The results were shown in Figure 6. At the initial stage, about the first 10 hours, the factor of safety for all rainfall patterns had similar and relatively small decline. As time elapsed, the factor of safety for delayed and

uniform rainfall patterns declined at an accelerated speed while the factor of safety for other three patterns had a relatively constant decline. At the end of time step, 48 hours later, the factor of safety for central, doubled, and uniform rainfall patterns decreased by 4.5%, 4.6%, and 7.2%, respectively. The factor of safety for the advanced rainfall pattern had the smallest drop of 4.1% while that for the delayed rainfall pattern had the greatest drop of 9.9%. It can be concluded that the delayed rainfall pattern threatens the slope stability the most among all the rainfall patterns.

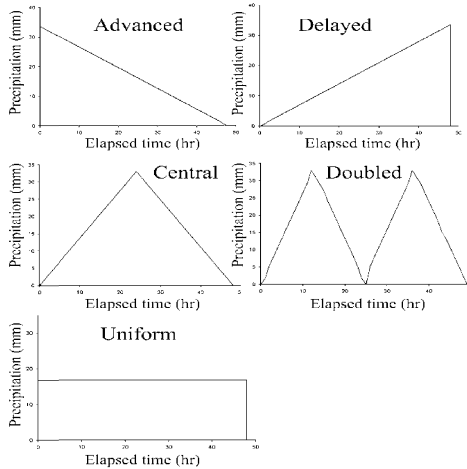


FIG. 5. Types of rainfall patterns adopted in this study.

Rainfall Intensity and Slope Stability

The slope stability under different rainfall intensity was also examined. The results were shown in Figure 7. The factor of safety decreased by 6.8~7.8% when the rainfall intensity at the levels from 11.4 mm/hr to 22.9 mm/hr. However, as the rainfall intensity increases to more than 22.9mm/hr, apparent declines in factor of safety were displayed. Most noticeably, the factor of safety dropped by 16.4% when the rainfall intensity reached to 68.7 mm/hr. Looking at the rainfall intensity at 68.7 mm/hr, 45.7 mm/hr, 22.9 mm/hr and 11.4 mm/hr after 10 hours, the corresponding decreases in factor of safety were 14%, 5.5%, 0.9% and 0.2%, respectively. It demonstrated that the slope stability depends on the degree of rainfall intensity.

The relationship between the rainfall intensity and factor of safety was shown in Figure 9. The factor of safety apparently dropped in a linear trend when the rainfall intensity increased from 22.9 to 54.9 mm/hr. However, the pace of decline eased significantly after the rainfall intensity reached to 68.7 mm/hr. It revealed that a threshold of rainfall intensity on the slope stability existed. Since the hydraulic conductivity of the colluvial cover is 1.63×10^{-5} m/sec (58.68 mm/hr), the rainfall may not fully infiltrate to the layer while the intensity greater than this value. Therefore, it can be concluded that the slope stability closely related to the degree of infiltration that

the layer possesses under various rainfall intensities.

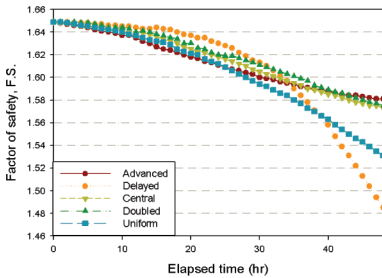


FIG. 6. The computed factor of safety on various rainfall patterns.

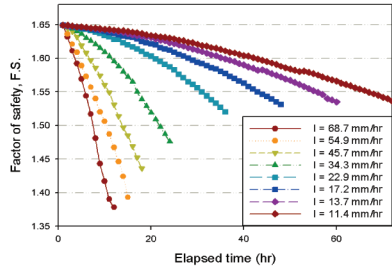


FIG. 7. The computed factor of safety on various rainfall intensity.

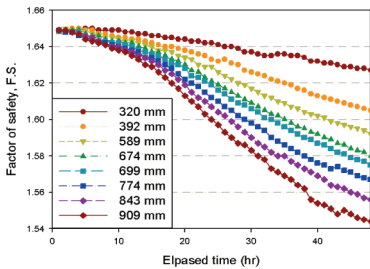


FIG. 8. The computed factor of safety on various rainfall amount.

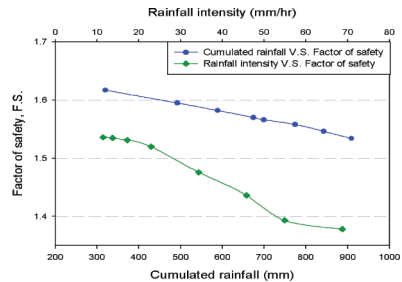


FIG. 9. The relationship between rainfall conditions and factor of safety.

Cumulative Rainfall and Slope Stability

The influence of the cumulative rainfall on the slope stability is finally discussed. The factor of safety under different cumulative rainfall was shown in Figure 8, in which various rainfall amounts applied in the analysis were obtained from rainfall frequency analysis with 48-hour duration. It is apparent that the degree of decline in the factor of safety increased as the rainfall amount increased. The decrease in factor of safety for rainfall amount of 320mm, 674mm and 909mm is 1.3%, 4.2% and 6.4%, respectively. Figure 9 represented the relationship between the rainfall amount and the factor of safety. It also showed that the slope stability slightly decreased as the rainfall amount increased. As the above section described, the groundwater at the landslide site is mainly located in the fractured weathered bedrock. Most rainfall may flow downward to the hillside through the fractures and difficult to remain in the pore space. Therefore, the groundwater may not be easy to rise. Under such circumstance, the factor of safety would not apparently descend.

CONCLUSIONS

This paper used the numerical model to determine the stability of an active landslide site under different rainfall conditions. In order to obtain practical results, the hydraulic parameters in seepage analysis were calibrated according to in-situ long term observed data. Two typhoon events were used to verify the model. The results indicated that the model is capable of simulating the real situation. The coupled stability analysis was then conducted to compute the factor of safety during the typhoon events. The results revealed that the landslide site is stable under the rainfall conditions for two typhoon events. The relationships between rainfall characteristics and slope stability were also discussed. In terms of the rainfall pattern, the delayed rainfall pattern is the type that threatens the slope stability the most. Besides, the simulation revealed that the factor of safety decreased as the rainfall intensity increased. Furthermore, the analysis indicated that the rainfall amount only slightly affect the slope stability. It is due to the higher hydraulic conductivity of the weathered bedrock that engendered the difficulty in accumulating pore water pressure in the layer under different accumulated rainfall amount.

REFERENCES

- Fredlund, D., Morgenstern, N., and Widger, R. (1978). "The shear strength of unsaturated soil." *Canadian Geotechnical Journal*, Vol.15 (3): 313-32.
- Fredlund, D.G. and Xing, A. (1994). "Equations for the soil-water characteristic curve." *Canadian Geotechnical Journal*, Vol. 31: 521-532.
- Gasmo JM, Rahardjo H, and Leong EC. (2000). "Infiltration effects on stability of residual soil slope." *Computer and Geotechnics*, Vol. 26: 145-165.
- Rahardjo, H., Li, X.W., Toll, D.G., and Leong, E.C. (2001). "The effect of antecedent on slope stability." *Geotechnical and geological Engineering.*, Vol. 19: 371-399.
- Blatz, J.A., Ferreira, N.J., and Graham, J., (2004). "Effects of near-surface environmental conditions on instability of an unsaturated soil slope." *Canadian Geotechnical Journal*, Vol. 41: 1111-1126.
- Casagli, N., Dapporto, S., Lbsen, M.L., Tofani, V., and Vannocci, P. (2006). "Analysis of the landslide triggering mechanism during the storm of 20th-21th November 2000, in Northern Tuscany." *Landslides*, Vol. 3: 13-21.
- Cascini, L., Gulla, G., and Sorbino, G. (2006). "Groundwater modelling of a weathered gneissic cover." *Canadian Geotechnical Journal*, Vol. 43: 1153-1156.
- GEO-SLOPE International Ltd. (2007). *Seepage Modeling with SEEP/W, user's guide second edition. GEO-SLOPE International Ltd.*, Calgary, Alta.
- GEO-SLOPE International Ltd. (2007). *Stability modeling with SLOPE/W, user's guide second edition. GEO-SLOPE International Ltd.*, Calgary, Alta.
- Calvello, M., Cascini, L., and Sorbino, G. (2007). "A numerical procedure for predicting rainfall-induced movements of active landslides along pre-existing slip surfaces." *International Journals for Numerical and Analytical Methods in Geomechanics*, Vol. 32: 327-351.
- Cascini, L., Cuomo, S. and Guida, D. (2008). "Typical source areas of May 1998 flow-like mass movements in the Campania region, Southern Italy." *Engineering Geology*, Vol. 96: 107-125.

Integrating Vegetation Role in Computer Simulation for Slope Stability: the Case Study of a Railway Embankment

Andrea Benedetto

Associate Professor, Dept. Sciences of Civil Engineering, University Roma Tre, via Vito Volterra, 60, 00146 Rome, Italy: benedet@uniroma3.it

ABSTRACT: The problem of slope stability has been studied for many decades, but the contribution of vegetation to stability has typically been treated empirically. In this paper we propose to include a rational model for the role of vegetation in a global computer simulation to evaluate stability. Vegetation can perform an important engineering function because of its influence on the soil, both in terms of hydrological and mechanical aspects. Here two advanced numerical models are coupled, one for the hydrological simulation of soil wetting and drying and one for geotechnical simulation of the slope stability. The simulation of a railway embankment has been carried out, and effects of different vegetation properties on stability investigated. This approach is very flexible, efficient and effective to postulate the expected Factor of Safety of a critical slip surface.

INTRODUCTION

Economical and social growth is, at once, consequence and cause of a wide development of new transportation infrastructures. High Speed Railways and Highways are the main lines of the actual. The old and oldest transportation infrastructures have different destinies all over the world: sometimes they are not considered for possible reuse and sometimes are rehabilitated for secondary aims or for low speed connections. But such railways have been often constructed at the beginning of the twentieth century using inadequate material. The reuse of such railways, constituted for example with clayey soil embankments, need some rehabilitation, structural stabilization and finally some stability check. Recently some researchers have been investigating on the contribution to stability of vegetation. The approach is always empirical. Here a new approach based on numerical simulation is proposed with the overall objective to develop a novel general method for checking the stability of vegetated embankments.

THE VEGETATION ROLE FOR SLOPE STABILITY

It is not easy to quantify the effect of vegetation but some empirical equations have been proposed that can be used to evaluate the contribution of vegetation to the Factor

of Safety (FoS) of a critical slip surface. Such a contribution depends on the RAR . RAR is the rate between the roots cross section (A_R) and the cross section of the area where the roots are (A):

$$RAR = \frac{A_R}{A} \quad (1)$$

It can be calibrated from empirical methods. The roots give a contribution to the stability increasing the shear strength (τ_v). This can be estimated, knowing the average roots cohesion (T_R), from the following empirical equation:

$$\tau_v = 1.2 \cdot T_R \cdot RAR \quad (2)$$

This contribution can be easily integrated in the Mohr-Coulomb equation. Vegetation also plays a role against stability. This is the obvious consequence of the vegetation weight (P_v). The evaluation of the vegetation weight can be done using the dendrometric tables or some empirical formulations. Also this contribution can be easily integrated in the Mohr-Coulomb equation. Moreover vegetation plays the fundamental role in the transpiration and in the suction that will be discussed in the following sections.

THE HYDROLOGICAL PROCESSES AT THE SLOPE SCALE

The two main hydrological processes are the infiltration and the evaporation/transpiration (*Griffiths and Lu, 2004*). Considering the small dimension of an embankment slope, the runoff can be neglected in a first approximation, especially in the case of vegetated slope where erosion is generally not present. Using the well known model proposed by Penman the potential evaporation (E_p) and transpiration (T_p) can be expressed as it follows (the variables are explained in *Chow et alii, 1988*):

$$E_p = \frac{1}{\lambda \rho_w} \cdot \left[\frac{\Delta}{\Delta + \gamma} (R_n - G) + \frac{c_p \rho_a (e_a^* - e_a)}{(\Delta + \gamma) \cdot r_a} \right] \quad (3)$$

$$T_p = \varepsilon_{pt} \cdot \frac{\Delta (R_n - G)}{\lambda \rho_w \cdot \left[\Delta + \gamma \cdot \left(1 + \frac{r_{c,\min}}{r_a} \right) \right]} \quad (4)$$

where: λ evaporation latent heat, ρ_w water density, γ psicrometric constant, R_n net solar radiation, G soil heat flux density, ρ_a air density, r_a aerodynamic resistance of vegetation, ε_{pt} Brutsaert's coefficient, Δ slope of the vapour head curve at saturation, $r_{c,\min}$ minimum resistance of vegetation, $r_{s,\min}$ minimum stomatic resistance.

The real evaporation (E) and transpiration (T) are limited by the value of E_p and T_p and depend on the climatic conditions. The quantitative evaluation of the effects of vegetation can be done only in two ways: the traditional one that it is based on the measurements of moisture content variability or the novel way, that is here proposed, using numerical simulation of all the processes.

THE NUMERICAL APPROACH

In this paper a full simulation approach is proposed to evaluate the stability of embankments. The steady boundary conditions are determined from the geometry and

geo-mechanical characteristics of the soils constituting the embankments. The boundaries are assigned through a finite element model of the embankment. The variable boundary conditions, such as the variability in time of rain intensity, air humidity, temperature are assigned from historical data bases. The initial conditions such as moisture content or water table level are assigned through the finite element model from initial hypothesis or measurements. Evaporation and transpiration are computed using the Penman equations, the soil moisture all over each element of the model is evaluated using the VS2DTI software. VS2DTI is a graphical user interface for simulating water and solute transport through variably saturated porous media (*Lappala et al., 1987*). The model of the soil assumed here is the Van Genuchten model with the SWCC curve for suction-water content relationship. For the determination of the SWCC curve the model of *Fredlund and Xing (1994)* is here used. The parametric equations of the SWCC model follow here (also in this case the variables are well explained in the mentioned literature):

$$\theta = \theta_s \cdot \left\{ \frac{1}{\ln \left[e + \left(\frac{\psi}{a} \right)^n \right] \right\}^m \quad m = 3.67 \cdot \ln \left(\frac{\theta_s}{\theta_i} \right) \quad n = \frac{1.31^{m+1}}{m \cdot \theta_s} \cdot 3.72 s \psi_i \quad (5)$$

$$s = \frac{\theta_i}{\psi_p - \psi_i} \quad a = \psi_i \quad (6)$$

where: θ , θ_s , θ_i normalized, saturation, volumetric at the inflection point of the SWCC curve water content, e Euler's number, ψ matrix suction, ψ_p suction in linear approximation, ψ_i suction at inflection. Here the equations of the *Van Genuchten* model follow (the variables are well explained in literature: *Porębska and alii, 2006*).

$$\Theta = \frac{1}{\left[1 + \left(\frac{\alpha}{h} \right)^n \right]^{-m}} \quad \Theta = \frac{\omega - \omega_r}{\omega_s - \omega_r} \quad m = 1 - \frac{1}{n} \quad (7)$$

where h total hydraulic head and α , m , n Van Genuchten's parameter

Integrating these equations in the finite elements domain it is possible to calculate the variability of the moisture content and the suction in time all over the embankment. The matrix suction depends on the moisture content in soil (*Vanapalli and alii, 1995*): as this reduces the matrix suction increases and with it the shear strength (τ_f) increases less than linearly. In this case the Fredlund equation has been assumed:

$$\tau_f = c' + [(\sigma - u_a) \cdot \tan \phi'] + [\psi \cdot \tan \phi^b] \quad (8)$$

$$\tan \phi^b = \Theta \cdot p \cdot \tan \phi' \quad (9)$$

MODEL CALIBRATION AND VALIDATION

Geometrical and geological characteristics

The numerical model has been applied to a real railway embankment. The

embankment is 7 m high, the section at ground level is 20 m wide and the slope is originally very safe as 1:3. The groundwater table is, on the average, 6 m deeper than the ground level. The main characteristics of soils are in table 1. For the FE simulation, half embankment (the embankment is symmetric) is schematized using a grid with 60 lines and 47 columns. The FEM is shown in figure 1.

Climatic data

For simulation a historical database has been used. Here the monthly data for temperature, air relative humidity and rainfall data over three years have been used.

Water content variability and SWCC curve calibration

Using the VS2DTI the process of wetting and drying of embankment has been simulated, assuming the evaporation and transpiration Penman's models. The moisture content profile and the hydraulic head all over the embankment in time (monthly variability) have been calculated. In figure 2 the water content profile in WLC (January) is shown (Vetiver vegetation is simulated). Using the equations (5) to (9) it is possible to calibrate the SWCC curves. The curves for WLC are shown in figure 3.

Scenarios of vegetation

Two different vegetations have been considered here and three different scenarios of vegetated embankment. The effects in terms of stability of Robinia and Vetiver are here evaluated for these 3 possible scenarios: (1) Robinia, (2) Vetiver and (3) Robinia + Vetiver. Robinia pseudoacacia, commonly known as the Black Locust, is a tree in the subfamily Faboideae of the pea family Fabaceae, with a trunk up to 0.8 m diameter (exceptionally up to 52 m tall and 1.6 m diameter in very old trees). Vetiver (*Chrysopogon zizanioides*) is a perennial grass of the Poaceae family. Vetiver can grow up to 1.5 meters high and form clumps as wide. Unlike most grasses, which form horizontally spreading mat-like root systems, vetiver's roots grow downward, 2–4 m in depth. The characteristics of Robinia and Vetiver are summarized in table 2 (Φ diameter; H height; V^* volume; γ_v bulk density; P_v weigh).

Table 1. Main soils characteristics of the railway embankment

Codes ref. figure 1	S1	S2	S3	S4	S5	S6
	BALLAST	TOP SOIL	BRICK GRAVEL	LCF London Clay Fill	WLC Weathered London Clay	ULC Unweathered London Clay
Hydraulic permittivity anisotropy coefficient (K_{zz}/K_{hh})	1	1	1	1	1	1
Horizontal hydraulic permittivity (K_{hh})	100 m/day	2 m/day	1.9 m/day	0.048 m/day	0.048 m/day	0.040 m/day
Specific storage (S_s)	0 m ⁻¹	0 m ⁻¹	0 m ⁻¹	0 m ⁻¹	0 m ⁻¹	0 m ⁻¹
Porosity (n)	40 %	30 %	30 %	30 %	30 %	30 %
Residual moisture content (RMC)	0 %	5 %	0.6 %	0.7 %	0.7 %	0.7 %
Van Genuchten's parameter a	0.1	0.007	0.032	0.8	0.8	0.8
Van Genuchten's parameter b	50	1.119	1.368	1.09	1.09	1.09

Table 2. Characteristics of Robinia and Vetiver (Focks, 2006)

	T_r [kN/m ³]	RAR	Φ [m]	H [m]	V^* [m ³]	γ_v [kN/m ³]	P_v [kN]
Robinia	68,000	0.0001	0.30	10.00	1.60	8.00	5.00
Vetiver	80,000	0.0004	-	1	-	-	1.00

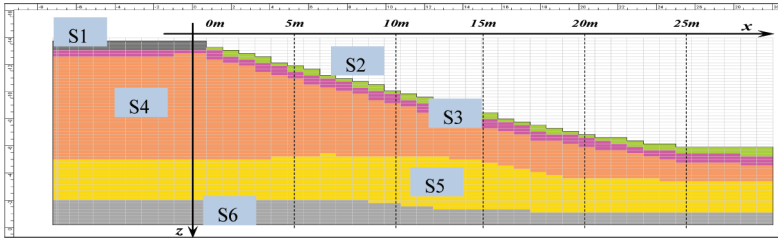


FIG. 1. Finite Elements Model of half embankment

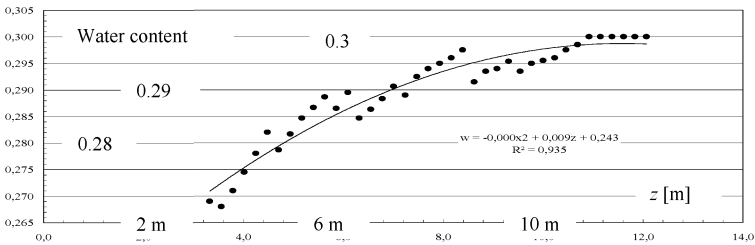


FIG. 2. Water content profile in WLC (January)

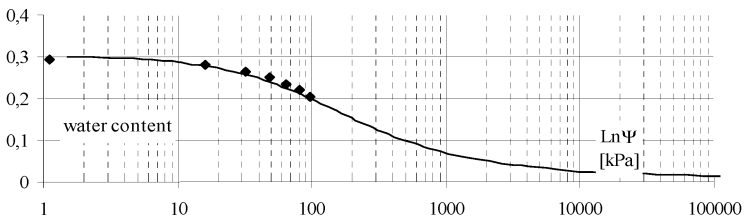


FIG. 3. Water content – suction SWCC curve in WLC

Evaluation of the Factor of Safety

The evaluation of the FoS of the railway embankment has been carried out using the traditional integral methods of Bishop and Fellenius. To apply these methods the outcomes of the FEM have been averaged in z. More in depth, from the FEM outcomes the average water content $w=f(\text{month})=\langle f(z, \text{month}) \rangle$ and the average hydraulic head $h=g(\text{month})=\langle g(z, \text{month}) \rangle$ are calculated (where f and g are the mean functions). Basing on the traditional stability model (Morgenstern and Price’s method), the variability of FoS over months has been evaluated using Bishop and Fellenius equations

and referring to the three vegetation scenarios. The outcomes are in table 3. As mentioned, in the present case the slope is originally very safe.

CONCLUSIONS

The problem of the stability of embankment has been evaluated in the case of non adequate material, integrating the role of vegetation. A numerical approach has been followed. This novel approach demonstrates that it is possible to quantify the contribution of the vegetation. The variability over time can be easily taken into account. The FoS increases on the average, for the simulated embankment respect to not vegetated slope, from 5 to 10 %, in the case of Robinia, from 84 to 91 %, in the case of Vetiver, and from 49 to 55 %, in the case of Mix. Finally the simulation over the time puts in light that the monthly variability of the FoS is very limited (less than 5%) and can be neglected, in a first approximation.

Table 3. Factors of Safety from different models scenarios (*Standard Dev.*).

Fellenius		Bishop		Fellenius			Bishop		
No vegetation		Robinia	Vetiver	Mix	Robinia	Vetiver	Mix		
2,73	2,89	3,01	5,21	4,22	3,05	5,33	4,30		
(0.055)	(0.058)	(0.048)	(0.058)	(0.058)	(0.057)	(0.069)	(0.054)		

ACKNOWLEDGMENTS

Author thanks Dr. Alessandro Simone for calculations and implementing models.

REFERENCES

- Chow, V.T., Maidment, D.R. and Mays, L.W. (1988). "Applied Hydrology." *McGraw Hill Inc.*, Singapore
- Focks, D.J.J. (2006). "Vetiver grass as bank protection against vessel – inducted loads." *Delft University of Technology* (Holland)
- Fredlund, D.G. and Xing, A. (1994). "Equation for the soil water characteristic curve." *Canadian Geotechnical Journal* (Canada).
- Griffiths, D.V. and Lu, N. (2004). "Unsaturated slope stability analysis with steady infiltration or evaporation using elasto – plastic finite elements." *Int. J. for numerical and analytical methods in geomechanics* (USA).
- Lappala, E.G., Healy, R.W. and Weeks, E.P. (1987). "Documentation of computer program VS2D to solve the equations of fluid flow in variably saturated porous media." *U.S. Geol. Survey Water-Res. Investig. Report*, vol. 83-4099. 184 p.
- Porębska, D., Slawiński C., Lamorski K. and Walczak R.T. (2006). "Relationship between van Genuchten's parameters of the retention curve equation and physical properties of soil solid phase." *International Agrophysics* (Poland).
- Vanapalli, S.K., Fredlund, D.G., Pufahl, D.E. and Clifton, A.W. (1995). "Model for the prediction of shear strength with respect to soil suction." *Canadian Geotechnical Journal* (Canada).

Optimal Design of Waste-Dump Slope of Open Pit Mine Based on Strength Reduction FEM

Jin-Sheng Lei^{1,2}, Da-Peng Zhu², Hui Peng¹, Yue Li²

¹Associate professor, College of Civil & Hydroelectric Engineering, China Three Gorges University, Yichang, 443002, China; lei-jinsheng@163.com

²Ph.D candidate, Faculty of Engineering, China University of Geosciences (Wuhan), Wuhan, 430073 China; zhudp@yangtzeu.edu.cn

ABSTRACT: Based on strength reduction theory, finite element method (FEM) was selected to analyze the potential destroy mode of some waste-dump slope of open pit mine in Tongchuan city of Shanxi province. Slippage surface develop character and corresponding safety factor variation disciplines under different slope height and angle also were obtained. According to principle of the maximal bear volume, the optimal slope height and angle would be defined. the potential destroy mode showed that waste-dump slope shoulder belongs to tensile failure, and waste-dump mass slides like a circle spoon, and slippage surface incise the bottom rock when the slope height reached some value. Slippage scope enlarged with the slope height increasing under the natural condition, and slippage surface trend rearward. Comprised with the natural condition, depth and scope of slippage surface was bigger under saturation condition. So the optimization design has important economic effects for reducing land occupation and increasing the maximum waste-dump capacity.

INTRODUCTION

With the increasing of the human engineering activities and the expanding of engineering field gradually, now the stability analysis and optimization design of high and steep slope become one of the frontier problems.

The high and steep dump-waste slope of open pit mine is one typical artificial accumulated slope, and its stability has direct influence on the operation and safety production of open-pit mine. Once the landslide occurs, it not only has a threat to people's lives and property, but also destroys the surrounding ecological environment. For an example, Antaibao waste dump of Pingshuo mine area (Zhang, 2004), Fengjiaxigou waste dump of Nafen open pit iron mine (Zhang, 2009)and waste dump of North Huolin River open-pit mine (Li, 2006), landslides occurred in these waste dumps with a great loss. Therefore, it has great theoretical significance and social effects to study the potential destroy mode and scope of the high and steep waste-dump slope for reducing engineering accident, and ensuring the normal operation of open-pit

mine, and protecting the security of people's lives and property.

At present, the research on waste-dump slope of open pit mine mainly focuses on the analysis and evaluation of slope stability (Pan, 2002, Huang, 2007). The main methods for stability evaluation are limit equilibrium method (LEM) and finite difference method (FDM). In recent years, finite element method (FEM) was widely used in geotechnical engineering field, because FEM considered the stress-strain relationships of rock or soil by different strength criterions, and it also met the condition of soil static equilibrium, so it overcome some shortages of the assumptions of LEM. However, there is less study on optimization design of waste-dump slope currently, and the optimization design has important economic effects for reducing land occupation and increasing the capacity of the maximum waste-dump.

In this paper, a typical waste-dump slope of open pit mine was taken for an example. The potential destroy mode, slippage surface develop character, and corresponding safety factor variation disciplines was get by strength reduction FEM, and last the optimal slope height and angle was defined.

DESCRIPTION OF STRENGTH REDUCTION THEORY

In nonlinear strength reduction FEM calculations, strength of rock and soil mass reduce continuously, and the slope reaches to an unstable condition when static force does not converge, and the corresponding reduction value is the safety factor (Jiang, 2003). The method needn't to suppose the slippage surface in advance, and when the slope destroyed, the stability coefficient of dump slope, the position and shape of the slippage surface can be obtained, and the distribution of stress and deformation also can be got.

When the soil mass just keep a balance, the stability factor is the ratio of actual shear strength to minimum shear stress for traditional soil mechanics (Zheng, 2004), the expressions is equations (1):

$$F_s = \frac{S}{S_f} = \frac{c + \sigma_n \tan \phi}{c_r + \sigma_n \tan \phi_r} = \sum M_{sf} \quad (1)$$

Where: S is actual strength of soil, S_f is failure strength of soil, $\sum M_{sf}$ is reduction factor when soil or rock mass destroy, c and ϕ are actual strength parameters of soil, σ_n is the actual normal stress component, c_r or ϕ_r are the shear strength parameters when the soil just keep a balanced stress state.

A CASE STUDY

Description of engineering geological conditions. The open-pit mine is located in Tongchuan City of Shanxi Province, which is 3.22~5.34km long from east to west, and 5.34 ~ 9.56km wide from north to south, and its total area is about 38.27 km², the highest and lowest elevations are 1451.83m, 1146.32m separately, so the maximum relative elevation is about 305.51m.

The typical section of the waste-dump slope of open pit mine is shown in the FIG 1. The main material of the waste is a mixture of soil and rock. Foundation stratum is made up of upper silt (Q₃), middle silty clay (Q₂) and the bottom bedrock, The

brown-yellow Q_3 silty soil is the bases of the loess landforms, which is of loose-slightly dense, and hard-plastic, and high-medium compression and vertical joint growth, and its average thickness is 21m. Red Q_2 silty clay is of dense, hard plastic and low-medium compression, which contained ferromanganese spots, calcium nodule and mica, and its average depth is 16m. The bedrock is the coarse gray sandstone of upside Shanxi Formation, moderately weathered, with the coarse-grained structure and the medium thick layered structure, and the level and oblique bedding could be seen.

Establishment of the model of elastic-plastic finite element. Three-dimensional dump was simplified as plane strain problems so that the computing time would be shorten, and the calculating slope model by FEM should be in conformity with the actual form, so the typical profile of mesh model was shown in FIG 2.

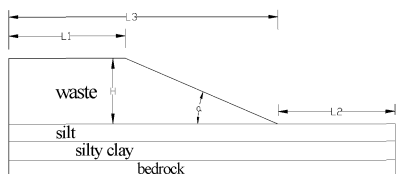


FIG. 1. Typical section of waste-dump.

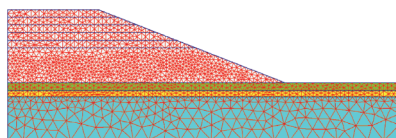


FIG. 2. Finite element mesh.

According to the characteristics of topography, for the sake of the boundary effect elimination, the boundary condition of slope is constructed as below: the lower boundary is 150 m below the ground, so the bedrock thickness is about 110m. The distance L_2 from the toe of slope to the right border is 300m around, and the distance L_1 from the slope shoulder to the left side boundary is about 1-2 times as long as the limit slope height H , and the distance L_3 from the toe of slope to the right side boundary is 800m. Both the horizontal and vertical directions of the lower boundary are restrained, and the left and right boundaries are restrained horizontally. It is considered to approximately obey the static soil pressure distribution at two sides. Only gravity load is considered, and impact of structures also is ignored.

All the rock and soil of dump slope adopt ideal elastic-plastic model, and obey the Mohr-Coulomb failure criterion. The mechanical parameters of the waste are defined by the method of engineering geological analogy, which is in accordance with the parameter of disposable materials which sampled from the sites nearby the open-cut coal mine dump. The mechanical parameters of silt, silty clay, and coarse sand are shown in Table 1, they are defined on the basis of the indoor test, field test and some local experiences.

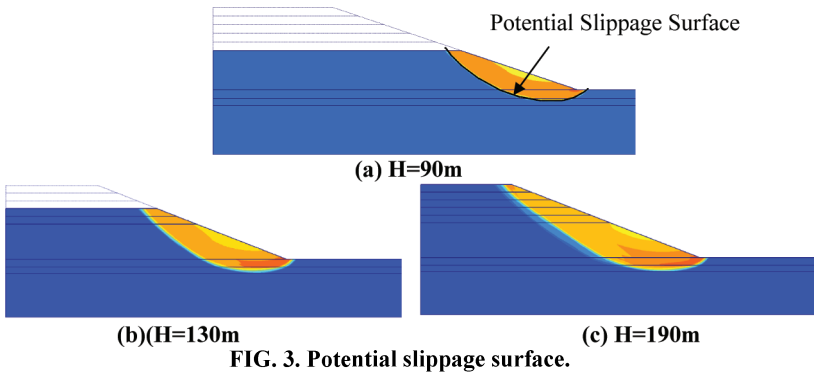
Because the site was lack of rain, so the water level fluctuation in waste-dump mass was ignored, just foundation soil would be considered to be saturation or nature condition.

Working conditions for calculation. The different slope height $H = 90\text{m}, 110\text{m}$, etc, and the different slope angle $\alpha = 21^\circ, 22^\circ$ were taken respectively for strength reduction finite element calculation under the natural and saturation conditions.

Scope of potential slippage surface and destroy mode. Taking the 21° slope for an example, when H changed as 90m, 130m, 190m, the potential slippage surfaces under nature condition were shown in Figure3 (a)-(c) respectively.

Table 1. Mechanics Parameters of Soil and Rock Mass.

Soil layer	Condition	Compression Modulus (MPa)	Poisson' Ratio	Cohesive Force (kPa)	Friction Angle (°)	Weight KN/m ³
Waste		4.2	0.31	20	28	19.7
Silt	natural	4.8	0.31	24	21	16.5
	saturated			17	17	19.3
Silty Clay	natural	11.3	0.34	45	17	20.5
	saturated			20	14	21.4
Sands tone		4021	0.15	250	43	25.5



Contrasting FIG 3 (a)-(c), when slope height is 90m, the potential slippage surface is near the interface between the silt and silty clay. When the height increases 40m to 130m, slippage surface moves to the interface between the silt and the bedrock. And then when the height adds 60m from 130m to 190m, the depth of the slip surface do not increase, but the range of the slip surface enlarges. Therefore, with the increasing of the slope height, the slippage scope enlarges until slippage surface reaches to the interface between the covering layer and the bedrock, meanwhile the whole slippage surface has the trend of moving backward.

Taking the 21° slope for an example, FIG 4 (a)-(b) shows the position of the slip surface under the saturated condition with H=110m ,190m.FIG 4 (a) shows that when the slope height is 110m, the depth of the slip plane has been increased to the nearby interface between silty clay and bedrock. When the height is 190m, the scope of the silty clay and silty incised by the potential slippage surface (FIG 4 (b)) under saturated condition is larger than that under the natural condition (FIG 3 (c)).

From FIG 3- FIG4 we can get the potential destroy mode: the upside waste-dump is pulled to destroy, and then it slides along the soil layer circle like a circle spoon, and the slippage surface incises the bottom rock when the slope height reaches some value. The main reason is that the waste of dump is soil-rock mixtures, and its strength is stronger than lower silt and silty clay. So the soil layer is easy to distort and move under waste material loads action.

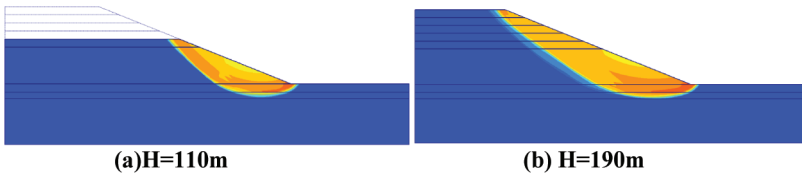


FIG. 4. Potential slippage surface.

Maximal height of waste-dump slope. The permissible safe factor is related with the importance grade of the project and service years, etc. As to important project, the safe factor should be taken between 1.30 and 1.50 (CIGIS, 2001). Meanwhile, when limit service time for the waste dump slope is more than 20 years, the safe factor should be taken between 1.20 and 1.50 (CCCA, 2005). Considering that the destroy mode of the waste dump is clear by strength reduction method, at the same time, the field hydrological geology and engineering geology are simple relatively. So the safety factor can take 1.30 under nature condition and 1.20 under the saturated condition to satisfy the above two specifications.

Base on the strength reduction theory, we get the stability coefficient contrast diagram under nature and saturated condition when the slope angle α changed as $21^\circ, 22^\circ$ and the height H changed as 90m, 110m, 130m, 150m, 170m, 190m separately. As shown in FIG 5, we can know:

(1) With the increase of the waste-dump slope height H , the slope stability descent gradually under the same slope angle and working conditions.

(2) Under the same emission height, when the slope angle is 21° , the stability factor of the waste-dump slope under he saturated condition is about 8%-11% lower than it when the slope angle is 22° , and is about 11%-13% lower than it under the nature condition .

(3) When the slope angle is 22° , the maximum height is about 170m under nature condition, but 140m under the saturated condition.

(4) When the slope angle is 21° and the height is from 90 m to 190m, all stability factors are more than 1.3 in the nature condition. In consideration of the linear distribution between the slope stability factor and the height, we get the formula by fitting (FIG 6): $FOS = 1.4626667 - 0.0013 \times (H - 120)$. When the safety factor is 1.30, the corresponding maximum height is 208m.

(5) Under saturated condition, the maximum height is 170m when the slope angle is 21° . So the optimal slope height and angle was 21° according to principle of the maximal bear volume.

CONCLUSIONS

(1) Under the natural condition, with the increasing of the height, the scope of slope sliding also enlarges continuously, until the slippage surface reaches to the interface between the covering layer and bottom rock, meanwhile the whole slip surface has the trend of moving backward.

(2) The depth and range of the foundation soil incised by the potential slip surface under saturated condition are bigger than that under the natural condition, and they have the same moving backward tendency.

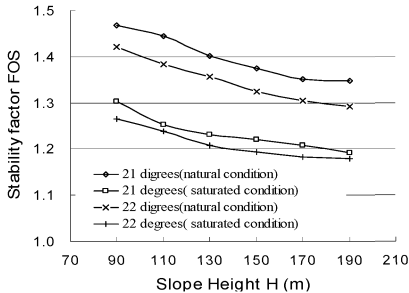


FIG. 5. Contrast diagram of FOS.

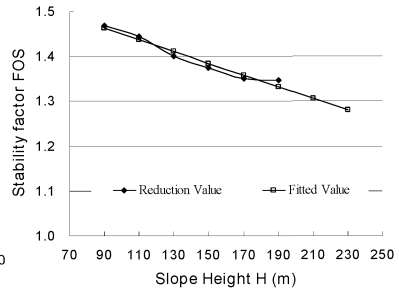


FIG. 6. Fitting chart of FOS and H.

(3) The potential destroy mode was that the upside waste-dump was pulled to destroy, and it slides like a circle spoon in waste-dump mass, and slippage surface incise the bottom rock when the slope height reached some value.

(4) Compared with slope height, the effect of slope angle is sensitive, so the angle should be controlled strictly on detailed design and later construction.

REFERENCES

- China Coal Construction Association (CCCA). (2005). "Code for design of open pit mine of coal industry." *China Planning Press*, 31-33. (in Chinese)
- China Institute of Geotechnical Investigation and Surveying (CIGIS). (2001). "Code for investigation of geotechnical engineering." *China Architecture and Building Press*, 40-41. (in Chinese)
- Huang, M. and Li, X.B. (2007). "Analysis on slope stability of a mine dump." *Engineering of Mining and Metallurgy*, Vol. 27 (5): 12-15. (in Chinese)
- Jiang, F.X. and Wang, Y.B. (2003). "Analysis on slope stability of waste-dump of Waitoushan." *Journal of Liaoning Engineering and Technology University*, Vol. 22 (suppl): 109-111. (in Chinese)
- Li, Y.J. and Qi, F.X. (2006). "Analysis and countermeasure on landslide mechanism of open-pit main waste-dump of north Huolin River." *Open-pit Mining Technology*, Vol. 3: 14-15. (in Chinese).
- Pan, J.P. and Huang, R.Q. (2002). "Study on 3-d numerical simulation of slope stability on open-pit mine dump of Panzhihua." *Journal of ChengDu University of Technology*, Vol. 29 (3): 329-333. (in Chinese).
- Zhang, W.G. and Xie, L.J. (2004). "Discussion on landslide mechanism of the waste-dump underlined loess." *Open-pit Mining Technology*, Vol. 3: 16-18. (in Chinese).
- Zhang, Z.B. and Li, L.B. (2009). "Analysis on slope stability of the east ditch of Fengjia of Nafen open-pit iron mine." *Bengang Technology*, Vol. 1: 1-5. (in Chinese)
- Zheng, Y.R. and Zhao, S.Y. (2004). "The application of finite element strength reduction in slope of soil and rock." *Chinese Journal of Rock Mechanics and Engineering*, Vol. 23 (19): 3381-3388. (in Chinese).

Risk Analysis of Individual Landslide in the Three Gorges Reservoir

Li-Xia Chen¹, Kun-Long Yin², Yang Wang³

¹ Doctor, Institute of Geometrics and Geophysics, China University of Geosciences, Hongshan district, Wuhan city, Hubei province, China; ch_l_x@163.com

² Prof., School of Engineering, China University of Geosciences, Hongshan district, Wuhan city, Hubei province, China; wangyangcug@126.com

³ Associate Prof., Graduator school, China University of Geosciences, Hongshan district, Wuhan city, Hubei province, China; yinkl@cug.edu.cn

ABSTRACT: Landslide along the reservoir bank with secondary surges can form a hazard chain, causing greater risk than the landslide itself. Taking Zhaoshuling landslide in the Three Gorges reservoir as an example, the methodology of landslide risk analysis, including risk identification, probability, vulnerability and hazard consequence are discussed in this paper. The landslide risk is identified by field inventory firstly. The annual probability is calculated by Monte Carlo method according to landslide geology environment. The hazard intensity, landslide velocity and volume moving into water are assessed by Newton's Second Law and kinematic equation. Based on the results, landslide initial surge height and propagation distance, which are important references for surge influence area, are calculated by Pan's method. In this area, elements at risk are identified and the vulnerability is assessed for buildings and persons. Based on the result of hazard and vulnerability, economic and people risk assessment is made. It shows that landslide may cause about 15.447 million RMB annual economic risk and 4.721 people risk with annual probability 0.07556, and about 7.008 million RMB annual economic risk and 10.04 people risk with annual probability 0.03406. These findings can help local authorities to manage landslide risk and make emergency measures.

INTRODUCTION

Landslide hazard is the combination of geological phenomena with human society and economic activities. Surge hazard caused by landslide can form a hazard chain, leading to stronger damage and higher risk which has been reported by many previous investigations (Yin and Peng, 2007). There are relatively the most landslides and most severe damage and losses in The Three Gorges reservoir in China. Therefore, research of landslides risk assessment and management and the related secondary hazard is very urgent now.

Since Gill (1974) and Stevenson (1977) proposed the concept of risk to landslide

research in the last century, the research of landslide risk assessment has been developed in many countries and regions. After that, Varnes (1984) developed a basic and uniform conception in a project of UNESCO. Hazard risk is defined as follows:

$$Risk = H \times V \times E$$

where H is the probability of landslide with a given intensity in a given time; V is the vulnerability of the property or people, and is defined as the level of potential damage, or degree of loss, of a given element (expressed on a scale of 0 to 1) subjected to a landslide of a given intensity (Fell, 1994; Leone et al., 1996; Wong et al., 1997). E is the element at risk (e.g. the value of the property).

Many countries and regions, where landslides hazards are frequent, have already done a lot of work on landslide risk assessment (Evans, 1997; Australian Geomechanics Society, 2007). For macroscopic risk control, these methodology and theory have been developed according to the demand of regional hazard risk management. But with the development of economy and society, macroscopic hazard risk control can not satisfy social requirement today. The demand of individual hazard risk research or special elements risk assessment is becoming a problem.

The objective of this study is to find out a valid method to assess the risk of individual landslide along reservoir bank. Fig. 1 shows the basic framework for individual landslide risk analysis along reservoir bank. This study is a first step toward risk management of individual landslide along reservoir bank.

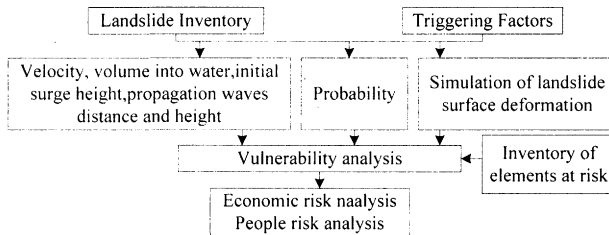


FIG. 1. The framework for risk analysis of landslide along reservoir bank

LANDSLIDE GEOLOGICAL SETTING

Zhaoshuling landslide locates in the Three Gorges reservoir, 74 km west of the famous dam (Fig. 2). A detailed longitudinal profile is shown in Fig. 3. The landslide is an extremely large rock landslide and located in fragment limestone of middle Triassic age. Three types of materials were identified during detailed field inventory: a middle Triassic substratum Badong group, described as brown-yellow limestone, fragment stones with soil and silt with fragment stones. Field survey shows that the landslide is relatively stable now. But the landslide has great probability to be unstable under water level fluctuation, or coupled with rainfall.

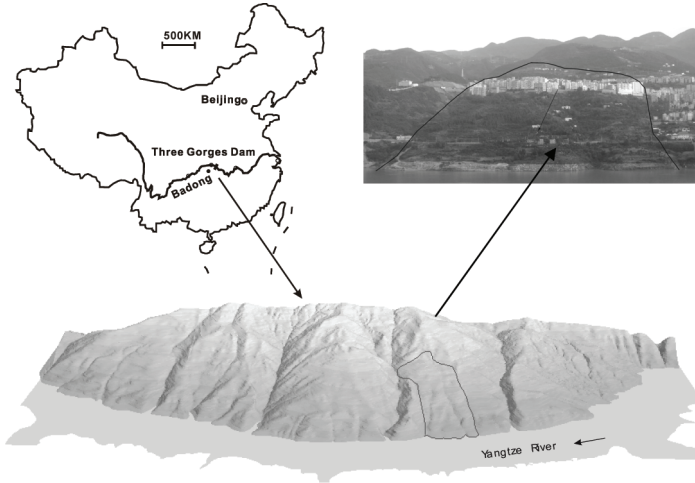


FIG. 2. Location and general view of Zhaoshuling landslide.

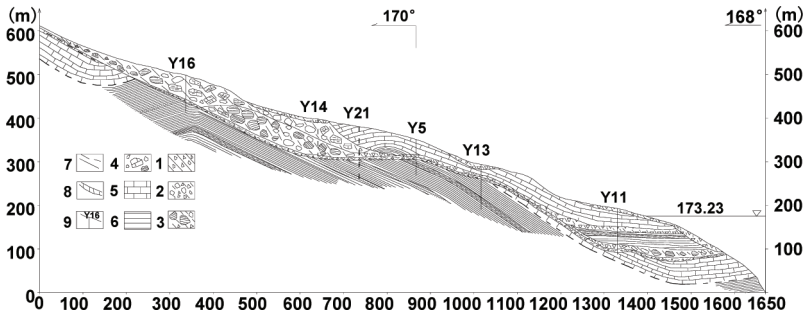


FIG. 3. Geological profile of Zhaoshuling landslide (Comprehensive investigation Bureau of Changjiang water resources commission, China,1995).

Legend: (1) Silt with fragment stones; (2) Fragment stones with silt; (3) Red silt stone fragments with silt; (4) Brawn limestone fragments with silt; (5) Limestone; (6) Mudstone, silt stone and muddy siltstone; (7) Geological boundary; (8) Slide zone; (9) Borehole.

PROBABILITY ANALYSIS OF LANDSLIDE STABILITY

Most landslide occurrence has great relationship with rainfall, especially extreme rainfall event. It is because the rainfall could increase pore pressures, and thus leads to rainfall-triggered landslides. Extreme rainfall event means the events with extreme values of multi-days accumulative rainfall or rainfall intensity. To obtain the

probability of rainfall induced landslide stability, assuming that extreme rainfall event is A , landslide event is B , then the probability can be expressed as

$$P = P[A]P[B|A].$$

If the probability of extreme rainfall event is in return period T , then $P[A]$ can be replaced by $1/T$. Based on the theory of Gumbel extreme value distribution, 17 years daily rainfall data from 1990 to 2006 were analyzed. In the Three Gorges reservoir, there are four periods for water level fluctuation: 145m, 145m to 175m, 175m, 175m to 145m. Rainfall analysis shows that different period has different rainfall characters. In this study, water level from 175m to 145m and extreme rainfall with ten return years' time was chosen as the condition for landslide risk analysis. It was found that the study area during this period mainly experiences long time but low intensity rainfall. Fig. 4 shows the expected rainfall in a given number of consecutive days for a given return time T in years, from which the value of rainfall with return time T can be easily obtained.

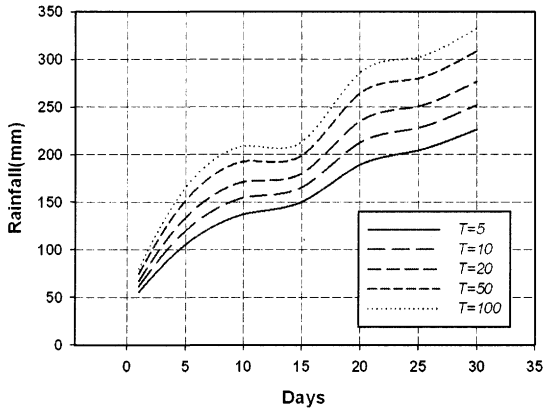


FIG. 4. Expected rainfall in a given number of consecutive days for a given return time T in years during the period of water level from 175m to 145m.

To obtain landslide probability under the above condition, seepage simulation was performed in this study. Then the method of transfer coefficient and Monte Carlo simulation was adopted. Because the landslide geological condition is highly complex, the predicted landslide velocity should be a value with some probability. Then landslide volume, initial water wave and propagation wave height based on velocity calculation should be also a value with corresponding probability. After cutting the landslide into multiple slices, the acceleration and speed for each slice can be calculated by considering the forces of water in reservoir (Wang, 2005). The landslide was thought to stop when the speed of some slice was not higher than zero. Then the number and volume of the landslide running into water can be obtained. Applying Pan's method (Pan, 1980), initial surge height, propagation wave distance, height and

climbing elevation were calculated. The result shows that the landslide may damage in the toe at a speed of 1.0 m/s with annual probability 0.07556, and about 894 thousands cubic meters rock and soil may move into water, causing initial surge 9.00 m ; and it may damage in the toe at a speed of 5.0 m/s with annual probability 0.03406, and about 3578 thousands cubic meters rock and soil may move into water, causing initial surge 43.2 m. It also indicated that the generated waves will propagate upstream and downstream, which will bring great risk to the ships, docks and residents living by the bank if the wave height exceeds the circular value. Fig. 5 shows the curves of propagation wave and climbing wave height along the reservoir if landslide damages in the toe and occurs at the speed of 5m/s.To induce such secondary risk, quantitative assessment should be made.

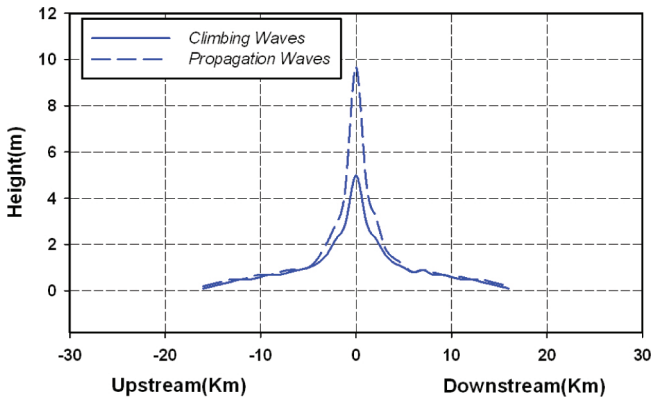


FIG. 5. Curves of propagation wave and climbing wave height along the river

INVENTORY SURVEY FOR ELEMENTS AT RISK AND VULNERABILITY ANALYSIS

With the help of quick bird images and field survey, economic characters of elements at risk were obtained and they are shown in Table 1. Table 2 and Table 3 respectively show people in buildings on the landslide and people in vehicles at risk. Table 4 shows docks and ships in propagation wave influence area.

Table 1. Economic characters of elements on landslide

Elements and characters		Count	Unit cost (Million RMB)	Elements and characters	Count	Unit cost (Million RMB)
Buildings	Brick-wood	513 m ²	0.0025	Pipeline	600 m	0.006
	Brick	145 m ²	0.005	Electricity transmit line	0.61 m	0.1
	Brick-concrete	4079 m ²	0.008	Vehicle Passenger	1.7	1.2

Note: *D—distance of docks to landslide sites; T* —Ship type; N*— Daily number of ships; H*— Height of propagation waves; τ_n —Ships inherent rolling period ; τ_e —Wave period; V*—ship Vulnerability .

The assessment of vulnerability is the key in risk analysis, but it is difficult especially in quantification (Crozier , 2005;Glade,2005). Dai (2002) pointed out that it is somewhat subjective and largely based on historic records. But if no historical records, simulation may be a feasible way for vulnerability analysis.

Vulnerability of buildings before landslide failure

Considering that buildings vulnerability has close relationship with landslide damage intensity, the buildings deformation was analyzed based on landslide surface deformation simulation results, the theory of building deformation and failure caused by mining (Yan, 1995). Based on the national building damage classification standard (China Coal Industry Bureau, 2000), vulnerability of all the buildings on landslide was semi-quantitatively evaluated. Table 5 presents the results with maximum damage degree of all the buildings.

Table 5. Deformation and damage degree of buildings on landslide

No.	ε (mm/m)		d_z (mm)		i (mm/m)		Degree or vulnerability(%)
	BA	BC	BA	BC	BA	BC	
1007	0.13	0.08	35.5	15.84	2.74	0.34	Extremely slight(5%)
2032	0.76	0	0	36.16	0	2.09	Extremely slight(5%)
2035	0.06	0.04	29.5	43.92	4.11	1.41	Slight(15%)
...

Note: ε — horizontal deformation ratio; i — tilt volume ratio; d_z — displacement in direction Z, mm; BA and BC— two vertical sides of buildings foundation.

The results show that only building No.2035 has a tilt deformation about 4.11 mm/m. According to the standard of China Coal Industry Bureau, the building damage may be slight and the relative damage degree may be 15%. But all the other buildings damage may be extremely slight and the degree may be 5%. It suggests that the damage of buildings on landslide would not be extremely serious or even not medium before landslide failure. It also indicates that there is no building damage risk.

Vulnerability of people before landslide failure

Before landslide failure, probable causalities may be caused indirectly by buildings collapse. Based on buildings damage degree, people vulnerability is determined by the following factors: building function, people stay time in buildings and people awareness for hazard. Then vulnerability can be expressed as:

$$V_{p/def} = V_{p/1} \times P_t \times V_{b/def} \tag{1}$$

Where, $V_{b/def}$ is the vulnerability of people in buildings; P_t is temporal probability of

people in buildings, which is the product of people's daily probability P_{-d} and annual probability P_{-s} in buildings; $V_{p/i}$ is the probability of people who can not escape successfully from buildings when it collapsed, which can be expressed as

$$V_{p/i} = ((\alpha \times w_\alpha) + (\beta \times w_\beta)) \times P_d.$$

Where, w_α and w_β is weight ($w_\alpha=0.4$, $w_\beta=0.6$); α is correct coefficients for different buildings function, which is 0.1,0.3,0.3 and 0.1 respectively for public, commerce, city resident and country resident house ; β is correct coefficients for different people awareness to landslide hazard , which is 0.1,0.5,0.5 and 0.8 respectively for public, commerce, city resident and country resident house ; P_d is the vulnerability of people in buildings if it collapsed (Finlay , 1997).

Vulnerability of people when landslide failure

Once landslide occurs, people will escape as soon as possible. The faster the landslide moves, the more difficult the people can escape. Except this, people with different age, health and education will also have different vulnerability. If there is pre-warning before landslide failure, the vulnerability is thought to be zero; if not, it is 1.0 when landslide velocity is over 5m/s, and it is zero when velocity is no more than 4m/min. If there is no pre-warning and the velocity is between 3m/min and 5m/s, the vulnerability can be:

$$V_{p,slide} = \sum_{i=1}^3 (w_i \times k_i) \quad (2)$$

Where, k_i, w_i is the correct coefficient for different characters of people (Chen, 2008).

The vulnerability of people in vehicles is mainly related with landslide velocity. Besides this, some other factors are also important, such as people responding velocity to landslide, people characters, vehicles location on landslide, road width, etc. If landslide velocity v_l is greater than vehicles velocity v_v , or v_v is zero, P_v is 1.0; if not, P_v is the ratio of v_l and v_v . According to this the vulnerability people in vehicles was obtained (Table 3)

Vulnerability of ships affected by generated waves

Ships in the river will be roll violently and even turn over if being attacked by waves. But it occurs only when the ratio of ship rolling period and wave period is in the range of 0.7 to 1.3 (Guo, Zhang, 2006). So it can be considered that the vulnerability of ships affected by generated waves is 1.0 when the ratio falls in the above range.

Ship rolling period varies with ship types. Wave period is determined by wavelength, water depth and wave velocity. Dong et al. (1999) described a detail method to obtain the above two values. Table 4 shows the vulnerability of ships in the influence area of propagation waves when landslide damaged in the toe.

RISK ANALYSIS

Economic risk analysis

Before landslide failure, deformation in landslide surface is not enough to bring damage to each kind of elements, so economic risk in this phase is zero. But once the

landslide moves into river, some elements will be immersed and fully damaged. The results shows that the annual economical risk of landslide damaged in the toe in ten years return time is 15.447 and 7.008 Million RMB if landslide fails with a velocity of 1m/s and 5m/s respectively.

People risk analysis

The result of vulnerability of buildings before landslide failure shows that there is no risk for buildings. Therefore, there is no risk for people in buildings in this phase. It indicates that people risk exist only when landslide occurs and move into the river. So people risk includes two parts: people in buildings and people in vehicles.

People risk in buildings can be calculated by Equ. (1) and the results are shown in Table 2. The results indicate that the risk of people in buildings is high if landslide occurs at the speed of 5m/s, but the probability of this event is very low. People risk in vehicles can be calculated by the following equation

$$N = \sum_{i=1}^n p \times p_p \times m_i \quad (3)$$

Where, n , is the number of roads in landslide influence area; p is landslide probability with some intensity; p_p is the vulnerability of people in vehicles; m_i is the number of people on the road. The results shown in Table 3 indicate that risk of people in vehicles is high at the speed of 5m/s and more than the case of landslide occurring at the speed of 1m/s.

Adding the above two result of people risk in buildings and in vehicles, we can obtain the total people risk in ten years return years. It is 4.721 and 10.04 when landslide occurs at the speed of 1m/s and 5m/s respectively.

Risk from generated water waves

The landslide is about 74km away from the Three Gorges dam. Based on the calculation results of propagation wave height, the farthest distance of propagation waves is only 27km. Therefore, there is no risk for the dam. But the results of ships vulnerability shown in Table 4 indicate that ships parking at the docks of No.Y1007, Y1014 and Y1017 would turn over due to the waves. The minimum wave height of all the docks is 2.6m, which means that wave risk exists for the docks and people on it. In the work of landslide risk management, channel closing and people evacuation is necessary. Comparing with the elevation of climbing waves and residents and buildings, we can semi-quantitatively determine who or which building is at risk. The results show that about 278 people and 55 buildings on the upstream shoreline and 1186 people and 69 buildings on the downstream shoreline will be at risk.

CONCLUSIONS

Large scale and quantitative landslide risk analysis is difficult issue, especially in the Three Gorges reservoir area, China. In this study, landslide risk analysis was discussed in detail. In hazard analysis, landslide velocity, volume moving into water, height of generated initial surges, distance of propagation waves and relative wave height were considered. The vulnerability of buildings on landslide is discussed. Besides this, the

vulnerability of people in vehicles and ships were also analyzed. Finally, economic and people risk on landslide body and in the area of generated water waves were quantitatively determined. It was found that the landslide annual probability was 0.07556 and 0.03406 respectively when landslide occurs at the speed of 1m/s and 5m/s. In landslide deformation phase, there is no economic and people risk. But once landslide occur at the speed of 1m/s, it will bring about 15.447 million RMB annual economic risk, about annual 2.21 people risk in buildings, about annual 2.511 people risk in vehicles. Once landslide occur at the speed of 5m/s, it will bring about 7.008 million RMB annual economic risk, about 4.29 annual people risk in buildings and about 5.75 people risk in vehicles on landslide body. In the area of generated waves, ships parking at the docks of No.Y1007, No.Y1014 and No.Y1017 are at the risk of turning over. About 278 people and 55 buildings on the upstream shoreline and 1186 people and 69 buildings on the downstream shoreline will be at risk. But there is no risk for the Three Gorges dam.

ACKNOWLEDGMENTS

The authors appreciate the support of the Research Foundation for Outstanding Young Teachers, China University of Geosciences (Wuhan), and National Natural Science Foundation of China (No. 40872176/D0214).

REFERENCES

- Crozier, M.J. and Glade, T. (2005). "Landslide hazard and risk: issues, concepts and approach." *Landslide Hazard and Risk* :1-40.
- Dai, F.C., Lee, C.F. and Ngai, Y.Y. (2002). "Landslide risk assessment and management: an overview." *Engineering Geology*, (64): 65-87.
- Dong, Y.Q., Ji, K. and Huang, Y.S. (1999). "Research of ship rolling stability in waves." *Ship mechanics*, Vol.3(2): 1-6.
- Evans, S. G. (1997). "Fatal landslides and landslide risk in Canada." *Landslide Risk Assessment*. Edited by Cruden D.M. and Fell R. Balkema, Rotterdam: 185-196.
- Finlay, P.J. and R. Fell. (1997). "Landslides: risk perception and acceptance." *Canadian Geotechnical Journal*, Vol.34(2): 169-188.
- Glade, T. and Crozier, M.J. (2005). "The nature of landslide hazard impact." *Landslide Hazard and Risk* :43-74.
- Guo, F.X. and Zhang, J.H. (2006). "Hazards of waves on the ship." *Ship manipulation in rough seas*(First Volume). Professional Committee of Ocean Ship of China Institute of Navigation.
- Pan, J.Z. (1980). "Analysis of building stability and landslide." Beijing: *Hydraulic Press*.
- Wang, Y. (2005). "The research on speed of the landslide and its surge hazard in reservoir." *Ph.D. thesis*. Wuan: China University of Geosciences.
- Yan, R.G. (1995). "Foundation mining subsidence and surface buildings". Beijing: *Metallurgical Industry Press*.
- Yin, Y.P. and Peng, X.M. (2007). "Failure mechanism on Qianjiangping landslide in the Three Gorges Reservoir region." *Hydrogeology and Engineering Geology*, (3):51-54.

Back-Analysis of Water Waves Generated by the Dayantang Landslide

Yang Wang¹, Kunlong Yin², Li Zhou³, Juan Du⁴

¹Three Gorges Research Center for geo-hazard, Ministry of Education, China University of Geosciences, Wuhan, 430074, Hubei, China, wangyangcug@126.com

²Three Gorges Research Center for geo-hazard, Ministry of Education, China University of Geosciences, Wuhan, 430074, Hubei, China, yinkl@cug.edu.cn

³Engineering Faculty, China University of Geosciences, Wuhan, 430074, Hubei, China, zhouli001206@126.com

⁴Engineering Faculty, China University of Geosciences, Wuhan, 430074, Hubei, China, dujuan0709@gmail.com

ABSTRACT: The Dayantang landslide, a fast-moving landslide that occurred on June 15, 2007, is located in Qingtaiping town of Shuibuya reservoir, Hubei province, China. Investigations showed that the landslide induced a huge water wave with wave runup of 50 m on the opposite bank. Based on analysis of the engineering geology and the in-situ survey after its sliding, back-analysis of water waves generated by the Dayantang landslide is used to determine the friction angle of the sliding zone in a state of movement. Newton's second law and the basic principles of kinematics are used to obtain landslide velocity, and the volume conversion law are applied to calculate the initial height of the water wave. The propagation process of the water waves is divided into two stages: a sharp-decay stage and a slow-decay stage. Wave runup on the opposite bank is calculated with the consideration of slope angle and runup azimuth. It is concluded that the reduction factor of friction angle of the sliding zone is between 0.75 and 0.95 with a 10% uncertainty of calculations, while it is between 0.8 and 0.9 with a 5% uncertainty of calculations.

INTRODUCTION

Shuibuya hydro-junction project is an important project exploited in Qing River in Hubei province, China. The Dayantang landslide is located on the north bank of Qing River in Qingtaiping Town. The landslide, with a volume of 300 million m³, occurred on June 15, 2007 while the water level rose from 250 m to 342 m, and it induced a huge water wave with wave runup of 50 m on the opposite bank. There were no casualties on the landslide, however, water wave resulted in 1 death and 7 missing.

The size of water waves generated by landslides are calculated by experiential method, experimental investigations or numerical analysis and simulation. The experiential method mainly includes a number of formulas: the Slingerland and Voight,

Noda, Huber and Hager and Synolakis, (Noda, 1970; Chen, 1984; Slingerland and Voight, 1982; Synolakis, 1987; Huber and Hager, 1997). Some experimental investigations were performed by Heinrich (1992), Fritz et al., (2003), Fritz et al., (2004), Ataie-Ashtiani and Najafi-Jilani, (2008). Numerical analysis and simulation mainly includes the Saint-Venant equation (Pérez et al., 2006), finite element method (Christopher and Bruce, 1977), finite difference method (Harbitz et al., 1993), boundary element method (Grilli et al., 2002), Navier-Stokes equation (Rzadkiewicz et al., 1996), wavelet transform method (Panizzo et al., 2002).

ENGINEERING GEOLOGY OF THE DAYANTANG LANDSLIDE

The Dayantang landslide is a dustpan plane, with the Miaotaizi mountain ridge as the western boundary (Fig.1, Fig.2), and a small-scale gully as the eastern one. It is about 600 m long and 10 m thick, with an area of $30 \times 10^4 \text{ m}^2$, a volume of $300 \times 10^4 \text{ m}^3$ and a gradient between 35° and 40° . The average width of the landslide area is 500 m, with a narrower back part of about 300 m and a wider front of 900 m. The elevation of back part of the landslide is 620 m, and the elevation of back part is 225 m.

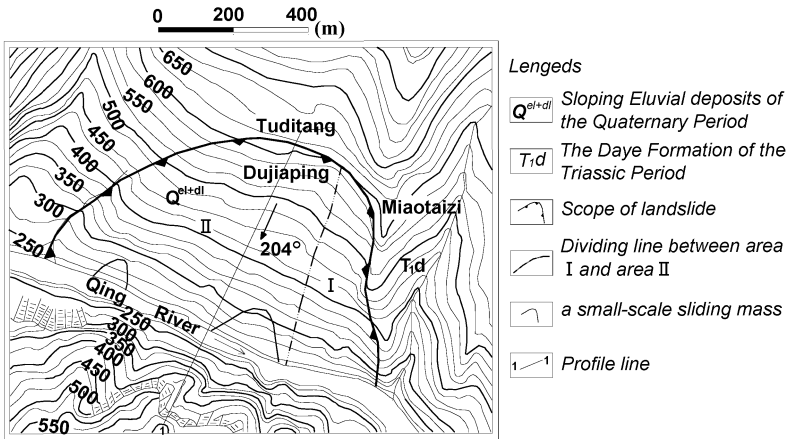


FIG. 1. Engineering geology map.

According to rock and soil characteristics, the Dayantang landslide can be divided into the eastern part (I) and the western part (II). The eastern part is middle-strong weathered rock mass, and the western part is sloping eluvial deposits of the Quaternary Period, composed of loose rubble soil with rubble content of 67% ~78%. The rubbles are attributed to limestone and muddy limestone. An average diameter of rubbles is above 0.5 m.

Bedrock in the landslide was formed in the Daye Formation of the Triassic Period, mainly composed of middle-thin layer limestone and muddy limestone, with an

attitude of $252^\circ \angle 9^\circ$ (Fig.3). Among the bedrock, there are thin weak carbon mudstone and carbon muddy limestone, which are greyish white, loose structure, and low intensity. The rock is cut into block-fracture sharp rock mass with large-density joints of $170^\circ \angle 81^\circ$ and $76^\circ \angle 74^\circ$.



FIG. 2. The photo of the landslide.

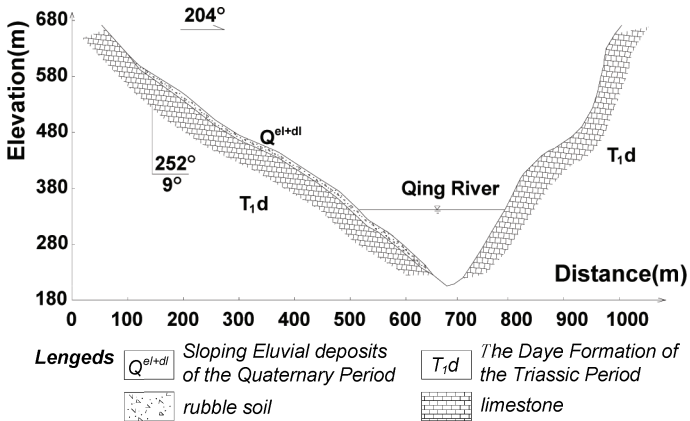


FIG. 3. The cross-section of the Dayantang landslide.

The deformation began to appear in the landslide on May 26, 2007 due to the rising

water level. The width of the crack reached to 2~6 cm on June 2, 2007, and a small-scale collapse appeared in the front part of the landslide on June 3, 2007. Because of continuous rainfall on June 13, 2007, a small-scale collapse with a volume of $20 \times 10^4 \text{ m}^3$ took place in the front of the landslide on June 14, 2007, and arc-shaped crack formed on the back part, with the maximum width of 12~20 cm. A large-scale landslide occurred at 4:56 PM on June 15, 2007 when the water level rose up to 342 m.

CALCULATIONS OF LANDSLIDE VELOCITY

The assumptions of the analysis are that the section in question is considered as a rigid body when it moves. According to Newton's second law and assumptions, an acceleration of section can be represented as (Wang, 2005):

$$a_i = \frac{\sum_{i=1}^n [(W_i \sin \alpha_i + \Delta U_i \cos \alpha_i - C_i L_i) - (W_i \cos \alpha_i - \Delta U_i \sin \alpha_i - U_{bi}) g \Phi_i]}{\sum_{i=1}^n M_i} \quad (1)$$

where a_i is the acceleration of section i , W_i is the weight, M_i is the mass, U_i is the water pressure of lower lateral wall, U_{i+1} is the water pressure of upper lateral wall, U_{bi} is the water pressure of bottom surface, ΔU_i is resultant water pressure from U_i and U_{i+1} , C_i is the cohesion of the sliding zone, ϕ_i is the internal friction angle of the sliding zone, L_i is the length of bottom surface, and N_i is the positive pressure acting on the bottom surface, α_i is the obliquity of sliding zone.

Velocity of section i can be calculated as follows:

$$V_{i2}^2 = V_{i1}^2 + 2 \cdot a_i \cdot L_i \quad (2)$$

where V_{i1} is the initial velocity, and V_{i2} is the terminal velocity

CALCULATION OF THE INITIAL WATER WAVE

The volume conversion law means that the water volume pushed away by the landslide is equal to the total volume generating water wave in the process of landslide movement on the assumption that the infiltration of the water in the pores of rock/soil mass is not taken into account.

Based on the volume conversion law, the initial water wave generated by the landslide can be calculated as (Wang, 2005):

$$V_1 = g \pi_1^2 \cdot \frac{h_1 (h_0 + h_1)^2}{(2h_0 + h_1)} \quad (3)$$

where g is the acceleration of gravity, h_1 is the height of initial water wave generated by the landslide, h_0 is the depth of the reservoir, t_1 is certain transitory time, V_1 is the volume of soil and rock sliding into the reservoir in t_1 .

CALCULATION OF THE PROPAGATION OF THE WATER WAVE

In terms of continuity equation, the movement equation of transient flow and the water head loss theory in an open channel in hydrodynamics, the decay process of

landslide surge is divided into two stages: sharp-decay stage and slow-decay stage. It is assumed that the sharp-decay stage is a kind of exponential decay (Li, 1982; Chen, 1984; Wang, 2005), and the propagation formula in this stage can be expressed as:

$$h_s(x, t) = h_1 e^{-\sqrt{k_1 x} - \sqrt{\frac{g}{h_1}} t} \tag{4}$$

where x is spread distance of the sharp-decay stage, t is time, h_s is the height of water wave, k_1 is a parameter relative to the height of initial water wave and the width and depth of the river.

It is assumed that the slow-decay stage is a kind of water head loss with propagation distance in open channel (Wang, 2005). The propagation formula in this stage can be expressed as:

$$h_s(x_1) = h_{s0} - \frac{2g(h_0 + h_{s0})^2 \cdot n^2}{(2h_0 + h_{s0}) \cdot R^3} \cdot x_1 \tag{5}$$

where h_{s0} is the height of water wave at the start point of slow-decay stage, R is the hydraulic radius, n is coarse factor, and x_1 is the spread distance of the slow-decay stage.

According to the stable wave height (Kamphis, J.W. and Bowering, R.J., 1971), the dividing point of the sharp-decay stage and slow-decay stage is about 37 times the depth of the reservoir.

CALCULATION OF THE RUNUP OF THE WATER WAVE

Wave runup on the opposite bank is calculated on the consideration of slope angle and runup azimuth (Wang, 2005):

$$\Delta h = \left[\left(\sqrt{\frac{\pi}{2\alpha}} - 1 \right) \cos \beta + 1 \right] h \tag{6}$$

where Δh is the height of wave runup on the opposite bank, h is the height of water wave, α is the slope angle, and β is the runup azimuth.

BACK-ANALYSIS OF WATER WAVES GENERATED BY THE DAYANTANG LANDSLIDE

The residual strength parameters of the sliding zone at rest are different from those in a state of movement. According to shear experiment, the cohesion and internal friction angle of the sliding zone of Dayantang landslide are determined as 28.0 kPa and 24.5°. Back-analysis of water waves generated by the landslide is used to determine the friction angle of the sliding zone in a state of movement. On the assumption that the cohesion of the sliding zone is zero, the reduction factor of friction angle of the sliding zone in a state of movement is A , i.e. the ratio of internal friction angle in a state of movement to that at rest is A . The section method is used to calculate velocity, and the landslide velocity and wave runup on the opposite bank with different values of A are calculated (Table 1).

The typical empirical models have also been used to analyze initial water wave and Wave runup (Table 1). The initial water wave generated by the Xintan landslide can be

calculated by Noda model (Noda, 1970), and Wave runup can be calculated by Pan model (Pan, 1980).

The results have not much difference between above-mentioned equations and typical empirical models. The results from above-mentioned equations are slightly larger than those from Noda model and Pan model (Table 1). The differences in initial water wave height are between 2.6% and 12.6%, and the differences in wave runup are between 2.9% and 4.8%.

Investigations showed that the average velocity of the landslide was about 15 m/s, and wave runup on the opposite bank is about 50 m. In combination with the calculation results, an appropriate value of A is between 0.75 and 0.95 with a 10% uncertainty of calculations, while A is between 0.8 and 0.9 with a 5% uncertainty of calculations.

Table 1. Results of water wave from back-analysis.

A	Landslide Velocity(m/s)	Initial water wave(m)		Wave runup(m)	
		Eq.3	Noda model	Eq.6	Pan model
0.75	14.28	52.5	45.9	54.2	51.6
0.80	13.66	51.6	45.4	53.3	51.0
0.85	13.01	49.1	43.8	50.7	49.2
0.90	12.40	46.3	43.2	47.8	46.5
0.95	11.75	43.1	42.0	44.5	43.2

CONCLUSIONS

In the back-analysis, the Newton's second law is used to obtain landslide velocity, and the volume conversion law is applied to calculate the initial height of water wave. The propagation process of landslide surge is divided into two stages: sharp-decay and slow-decay. These calculation models not only take continuity of the landslide movement and landslide-generated water wave in reservoir into account, but also forces of landslide, the depth of the reservoir and the volume of soil and rock sliding into the reservoir.

Back-analysis of water waves generated by the landslide is used to determine the friction angle of the sliding zone in a state of movement. The reduction factor of friction angle of the sliding zone is between 0.75 and 0.95 with a 10% uncertainty of calculations, while it is between 0.8 and 0.9 with a 5% uncertainty of calculations.

The results have significance for the selection of the friction angle of a sliding zone in a state of movement, the calculations of landslide velocities and water wave generated by the landslide.

ACKNOWLEDGMENTS

The authors appreciate the support of National Natural Science Funding of China (No: 40872176), the New Teacher Project of Doctor-Point Funding from Ministry of Education of China (No: 20070491015) and the Research Foundation for Outstanding Young Teachers, China University of Geosciences (Wuhan).

REFERENCES

- Noda, E. (1970). "Water waves generated by landslides." *Journal of the Waterways, Harbors and Coastal Engineering Division, ASCE*, Vol. 96(4): 835 – 855.
- Slingerland, R. L. and Voight, B. (1982). "Evaluating hazard of landslide-induced water waves." *Journal of the Waterways, Harbors and Coastal Engineering Division, ASCE*, Vol. 108(4), 504–512.
- Chen, X.D. (1984). Experiential method of surge triggered by landslide in reservoir and design of program. *Science and Research School in Zhongnan Institute of Reconnaissance and Design of the Ministry of Water Conservancy and Electric Power, Changsha*.
- Synolakis, C.E. (1987). "The run-up of solitary waves." *Journal of Fluid Mechanics*, Vol. 185: 523–545.
- Huber, A. and Hager, W.H. (1997). Forecasting impulse waves in reservoirs. *Commission Internationale des Grands Barrages*, Florence, 993-1005.
- Heinrich, P.(1992). "Nonlinear water waves generated by submarine and aerial landslides." *Journal of Waterway, Port, Coastal, and Ocean Engineering Division, ASCE*, Vol. 118(3): 249–266.
- Fritz, H.M., Hager, W.H. and Minor, H.E. (2003). "Landslide generated impulse waves. Part 1: Instantaneous flow fields." *Experiments in Fluids*, Vol. 35: 505–519.
- Fritz, H.M., Hager, W.H. and Minor, H.E. (2004). "Near Field Characteristics of Landslide Generated Impulse Waves." *Journal of Waterway, Port, Coastal, and Ocean Engineering Division, ASCE*, Vol. 130(6): 287– 302.
- Ataie-Ashtiani, B. and Najafi-Jilani, A. (2008). "Laboratory investigations on impulsive waves caused by underwater landslide." *Coastal Engineering*, Vol.55:989–1004.
- Pérez, G., García-Navarro, P. and Vázquez-Cendón, M.E. (2006). "One-dimensional model of shallow water surface waves generated by landslides." *Journal of Hydraulic Engineering, ASCE*, Vol. 132(5): 462-473.
- Christopher, G.K. and Bruce, L. (1977). "Finite element approach to waves due to landslides." *Journal of the Hydraulics Division, ASCE*, Vol. 103(9): 1021-1029.
- Harbitz, C.B., Pedersen, G. and Gjevik, B. (1993). "Numerical simulations of large water waves due to landslides." *Journal of Hydraulic Engineering, ASCE*, Vol. 119(12): 1325-1342.
- Grilli, S.T., Vogelmann, S. and Watts, P. (2002). "Development of 3D numerical wave tank for modelling tsunami generation by underwater landslides." *Engineering Analysis with Boundary Elements*, Vol. 26: 301-313.
- Rzadkiewicz, S.A., Mariotti, C. and Heinrich P. (1996). "Modelling of submarine landslides and generated water waves." *Phys. Chem. Earth*, Vol. 21(12): 7-12.
- Panizzo, A., Bellotti, G. and Girolamo, P.E. (2002). "Application of wavelet transform analysis to landslide generated waves." *Coastal Engineering*, Vol. 44: 321-338.
- Li, W.X. (1982). Differential equations of hydraulics and its application. *Shanghai Science and Technology Press*, Shanghai.
- Wang, Y. (2005). The research on speed of the landslide and its surge hazard in reservoir, China University of Geosciences, Wuhan.

- Kamphis, J.W. and Bowering, R.J. (1971). "Impulse Waves Generated By Landslides." *Proceedings of the 12th Coastal Engineering Conference, ASCE*, 689-699.
- Pan, J.Z. (1980). "Stability of construction against sliding and analysis of landslide." *Water Conservancy Press, Beijing*.

Stochastic Durability Analysis of Under-Water Concrete Structure of Hangzhou Bay Bridge

Zhuo Zhao¹, Yan Zhang² and Changyong Ye³

¹Professor, Civil engineering institute, Zhengzhou University, Zhengzhou 450002, China, zzhao_99@163.com

²Doctor, Civil engineering institute, Zhengzhou University, Zhengzhou 450002, China, zhangyan@zzu.edu.cn

³Engineer, Ningbo high-grade highway construction headquarter, Ningbo 315192, China, 15057480072@zj139.com

ABSTRACT: The service offshore environment of under-water concrete structure of Hangzhou Bay Bridge is the most serious environment for concrete structure, the problem of structural durability is very prominent. Based on the characters of material, structural design, corrosiveness of service environment and site detection results, the stochastic characters of durability influencing factors such as concrete cover depth, initial chloride concentration, chloride diffusion coefficient, threshold chloride concentration and structural surface concentration of chloride are analysis. And through Monte Carlo stochastic simulation, the statistics distribution character of service life of under-water concrete structure is gained, which will provide theory method and foundation for the structural durability design, construction and quality control of similar project.

INTRODUCTION

Hangzhou Bay Bridge is located at Hangzhou Bay, which has high temperatures, high humidity, contents high salinity and a large of chloride in the sea water. Because of tidal fluctuation effects and corrosion environment of the marine atmospheric, the service life of the bridge will have a significant adverse impact.

Based on the design, construction features, comprehensive consideration of the corrosive marine environment of Hangzhou Bay, the stochastic durability analysis theories and methods of under-water concrete structure of Hangzhou Bay Bridge are established, which will ensure the 100 years design life of Hangzhou Bay Bridge, improve the durability design and evaluation theory and method of concrete structures under marine environment.

DURABILITY LIFE OF UNDER-WATER CONCRETE STRUCTURE

Corrosion damage of under-water concrete structures by chloride

As for reinforced concrete structure, the corrosion process is generally divided into three phases (Zhao et al., 2005): the initial stage of Structure's steel corrosion, t_0 as its mark time point; the stage of the development of the corrosion before concrete cracking, t_{cr} as its mark time point; the stage of the corrosion damage development after concrete cracking.

For the under-water concrete structure of Hangzhou Bay Bridge, due to the adverse nature of its service environment and based on relevant standards (CECS 220:2007; GB/T 50476-2008), the durability failure criteria of the reinforced concrete structures (or components) will be established as:

When at certain time the surface of certain concrete structures (or components) appears cracks that caused by the corrosion of the reinforcement, the durability of the concrete structures (or components) is failure, and reaches its durable service life t_{cr} .

Diffusion rate model of the chloride ions

According to Fick's second diffusion law, the diffusion process of chloride ions in un-cracking concrete is normally described as:

$$C_x = (C_s - C_0) \left[1 - \operatorname{erf} \left(\frac{x}{2\sqrt{Dt}} \right) \right] + C_0 \quad (1)$$

Wherein, C_x is the chloride concentration at depth x at time point t ; C_s is the chloride concentration on the concrete surface; C_0 is the initial chloride concentration in concrete; $\operatorname{erf}(Z)$ is the error function.

When at certain time, C_x achieves threshold chloride concentration C_{cr} , which leads to the corrosion of the reinforcement at concrete cover depth a , the initial corrosion time t_0 of reinforcement caused by chloride ions diffusion can be solved as:

$$t_0 = \frac{a^2}{4D} \left[\operatorname{erf}^{-1} \left(\frac{C_s - C_{cr}}{C_s - C_0} \right) \right]^2 \quad (2)$$

After the structural steel began to corrosion, t_c , which is the time period from the beginning of steel corrosion to concrete crack due to corrosion product can be expressed as (CECS 220, 2007):

$$t_c = \frac{\delta_{cr}}{\lambda_{cl}} \quad (3)$$

Wherein, $t_0 + t_c = t_{cr}$; δ_{cr} is the critical corrosion depth when the concrete cover is cracked (mm), which can be calculated according to equation (4); λ_{cl} is the average corrosion rate of steel before concrete crack in the chloride environment (mm/a), which can be calculated according to equation (5).

$$\delta_{cr} = 0.015(a/d)^{1.55} + 0.0014f_{chik} + 0.016 \quad (4)$$

Wherein, f_{cuk} is the assessment compressive strength of concrete (MPa); d is the diameter of the reinforcement (mm); a is concrete cover depth (mm).

$$\lambda_{cl} = 11.6 \times i \times 10^{-3} \tag{5}$$

Wherein, i is the corrosion current density of the reinforcement ($\mu A/cm^2$), which can be calculated according to equation (6).

$$\ln i = 8.617 + 0.618 \ln C_{cr} - \frac{3034}{T + 273} - 5 \times 10^{-3} \rho + \ln m_{cl} \tag{6}$$

Wherein, T is the temperature of steel surrounding ($^{\circ}C$); m_{cl} is the local environmental coefficient; ρ is the resistivity of the concrete ($k\Omega \cdot cm$).

DISTRIBUTION CHARACTERISTICS OF DURABILITY FACTORS

Considering under-water concrete structure of Hangzhou Bay Bridge, t_0 and t_c is the key time period for studying the durability life of under-water concrete.

Distribution characteristics of factors that affect t_0

Based on the Fick's second diffusion law, a , C_0 , C_s , C_{cr} , D and other related parameters are the main parameters to confirm t_0 .

(1) a : based on GB/T 50283-1999, the concrete cover depth subject to normal distribution, and its statistical characteristics is $\mu_a = 1.0178$, $\delta_{\Omega a} = 0.0496$.

(2) C_0 : site construction test result (Cai et al., 2006; Zhao et al., 2005) show that the initial chloride content in the concrete mixture is about 0.006% ~ 0.008% of the total cementitious materials. Based on the relevant standards and research results, C_0 can be suggested as normal distribution.

(3) C_s : CECS 220:2007 give a reference table of concrete surface concentration of the chloride ion at different marine environment areas, as shown in Table 1. Based on the relevant research results (Ma and Zhang, 2007), it can be suggested as normal distribution.

Table 1. Surface concentration of chloride ions.

f_{cuk} (MPa)	40	30	25	20
C_s (kg/m ³)	8.1	10.8	12.9	20

(4) C_{cr} : This can be suggested as normal distribution of $\mu = 0.35\%$, $\sigma = 0.05\%$ (Total weight of cementitious materials).

(5) D : through test of chloride ion permeability coefficient of the Hangzhou Bay Bridge, the diffusion coefficient obeys normal distribution, as shown in Table 2.

Table 2. Site detection results of chloride diffusion coefficient (8 weeks age).

Number of Tested Box Girder	Average ($10^{-12} \text{m}^2/\text{s}$)	Standard Deviation ($10^{-12} \text{m}^2/\text{s}$)	Variable Coefficient
267	0.8411	0.0821	0.0976

Distribution characteristics of factors that affect t_c

The cushion cap of the Hangzhou Bay Bridge using C40 concrete, based on the relevant standards and research results (GB/T 50283-1999), the selected distribution feature of the relevant factors are shown in Table 3

Table 3. Statistical distribution of factors that affect t_c .

Parameters	μ_{Ω_i}	δ_{Ω_i}	Types of Probability distribution
Concrete Strength	1.4804	0.1578	Normal
Diameter of Reinforcement	1.0	0.035	Normal
Concrete Resistivity	1.0	0.3	Normal

PROBABILITY DISTRIBUTION OF DURABLE SERVICE LIFE

Based on the characteristics of the design, construction and service environment of the Hangzhou Bay Bridge's cushion cap at the wave's splash zone, the statistical distribution characteristics of the factors that affect durable service life can be suggested as shown in Table 4.

Table 4. Statistical distribution characteristics of factors.

Parameters	Types of the Probability distribution
Concrete cover depth (mm)	N(55.979,2.728)
Initial chloride concentration (kg/m^3)	N(0.032,0.0026)
Chloride diffusion coefficient ($10^{-12} \text{m}^2/\text{s}$)	N(2.0,0.1952)
Threshold chloride concentration (kg/m^3)	N(1.65,0.24)
Surface chloride concentration (kg/m^3)	N(8.1,0.474)

Based on the above statistical values, considering the changes of the diffusion coefficient of the chloride ions, through Monte Carlo stochastic simulation, the statistical distribution of durable service life of under-water concrete structures can be obtained.

The simulation result of the approximate probability density of durable service life t_{cr} and t_0 are shown in Figure 1.

The K-S testing negative t_{cr} of the under-water concrete structures obey the normal

distribution assumption, rather than deny its distribution subject to the log-normal distribution assumptions of LOGN (4.9653, 0.1354).

If takes the reliability rate as 95%, the desirable design standards value of durable service can be taken as 115(a) ; if takes the reliability rate as 90%, then the desirable design standards value of durable life can be taken as 121 (a).

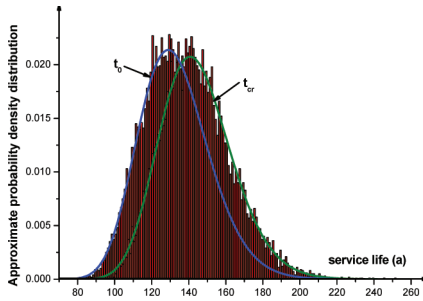


FIG. 1. Distribution of Approximate Probability Density of t_{cr} and t_0 .

CONCLUSION

Based on the corrosiveness characters of Hangzhou Bay and relevant site test results of Hangzhou Bay Bridge, the statistical distribution of the factors that affect durable service life of the under-water concrete structure, such as concrete cover depth, concrete Strength, diameter of reinforcement, the concrete resistivity, initial chloride concentration, surface concentration of chloride ions, threshold chloride concentration, chloride diffusion coefficient and other relevant factors are analyzed. And the probability distribution characteristics of durable service life of Hangzhou Bay Bridge cushion cap structure is obtained, the standard design values of durable service life is suggested according to different reliability rate. The research result provides methods and theoretical basis for the durability design, construction and quality control for similar projects.

REFERENCE

- Cai, Y.Z., Wang, W.X. and Bo, X.Z. (2006). "Study on the concrete formulation of C50 durable concrete of box beam used in Oceanic condition of the Box Beam of Hangzhou bay bridge." *Concrete*, Vol. 2006(6): 69-72.
- CECS 220-2007 (2007). *Standard for Durability Assessment of Concrete Structures*. China Architecture & Building Press, Beijing.
- GB/T 50476-2008 (2008). *Code for Durability Design of Concrete Structures*. China Architecture & Building Press, Beijing.
- GB/T 50283-1999 (1999). *Unified Standard for Reliability Design of Highway Engineering Structures*. China Planning Press, Beijing.
- Ma, Y.L. and Zhang, A.L. (2007). "Probabilistic model of corrosion initiation time of steel bar in concrete structure." *Journal of Hydraulic Engineering*, Vol. 38(5): 630-635.

Zhao, Z., Ma, Y.L. and Li, F. (2005). "Phase-model of corrosion rate of steel bar under chloride environment." *Industrial Construction*, Vol. 35(382): 1-4.

Zhao, J.F., Su, Z.P. and Ouyang H.L. (2005). *Research on Formulation of C50 Durable Concrete Used in Oceanic Condition*. China Communications Press, Beijing.

Critical State Stress Analysis for Soil Body of Potential Heave

Jian-Min Yang¹, Gang Zheng²

¹Lecturer, Department of Civil Engineering, Tianjin University, Tianjin 300072, China, yjmwork@yahoo.cn

²Professor, Department of Civil Engineering, Tianjin University, Tianjin 300072, China, zhengzige2004@yahoo.com.cn

ABSTRACT: High head hydraulic pressure in confined aquifer could cause failure of heaving if the confined aquifer was buried under the bottom of excavation. Therefore, analysis of heaving stability plays a significant role in the dewatering design. The objective of analysis is to determine drawdown as well as layout of wells and land subsidence due to water withdrawal. Currently, the formula widely used in the industry is based on the pressure balance theory. Physical meaning of the formula is that the effective stress of the soil below the bottom of excavation is ensured to be greater than zero. Terzaghi derived a similar formula for excavation in sand. This paper compares these two approaches and verifies that these two approaches are essentially similar in case of safety factor of heaving being unity.

INTRODUCTION

In order to decrease settlement due to groundwater pumping during excavation, the water level in the pumping wells must be strictly controlled, especially for deep excavation in soft clay. As for dewatering from artesian aquifer, result of the formula to check stability of heaving directly determine the drawdown in the pumping wells, so that the result influences the magnitude of land settlement. The method to check the stability of heaving related to the safety of excavation, and it relate to the magnitude of land subsidence. The conservative result of the checking formula will increase land subsidence, but the immoderate result may result in accident. So the formula to check the stability of heaving is important for excavation engineering during dewatering.

The formula to check the stability of heaving in the Chinese Code (MCPRC, 2002) is based on Terzaghi's pressure balance theory. The formula guarantees the effective stress of the soil greater than zero. So it was widely applied in practice.

REVIEW OF THE HEAVING INSTABILITY RESEARCH

The check formula (1) for heaving instability in Chinese Code (MCPRC, 2002) is widely applied. The mechanism of heaving is illustrated in Figure 1 for excavation where the uplift forces from confined aquifer acting upon the bottom of the excavation.

The check formula for heaving instability is:

$$\frac{\gamma_{ssat}(t + \Delta t)}{P_w} \geq 1.1 \tag{1}$$

where γ_{ssat} =unit saturate weight of the soil above the confined aquifer (kN/m³), $t + \Delta t$ =height of the soil above the confined aquifer (m), P_w =hydrostatic pressure (kPa).

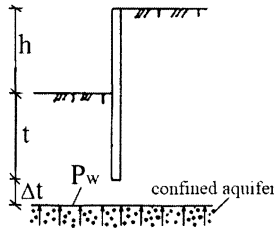


FIG. 1. The schematic of checking the anti-seepage stability.

Eq. (1) represent the saturate weight of the soil above the confined aquifer is greater than the hydrostatic pressure from the artesian aquifer. Value 1.1 is the safety factor; it ranges from 1.05 to 1.20 in local regulation. Engineering practice indicates that the Eq. (1) is conservative. For example, the safety factor calculated from Eq. (1) for some finished excavation before 1990 in Changzhou ranges from 0.49 to 0.67 (Liang, 1996).

Liang (1996) and Ma et al (2004) have made some improvement to modify the Eq. (1) based on the continuum mechanics such as elastic mechanics, material mechanics and structural mechanics. While soil differs from steel and concrete, the above improvement hasn't been implied widely.

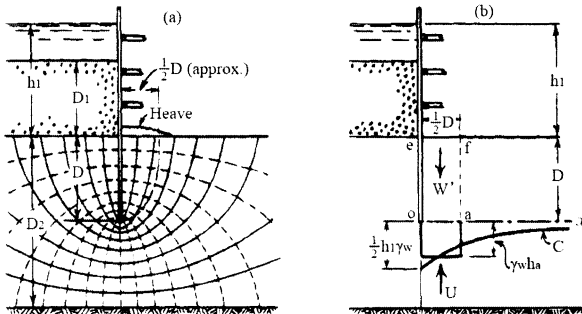


FIG. 2. Use of flow net to determine factor of safety of row of sheet piles in sand with respect to piping.(a)Flow net; (b) Forces acting on sand within zone of potential heave.

Terzaghi (1922) proposed the equation (2) after analyzed the safety of row of sheet piles in sand with respect to piping by flow net and experiment in sand. It is illustrated in Figure 2.

$$F = \frac{W'}{U} = \frac{D\gamma'}{h_a\gamma_w} \quad (2)$$

where F =safety factor of heaving (-), W' =submerged weight of soil (kN), U =excess hydrostatic pressure (kN), D =depth of sheet piles under the bottom of the excavation (m), h_a =height of excess hydrostatic head (m), γ' =submerged unit weight of soil (kN/m³), γ_w =unit weight of water (kN/m³).

TRANSFORMATION OF THE TERZAGHI EQUATION

When the safety factor of heaving is equal to unity, the Terzaghi's equation (2) transform as follow:

$$1 = \frac{D\gamma'}{h_a\gamma_w} \quad (3)$$

$$h_a\gamma_w = D\gamma' \quad (4)$$

$$h_a\gamma_w + D\gamma_w = D\gamma' + D\gamma_w \quad (5)$$

$$(h_a + D)\gamma_w = D\gamma_{ssat} \quad (6)$$

$$1 = \frac{D\gamma_{ssat}}{(h_a + D)\gamma_w} = \frac{D\gamma_{ssat}}{P_w} \quad (7)$$

Therefore, at the critical state of safety factor of heaving being unity, the Terzaghi's equation (2) is same as the check formula of equation (1) in Chinese Code (MCPRC, 2002). Terzaghi's equation (2) implies the meaning of pressure balance in Eq (1).

THE FORMULA GUARANTEE EFFECTIVE STRESS GREATER THAN 0

Figure 1 and the check formula of equation (1) in Chinese Code (MCPRC, 2002) illustrate that, for soil body beneath the excavation face, if safety factor is greater than 1, then the total stress is greater than the pore water pressure. Thus, this formula guarantees that the effective stress of soil is greater than zero. The soil will not float if its effective stress is greater than zero.

CRITICAL STATE ANALYSIS OF FORMULA

The failure type of soil is shear and tension. If the minor principal stress is greater than zero, then it will not fail in tension. As shown in Figure 3, assumed that the horizontal and vertical directions are the principal stress direction of soil of potential heave, the critical stress state is analyzed as follow.

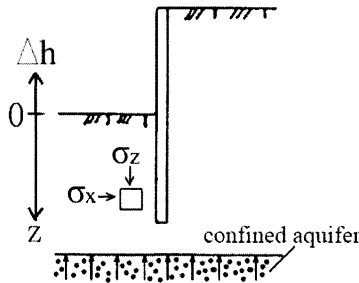


FIG. 3. The force diagram of soil beneath the excavation face.

The situation of earth pressure at rest

In the situation of earth pressure at rest, the principal stress directions are horizontal and vertical ,the principal stress are:

$$\sigma_z = \gamma'_s z \tag{8}$$

$$\sigma_x = (1 - \sin \phi) \gamma'_s z \tag{9}$$

where γ'_s =submerged unit weight of soil (kN/m³), z =depth of soil under the bottom of the excavation (m), ϕ =friction angle (°).

Coefficient of earth pressure at rest K_0 is equal to $(1 - \sin \phi)$.

If the water head of the confined aquifer beneath the excavation face increases Δh , the principle stress of soil becomes:

$$\sigma_z = \gamma'_s z - \gamma_w \Delta h \tag{10}$$

$$\sigma_x = (1 - \sin \phi) \gamma'_s z - \gamma_w \Delta h \tag{11}$$

Assumed that the soil would fail in tension if the minor principle stress fell to 0, then

$$\sigma_x = (1 - \sin \phi) \gamma'_s z - \gamma_w \Delta h = 0 \tag{12}$$

$$\Delta h = (1 - \sin \phi) \frac{\gamma'_s}{\gamma_w} z \tag{13}$$

The critical water head at failure of tension is:

$$h_{cr}^{11} = z + (1 - \sin \phi) \frac{\gamma'_s}{\gamma_w} z = \left(\frac{\gamma_{ssat}}{\gamma_w} - \sin \phi \frac{\gamma'_s}{\gamma_w} \right) z \tag{14}$$

where h_{cr} =critical water head (m), γ_{ssat} =saturated unit weight of soil (kN/m³).

Assumed that the soil failed in shear and obeyed Mohr-coulomb strength rule:

$$\sigma_x = \sigma_z \tan^2 \left(45^\circ - \frac{\phi}{2} \right) - 2c \tan \left(45^\circ - \frac{\phi}{2} \right) \tag{15}$$

The critical water head at failure of shear is:

$$h_{cr}^{12} = z + \frac{\left(\tan^2 \left(45^\circ - \frac{\phi}{2} \right) + \sin \phi - 1 \right) \gamma'_s z - 2c \tan \left(45^\circ - \frac{\phi}{2} \right)}{\left(\tan^2 \left(45^\circ - \frac{\phi}{2} \right) - 1 \right) \gamma_w} \quad (16)$$

The factual critical water head at failure is:

$$h_{cr}^1 = \min(h_{cr}^{11}, h_{cr}^{12}) \quad (17)$$

The situation between rest and active earth pressure, $K_\lambda \in (K_0, 1)$

K_λ is earth pressure coefficient and

$$K_\lambda \in (K_0, 1) \quad (18)$$

If the water head of the confined aquifer beneath the excavation face increases Δh , the critical water head at failure of tension and shear are:

$$h_{cr}^{21} = z + K_\lambda \frac{\gamma'_s}{\gamma_w} z = \left(1 + K_\lambda \frac{\gamma'_s}{\gamma_w} \right) z \quad (19)$$

$$h_{cr}^{22} = z + \frac{\left(\tan^2 \left(45^\circ - \frac{\phi}{2} \right) - K_\lambda \right) \gamma'_s z - 2c \tan \left(45^\circ - \frac{\phi}{2} \right)}{\left(\tan^2 \left(45^\circ - \frac{\phi}{2} \right) - 1 \right) \gamma_w} \quad (20)$$

The factual critical water head at failure is:

$$h_{cr}^2 = \min(h_{cr}^{21}, h_{cr}^{22}) \quad (21)$$

The situation between rest and passive earth pressure, $K_\lambda \in [1, K_p)$

K_p is passive earth pressure coefficient. If the water head of the confined aquifer beneath the excavation increases Δh , the critical water head at failure of tension and shear are:

$$h_{cr}^{31} = z + \frac{\gamma'_s}{\gamma_w} z = \frac{\gamma_{ssat}}{\gamma_w} z \quad (22)$$

$$h_{cr}^{32} = z + \frac{\left(\tan^2 \left(45^\circ + \frac{\phi}{2} \right) - K_\lambda \right) \gamma'_s z + 2c \tan \left(45^\circ + \frac{\phi}{2} \right)}{\left(\tan^2 \left(45^\circ + \frac{\phi}{2} \right) - 1 \right) \gamma_w} \quad (23)$$

The factual critical water head at failure is:

$$h_{cr}^3 = \min(h_{cr}^{31}, h_{cr}^{32}) \quad (24)$$

The situation of passive earth pressure

In the situation of passive earth pressure, the soil is at critical state of shear failure. If the soil is at the failure of tension, the vertical principle stress is zero, the critical water head is:

$$h_{cr}^4 = z + \frac{\gamma'_s}{\gamma_w} z = \frac{\gamma_{ssat}}{\gamma_w} z \quad (25)$$

Equation (25) is same as equation (1) and (2).

CONCLUSIONS

The check formula for heaving instability in Chinese Code (MCPRC, 2002) is based on pressure balance theory. When safety factor of heaving being unity, the Terzaghi's equation is same as the check formula in Chinese code. The formula in Chinese code guarantees effective stress greater than zero. The critical water heads in four situation of earth pressure at rest, $K_\lambda \in (K_0, 1)$, $K_\lambda \in [1, K_p)$ and passive earth pressure were derived.

ACKNOWLEDGMENTS

The authors gratefully acknowledge the financial support for this study provided by the National Natural Science Foundation (No.50908160).

REFERENCES

- MCPRC, Ministry of Construction of the People's Republic of China. (2002). *Code for Design of Building Foundation* (GB50007-2002). Beijing: China Architecture & Building Press (in Chinese).
- Liang, Y.R. (1996). "Analysis of heaving for strip foundation pit." *Chinese Journal of Geotechnical Engineering*. Vol. 18 (1):75-79 (in Chinese).
- Ma, S.C., Yin, C.J. and Zou, Y.h. (2004). "Analysis and calculation of the pit base plate thickness of bearing resistance water foundation." *Engineering Mechanics*, Vol. 21(2): 204-208 (in Chinese) .
- Terzaghi, K. Peck, R.B., and Mesri, G. (1996). *Soil Mechanics in Engineering Practice (3rd Edition)*. John Wiley & Sons. Inc. New York.

Effect of Piping on Shear Strength of Levees

Ming Xiao¹, P.E., M. ASCE, and Jose Gomez², S.M. ASCE

¹ Assistant Professor, Department of Civil and Geomatics Engineering, M/S EE94. California State University, Fresno, California 93740. USA. Phone: 1-559-278-7588. Email: mxiao@csufresno.edu
² Graduate student, Department of Civil and Geomatics Engineering, California State University, Fresno, CA, USA.

ABSTRACT: Internal soil erosion in the form of piping causes excessive seepage and progressively enlarged channels inside levees and earth dams. This paper reports the experimental study on the effect of piping on soil's shear strength, which can be used to realistically evaluate the stability of existing levees and earth dams that have been subjected to prolonged erosion. Triaxial compression tests are performed on a sandy clay soil. A soil specimen (10.2cm in diameter) without piping channel is first tested as a control sample. Then a single hole is formed using a mini hand auger in the soil during the specimen preparation to simulate a piping channel. Three piping inclinations are studied: vertical, inclined, and horizontal. For each piping channel inclination, three hole diameters are tested. After saturation, consolidated-undrained (CU) compression tests are performed to simulate the slow piping formation followed by a quick hydraulic loading during a flooding. For each channel inclination and diameter, three-stage compressions on the same specimen are conducted to obtain three Mohr's circles in order to obtain the cohesion and the internal friction angle of the soil element with piping. The experiments showed deteriorating effect of piping on effective internal friction angle (ϕ). ϕ decreases with the increase of diameter of vertical holes. It was also observed that ϕ is not affected by the channel diameters when the piping channel is horizontal or inclined, although ϕ does decrease by an average of 28% of specimens with horizontal and inclined holes when compared with that of the control specimen.

INTRODUCTION

Subsurface erosion has been one of the most prevalent causes of catastrophic failure of levees and earth dams, such as the 1972 failure of the Buffalo Creek dam in West Virginia (Wahler & Associates, 1973) and the 1990 collapsing of embankment earth dam in South Carolina (Leonards and Deschamps, 1998). During Hurricane Katrina, three levee breaches were possibly caused by underseepage-induced failure due to piping (Seed et al., 2008a, 2008b; Sills et al, 2008). Subsurface erosion changes the structure of the base soil. It results in fractures in a levee and changes the stress and strain conditions around the fractures. As a result, localized shear strength reduction

is possible. In the stability analysis of levees using the finite element method, each element is assigned a strength value (c and ϕ). If a piping channel penetrates a soil element, the shear strength of this element should reflect the effect of piping on the possible shear strength variation. Furthermore, various sizes and orientations of piping channels make the strength variation less predictable. Fig 1 shows three piping channel orientations in soil elements in and beneath a levee. The purpose of this paper is to study the effect of piping erosion on the strength of levees. Quantification of the effect of erosion on soil's shear strength may provide valuable information for realistic levee stability analysis.

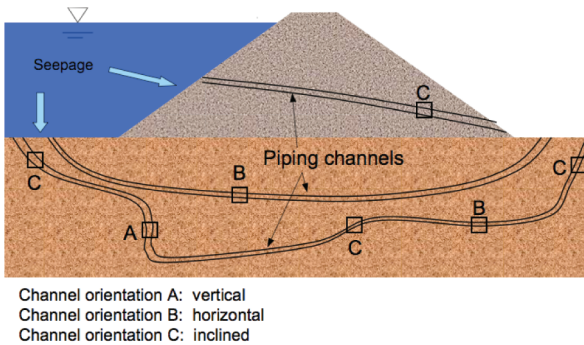


FIG. 1. Piping channels in and beneath levees.

EXPERIMENTAL METHODS

Triaxial tests are used in this study to measure the shear strength of soil specimens with and without piping channels, respectively. A sandy clay soil is tested in this study. The grain size distribution is shown in Fig 2. The liquid limit is 33 and the plastic limit is 22. The soil specimens used in the triaxial tests are 10.2 cm in diameter and 15.24 cm in height. The triaxial experimental setup (vendor: ELE International) is shown in Fig 3, which includes the triaxial load frame, triaxial cell, control panel to maintain pressurized water, and load, displacement, pressure, and volume change transducers, and an automatic data acquisition unit. The soil was compacted to 85% of its maximum dry density (1.65 g/cm^3) at the optimum water content (19%) to simulate the natural and erosion-prone soil condition. The soil was compacted with six uniform layers using a small tamper to ensure uniform density. All the soil specimens were compacted following the same approach and using the same soil mass and volume to minimize the effect of density and heterogeneity on soil strength.

Internal channels in levees may be caused by internal erosion, hydraulic fracturing, or burrowing animals such as beavers. To form a simulated piping channel, a mini hand auger of three different sizes (2.52cm, 1.87cm, and 1.30cm) is used to drill a hole during the specimen preparation (Fig 4). The hole in each specimen penetrates

the specimen. Three orientations are used: horizontal, vertical, and inclined by 60° (measured from the horizontal direction). For the specimens with a horizontal hole, the hole penetrates through the specimen. To prevent the cave-in and break of the membrane during saturation, a plastic mesh that is slightly larger than the hole diameter was used to cover the hole. Including the control specimen (no piping hole), ten tests were conducted. The saturation process of each specimen took from 71 to 90 days to complete and the final B values are from 85% to 93%. In order to expedite

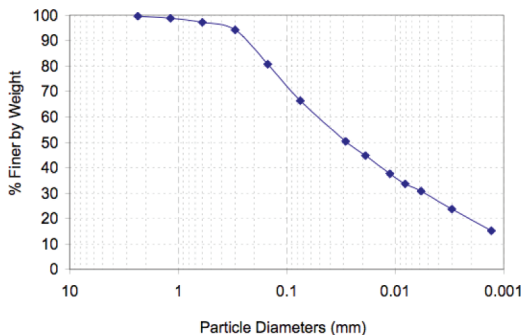


FIG. 2. Grain size distribution of the sandy clay.

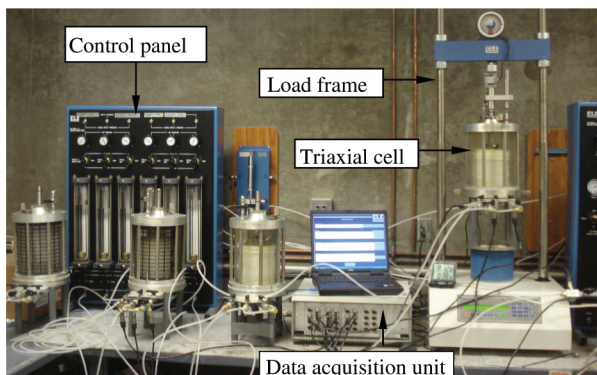


FIG. 3. Experimental Setup.

the tests, four specimens with different hole sizes and orientations are saturated concurrently (Fig 3). At the end of the saturation, 1-day consolidation is conducted. Then undrained compression is conducted on the specimen with the pore-pressure and back-pressure valves closed. According to the American Society for Testing and Materials (ASTM) specification D2850, Test Method for Unconsolidated Undrained

Triaxial Compression Test on Cohesive Soils (ASTM, 2006), the axial strain rate was chosen to be 0.5 %/min (or 0.762 mm/min for the specimens used in this study) during the undrained compression. The axial load was measured by the S-type load transducer, and the deviator stress was calculated by the DS7 software (ELE International) using the corrected cross sectional area. The axial deformation was measured by the LVDT transducer. The pore- and back-pressure transducers measure the pore pressure variation during the compression. In order to obtain three Mohr's circles to derive the c and ϕ values, multiple-stage compressions are conducted on the same specimen — the first compression is terminated when the stress-strain curve starts to level off at a small strain, then consolidation is conducted at a higher confining pressure; at the end of the consolidation, the second undrained compression is conducted; the third compression followed the same approach. A sample stress-strain curve for a vertical hole of 1.87 cm is shown in Fig 5. The Mohr's circles are plotted using the effective minor and major principal stresses, and the effective internal friction angles and the effective cohesions are obtained from the Mohr-Coulomb failure envelopes.



FIG. 4. Hole formation in soil specimen.

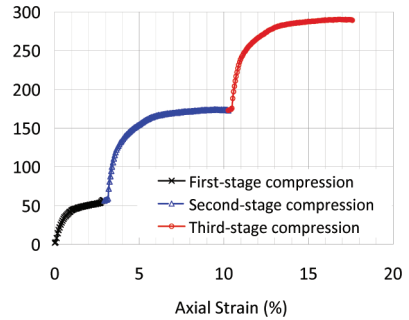


FIG. 5. Stress-strain curve of multiple compression tests on the same specimen.

RESULTS AND ANALYSES

The ten consolidated-undrained (CU) tests with multiple-stage compressions yield the following strength data as presented in Fig 6 and Fig 7. The undrained effective cohesion (c') and internal friction angle (ϕ') of the control specimen are 0 and 40.6° , respectively. The effective cohesion values of the specimens with inclined and horizontal holes are in a low range of 0 to 10.3 kN/m^2 , which can be practically

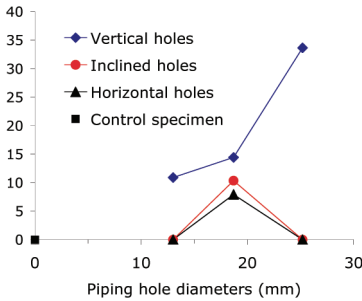


FIG. 6. Variation of effective cohesion with piping orientations and diameters.

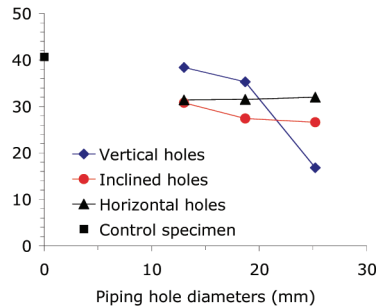


FIG. 7. Variation of effective internal friction angle with piping orientations and diameters.

considered negligible. But for the specimens with vertical holes, effective cohesion increases as the hole diameter increases. The authors are yet able to explain this phenomenon. Fig 7 shows the variation of effective friction angles with piping diameters and orientations. Under the CU loading condition, effective friction angle of normally consolidated clays seem to control the soil strength, because $c' \approx 0$ and ϕ' exhibits large values. For the specimens with vertical holes, ϕ' decreases from 38.4° to 16.8° as the hole increases in diameter, the highest reduction is 58% compared to the control specimen without piping. This indicates the deteriorating effect of piping sizes on shear strength. For the specimens with horizontal and inclined holes, although ϕ' reduced by an average of 28% compared to the control specimen, the variation of ϕ' with hole diameters is small (31.4° to 26.6°). ϕ' remains unchanged for the different sizes of horizontal holes. This ongoing study still tries to explain the observation that ϕ' is not affected by the hole diameters when the piping channel is inclined or horizontal. In the control specimen, distinctive failure plane was observed after the compression; while no obvious failure plane was shown in all the nine specimens with simulated piping holes, the specimens simply bulged and the failure was indicated by the plateaus on the stress-strain curves.

CONCLUSIONS

This paper reports a preliminary experimental study on the quantitative effect of piping channel orientations and diameters on shear strength of a sandy clay soil. The research observed deteriorating effect of piping on effective internal friction angle. ϕ' decreases with the increase of diameter of vertical holes, the maximum reduction is 58%. It is also observed that ϕ' is not affected by the channel diameters when the piping channel is horizontal or inclined, although ϕ' does decrease by an average of 28% when compared with that of the control specimen. This research is still in progress to explore the fundamental mechanisms of the piping effect on the cohesion and internal friction angle in order to explain the aforementioned experimental observations.

ACKNOWLEDGEMENT

The research is partially funded by the California State University, Fresno and Precision Civil Engineering, Inc. Steve Scherer, Technician at CSU Fresno helped construct the experimental setup. Exequiel Sinco, graduate student at CSU Fresno, helped on specimen preparation and setup. These supports are greatly appreciated.

REFERENCES

- American Society for Testing and Materials (ASTM) (2006). "Test Method for Unconsolidated Undrained Triaxial Compression Test on Cohesive Soils". 2006 Annual Book of ASTM Standards, Soil and Rock (I), Section 4, Volume 04.08. Designation: D 2850. ASTM International.
- Leonards, G.A., and Deschamps, R.J. (1998). "Failure of Cyanide overflow pond dam." *J. of Performance of Constructed Facilities*, 12 (1): 3-11.
- Seed, R. B., Bea, R.G., Abdelmalak, R. I., Athanasopoulos-Zekkos, A., Boutwell, G.P., Bray, J.D., Cheung, C., Cobos-Roa D., Ehrensing, L., Harder Jr., L.F., Pestana, J.M., Riemer, M.F., Rogers, J.D., Storesund, R., Vera-Grunauer, X., and Wartman, J. (2008a). "New Orleans and Hurricane Katrina. II: the central region and the lower Ninth Ward." *J. of Geotechnical and Geoenvironmental Engrg.* 134 (5): 718-739.
- Seed, R. B., Bea, R.G., Abdelmalak, R. I., Athanasopoulos-Zekkos, A., Boutwell, G.P., Bray, J.D., Cheung, C., Cobos-Roa D., Cohen-Waeber, J., Collins, B.D., Harder Jr., L.F., Kayen, R.E., Pestana, J.M., Riemer, M.F., Rogers, J.D., Storesund, R., Vera-Grunauer, X., and Wartman, J. (2008b). "New Orleans and Hurricane Katrina. IV: Orleans East Bank (Metro) Protected Basin." *J. of Geotechnical and Geoenvironmental Engrg.* 134 (5): 762-779.
- Sills, G.L., Vroman, N.D., Wahl, R.E., Schwanz, N.T. (2008). "Overview of New Orleans levee failures: lessons learned and their impact on national levee design and assessment." *J. of Geotechnical and Geoenvironmental Engrg.* 134 (5): 556-565.
- Wahler, W.A. and Associates. (1973). "Analysis of coal refuse dam failure, Middle Fork Buffalo Creek, Saunders West Virginia." National Technical Service Rep. PB-215, Washington, D.C., 142-143.

Study on the New Deformation Characteristics of the Pumped Aquifers in Su-Xi-Chang Area, China

Fei Wang¹, Linchang Miao², Ph.D., and Weihua Lv³

¹Ph.D. Candidate, Institute of geotechnical engineering, Southeast University, Nanjing, China, 210096, feiwangseu@gmail.com

²Professor, Institute of geotechnical engineering, Southeast University, Nanjing, China, 210096, lc.miao@seu.edu.cn

³Ph. D. Student, Institute of geotechnical engineering, Southeast University, Nanjing, China, 210096, whlv@seu.edu.cn

ABSTRACT: With the survey data of land subsidence in Su-Xi-Chang area, we found the deformation in the pumped aquifers cannot be neglected, even which is comparable with the adjacent aquitards. A series of lab high pressure compression tests on Suzhou aquifer sand from five different depths using costume-made setup were used to verify the compressibility of the aquifer sand. The test results show that the compression index of aquifer sand is close to some kinds of clay. With the comparison of the grain size distribution before and after testing, it can be concluded that the permanent rearrangement of sand grains is partly responsible for the sand compression.

INTRODUCTION

Land subsidence has been extensively investigated, not only due to the widely distribution, but also due to its serve damage and becoming worse conditions. The excessive groundwater pumping is mainly responsible for the land subsidence. As one of the most developed area in China, the water usage in Su(zhou)-(Wu)Xi-Chang (zhou) area is always increasing. The area where the ground surface deformation exceeds 200mm was 5800km² in 2002, that means half of the Su-Xi-Chang area is suffering the land subsidence, which is becoming an important limitation of the economy developing. Many investigators have focused on the land subsidence in this area (Chai et al., 2004; Shen et al., 2006; Shi et al., 2007; Zhang et al., 2007.).

It is generally accepted that the consolidation of the confined aquitards is the

main cause of the land subsidence due to groundwater pumping (Poland, 1984). However, in the survey data of the Su-Xi-Chang area, the deformation in the pumped aquifer is almost equal to the deformation of its adjacent aquitards which is the new characteristic of the land subsidence. The deformation at different layers was measured using the deep benchmarks. Figure 1 clearly shows this phenomenon. The thicknesses of the 3rd aquifer and aquitard are 24.1 and 26.3m respectively, whilst the deformations in those two layers from 1990 to 2003 are both almost 100mm. What made the fairly deformation in sand layers? The possible reason is the high compressibility of the aquifer sand. Some one may argue that the deformation of the aquifer should be caused by the compaction of the interbedded clay in the aquifer. As mentioned above, the aquitard and the aquifer have almost same thickness and deformation, which means that the strain of these two layers is close. Thus, it can be imagined that if the deformation of the aquifer is caused by the interbedded compaction, what high compressibility the interbedded clay should have. A series of lab tests was conducted to investigate the new compression behavior of aquifer sand in Suzhou.

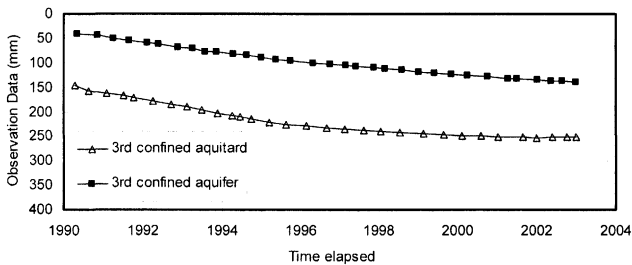


FIG. 1. Land Subsidence Developing in Changzhou.

EXPERIMENTAL STUDY

Tested Material and Setup

The tested soil specimens were taken from the aquifer system in Suzhou. The depth reached to 250m. Aquifer sand at five different deep places (i.e., 41.5, 66, 92.3, 147, and 223.2m from the ground surface) was drilled out.

The high-pressure compression test equipment was used to perform relative high pressure compression tests. The pressure can reach 20MPa at most, which is provided by the compressed air and stored in a steel box. The principle of the test setup is same as the general one-dimensional consolidation test setup. The setup is computer-controlled, and the criteria for the next step loading can be set manually before the test. The typical criteria for the loading incremental are the creep

deformation in 24 hrs not greater than 0.5mm. Figure 2 shows the schematic figure of the test setup. There are three portions in the whole equipment, namely; the air pump, the compression setup, and the computer controller. The inner diameter of the specimen is 60mm, while the thickness is 20mm.

Test Procedure

Before the test, the grain size distribution curves for different deep aquifer sand were obtained using sieve analysis test to demonstrate the changing of the grain size due to compression. The compressive pressures were assigned as 100, 200, 400, 800, 1600, and 3200kPa. For each pressure, two specimens were tested to insure the credibility of the test results.

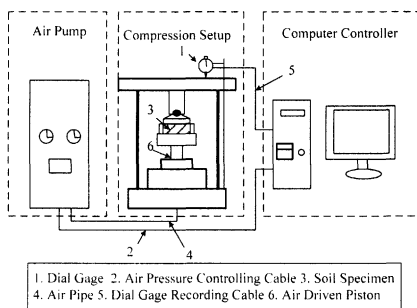


FIG. 2. Setup of the High-pressure Compression Test.

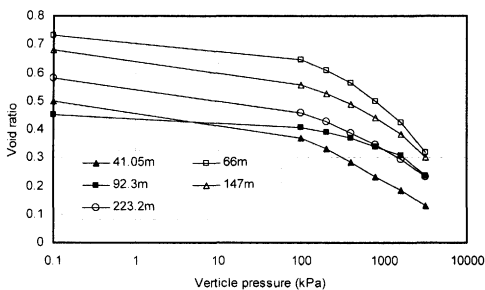


FIG. 3. Compression Curves of Aquifer Sand at Different Depth.

TEST RESULTS ANALYSIS

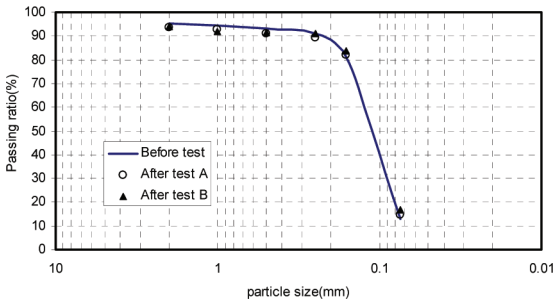
Figure 3 are the compression curves of the aquifer sand at different depth. It demonstrates that the aquifer sand can be compressed when the compressive pressure

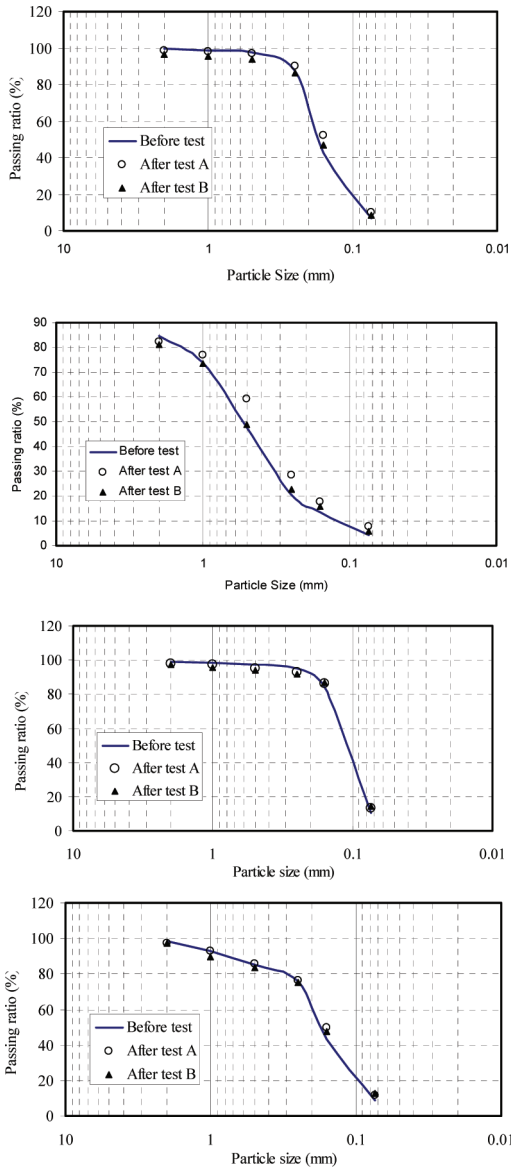
is greater than a constant value, which is related to the grain size distribution, the mineral inclusions, the shape of grain size, the confining pressure and the shear stress in the sand (Lee and Farhoomand, 1967). Generally, the compressive pressure cannot reach this value; therefore, the deformation of sand is not significant. However, with the increasing of pumping depth, the overburden stress of the aquifer might reach and greater than this value; thus, the aquifer is becoming more compressible. Table 1 summarizes the compression index of those sand specimens after the big compaction happens. The compression index ranges from 0.10 to 0.20, which is comparable with the compression index of some kinds of clay. Based on the compression tests, we can conclude that the compression of the aquifer sand layer cannot be neglected; conversely, it may dominate the ground surface deformation.

Table 1 Summary of the Compression Index.

Depth/m	41.05	66.0	92.3	147	223.2
Compression Index	0.16	0.21	0.11	0.17	0.16

Figure 4 shows the comparison of grain size distribution of the aquifer sand. The solid line presents the grain size distribution curve before testing, while the markers are the grain size after testing. The characters “A” and “B” were used to separate the two specimens from the same depth. It clearly shows that compression makes the finer portion of the grain size increasing which is most obvious in Figure 4 (c). It can be concluded that the permanent rearrangement of sand grains is another reason of sand compression, which can significantly reduce the permeability of the aquifer.





CONCLUDING REMAEXS

Based on the land subsidence observation data in Su-Xi-Chang area, China, the deformation of pumped aquifer can not be neglected. The compression behavior of aquifer sand can be verified. From the test result, the following conclusions can be obtained:

- (1) With the groundwater pumping developing, the new deformation characterize of pumped aquifer should be paid much attention;
- (2) The compression index of aquifer sand in Suzhou area is comparable with some kinds of clay; and
- (3) Permanent rearrangement of sand grains is partly responsible for the sand compression.

ACKNOWLEDGEMENTS

This paper is a part of the project No.50878051 which is supported by the National Natural Science Fund of China; and the project "Jiangsu Six Top Talent Project" which is supported by the Jiangsu Provincial Government. The authors wish to express their gratitude for the support given to this work.

REFERENCES

- Chai, J.C., Shen, S.L., Zhu, H.H., and Zhang, X.L., (2004). "Land subsidence due to ground water drawdown in Shanghai." *Geotechnique*, Vol.54, No.2, 143-147.
- Lee, K.L., and Farhoomand, I. (1967). "Compressibility and crushing of granular soil in anisotropic triaxial compression." *Canadian Geotechnical Journal*, 4(1), 68-99.
- Poland, J. F. (1984). "Guidebook to Studies of Land Subsidence due to Ground-Water Withdrawal." *American Geophysical Union*, Chelsea, Michigan.
- Shen, S.L., Xu, Y.S., and Hong, Z.S. (2006). "Estimation of land subsidence based on groundwater flow model." *Marine Georesource and Geotechnology*, Vol. 24, 149-167.
- Shi, X.Q., Xue, Y.Q., Ye, S.J, Wu, J.C., Zhang, Y., and Yu, J. (2007). "Characterization of land subsidence induced by groundwater withdrawals in Su-Xi-Chang area, China." *Engineering Geology*, Vol. 52, 27-40.
- Zhang, Y., Xue, Y.Q., Wu, J.C., Ye, S.J., Wei, Z.X., Li, Q.F., and Yu, J. (2007). "Characteristics of aquifer system deformation in Southern Yangtse Delta, China." *Engineering Geology*, 90:160-173.

Parametric Studies of Ground Deformation Induced by Pneumatic Caisson Construction in Soft Soils

Hailin Wang¹, Fangle Peng², Yong Tan³ and Zhenliang Xu⁴

¹Department of Geotechnical Engineering, Tongji University, 1239 Siping Road, Shanghai 200092, P. R. China; Email: hailin_wang@126.com

²Department of Geotechnical Engineering, Tongji University, 1239 Siping Road, Shanghai 200092, P. R. China; Email: pengfangle@tongji.edu.cn

³Department of Geotechnical Engineering, Tongji University, 1239 Siping Road, Shanghai 200092, P. R. China; Email: tanyong21th@hotmail.com

⁴Shanghai Urban Construction Design & Research Institute, 3447 Dongfang Road, Shanghai 200125, P. R. China; Email: guidao5@sucdri.com

ABSTRACT: This paper presents a thorough finite element (FE) parametric study of ground deformation caused by the new pneumatic caisson (NPC) construction. In this study, the effects of several parameters which may affect the ground deformation were investigated in terms of two aspects: surface settlements, and soil upheavals beneath the caisson. These parameters are (1) skin friction, (2) compressed air pressures, (3) embedment depth, and (4) distance from the caisson of the protection wall. Based on the proposed FE simulation techniques, the effects of these parameters were quantified and discussed, and the factors that help to reduce ground deformations were identified. Results showed that the compressed air pressures played a very important role in preventing upheavals of soils at the caisson base. Finally, some suggestions and recommendations for NPC construction were reached.

INTRODUCTION

Pneumatic caissons are similar to open caissons except that they are provided with airtight bulkheads above the cutting edge (called the working chamber). The chamber is pressurized to the extent necessary to control the inflow of soils and water. Traditionally, workers have to enter into the working chamber and conduct the excavation under high pressures, high temperatures, and high humidity. While in the new pneumatic caissons (NPC), both excavation and discharging of soils are done by the automated excavation and remote controlling systems (Peng et al., 2009). Pneumatic caissons have been constructed in many countries and areas, especially in Japan (Peng et al., 2004). In China, there are some traditional pneumatic caissons completed many years ago and the NPC method has never been used in practice. In 2007, this method was successfully applied to construct one tunnel shaft in Shanghai, China. As the NPC

is increasingly used in practice, the high sensitive, unstable ground and deep excavations have been/will be encountered more frequently, which results in adverse impacts on environment. Therefore, this NPC method is also facing the challenges in the control of ground deformation, especially when adopted in the densely populated area.

Some studies (Umeda et al., 2006; Inoue et al., 2006) have been conducted to investigate ground deformations induced by the NPC construction. Hong et al. (2005) studied the distribution of the skin friction by analytical methods and field measurements. Peng et al. (2009) introduced a procedure of how to model the whole construction process of NPC using FEM techniques, and the predicted ground deformations were verified by field measurements. However, no efforts were made to investigate the effects of parameters (skin friction and compressed air pressures) on ground deformations during NPC construction. Besides this, in some cases, a supplementary method as protection walls (usually made up of sheet piles) is adopted to mitigate the influence of NPC construction on the adjacent structures. The effects of wall parameters (wall distance and embedment depth) also need to be investigated.

The purposes of this study were to identify the parameters that might affect ground deformations during the NPC construction, to quantify their influences, and to find out an optimized solution of reducing ground deformations. These were achieved by a series of comprehensive finite element (FE) analyses. Then, figures which depict the effects of these parameters were produced. These figures will provide some useful references for the NPC construction in the soft grounds.

TUNNEL SHAFT CONSTRUCTION IN SHANGHAI USING NPC

The shaft construction using NPC presented in this study was one part of the shield tunneling project of Metro Line 7 in Shanghai, which would be used as a shield working shaft initially and as a ventilation shaft in operation. The tunnel shaft was very close to Huangpu River, and thus it was critical to control ground deformations and groundwater movements to ensure the construction safety. As shown in Fig. 1, the shaft was a caisson structure with the external dimensions of 25.2 m (L) \times 15.6 m (W) \times 27.7 m (H), which included the working chamber. Its total sinking depth was around 29.06 m. The caisson structure is fabricated in six segments on the ground surface. Before sinking, one shallow excavation is made for the treatment of shallow ground. When the first three segments are made, the caisson sunk by 6.00 m. Afterwards, the caisson sunk in three stages. Depths of sinking in each stage are 4.20 m, 8.80 m, and 10.06 m, respectively.

The construction started in November, 2006 and ended in October, 2007. Observed data showed that, the caisson construction caused very small soil movements in the first three sinking stages. However, in the last sinking stage the measured values increased dramatically, and even some measured points around the caisson were damaged by excessive settlements. Fortunately in this shaft construction, its adjacent buildings and pipelines were free from damage. The failure in the last sinking stage raised such questions: (1) What role does the skin friction play in NPC-induced ground movements such as surface settlements and soil upheavals beneath the caisson? (2) What is the effect of the compressed air pressures? (3) If protection walls were installed around the caisson, is it effective to minimize the environmental effects? (4) What are the suitable

embedment depth and wall distance for the protection walls? To answer these questions, a series of FE analyses were carried out and the analysis results will be presented and discussed in the following sections.

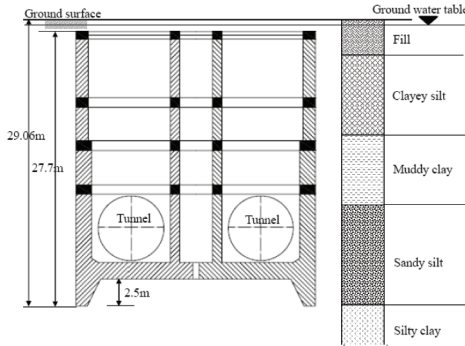


FIG. 1. Profile of the shaft and soil conditions.

PARAMETRIC STUDIES BY FEM

The FE analyses were performed using the two-dimensional finite element code PLAXIS 8.2 (Brinkgreve et al., 2002). Because of symmetrical geometry, a plane-strain model with half geometry was adopted and a typical finite element mesh made of 15-node triangle elements is shown in Fig. 2. In the mesh the caisson structure was not incorporated and the interaction between the caisson and its surrounding soils was implemented through applying vertical distributed forces (i.e. the skin friction and cutting force) to the soil on the contact surface. In addition, the protection wall and the compressed air pressures were taken into consideration.

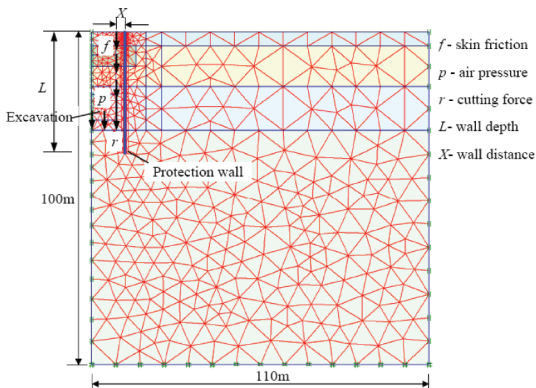


FIG. 2. Typical FEM mesh in the present study.

In the parametric numerical simulation, the caisson sinking process was modeled by four continuous stages. Corresponding forces (skin friction f , cutting force r , and air pressures p) were applied to the soils in each stage. In the meantime, the “excavated” soil elements were deactivated accordingly. The ground water table within the region of the caisson was also updated in each stage. In this study, several sets of FE analyses were performed by varying values of each aforementioned parameter, based on the “standard” conditions (i.e. the actual construction conditions of the tunnel shaft in Shanghai). In the “standard” conditions no protection walls were adopted.

The detailed introduction on how to model the whole construction process of NPC using PLAXIS 8.2 along with the validation of the analysis procedure by field measurements is reported by Peng et al. (2009) and will not be repeated here.

Effects of skin friction

The first investigated parameter is the skin friction, f , between the caisson and its surrounding soils. During the NPC construction, the skin friction f is not constant, and it is highly dependent on soil properties, smoothness of the caisson wall, and other construction conditions. Especially, f could be reduced largely in situations where some measures are taken to aid sinking, such as air or slurry coating method. Therefore, it will be effective to investigate the effects of these auxiliary construction measures indirectly by parametric studies of f . In the “standard” conditions, f was given a value 20 kPa. In the present parametric study, five cases of numerical analyses were performed on the above mentioned Shanghai shaft project, with f of 0 kPa, 10 kPa, 20 kPa, 30 kPa, and 40 kPa, respectively. In these FE analyses, no protection wall was incorporated.

Figs. 3(a) and 3(b) present variation of the final surface settlements and soil upheavals beneath the caisson with the skin friction f . In Fig. 3(a), the x-coordinate is the distance away from the outside wall of the caisson (D). The modeling results showed that at the same final sinking depth, the maximum surface settlement, δ_m , occurring at the periphery of the caisson, increased significantly with increasing of the skin friction f . When f increased from 10 kPa to 40 kPa, δ_m was almost increased by 12 times, up to 15.5 cm. In the meantime, the surface settlement profile tended to move downwards as f increased.

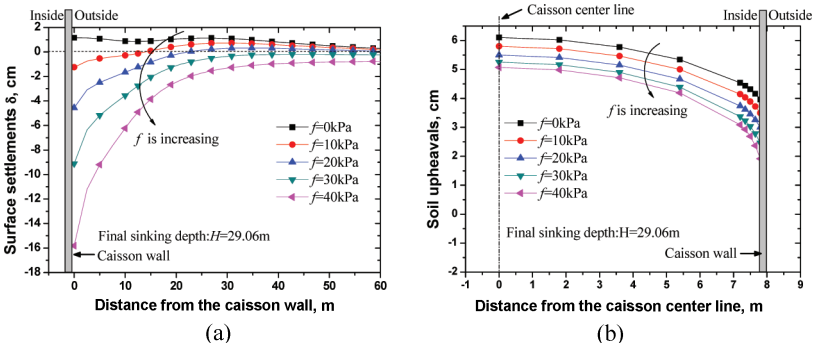


FIG. 3. Variation of surface settlements and soil upheavals with f .

In Fig. 3(b), the x-coordinate is the distance away from the center line of the caisson. As the excavation under the caisson started, soil upheavals beneath the caisson would occur due to unloading. Upheavals located in the center line of the caisson were more significant. From Fig. 3(b), it can be seen that upheavals beneath the caisson decreased linearly with the increase of f , but in a relatively gentle rate. This can be attributed to the downdrag action caused by f , which restrained upward movements of soils beneath the caisson to some extent.

Effects of compressed air pressures

Compressed air pressures in the working chamber play an important role in the NPC construction to control the inflow of soil and water. The air pressures are adjusted timely according to the ground water table levels. To investigate its effects on ground movements, the air pressure p was varied from $0.7p_0$ to $1.3p_0$, where p_0 is the recorded value in the shaft construction. In this set of FE analyses, the “standard” construction conditions were applied, i.e. $f = 20$ kPa, no protection wall and so on. Fig. 4(a) summarized the final surface settlements at different air pressures p . From this graph, it can be found that p imposes limited effects on surface settlements, and for various p , the surface settlement profiles are similar. On the contrary, upheavals beneath the caisson are very sensitive to p , as shown in Fig. 4(b). From Fig. 4(b), it can be observed that the upheavals were inversely proportional to p . This fact can be interpreted by that the compressed air pressures could counteract the unloading to a large extent. This has also been considered a significant advantage of NPC to other braced excavation methods for minimizing the construction effects on environments.

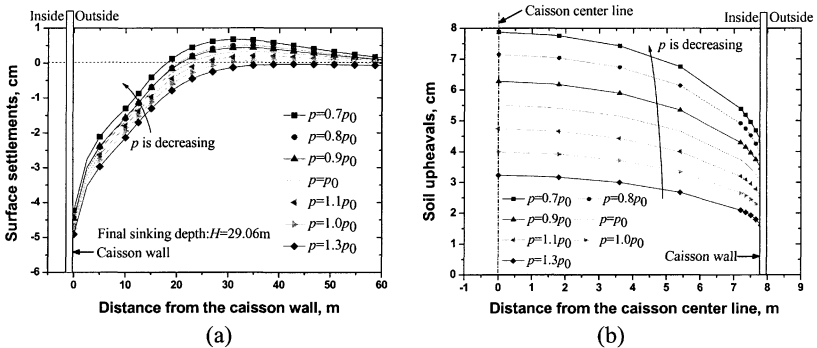


FIG. 4. Variation of surface settlements and soil upheavals with p .

It should be noted that, in theory, the air pressure p equals to the groundwater pressures at depth of the caisson base. However, it could be adjusted within some ranges according to the actual ground water table levels in the working chamber, and especially in some cases, the air pressure p is reduced designedly to aid the caisson sinking. The above study results will provide some useful information on the environmental effects.

Effects of embedment depth

In NPC constructions, a supplementary method as a protection wall is sometimes

adopted in consideration of reducing the construction influence on the adjacent structures, especially in densely populated area. However, the design method of the protection wall has not been established yet. In this section and the following, the effects of the protection wall (wall embedment depth L and wall distance X) will be investigated by numerical parametric study.

As for the embedment depth L , a series of FE analysis were performed, in which L was varied from 10 m to 40 m, keeping the wall distance $X = 1.0$ m. Considering that the protection wall was usually made up of sheet piles, the protection wall stiffness, EI , was given a value $1.0e+6$ kN·m²/m. In the analysis, the case without protection wall was also incorporated.

Fig. 5 presents variation of the final surface settlements and upheavals beneath the caisson with L at $X = 1.0$ m. From Fig. 5(a), it can be observed that when L was smaller than the final excavation depth H , the wall embedment depth L imposed little effect on the final surface settlements. The surface settlement profile with protection walls was closely similar to that with no walls. This could be interpreted that the short walls could not effectively prevent the surrounding soils moving toward the caisson bottom. The surface settlements might even a little bigger, due to the additional friction between the protection wall and soils. While $L \geq H$, the protection wall became very effective to reduce the surface settlements. Outside the protection wall, the surface settlements were no more than 5 mm. There were even upheavals at the perimeter of the protection wall, which might be induced by unloading. Within the areas between the caisson and the protection wall, the surface settlements were substantially decreased to half as compared with that without protection wall. It is also found that, the longer the protection wall, the smaller the surface settlements. However, increasing wall embedment length means increasing project costs. An optimum design of a protection wall requires an embedment depth that achieves the balance between serviceability and cost. Therefore, it may be appropriate that the embedment depth L of the protection wall is designed to equal the excavation depth. Inoue (2007) also confirmed this.

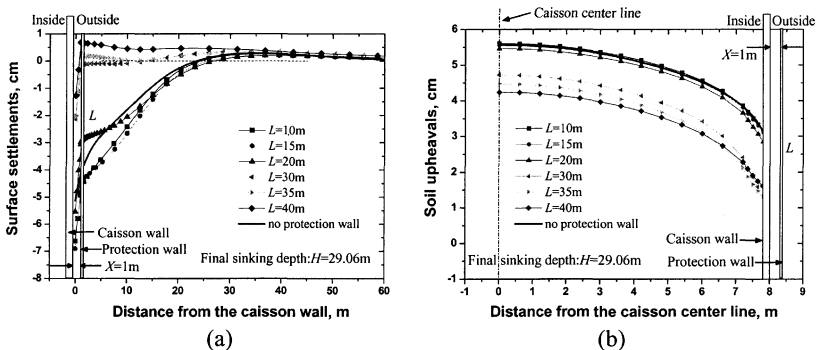


FIG. 5. Variation of surface settlements and soil upheavals with L .

Fig. 5(b) presents the effects of the wall embedment depth on the upheavals beneath the caisson. As described above, when $L < H$, the protection wall imposed little effect on

soil upheavals. While $L > H$, the soil upheavals were reduced sharply as a result of existence of the protection wall and decreased slowly with increasing of L . However, in general, soil upheavals were not very sensitive to L .

Effects of wall distance

As for the wall distance X , five sets of FE analyses were performed. In the analyses X was varied from 1.0 m to 4.0 m, keeping the wall embedment depth $L = 30$ m and $EI = 1.0e+6$ kN·m²/m. Fig. 6 presents variation of the final surface settlements and upheavals beneath the caisson with X at $L = 30.0$ m. From Fig. 6(a) it can be seen that, the wall distance X had significant effects on the surface settlement profile. With decreasing of X , the surface settlement profile became much flatter. When $X = 1.0$ m, the surface settlements outside the protection wall could be negligible. In the case of no protection wall, some surface upheavals existed beyond some distance from the caisson, due to the cutting and extruding action of the caisson cutting edge. While in the other cases, under isolation due to the protection wall, the upheavals were minimized significantly. Fig. 6(b) showed that soil upheavals beneath the caisson were proportional to X . With X decreased, soil upheavals also decreased.

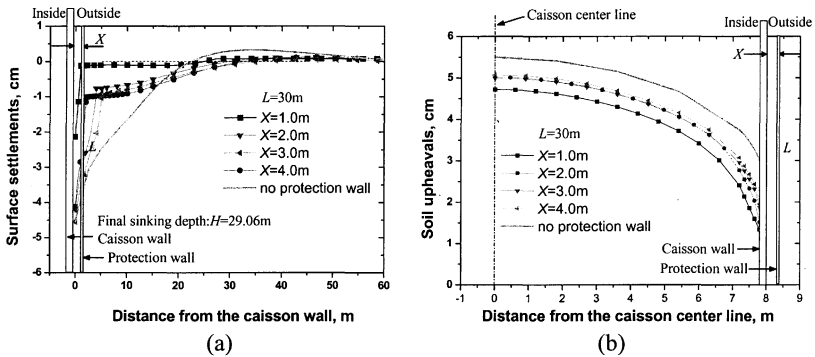


FIG. 6. Variation of surface settlements and soil upheavals with X .

CONCLUSIONS

This paper presents a thorough parametric study on FE-predicted ground movements induced by the NPC construction, in terms of the two aspects: surface settlements and upheavals beneath the caisson. Based on the parametric studies, the main conclusions and suggestions can be drawn as follows:

- 1) The skin friction f is a key factor in determining surface settlements due to NPC construction. The modeling results showed that reducing the skin friction could result in nonlinear substantial reduction of surface settlements during NPC construction. Thus, to minimize the environmental effects caused by NPC, it is necessary to take some measures to reduce the skin friction, such as air or slurry coating method.
- 2) Variation of the compressed air pressure p caused few changes in surface settlements. While, for a certain excavation depth, p is the most important factor in

determining soil upheavals beneath the caisson. The air pressure could, to a great extent, counteract the unloading due to excavation and then reduce soil upheavals. The upheavals were inversely proportional to p . The results will provide some references on the environmental effects when the air pressure is adjusted within the allowed ranges.

3) If the protection wall was applied, it was very effective to reduce the surface settlements at $L \geq H$; and it imposed little effect while $L < H$. To achieve the balance between serviceability and cost, $L = H$ was appropriate. At the same embedment depth, surface settlements decreased with decreasing of X , and the surface settlement profile became much flatter. If it was possible, the protection wall should be placed as much as close to the caisson. In addition, X and L had limited effects on soil upheavals beneath the caisson. These findings are of practical use, which can lead to an economical construction of a protection wall for NPC construction.

ACKNOWLEDGEMENTS

This work was supported by funds from Grant 2006BAJ27B02-02 from National Key Technology R&D Program as well as Shuguang Project (No.05SG25), NSFC (No.50679056), NCET (06-0378) and Shanghai Leading Academic Discipline Project (B308).

REFERENCES

- Brinkgreve, R.B.J., Al-Khoury, R., Bakker, K.J., Bonnier, P.G., Brand, P.J.W., Broere, W., Burd, H.J., Sotys, G., Vermeer, P.A., and Haag, D.D. (2002). "PLAXIS—finite element code for soil and rock analyses." *User's Manual Ver. 8*. A.A. Balkema, Rotterdam, the Netherlands.
- Peng, F. L., Sun, D. X., Ohuchi, M., and Bai, Y. (2004). "Pneumatic caisson construction technology for very deep underground engineering." *Underground Space*, 24(5), 699-703 (in Chinese).
- Peng, F. L., Wang, H.L., Guo, J.G., and Xu, Z.L. (2009). "Measurement and Simulation of Ground Deformation Due to Pneumatic Caisson Construction." *Contemporary Topics in Ground Modification, Problem Soils, and Geo-Support*, ASCE, GSP 187, 41-48
- Umeda, N., Fujii, N., and Inoue, T. (2006). "Numerical modeling of pneumatic caisson method." *Journal of Applied Mechanics*, Vol.9, 603-612 (in Japanese).
- Inoue, T., Fujii, N., and Ohuchi, M. (2006). "Numerical simulation of ground deformation due to pneumatic caisson tunnel." *Journal of tunnel engineering*, Vol.16, 155-164 (in Japanese).
- Hong, W.P., Yea, G.G., Kim, T.H., and Nam, G.M. (2005). "Evaluation of unit skin friction to large size pneumatic caisson during the process of sinking." *Proc. 15th International Offshore and Polar Engineering Conference*, Seoul, 555-561.
- Inoue, T., Fujii, N., Ohuchi, M., Shimoma, M., and Tamura, T. (2007). "Numerical simulation of ground deformation due to pneumatic caisson work using protection wall." *Proc. of the symposium on underground space*, JSCE, Vol.12, 298-302 (in Japanese).

Simultaneous Modeling of Internal Erosion and Deformation of Soil Structures

Kazunori Fujisawa¹, Akira Murakami² and Shin-ichi Nishimura³

¹ Assistant Professor, Graduate School of Environmental Science, Okayama University, 3-1-1Tsuchimanaka, Okayama-City, Okayama, Japan; kazunori@cc.okayama-u.ac.jp

² Professor, Graduate School of Environmental Science, Okayama University, 3-1-1Tsuchimanaka, Okayama-City, Okayama, Japan; akira_m@cc.okayama-u.ac.jp

³ Associate Professor, Graduate School of Environmental Science, Okayama University, 3-1-1Tsuchimanaka, Okayama-City, Okayama, Japan; theg1786@cc.okayama-u.ac.jp

ABSTRACT: Piping, as the result of internal erosion of embankments, is a primary cause of embankment breaks. Moreover, hollows or cavities of soil structures have been occasionally reported due to erosion within soils. The inner states of embankments are needed to be estimated to take appropriate measures for the prevention of the accidents of soil structures. In this study, simultaneous modeling of the internal erosion and the deformation of soils is carried out. As for the internal erosion, the equations governing the erosion and the transport of fine particles within a soil mass are derived with the concept of erosion rates of soils. Additionally, the constitutive model which can describe the deformation of soils caused by the internal erosion is proposed in this paper.

INTRODUCTION

Piping is the phenomenon that a flow path, where the seepage flow concentrates, appears within soil structures. Usually the flow path is created due to the erosion and the migration of soil particles. Piping is the primary cause of dam breaks. Actually, Foster et al. (2000) investigated world-wide embankment dam failures and accidents, and reported that 46 % of them were triggered by piping. The water leakage from aging irrigation ponds, which are small embankment dams to store irrigation water, has been frequently reported in Japan. This phenomenon is considered to result from piping. Therefore, piping is a serious problem for soil structures subjected to seepage flow.

Up to now, there have been a dozen studies on piping. However, the computational methods for evaluation of piping potential are currently limited. Piping is a phenomenon deeply related with erosion within soils, although soil mechanics, at present, cannot deal with the internal erosion of soils and the transport of eroded soil particles. In order to treat the internal erosion and the transport of eroded fine particles within soils, the following must be considered: (1) the velocity field of the intergranular

saturated-unsaturated seepage flow, (2) the increase in the porosity of soils owing to the erosion, and (3) the transportation of the eroded soil particles through the soil pores. In this paper, first, the governing equations for the above three items are introduced with the Eulerian formulation. Secondly, the simultaneous modeling of the internal erosion and the deformation of soils is presented, proposing a constitutive model describing the change of the state surface due to the erosion.

GOVERNING EQUATIONS FOR INTERNAL EROSION

The erosion rate of soils is introduced and the soil phases are considered here in advance of deriving the governing equations. The erosion rate is defined as the volume of the eroded soil particles from the unit surface area of the erodible region within a unit of time, which has the dimensions of velocity. The previous empirical studies and the recent semi-theoretical investigations have adopted the following form for the erosion rate as a function of the shear stress exerted onto the erodible soil particles (e.g., Reddi et al. 2000; Indraratna et al. 2009):

$$E = \alpha(\tau - \tau_c) \quad (1)$$

where E , α , τ , and τ_c denote the erosion rate, the erodibility coefficient, the shear stress, and the critical shear stress, respectively. If shear stress τ , exerted by a fluid, is smaller than critical shear stress τ_c , erosion does not occur.

Figure 1 shows the four phases of soils in order to deal with internal erosion and the transport of the detached soil particles from the soil skeleton. Soils are usually divided into three phases, namely, pore air, pore water, and soil particles. When the internal erosion of soils is considered, however, two types of soil particles exist, i.e., the particles of the soil skeleton and those eroded or detached from the soil fabric.

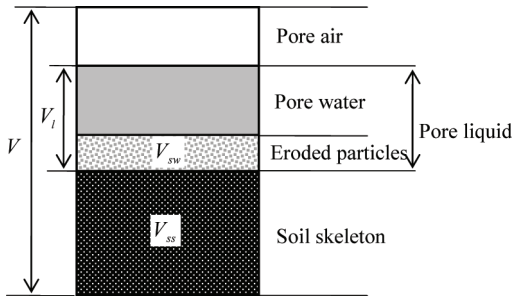


FIG. 1. Four phases of soils for considering internal erosion.

As shown in Figure 1, the mixture of pore water and eroded soil particles is defined as the pore liquid in this paper. V , V_{ss} , V_{sw} , and V_l denote the volume of the soil mass, the soil skeleton, the eroded soil particles, and the pore liquid, respectively. Using these definitions, the soil properties are introduced as follows:

$$\theta = V_l / V, \quad n = (V - V_{ss}) / V, \quad C = V_{sw} / V_l \quad (2)$$

where θ , n , and C denote the volumetric liquid content, the porosity, and the

concentration of detached soil particles from the soil fabric contained in the pore water, respectively.

Adopting the concept of the erosion rates E and the definition of the soil properties in equation (2), governing equations to analyze the internal erosion of saturated soils are derived as follows:

$$\frac{\partial n}{\partial t} + \frac{\partial v_i}{\partial x_i} = E A_e \tag{3}$$

$$\frac{\partial(1-n)}{\partial t} = -E A_e \tag{4}$$

$$\frac{\partial nC}{\partial t} + \frac{\partial C v_i}{\partial x_i} = E A_e \tag{5}$$

where t , x_i , n , v_i , A_e and C denote time, Cartesian coordinates, the porosity, the velocity of the pore fluid, the surface area of the erodible region per unit volume and the concentration of soil particles within the pore fluid, respectively. In the above equations (3) to (5), the Einstein summation convention is applied (the summation convention will be applied hereafter with respect to subscripts). The following Darcy’s law is applicable to the flow of the pore fluid;

$$v_i = k_s \frac{\partial h}{\partial x_i}, \quad h = z + \frac{u_w}{\rho g} \tag{6}$$

where k_s , h , z , u_w , ρ , g denote the permeability, the hydraulic head, the elevation head, the pressure and the density of pore liquid and the gravitational acceleration, respectively. With the aid of equations (4) and (6), equation (3) can be reduced into

$$\frac{\partial}{\partial x_i} \left(k_s \frac{\partial}{\partial x_i} \left(z + \frac{u_w}{\rho g} \right) \right) = 0 \tag{7}$$

The shear stress exerted onto erodible soil particles needs to be estimated in order to evaluate the erosion rate of soils, as seen from equation (1). Efforts to estimate the shear stress in the interior of soils have required the idealization of the soil pores as an ensemble of pore tubes. However, the pore tube dimensions distribute within soils and it is quite difficult to determine the spatially distributed values of shear stress. To overcome this difficulty, the representative pore tube dimensions have frequently been used. If the permeability and the porosity of a soil material are given, representative pore diameter \hat{D} is obtained as

$$\hat{D} = 4\sqrt{2K/n} \tag{8}$$

where K denotes the intrinsic permeability, defined as

$$K = k_s \mu / (\rho g) \tag{9}$$

where μ is the viscosity of the pore liquid. Assuming the Hagen-Poiseuille flow in the pore tube, the shear stress exerted onto the pore wall is estimated by the following equation (e.g., Reddi et al. 2000):

$$\tau = \rho g I \sqrt{2K/n} \tag{10}$$

where I stands for the hydraulic gradient. The erosion rate E can be estimated with equations (1) and (10) when the permeability, the porosity and the hydraulic gradient are determined.

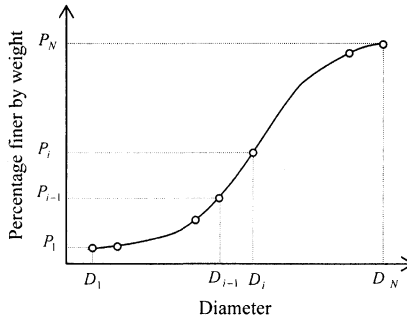


FIG. 2. Illustration of particle distribution curve.

EROSION MODEL

The surface area of erodible soil particles per unit volume of soils, A_e , is required in order to assess how much and how fast the soils erode. However, very few studies have been done on the erodibility within soils and it is considerably difficult to estimate the amount of erodible particles in ordinary soils with a wide range in particle distribution. Therefore, a simple model for the internal erodibility of soils is proposed here in advance of the subsequent numerical analysis.

Supposing a particle distribution curve is given, as shown in Figure 2, the soil particles with a diameter between D_{i-1} and D_i account for the percent of $P_i - P_{i-1}$ by weight. Letting ρ_s denote the density of the soil grains, the particles with a diameter between D_{i-1} and D_i weigh $\rho_s(1-n)(P_i - P_{i-1})$ within the unit volume of the soil, because the soil mass of the unit volume contains the soil particles of $\rho_s(1-n)$ by weight. Using the following averaged particle diameter D'_i as the representative value of the fraction

$$D'_i = (D_{i-1} + D_i) / 2 \quad (11)$$

the surface area of the fraction existing within the unit volume of the soil mass, A_e^i , is obtained as follows:

$$A_e^i = \rho_s(1-n)(P_i - P_{i-1}) \frac{A_2(D'_i)^2}{\rho_s A_3(D'_i)^3} \quad (12)$$

where A_2 and A_3 are the shape coefficients used to calculate the surface area and the volume, respectively. The erodible particles are assumed to be the soil particles which are smaller than the pore size. Considering representative pore size \hat{D} , given by equation (8), with porosity n and intrinsic permeability K , the surface area of the erodible particles is determined by the following equation:

$$A_e = \sum_{U_i < \hat{D}} A_e^i = \sum_{U_i < \hat{D}} A_2(1-n)(P_i - P_{i-1}) / (A_3 D'_i) \quad (13)$$

Due to erosion, the material parameters of the density and the viscosity of the pore liquid and the permeability vary. The density and the viscosity of the pore liquid are updated with the following equations:

$$\rho = C\rho_s + (1-C)\rho_w \quad (14)$$

$$\mu = \eta(1 + 2.5C) \quad (15)$$

where ρ_w and η denote the density and the viscosity of pure water, respectively. The permeability varies because of changes in the fluid viscosity, so that it is also updated as follows :

$$k_s = D_r^2 \frac{\rho g}{\mu} \frac{C_T n^2}{(1-n)^3} \quad (16)$$

where C_T and D_r are the material constant and the representative particle diameter, respectively.

REPRODUCTION OF THE EXPERIMENTAL RESULTS

The applicability of the concept presented above is verified here. Reddi et al. (2000) conducted internal erosion tests using a material comprising 70% Ottawa sand and 30% kaolinite clay by weight. Details of the experiments are presented in their paper; thus, only a brief explanation is given here.

Reddi et al. (2000) compacted the test material in the mold and prepared a cylindrical sample with the dimensions of 101.6 mm in diameter and 50 mm in thickness. The sample was saturated with and permeated by distilled water, and the seepage flow in the thickness direction was generated, which caused erosion in the interior of the sample. They measured the turbidity of the effluent, which was converted to the discharge rate of kaolinite. During the experiments, they controlled the inflow rate and recorded the water pressure at the inlet of the sample.

The dashed line in Figure 3 shows the recorded discharge rate of kaolinite. During the tests, the flow rate was increased linearly from 0 to 200 ml/min up to 900 minutes and then kept constant at 200 ml/min after that. Since the pore water pressure was continuously measured, an alteration of the permeability was experimentally obtained during the tests. In order to verify the proposed concept, a reproduction of the experimental data by the numerical simulation was carried out. The numerical results of the kaolinite discharge rate are shown as the solid line in Figure 3. It can be seen that the numerical results provide a good agreement with the experimental data.

The finite element method was used to solve equation (7) and the finite volume approach was applied for equation (5). As the boundary conditions, the flow rate equivalent to their control was imposed on the top and the atmospheric pressure was applied as the pore liquid pressure at the bottom. Integrating the kaolinite discharge rate in Figure 3, with respect to time, the initial surface area of the erodible soil particles was determined by obtaining the total eroded soil mass ($=1.1 \times 10^{-3}$ kg) and multiplying it by the specific surface area of kaolinite ($=20 \times 10^3$ m²/kg). Dividing it by the volume of the test sample ($=4.05 \times 10^{-4}$ m³), the surface area per unit volume A_r was obtained. Other parameters for the gravitational acceleration ($=9.8$ m/s²), the density of water ($=1000$ kg/m³), the soil particles ($=2600$ kg/m³), and the viscosity of pure water ($=1.005 \times 10^{-3}$ kg/m s) were given, and the critical shear stress ($=1.1$ Pa) and the initial porosity ($=0.27$)

were provided by the results of Reddi et al. (2000). Only the erodibility coefficient, α , could not be determined. Thus, its value was arbitrarily given as $5.5E-8 \text{ m}^3/\text{kN}\cdot\text{s}$ to match the experimental data shown in Figure 3. Up to now, the direct determination of the erodibility coefficient for internal erosion has not been done due to the great difficulty involved in doing so. Khilar et al. (1985) and Reddi et al. (2000), however, indicated that the erodibility coefficient of internal erosion is even smaller than that of surface erosion, namely, in the range of $1.0E-4$ to $1.0E-3 \text{ m}^3/\text{kN}\cdot\text{s}$. The estimated value of the coefficient, $5.5E-8 \text{ m}^3/\text{kN}\cdot\text{s}$, is consistent with their indication.

This analysis has shown that the numerical results seen in Figure 3 agree well with the experimental data and that the proposed approach can reproduce the observed data sufficiently well.

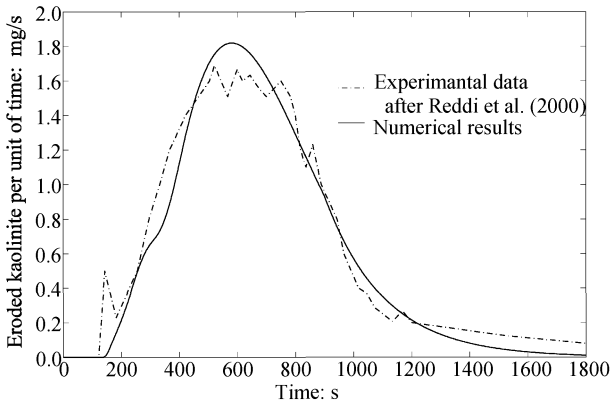


FIG.3. Relationship between discharge rate of kaolinite and elapsed time (after Reddi et al., 2000)

CONSTITUTIVE MODEL TREATING DEFORMATION DUE TO INTERNAL EROSION

Due to the erosion and transport of fine soil particles, the deformation of the soil will be induced. Wood & Maeda (2008) have reported that the internal erosion affects the critical state of the soil. As they indicated, the critical state line moves upward (See Figure 4), which means the soil reaches shear failure at the higher void ratio. Therefore, the failure and the internal erosion are significantly related with each other, and the deformation and erosion of soils need to be simultaneously estimated.

Figure 4 shows the change of CSL (critical state line) and NCL (normal consolidation line) caused by the loss of the fine particles due to the erosion. As seen in the figure, NCL as well as CSL vary the locations due to the erosion and move upward in the conventional semi-logarithmic compression plane (specific volume and logarithm of mean stress). For simplicity, these two lines are assumed to move in parallel, which corresponds to the parallel shift of the state surface. When the increment of the void

ratio due to erosion Δe_e is greater than the displacement of NCL and CSL $\Delta \Gamma$, the stress point enters the plastic region and the plastic compression occurs. Dividing the variation of the void ratio Δe into the parts due to the erosion Δe_e and the deformation Δe_d as follows;

$$\Delta e = \Delta e_e + \Delta e_d, \tag{17}$$

the following yield function can be obtained on the basis of Cam-clay model.

$$\Delta \Gamma - \Delta e_e - \Delta e_d^p = \frac{\lambda - \kappa}{M} \left(\frac{q}{p'} \right) + (\lambda - \kappa) \ln \frac{p'}{p_0} \tag{18}$$

$$\Delta e_d^p = -(1 + e_0) \Delta \epsilon_v^p \tag{19}$$

where λ , κ , M , p' , q , Δe_d^p and $\Delta \epsilon_v^p$ denote the compression and swelling index, the slope of the failure line, the effective mean stress, the deviator stress, the plastic component of the void ratio change and the volumetric plastic strain change. p_0 and e_0 are the reference effective mean stress and void ratio, respectively. This above procedure can be applied to any existing constitutive model based on the critical state concept. Using the yield function of equation (18), the elasto-plastic deformation due to the internal erosion can be calculated by the equilibrium equation of a soil mass. However, it has to be noted that equations (3) to (5) must be modified, as follows, by the Lagrangian formulation considering the deformation of the soil;

$$\dot{n} + n D_{kk} + \frac{\partial v_i}{\partial x_i} = E A_c \tag{20}$$

$$-\dot{n} + (1 - n) D_{kk} = -E A_c \tag{21}$$

$$(C\theta) + C\theta D_{kk} + \frac{\partial C v_i}{\partial x_i} = E A_c \tag{22}$$

where D_{ij} denotes the stretching tensor for the deformation of the soil.

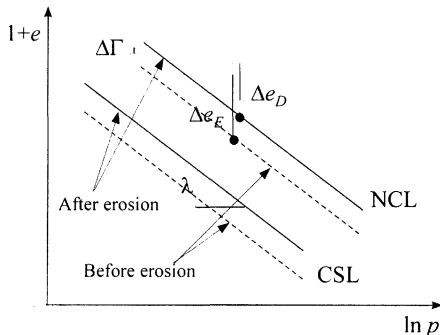


FIG.4. Conceptual diagram of the alteration of the state surface owing to internal erosion (Upward shift of NCL and CSL).

SUMMARY

This paper has presented the simultaneous modeling of the internal erosion and the deformation of soils. In order to describe internal erosion, the concept of the four phases of soils has been introduced. Usage of the erosion rate of soils has enabled the simple derivation of the governing equations for the seepage flow, the changes in porosity, and the transport of the detached soil particles from the soil skeleton. Considering upward shift of the state surface of soils, an example of the constitutive models describing the deformation due to the internal erosion has been proposed on the basis of the Cam-clay model.

REFERENCES

- Foster, M., Fell, R. and Spannagle, M. (2000). "The statistics of embankment dam failures and accidents.", *Can. Geotech. J.*, Vol. 37: 1000-1024.
- Indraratna B., Muttuvel T. and Khabbaz H. (2009). "Modelling the erosion rate of chemically stabilized soil incorporating tensile force-deformation characteristics.", *Can. Geotech. J.*, Vol. 46: 57-68.
- Khilar, K. C., Fogler, H. S. and Gray, D. H. (1985). "Model for piping-plugging in earthen structures.", *Journal of Geotechnical Engineering, ASCE*, 111(7): 833-846.
- Reddi, L. N., Lee, In-M and Bonala, M. V. S. (2000). "Comparison of internal and surface erosion using flow pump test on a sand-kaolinite mixture.", *Geotechnical Testing Journal*, Vol. 23(1): 116-122.
- Wood M.D. and Maeda K. (2008). "Changing grading of soil: effect on critical state.", *Acta Geotechnica*, 3:3-14.

Closed-Form Solutions of the Homogeneous Isotropic Elastic Half Space Subjected to a Circular Plane Heat Source

John C.-C. Lu¹, Wei-Chih Lin² and Feng-Tsai Lin³

¹Associate Professor, Department of Civil Engineering & Engineering Informatics, Chung Hua University, Hsinchu 30012, Taiwan, R.O.C.; cclu@chu.edu.tw

²Graduate Student, Department of Civil Engineering & Engineering Informatics, Chung Hua University, Hsinchu 30012, Taiwan, R.O.C.; m09504002@chu.edu.tw

³Assistant Professor, Department of Naval Architecture, National Kaohsiung Marine University, Kaohsiung 81157, Taiwan, R.O.C.; flin@mail.nkmu.edu.tw

ABSTRACT: This paper presents analytical solutions of the steady state displacements and temperature increments of a half space subjected to a circular plane heat source on the basis of the fundamental solutions of the half space due to a point heat source. The half space is modeled as a homogeneous isotropic linear elastic medium. The software Mathematica is used to complete symbolic calculations, and the closed-form solutions are presented. The governing equations of the mathematical model are based on the theory of thermoelasticity. The thermal stresses of the half space obey Newton's second law and Hooke's law. Besides, the energy conservation and heat conduction law are introduced to formulate the governing equations of thermal flow. The solutions can be used to test numerical models and the detailed numerical simulations of the thermoelastic processes near the buried heat sources.

INTRODUCTION

Heat source buried in the stratum leads to thermo-mechanical responses. The heat source such as a canister of radioactive waste can cause temperature rise in the soil. Nuclear wastes are usually deposited very deep, such as 200 to 700 meters below ground, so that they can be isolated from the living environment of human beings. Many studies suggested that linear theory was adequate for a repository design based on technical conservatism. For example, Hueckel and Peano (1987) indicated that European guidelines require that temperature increments in the soil close to the heat source should not exceed 80°C while the temperature increments at the ground surface is limited to less than 1°C. Given the modest temperature increments, Hollister *et al.* (1981) observed that any significant non-linear behavior and/or plastic deformation of the soil would be confined to a relatively small volume of soil around the waste canister itself. In this case, a linear model can provide a reasonable approximation for the assessment of a proposed design (Smith and Booker, 1996).

Lu and Lin (2006) displayed the transient ground surface displacement produced by a point heat source/sink through analog quantities between poroelasticity and thermoelasticity. Booker and Savvidou (1984, 1985), Savvidou and Booker (1989) derived an extended Biot theory including the thermal effects and presented solutions of thermo-consolidation around the spherical and point heat sources. Beside, Lu and Lin (2007) presented analytical solutions of the transient thermo-consolidation deformation due to a point heat source of constant strength buried in a saturated isotropic porous elastic half space.

The ground surface is predominantly modeled as a flat surface in the study of ground surface responses of geomechanics problems (Nowacki, 1986). The sedimentary soils or rocks usually have laminated structures. The original primary layers of strata are always laid out horizontally on mathematical formulation, and abundant groundwater can be found from the layers with relatively high permeability. The groundwater moving velocity is generally very slow, and thermal conduction generated by nuclear waste or geothermal can occur in the laminated strata. The circular plane heat source is introduced in this paper on the modeling of thermal conduction through the layered strata.

In this paper, attention is focused on the analytical solutions of the displacements and temperature increments for an isotropic stratum subject to a circular plane heat source. The homogeneous isotropic soil mass is modeled as a linear elastic isothermal half space. The governing equations of the mathematical model are based on the theory of thermoelasticity. The software Mathematica is used to derive the fundamental solutions of the half space due to a point heat source. The solutions can be used to test numerical models and the detailed numerical simulations of the thermoelastic processes near the buried heat sources.

MATHEMATICAL MODELS

The governing equations of the mathematical model are based on the theory of thermoelasticity. The thermal stresses of the half space should obey Newton's second law and Hooke's law. Besides, the energy conservation and heat conduction laws are introduced to formulate the basic equations of thermal flow. Figure 1 presents a point heat source buried in an elastic half space at a depth h . The stratum is considered as a homogeneous isotropic medium with a vertical axis of symmetry. Considering a point heat of constant strength Q located at point $(0, h)$, the basic governing equations of the elastic stratum for linear axially symmetric deformation can be expressed in terms of displacements u_i and temperature increment of the stratum ϑ in the cylindrical coordinates (r, θ, z) as follows (Lu and Lin, 2006):

$$G\nabla^2 u_r + \frac{G}{1-2\nu} \frac{\partial \varepsilon}{\partial r} - G \frac{u_r}{r^2} - \beta \frac{\partial \vartheta}{\partial r} = 0, \quad (1a)$$

$$G\nabla^2 u_z + \frac{G}{1-2\nu} \frac{\partial \varepsilon}{\partial z} - \beta \frac{\partial \vartheta}{\partial z} = 0, \quad (1b)$$

$$\lambda_r \nabla^2 \vartheta + \frac{Q}{2\pi r} \delta(r) \delta(z-h) = 0, \quad (1c)$$

in which $\nabla^2 = \partial^2/\partial r^2 + 1/r \partial/\partial r + \partial^2/\partial z^2$ is the Laplacian operator. The displacements u_r and u_z are in the radial and axial directions, respectively. ϑ is the temperature increment measured from the reference state, $\varepsilon = \partial u_r/\partial r + u_r/r + \partial u_z/\partial z$ is the volume strain of the stratum and the thermal expansion factor $\beta = 2G(1+\nu)\alpha_s/(1-2\nu)$. The constants ν , G and α_s are Poisson's ratio, shear modulus, and linear thermal expansion coefficient of the skeletal materials, respectively. The constant λ_t define the thermal conductivity of the thermoelastic medium. The symbol $\delta(x)$ is the Dirac delta function.

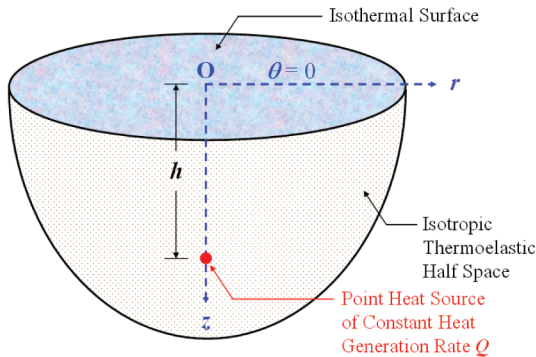


FIG. 1. Point heat source buried in a thermoelastic half space.

The half space surface at $z = 0$ is treated as a traction-free and isothermal boundary for all times $t \geq 0$. Its mathematical statements of the boundary conditions are:

$$\sigma_{rz}(r, 0) = 0, \sigma_{zz}(r, 0) = 0, \text{ and } \vartheta(r, 0) = 0. \tag{2a}$$

Here σ_{ij} are the incremental stress components. The rational basis of the isothermal assumption on the flat surface is that the nuclear waste or geothermal is deposited or generated at a great depth on the mathematical modeling. Besides, the ground surface is in contact with atmosphere, and it is kept at isothermal condition at each specific time.

It's reasonable to assume that the point heat source has no effect at the boundary $z \rightarrow \infty$ for all times. Hence

$$\lim_{z \rightarrow \infty} \{u_r(r, z), u_z(r, z), \vartheta(r, z)\} = \{0, 0, 0\}. \tag{2b}$$

The analytical solutions of displacements and temperature increments of the stratum

can be derived from the differential equations (1a)-(1c) corresponding with the boundary conditions at $z = 0$ and $z \rightarrow \infty$.

FUNDAMENTAL SOLUTIONS

Using Hankel integral transformation with respect to the variable r , the fundamental solutions of the long-term horizontal displacement $u_r(r, z)$, vertical displacement $u_z(r, z)$ and temperature increment $\vartheta(r, z)$ of the isothermal half space due to a point heat source are obtained as follows:

$$u_r(r, z) = \frac{(1+\nu)\alpha_s Q}{8\pi(1-\nu)\lambda_\gamma} \left[\frac{r}{\tilde{R}_1} - \frac{r}{\tilde{R}_2^*} + (3-4\nu) \frac{rh}{\tilde{R}_2 \tilde{R}_2^*} - \frac{rz}{\tilde{R}_2 \tilde{R}_2^*} - \frac{2hrz}{\tilde{R}_2^3} \right], \quad (3a)$$

$$u_z(r, z) = \frac{(1+\nu)\alpha_s Q}{8\pi(1-\nu)\lambda_\gamma} \left[\frac{z-h}{\tilde{R}_1} - (3-4\nu) \frac{h}{\tilde{R}_2} - \frac{z}{\tilde{R}_2} - \frac{2hz(z+h)}{\tilde{R}_2^3} \right], \quad (3b)$$

$$\vartheta(r, z) = \frac{Q}{4\pi\lambda_\gamma} \left(\frac{1}{\tilde{R}_1} - \frac{1}{\tilde{R}_2} \right), \quad (3c)$$

where $\tilde{R}_1 = \sqrt{r^2 + (z-h)^2}$, $\tilde{R}_2 = \sqrt{r^2 + (z+h)^2}$ and $\tilde{R}_2^* = \sqrt{r^2 + (z+h)^2} + z+h$. The Eqs. (3a)-(3c) are the fundamental solutions of the thermoelastic half space due to a point heat source.

CLOSED-FORM SOLUTIONS

The closed-form solutions of the horizontal displacement $u_r(r, z)$, vertical displacement $u_z(r, z)$ and temperature increment $\vartheta(r, z)$ due to a circular plane heat source with radius b buried at a depth h , as shown in Figure 2, can be derived from Eqs. (3a)-(3c). Considering a unit area dA located at a distance s from the center of circular plane heat source. The heat strength of this unit area is $q dA$, and it can be approximated as a point heat source. The increment of displacements u_r , u_z and temperature increment ϑ due to the elementary circular plane heat source can be obtained by substituting $r-s$ for r and $qs ds d\theta$ for Q in Eqs. (3a)-(3c). Thus, the total increment of displacements and temperature rise of the stratum can be determined by the integration with radial limits of $s = 0$ to $s = b$ and circumferential limits of $\theta = 0$ to $\theta = 2\pi$. Using Mathematica to complete the symbolic calculations, the closed-form solutions are given as below:

$$u_r(r, z) = \frac{(1+\nu)\alpha_s q}{8(1-\nu)\lambda_\gamma} \left\{ rR_{r,z-h} - (r+b)R_{r-b,z-h} + (z-h)^2 \ln \frac{R_{r,z-h}^*}{R_{r-b,z-h}^*} \right\}$$

$$\begin{aligned}
 & - \left[2b(z+h) + rR_{r,z+h} - (r+b)R_{r-b,z+h} - (z+h)^2 \ln \frac{R_{r,z+h}^*}{R_{r-b,z+h}^*} - 2r(z+h) \ln \frac{R_{z+h,r}}{R_{z+h,r-b}} \right] \\
 & + 2(3-4\nu)h \left[-b + (z+h) \ln \frac{R_{r,z+h}^*}{R_{r-b,z+h}^*} + r \ln \frac{R_{z+h,r}}{R_{z+h,r-b}} \right] \\
 & - 2z \left[-b + (z+h) \ln \frac{R_{r,z+h}^*}{R_{r-b,z+h}^*} + r \ln \frac{R_{z+h,r}}{R_{z+h,r-b}} \right] - 4hz \left(\frac{b}{R_{r-b,z+h}} - \ln \frac{R_{r,z+h}^*}{R_{r-b,z+h}^*} \right) \Bigg\}, \quad (4a)
 \end{aligned}$$

$$\begin{aligned}
 u_z(r,z) = & \frac{(1+\nu)\alpha_s q}{4(1-\nu)\lambda_r} \left\{ (z-h) \left(R_{r-b,z-h} - R_{r,z-h} + r \ln \frac{R_{r,z-h}^*}{R_{r-b,z-h}^*} \right) \right. \\
 & - \left[(3-4\nu)h + z \right] \left(R_{r-b,z+h} - R_{r,z+h} + r \ln \frac{R_{r,z+h}^*}{R_{r-b,z+h}^*} \right) \\
 & \left. - \frac{2hz}{z+h} \left[R_{r,z+h} - \frac{r(r-b) + (z+h)^2}{R_{r-b,z+h}} \right] \right\}, \quad (4b)
 \end{aligned}$$

$$\mathcal{G}(r,z) = \frac{q}{2\lambda_r} \left(R_{r,z+h} - R_{r,z-h} + R_{r-b,z-h} - R_{r-b,z+h} + r \ln \frac{R_{r,z-h}^* R_{r-b,z+h}^*}{R_{r,z+h}^* R_{r-b,z-h}^*} \right), \quad (4c)$$

in which $R_{i,j} = \sqrt{i^2 + j^2}$, $R_{i,j}^* = i + \sqrt{i^2 + j^2}$, and $i, j = r, r-b, z-h, z+h$.

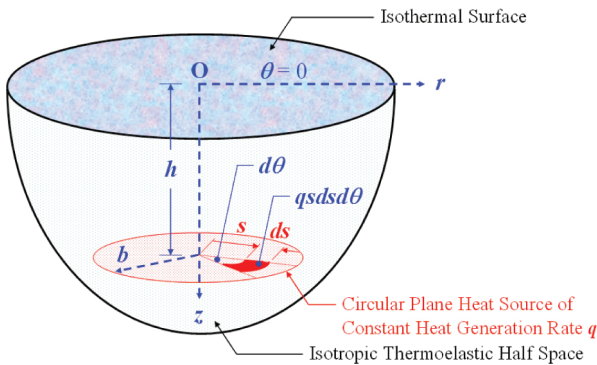


FIG. 2. Circular plane heat source in a thermoelastic half space.

The ground surface horizontal and vertical displacements are found when $z = 0$:

$$u_r(r, 0) = \frac{(1+\nu)\alpha_s q h^2}{\lambda_t} \left[-\bar{b} + \bar{r} \ln \frac{\sqrt{\bar{r}^2 + 1} + 1}{\sqrt{(\bar{r} - \bar{b})^2 + 1} + 1} + \ln \frac{\sqrt{\bar{r}^2 + 1} + 1}{\sqrt{(\bar{r} - \bar{b})^2 + 1} + \bar{r} - \bar{b}} \right], \quad (5a)$$

$$u_z(r, 0) = \frac{(1+\nu)\alpha_s q h^2}{\lambda_t} \left[\sqrt{\bar{r}^2 + 1} - \sqrt{(\bar{r} - \bar{b})^2 + 1} + \bar{r} \ln \frac{\sqrt{(\bar{r} - \bar{b})^2 + 1} + \bar{r} - \bar{b}}{\sqrt{\bar{r}^2 + 1} + \bar{r}} \right], \quad (5b)$$

where $\bar{r} = r/h$ and $\bar{b} = b/h$. The solutions can be used to test numerical models and the detailed numerical simulations of the thermoelastic processes near the buried heat sources.

NUMERICAL RESULTS

The normalized parameter of circular plane heat surface radius b to depth h ratio (b/h) is used to verify the proposed solutions. The profiles of vertical and horizontal displacements at the ground surface $z=0$ are normalized by $[q\alpha_s(1+\nu)h^2]/\lambda_t$ as shown in Figures 3 and 4, respectively. The results shown in Figures 3 and 4 indicate that the higher normalized parameter b/h can induce larger displacements on the ground surface. Figure 3 shows that the negative ground surface horizontal displacement value indicates displacement toward the axial symmetric center near the circular plane heat source, and the positive value indicates that ground surface horizontal displacement is outward from axial symmetric center. Figures 3 and 4 also concluded that the thermoelastic ground surface deformations due to a circular plane heat source reached their extreme values near the edge of heat source, i.e., r equals b , and then, the displacements reduced at the remote ground surface boundary.

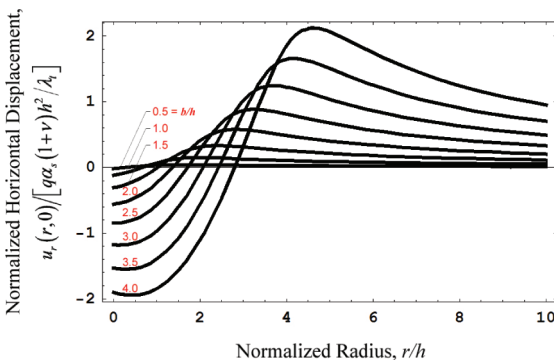


FIG. 3. Normalized horizontal displacement profile at the ground surface $z = 0$ due to circular plane heat source.

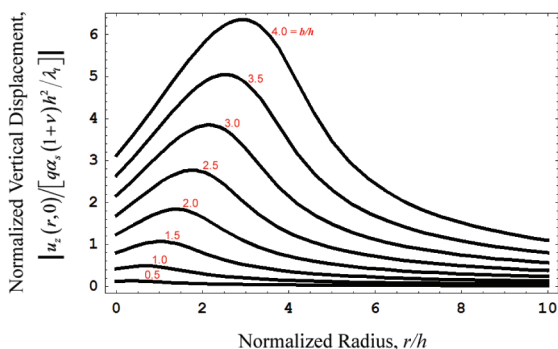


FIG. 4. Normalized vertical displacement profile at the ground surface $z = 0$ due to circular plane heat source.

CONCLUSION

On the basis of the fundamental solutions due to a point heat source, analytical solutions of the long-term horizontal displacement, vertical displacement and temperature increment of a thermoelastic half space subject to a circular plane heat source were obtained. Using the software Mathematica to complete the symbolic calculations, this study presents the closed-form solutions to this kind of problems. The solutions provide valuable information to test numerical models and numerical simulations of the thermoelastic processes near the buried heat sources. The results show:

1. The numerical results indicate that the larger normalized circular plane heat source radius b/h can induce larger displacements of the ground surface.
2. It is reasonable to find that the long-term thermoelastic ground surface deformations due to a circular plane heat source reached their extreme values near the edge of plane heat source and then reduced at the remote ground surface boundary.

ACKNOWLEDGMENTS

This work is supported by the National Science Council of Republic of China through grant NSC-98-2815-C-216-007-E, and also by the Chung Hua University under grant CHU-98-2815-C-216-007-E.

REFERENCES

- Booker, J.R. and Savvidou, C. (1984). "Consolidation around a spherical heat source." *International Journal of Solids and Structures*, Vol. 20 (11/12): 1079-1090.
- Booker, J.R. and Savvidou, C. (1985). "Consolidation around a point heat source." *International Journal for Numerical and Analytical Methods in Geomechanics*, Vol. 9 (2): 173-184.

- Hollister, C.D., Anderson, D.R. and Heath, G.R. (1981). "Seabed disposal of nuclear wastes." *Science*, Vol. 213 (4514): 1321-1326.
- Hueckel, T. and Peano, A. (1987). "Some geotechnical aspects of radioactive waste isolation in continental clays." *Computers and Geotechnics*, Vol. 3 (2-3): 157-182.
- Lu, J. C.-C. and Lin, F.-T. (2006). "The transient ground surface displacements due to a point sink/heat source in an elastic half-space." *Advances in Unsaturated Soil, Seepage, and Environmental Geotechnics* (GSP 148), ASCE, Shanghai/China: 210-218.
- Lu, J. C.-C. and Lin, F.-T. (2007). "Thermo-consolidation due to a point heat source buried in a poroelastic half space." *Proceedings of the 3rd IASTED International Conference on Environmental Modelling and Simulation*, Honolulu, Hawaii/U.S.A.: 48-53.
- Nowacki, W. (1986). *Theory of Asymmetric Elasticity*. Pergamon Press, Oxford.
- Savvidou, C. and Booker, J.R. (1989). "Consolidation around a heat source buried deep in a porous thermoelastic medium with anisotropic flow properties." *International Journal for Numerical and Analytical Methods in Geomechanics*, Vol. 13 (1): 75-90.
- Smith, D.W. and Booker, J.R. (1996). "Boundary element analysis of linear thermoelastic consolidation." *International Journal for Numerical and Analytical Methods in Geomechanics*, Vol. 20 (7): 457-488.

Golden Ratio in the Point Heat Source Induced Horizontal and Vertical Displacements of an Isotropic Elastic Half Space

Feng-Tsai Lin¹ and John C.-C. Lu²

¹Assistant Professor, Department of Naval Architecture, National Kaohsiung Marine University, Kaohsiung 81157, Taiwan, R.O.C.; ftlin@mail.nkmu.edu.tw

²Associate Professor, Department of Civil Engineering & Engineering Informatics, Chung Hua University, Hsinchu 30012, Taiwan, R.O.C.; cclu@chu.edu.tw

ABSTRACT: Based on three-dimensional thermoelasticity, the homogeneous isotropic stratum is modelled as a linear elastic half space. Analytical solutions of the transient and long-term horizontal and vertical displacements due to a point heat source are presented. Utilizing Laplace and Hankel integral transforms, the closed-form solutions of displacements of the ground surface are obtained. The displacements affected by thermally parameters are illustrated and discussed. The maximum ground surface horizontal displacement can be exactly derived, and it is around 30% of the maximum ground surface vertical displacement. Moreover, the golden ratio, known as $\phi = 1.618$, appears in the maximum ground surface horizontal displacement and corresponding vertical displacement of a half space. The study concludes that golden ratio emerges in this phenomenon and the horizontal displacement should be properly considered in the prediction of vertical displacement induced by a buried heat source.

INTRODUCTION

The golden ratio ϕ is well known in mathematics, science, biology, art, architecture, nature and beyond (Sen and Agarwal, 2008), which is the irrational algebraic number $(1 + \sqrt{5})/2 \approx 1.6180339887$ (Livio, 2002; Dunlap, 1997). It is interesting to find that the golden ratio exists in the point heat source induced displacements of a homogeneous isotropic thermally elastic half space. Examples of the golden ratio in engineering include the study of shear flow in porous half space (Puri and Jordan, 2006), classical mechanics of coupled-oscillator problem (Moorman and Goff, 2007), and consolidation settlement due to a point sink (Lu and Lin, 2008), etc.

Nuclear wastes are usually deposited at a great depth, such as 200 to 700 meters below ground, so that they can be isolated from the living environment of human beings. It suggested that linear theory was adequate for a repository design based on technical conservatism. For example, Hueckel and Peano (1987) indicated that European guidelines require that temperature increments in the soil close to the heat source should

not exceed 80°C while the temperature increments at the ground surface is limited to less than 1°C. Given these modest temperature increments, Hollister *et al.* (1981) observed that any significant non-linear behavior and/or plastic deformation of the soil would be confined to a relatively small volume of soil around the waste canister itself. In this case, a linear model can provide a reasonable approximation to the assessment of a proposed design (Smith and Booker, 1996).

Attention is focused on the analytical solutions of the transient and long-term ground surface displacements of an isotropic stratum due to a point heat source. The responses of the stratum were satisfactorily modeled by assuming it as a thermoelastic continuum (Booker and Savvidou, 1985). Lu and Lin (2006) displayed transient ground surface displacement produced by a point heat source/sink through analog quantities between poroelasticity and thermoelasticity. Booker and Savvidou (1984, 1985), Savvidou and Booker (1989) derived an extended Biot theory including the thermal effects and presented solutions of thermo-consolidation around the spherical and point heat sources. In their solutions, the flow properties are considered as isotropic or transversely isotropic, whereas the elastic and thermal properties of the soils are treated as isotropic.

Based on Biot's three-dimensional consolidation theory of porous media, analytical solutions of the transient thermo-consolidation deformation due to a point heat source of constant heat generation rate buried in a saturated isotropic porous elastic half space were presented by Lu and Lin (2007). In this paper, the point heat source induced transient ground surface displacements of a thermoelastic medium are derived by using Laplace and Hankel integral transforms. The soil mass is modeled as a homogeneous isotropic thermally elastic half space. The case of isothermal half space boundary is investigated. Results are illustrated and discussed to provide better understanding of the ground surface displacements due to a point heat source. The solutions can be used to test numerical models and the detailed numerical simulations of the thermoelastic processes near buried heat sources.

THE GOLDEN RATIO

The golden ratio ϕ can be derived from a geometrical line segment in extreme and mean ratio as shown in Figure 1, where the ratio of the full length 1 to the length of x is equal to the ratio of longer section x to shorter section $1-x$:

$$\frac{1}{x} = \frac{x}{1-x}. \quad (1)$$

Assuming $x = 1/\phi$, hence, ϕ satisfies

$$\phi^2 - \phi - 1 = 0. \quad (2)$$

The golden ratio is the positive root of Eq. (2):

$$\phi = \frac{1 + \sqrt{5}}{2}. \quad (3)$$

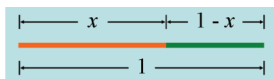


FIG. 1. Dividing the unit interval according to the golden ratio.

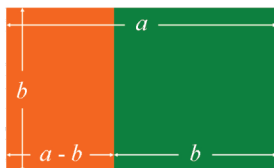


FIG. 2. The golden rectangle.

Figure 2 displayed another geometric description of golden ratio through the golden rectangle. Given a rectangle with sides' ratio $a : b$, the removing of square section leaves a remaining rectangle with the same ratio as the original rectangle, i.e.,

$$\frac{b}{a-b} = \frac{a}{b} \tag{4}$$

Thus, this solution is also the golden ratio ϕ :

$$\phi = \frac{a}{b} = \frac{1+\sqrt{5}}{2} \tag{5}$$

Based on the theory of thermoelasticity, this study modelled the stratum as a homogeneous isotropic thermally elastic half space. Closed-form solutions of the transient and long-term ground surface deformations of the stratum due to a point heat source of constant heat generation rate are presented in this paper. It is interesting to find that the golden ratio ϕ appears in the point heat source induced maximum ground surface horizontal displacement and corresponding vertical displacement of a thermoelastic half space.

MATHEMATICAL MODELS

The ground surface is in contact with atmosphere, and it is kept at isothermal condition at each specific time. Figure 3 is a hemi-sphere geometry that presents the relationship between the radius r and a point heat source buried in an elastic half space at depth h . The stratum is considered as a homogeneous isotropic medium with a vertical axis of symmetry. Assuming the model is decoupled, i.e., the thermal field \mathcal{G} is independent of the displacement fields u_r and u_z in the heat equation (6c) (Nowacki, 1975) and considering a point heat source of constant heat generation rate Q located at point $(0, h)$. The basic governing equations of the elastic stratum for linear axially

symmetric deformation can be expressed in terms of displacements u_i and temperature increment of the stratum \mathcal{G} in the cylindrical coordinates (r, θ, z) as follows (Lu and Lin, 2006):

$$G\nabla^2 u_r + \frac{G}{1-2\nu} \frac{\partial \varepsilon}{\partial r} - G \frac{u_r}{r^2} - \beta \frac{\partial \mathcal{G}}{\partial r} = 0, \tag{6a}$$

$$G\nabla^2 u_z + \frac{G}{1-2\nu} \frac{\partial \varepsilon}{\partial z} - \beta \frac{\partial \mathcal{G}}{\partial z} = 0, \tag{6b}$$

$$\lambda_t \nabla^2 \mathcal{G} - c_\varepsilon \frac{\partial \mathcal{G}}{\partial t} + \frac{Q}{2\pi r} \delta(r) \delta(z-h) u(t) = 0, \tag{6c}$$

in which $\nabla^2 = \partial^2/\partial r^2 + 1/r \partial/\partial r + \partial^2/\partial z^2$ is the Laplacian operator. The displacements u_r and u_z are in the radial and axial directions, respectively. The parameter \mathcal{G} is temperature increment measured from the reference state, and the parameter $\varepsilon = \partial u_r/\partial r + u_r/r + \partial u_z/\partial z$ is volume strain of the stratum. The constants ν , G and α_s are Poisson's ratio, shear modulus, and linear thermal expansion coefficient of the skeletal materials, respectively. The constants λ_t , ρ and c define the thermal conductivity, density and the specific heat of the thermoelastic medium, respectively. The coefficient $c_\varepsilon = \rho c$, and the thermal expansion factor $\beta = 2G(1+\nu)\alpha_s/(1-2\nu)$. The symbols $u(t)$ and $\delta(x)$ are called the Heaviside step function and Dirac delta function, respectively.

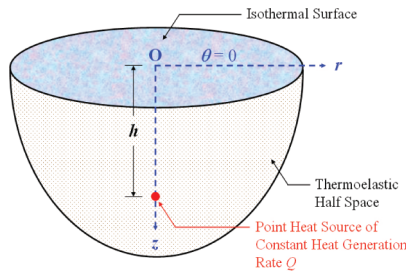


FIG. 3. Point heat source induced ground surface displacements model.

The half space surface, $z = 0$, is treated as a traction-free and isothermal boundary for all times $t \geq 0$. Its mathematical statements of the boundary conditions are:

$$\sigma_{rz}(r, 0, t) = 0, \sigma_{zz}(r, 0, t) = 0, \text{ and } \mathcal{G}(r, 0, t) = 0. \tag{7a}$$

Here σ_{ij} are the incremental stress components. It is reasonable to assume that the

point heat source has negligible displacement effect when $z \rightarrow \infty$ for all times. Hence

$$\lim_{z \rightarrow \infty} \{u_r(r, z, t), u_z(r, z, t), \vartheta(r, z, t)\} = \{0, 0, 0\}. \tag{7b}$$

Assuming no initial change in displacements and temperature increment for the thermoelastic medium, the initial conditions at time $t = 0$ of the mathematical model due to a point heat source can be treated as:

$$u_r(r, z, 0) = 0, u_z(r, z, 0) = 0, \text{ and } \vartheta(r, z, 0) = 0. \tag{8}$$

The transient ground surface displacements can be derived from the differential equations (6a)-(6c) corresponding to the boundary conditions at $z = 0, z \rightarrow \infty$, and initial conditions at time $t = 0$.

ANALYTIC SOLUTIONS

The analytical focus is on horizontal and vertical displacements of the ground surface, $z = 0$, due to a point heat source. Using Laplace integral transformation with respect to variable t and Hankel transformation with respect to the variable r , the transient horizontal displacement $u_r(r, 0, t)$ and vertical displacement $u_z(r, 0, t)$ of the isothermal ground surface due to a point heat source are obtained as follows:

$$u_r(r, 0, t) = \frac{(1+\nu)\alpha_s Q}{\pi\lambda_i} \left\{ \frac{ctr}{(h^2+r^2)^{3/2}} - \int_0^{ct} \frac{(ct-\tau)hr}{16\tau^3} \exp\left(-\frac{r^2+2h^2}{8\tau}\right) \left[I_0\left(\frac{r^2}{8\tau}\right) - I_1\left(\frac{r^2}{8\tau}\right) \right] d\tau \right\}, \tag{9a}$$

$$u_z(r, 0, t) = \frac{(1+\nu)\alpha_s Q}{\pi\lambda_i} \left\{ -\frac{cth}{(h^2+r^2)^{3/2}} \operatorname{erf}\left(\frac{\sqrt{h^2+r^2}}{2\sqrt{ct}}\right) + \frac{h}{h^2+r^2} \sqrt{\frac{ct}{\pi}} \exp\left(-\frac{h^2+r^2}{4ct}\right) - \frac{h}{2\sqrt{h^2+r^2}} \operatorname{erfc}\left(\frac{\sqrt{h^2+r^2}}{2\sqrt{ct}}\right) \right\}, \tag{9b}$$

where the parameter $c = \lambda_i/c_e$. The special functions $\operatorname{erf}(x)$ and $\operatorname{erfc}(x)$ denote the error function and complementary error function, respectively; and $I_\nu(x)$ is known as the modified Bessel function of the first kind of order ν . The long-term ground surface horizontal and vertical displacements are found when $t \rightarrow \infty$:

$$u_r(r, 0, \infty) = \frac{(1+\nu)\alpha_s Q}{2\pi\lambda_i} \frac{hr}{R(R+h)}, \tag{10a}$$

$$u_z(r, 0, \infty) = -\frac{(1+\nu)\alpha_s Q}{2\pi\lambda_i} \frac{h}{R}, \quad (10b)$$

where $R = \sqrt{r^2 + h^2}$. The maximum ground surface horizontal displacement $u_{r, \max}$ and vertical displacement $u_{z, \max}$ of the half space due to a point heat source are derived from Eqs. (10a) and (10b) by letting $r = \sqrt{\phi}h \approx 1.272h$ and $r = 0$, respectively:

$$u_{r, \max} = \frac{(1+\nu)\alpha_s Q}{2\pi\lambda_i} \frac{\sqrt{\phi}}{\sqrt{1+\phi}(\sqrt{1+\phi}+1)} = \frac{(1+\nu)\alpha_s Q}{2\pi\lambda_i} \frac{1}{\sqrt{\phi^5}} \approx 0.3003 \frac{(1+\nu)\alpha_s Q}{2\pi\lambda_i}, \quad (11a)$$

$$u_{z, \max} = u_z(0, 0, \infty) = -\frac{(1+\nu)\alpha_s Q}{2\pi\lambda_i}, \quad (11b)$$

in which $\phi = (1+\sqrt{5})/2 \approx 1.618$ is known as the golden ratio. The maximum ground surface horizontal and vertical displacements can be exactly derived as shown in Eqs. (11a)-(11b), and $u_{r, \max}$ is around 30% of $u_{z, \max}$. The value $r = \sqrt{\phi}h$ is derived when $du_r(r, 0, \infty)/dr$ is equal to zero, i.e.,

$$\frac{du_r(r, 0, \infty)}{dr} = \frac{(1+\nu)\alpha_s Q}{2\pi\lambda_i} \frac{h\sqrt{h^2+r^2}(h^2-r^2)+h^4}{(h^2+r^2)^{1.5}(\sqrt{h^2+r^2}+h)^2} = 0. \quad (12)$$

This leads to solutions of $r = \pm\sqrt{(1+\sqrt{5})/2}h$ and $r = \pm\sqrt{(1-\sqrt{5})/2}h$. However, only $r = \sqrt{(1+\sqrt{5})/2}h$ is realistic for $r \in [0, \infty)$.

It is interesting to find that the golden ratio ϕ is not only appeared in the point heat source induced maximum ground surface horizontal displacement but also on the corresponding vertical displacement by letting $r = \sqrt{\phi}h$ in Eq. (10b). Hence, we have:

$$u_z(\sqrt{\phi}h, 0, \infty) = -\frac{(1+\nu)\alpha_s Q}{2\pi\lambda_i} \frac{1}{\sqrt{1+\phi}} = u_{z, \max} \frac{1}{\phi} \approx 0.618u_{z, \max}. \quad (13)$$

This shows that the ground surface vertical displacement is around 61.8% of the maximum ground surface vertical displacement $u_{z, \max}$ at $r = \sqrt{\phi}h$, where the maximum ground surface horizontal displacement $u_{r, \max}$ occurred. Besides, the Eqs. (11a)-(11b) show that the maximum ground surface horizontal and vertical displacements are not directly dependent on the buried depth h of the point heat source.

The profiles of normalized vertical and horizontal displacements at the ground surface

$z = 0$ for different dimensionless time factor $\sqrt{ct/h^2}$ are shown in Figures 4(a) and 4(b), respectively. Figure 4(a) shows the relationship between normalized radius $r/h = \sqrt{\phi}$ and normalized maximum horizontal displacement $|u_{r \max}/u_{z \max}| = 1/\sqrt{\phi^5}$. Figure 4(b) shows the corresponding vertical displacement when horizontal displacement is at its maximum. The ground surface reveals significant horizontal displacement. For example, Fig. 4(a) shows that the maximum ground surface horizontal displacement is around 30% of the maximum ground surface vertical displacement at $r/h \approx 1.272$, which can also be found from the ratio of Eqs. (11a) and (11b).

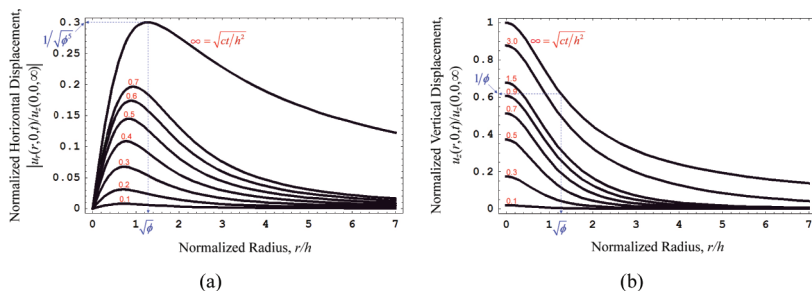


FIG. 4. Normalized displacement profiles at the ground surface $z = 0$ for isothermal half space.

CONCLUSION

Closed-form solutions of the transient and long-term displacements due to a point heat source of an isothermal elastic half space were obtained by using Laplace and Hankel transformations. The results show:

1. The maximum ground surface horizontal displacement is around 30% of the maximum surface vertical displacement at $r/h \approx \sqrt{\phi} = 1.272$, where $\phi = (1 + \sqrt{5})/2 \approx 1.618$ is known as the golden ratio.
2. It is interesting to find that the golden ratio ϕ also appears in the corresponding vertical displacement of the thermoelastic half space. The ground surface vertical displacement is around 61.8% of the maximum ground surface vertical displacement at $r = \sqrt{\phi}h$.
3. The magnitude of maximum ground surface horizontal displacement and vertical displacement are independent of the buried depth h of the point heat source.

ACKNOWLEDGMENTS

This work is supported by the National Science Council of Republic of China through grant NSC-98-2815-C-216-007-E, and also by the Chung Hua University under grant CHU-98-2815-C-216-007-E.

REFERENCES

- Booker, J.R. and Savvidou, C. (1984). "Consolidation around a spherical heat source." *International Journal of Solids and Structures*, Vol. 20 (11/12): 1079-1090.
- Booker, J.R. and Savvidou, C. (1985). "Consolidation around a point heat source." *International Journal for Numerical and Analytical Methods in Geomechanics*, Vol. 9 (2): 173-184.
- Dunlap, R.A. (1997). *The Golden Ratio and Fibonacci Numbers*. World Scientific Publishing, Singapore.
- Hollister, C.D., Anderson, D.R. and Heath, G.R. (1981). "Seabed disposal of nuclear wastes." *Science*, Vol. 213 (4514): 1321-1326.
- Hueckel, T. and Peano, A. (1987). "Some geotechnical aspects of radioactive waste isolation in continental clays." *Computers and Geotechnics*, Vol. 3 (2-3): 157-182.
- Livio, M. (2002). *The Golden Ratio: The Story of Phi, the World's Most Astonishing Number*. Broadway Books, New York.
- Lu, J. C.-C. and Lin, F.-T. (2006). "The transient ground surface displacements due to a point sink/heat source in an elastic half-space." *Advances in Unsaturated Soil, Seepage, and Environmental Geotechnics* (GSP 148), ASCE, Shanghai/China: 210-218.
- Lu, J. C.-C. and Lin, F.-T. (2007). "Thermo-consolidation due to a point heat source buried in a poroelastic half space." *Proceedings of the 3rd IASTED International Conference on Environmental Modelling and Simulation*, Honolulu, Hawaii/U.S.A.: 48-53.
- Lu, J. C.-C. and Lin, F.-T. (2008). "Modelling of consolidation settlement subjected to a point sink in an isotropic porous elastic half space." *Proceedings of the 17th IASTED International Conference on Applied Simulation and Modelling*, Corfu/Greece: 141-146.
- Moorman, C.M. and Goff, J.E. (2007). "Golden ratio in a coupled-oscillator problem." *European Journal of Physics*, Vol. 28 (5): 897-902.
- Nowacki, W. (1975). *Dynamic Problems of Thermoelasticity*. Noordhoff International, Leyden.
- Puri, P. and Jordan, P.M. (2006). "On the steady shear flow of a dipolar fluid in a porous half-space." *International Journal of Engineering Science*, Vol. 44 (3-4): 227-240.
- Savvidou, C. and Booker, J.R. (1989). "Consolidation around a heat source buried deep in a porous thermoelastic medium with anisotropic flow properties." *International Journal for Numerical and Analytical Methods in Geomechanics*, Vol. 13 (1): 75-90.
- Sen, S.K. and Agarwal, R.P. (2008). "Golden ratio in science, as random sequence source, its computation and beyond." *Computers and Mathematics with Applications*, Vol. 56 (2): 469-498.
- Smith, D.W. and Booker, J.R. (1996). "Boundary element analysis of linear thermoelastic consolidation." *International Journal for Numerical and Analytical Methods in Geomechanics*, Vol. 20 (7): 457-488.

Engineering Characteristics of Bottom Ash in Municipal Solid Waste Incinerators

Peng-Fei Fang¹, Xiang-Rong Zhu², Hong-Shui Chen³, and Wei Chen⁴

¹Associate professor, Ningbo Institute of Technology, Zhejiang University, Ningbo 315100, China; fpf@nit.zju.edu.cn

²Professor, Institute of Geotechnical Engineering, Zhejiang University, Hangzhou 310027, China; zhuxr@nit.zju.edu.cn

³Senior Engineer, Ningbo Urban Construction Investment Holding Co.Ltd, Ningbo 315010, China; chhs@163.com

⁴Engineer, Ningbo Institute of Technology, Zhejiang University, Ningbo 315100, China; chenw@163.com

ABSTRACT: Incineration of municipal solid waste (MSW) produces by-products which can be broadly classified as bottom and fly ashes, and the bottom ash is the primary by-product that accounts for 80% of the total. The main goal of the present work is to study the engineering properties of the incineration bottom ash, produced by Ningbo Municipal Solid Waste Incineration Plan in China. The study includes physical and engineering properties, such as radioactive nuclide, particle size distribution, physical and chemical compositions, organic matter content, mud content, moisture content, apparent and bulk densities, water absorption rate, solidity, bearing capacity, etc. The test results indicate that the harmful substance content of the bottom ash agrees with the environmental regulations. Compared with natural aggregates, the bottom ash has more uniform particle size distribution, more complex constituents, higher strength, higher water content, higher water absorption rate and lower density. So the engineering characteristics of the bottom ash are close to those of natural aggregates, and its engineering application is feasible.

INTRODUCTION

To release the pressure of the increasing municipal solid waste, many cities begin to build the Municipal Solid Waste Incinerator (MSWI) in China recently (Shi et al., 2004). Incineration of municipal solid waste produces by-products which can be broadly classified as bottom and fly ashes, and the bottom ash is about 80% (Aubert et al., 2004; Yuan et al., 2004). At present, the bottom ash and fly ash are combined for disposal in most operating facilities. The high cost of treatment, the shortage of landfill space, and the increased environmental awareness have prompted the search for alternative uses of the ash other than disposal. Bottom ash is mainly composed of Si, Fe, Ca, Al, Na and K, etc., in the form of oxides, and thus, presents a similar composition to

that of geological materials (Forteza et al., 2004; Lin et al., 2003; Zhang et al., 2002). As a result, many researchers in Europe and America tend to use these residues as aggregate substitutes in roads, highway pavements and other constructions, leading to beneficial reutilization of resources and reduction in environmental impacts (Chimenos et al., 1999; Forteza et al., 2004; Jurič et al., 2006). The use of incineration ash in various engineering applications has gained a considerable attention worldwide. However, the research on using the incineration residues was very limited in China.

To reduce environmental pollution and alleviate the pressure of landfill, it is important to study the technology of reclamation and treatment of incineration residues in China. Through studying the engineering properties of the incineration bottom ash, produced by Ningbo Municipal Solid Waste Incineration Plan in China, such as particle size distribution, physical and chemical compositions, organic matter content, mud content, moisture content, apparent and bulk densities, water absorption rate, solidity, bearing capacity, etc., it is shown that the engineering characteristics of the bottom ash are close to those of natural aggregates, and its engineering application is feasible.

MATERIALS

Ningbo Municipal Solid Waste Incineration Plan in China was built in 2001, which disposes 900 tons MSW per day and produces over 60,000 tons of the bottom ash annually, in which parts of residues are used to produce cement block and the rest are landfilled. Presently, the landfill in Ningbo is confronted with a saturated state and the storage capacity has exceeded 140,000 tons. So finding a new way is necessary. If the bottom ash is used as an aggregate in roads, the vast land resources can be saved, which is also helpful to preserve the ecological environment.

The study aimed to characterizing the bottom ash produced by Ningbo Municipal Solid Waste Incineration Plan with the goal of using it in the construction industry. The test materials chosen have been landfilled over one year.

EXPERIMENTS

Chemical Properties

Radioactive Nuclide

As an aggregate in roads, the bottom ash should be of no environmental pollution. Especially, there is no pollution to the ground water resources. This test was based on the China specification GB6566-2001 (2001). The test result is shown in Table 1. The bottom ash meets the requirements of environmental protection.

Table 1. Experiment Results of Radioactive Nuclide.

Item	Requirements by Regulation	Test Results	Evaluation
Internal Exposure Index (I_{Ra})	≤ 1.0	0.22	Qualified
External Exposure Index (I_T)	≤ 1.3	0.50	Qualified

Elemental Composition

Bottom ash is mainly composed of Si, Al, Fe, Ca, K, Na, Pb, and S, in the form of oxides, sulphate and silicate. The composition of bottom ash was approximately determined by the acidic digestion of the sample in a microwave oven and further analyses of metals and sulfur were conducted using Inductive Coupled Plasma. In addition, mercury is analyzed by the cold vapor technique and arsine by atomic fluorescence with hydride generation (Forteza, 2004). Some of the results are shown in Table 2.

Table 2. Metal Contents in Bottom Ash.

Items	Mn	As	Cd	Cr	Cu	Hg	Pb	Sb	Zn	Ni	Sn
Content (mg/kg)	310	21	10	550	1800	0.8	2500	110	1000	190	1000

Mica

Mica in aggregates may affect the workability and strength of concrete because it has no cohesion with cement pastes. At the same time, mica has a negative influence on the frost resistance and permeability of concrete. Mica content determination was performed according to the China specification JTJ 058-2000 (2000). Particles that are greater than 5 mm or less than 0.315 mm, were separated. Two samples were used, which were dried at $105\text{ }^{\circ}\text{C} \pm 5\text{ }^{\circ}\text{C}$ until a constant weight was reached. Mica was examined using steel needle and magnifying glass. The test result shows that there is no mica in bottom ash.

Organic Matter

Organic matter in bottom ash can reduce the strength of cement-stabilized soil or lime-stabilized soil. A high content of organic compounds will delay the setting time and strength of concrete. Particularly, it will affect the engineering properties of aggregate. Organic matter content was determined by oxidation with potassium permanganate, according to the China specification JTJ 051-93 (1993). Test results are listed in Table 3 from eight samples.

Table 3. Test Results of Organic Matter Content.

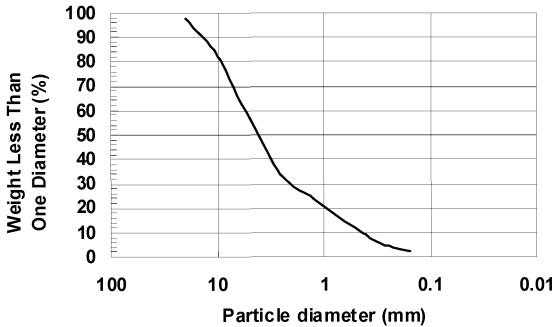
Sample	Organic Matter Content (%)	Average (%)
1	4.25	4.78
2	5.35	
3	5.13	
4	4.66	
5	5.50	
6	4.21	
7	5.00	
8	4.13	

According to the China specification JTJ 034-2000 (2000), the organic matter content of aggregate in cement-stabilized soil must be less than 2%. Otherwise, the aggregate needs to be treated by lime before use.

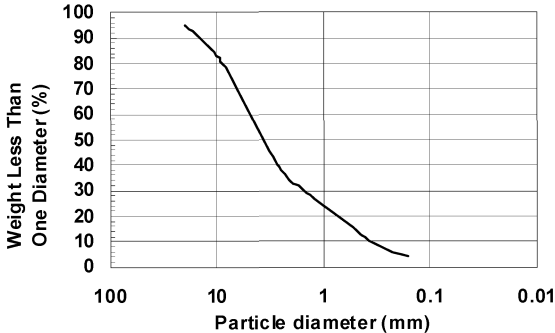
Physical and Mechanical Properties

Particle Size Distribution

Bottom ash is composed of scoria, brick, glass, ceramics, stone, metal and organic matter. Particle size distribution of aggregate is closely related to its compression resistance, permeability and frost resistance. It is generally recognized that the well-graded aggregates have high bearing capacity, high shear strength and good stability. Distribution of the aggregate sizes was characterized by using standard sieves of different sizes. The sizes of the sieves were: 20, 10, 5, 2.5, 1.25, 0.63, 0.315, 0.16 mm, according to the China specification JTJ 058-2000 (2000). The size distribution curves are shown in Fig. 1.



(a) Sample 1



(b) Sample 2

FIG. 1. Gradation curves of bottom ash.

According to the gradation curve, coefficient of uniformity (C_u) and coefficient of curvature (C_c) can be obtained, which are two quantitative indices for evaluating well-graded or poorly-graded aggregates. C_u shows the particle size distribution of gradation curve; while C_c expresses the distribution shape. The results for sample 1 are: $C_u=12.2$, $C_c=1.96$; and for sample 2 are: $C_u=12.9$, $C_c=1.74$. The specification JTJ 034-2000 (2000) shows that the aggregate is well-graded when $C_u \geq 5$ and $C_c = 1 \sim 3$. Test results also show that the maximum particle size is not more than 23.5 mm.

Apparent Density and Accumulated Density

According to the China specification JTJ 058-2000 (2000), apparent density is determined by using the volumetric flask method and accumulated density is by cylinder (1L bulk volume, 108 mm inside diameter and 109 mm height). Test results are shown in Table 4.

Table 4. Results of Apparent Density, Accumulated Density and Mud Content.

Items	Apparent Density	Accumulated Density	Mud Content
Test Results	1.96 g/cm ³	0.938 g/cm ³	4.3%

The apparent density of natural stone is in the range of 2.5-3.3 g/cm³. So the apparent density of bottom ash is less than that of natural stone, which relates to its physical composition. At the same time, Table 5 shows that the accumulated density of bottom ash is only 0.938 g/cm³, which is less than that of ordinary sand with an accumulated density from 1.4 g/cm³ to 1.7 g/cm³.

According to the apparent density and the accumulated density, the percentage of voids can be obtained, which is 52%.

Mud Content

Mud content has an influence on the cohesiveness between binder materials and aggregates, and on the strength and durability of concrete. Mud content is used mainly to measure the content of particles with a diameter less than 0.075 mm in bottom ash, according to the China specification JTJ 058-2000 (2000). The test result is shown in Table 4. According to the China specification JTJ 034-2000 (2000), the maximum mud content of aggregate in cement-stabilized soil should be less than 7%.

Invariability

Invariability is a key index measuring the frost resistance of aggregate. The test procedure was as follows: the bottom ash was soaked in a saturated solution of sodium sulfate. Then, the sample was dried and weighed according to the China specification JTJ 058-2000 (2000). The total weight loss indicates the invariability of bottom ash. The test results show that the invariability loss is 1.7%.

Loss on Ignition

Loss on Ignition represents whether the MSW was burned fully or not. The bottom ash was burned at 950 °C and the weight loss was measured with a value of 7.5% according to the China specification JTJ 051-93 (1993), which is greater than that of fly ash type I (5%), and less than that of fly ash type II (8%), as specified in the China specification of GB 1596-2005 (2005). The reason may be that there are some knitted fabrics and plastics in bottom ash.

Water Absorption

Water absorption may affect water content of aggregate, and the strength and stability of mixture. The water absorption of bottom ash determined by the method specified in the China specification JTJ 058-2000 (2000), is 21.6%. The value is greater than that of natural stone which ranges from 0.2% to 7.0%.

Bearing Capacity

The CBR index (California Bearing Ratio Test) provides a measurement of the impact resistance of the compacted aggregate. It is determined as the ratio between the impact load causing a given penetration in the samples and a fixed pattern, as stated in the China specification JTJ 051-93 (1993). The results obtained are given in Table 5. The results show that the maximum dry density is 1.49 g/cm³, and the optimum water content is 18.2%. Because the water absorption is relatively high and cohesive strength among particles is small, the bottom ash could be considered as cohesionless soil.

Table 5. Test Results of the CBR Index.

Test	CBR	Swelling Amount	Dry Density	Water Absorption
1	19.6%	0.035%	1.42 g/cm ³	99 g
2	19.8%	0.021%	1.41 g/cm ³	62 g

Table 6. Summary of Test Results for Aggregate in Gravel-cement Base.

Items	Condition in Regulation for Road Works	Test Results	Fulfilled
Particle Size Distribution	$C_u \geq 5, C_c = 1 \sim 3$	Sample 1: $C_u = 12.2, C_c = 1.96$; sample 2: $C_u = 12.9, C_c = 1.74$	Yes
Organic Matter	< 2%	4.78%	No
Mud Content	< 7%	4.3%	Yes
Loss on Ignition	< 8%	7.5%	Yes
Invariability	< 12%	1.7%	Yes

Possibility of Using Bottom Ash in Gravel-cement Base

According to the China Technical Specifications JTJ 034-2000 (2000) for road works,

the bottom ash as aggregate substitutes in gravel-cement may be considered. The gravel-cement is produced by homogeneously mixing aggregates, cement, water, and additives, and then compacting them into layers. The gravel-cement allows the formation of more resistant bases than granular layers and is, therefore, adequate for roads with heavy traffic.

Table 6 reveals that the incineration bottom ash meet the requirements for gravel-cement bases except organic matter. So the bottom ash must be treated by lime before used as aggregates, according to the specification JTJ034-2000 (2000).

CONCLUSIONS

In this study, the chemical, physical and mechanical properties of bottom ash from Ningbo Municipal Solid Waste Incinerator, were studied for its potential application on the base of roads.

Radioactive nuclide test shows that the I_{Ra} is 0.22 and the I_r is 0.50. So the bottom ash meets the requirements of environmental protection. The test result shows that there is no mica in bottom ash. The organic matter content of bottom ash is 4.78%, which is greater than what is specified in cement-stabilized soil. The bottom ash needs to be treated by lime before use. The obtained gradation curves cover the whole range between sand (maximum aggregate size is below 5 mm) and gravel (maximum aggregate size is above 5 mm).

The apparent density and the accumulated density of bottom ash are all less than those of natural stone. The percentage of voids of bottom ash reaches 52%. The water absorption is greater than that of natural stone. The Mud content is 4.3%. The invariability and loss on ignition are 1.7% and 7.5% respectively. The maximum dry density is 1.49 g/cm^3 , and the optimum water content is 18.2%. Because the organic matter content is 4.78%, which is greater than that of aggregate in cement-stabilized soil, the bottom ash must be treated by lime before used as aggregates.

The test results indicate that using bottom ash as a gravel-cement base is feasible regarding both the environmental safety and the structural properties of this residue. It is notable that the bottom ash is so highly heterogeneous that test results may vary significantly under any conditions. Therefore, a continuous quality control on the main chemical and engineering properties are essential.

REFERENCES

- Aubert, J. E., Husson, B. and Vaquier, A. (2004). "Use of municipal solid waste incineration fly ash in concrete." *Cement and Concrete Research*. Vol. 34(5): 957-963.
- Chimenos, J. M., Segarra, M., Fernández, M. A., Espiell, F.. (1999). "Characterization of the bottom ash in municipal solid waste incinerator." *Journal of Hazardous Materials*, Vol. 64(3): 211-222.
- China National Standard GB 6566-2001. (2001). Limit of radionuclide in building materials.
- China National Standard GB/T 1596-2005. (2005). Fly ash used for cement and concrete.

- China Trade Standard JTJ 051-93. (1993). Test Methods of Soil for Highway Engineering.
- China Trade Standard JTJ 034-2000. (2000). Technical Specifications for Construction of Highway Roadbases.
- China Trade Standard JTJ 058-2000. (2000). Test Methods of Aggregate for Highway Engineering.
- Dai, J. D., and Jing, J.. (2006). "Slag from incinerator application on Municipal Engineering." *China Municipal Engineering*, Vol. 31(5): 25-26.
- Forteza, R., Far, M., Seguí, C., Cerdá, V.. (2004). "Characterization of bottom ash in municipal solid waste incinerators for its use in road base." *Waste Management*, Vol. 24(9): 899-909.
- Jurič, B., Hanžič, L., Ilič, R., Samec, N.. (2006). "Utilization of municipal solid waste bottom ash and recycled aggregate in concrete." *Waste Management*, Vol. 26(10): 1436-1442.
- Lin, K. L., Wang, K. S., Tzeng, B. Y., Lin, C. Y.. (2003). "The reuse of municipal solid waste incinerator fly ash slag as a cement substitute." *Resources, Conservation and Recycling*, Vol. 39(2): 315-324.
- Shi, A. J., He, P. J., Shao, L. M., Li, X. J.. (2004). "Engineering Characteristics of Cinder from Municipal Domestic Refuse Incinerator." *Environmental Engineering*, Vol. 22(1): 47-50.
- Yuan, F., Fang, Y., Song, C., Zhang, Z.. (2004). "Study on the utility of MSW combustion ash in cement blending material." *New Building Materials*, Vol. 31(6): 17-19.
- Zhang, H. and He, P.. (2002). "Beneficial Utilization of Municipal Waste Combustion Ash." *Environmental Health Engineering*, Vol. 10(1): 6-10.

Strength Comparison of Cement Solidified/Stabilized Soils Contaminated by Lead and Copper

Lei Chen¹, Song-Yu Liu², Yan-Jun Du³, and Fei Jin⁴

¹ PhD Candidate, Institute of Geotechnical Engineering, Southeast University, Nanjing 210096, China; clove.chenlei@gmail.com

² Professor, PhD, Institute of Geotechnical Engineering, Southeast University, Nanjing 210096, China; liusy@seu.edu.cn

³Corresponding author, Professor, PhD, Institute of Geotechnical Engineering, Southeast University, Nanjing 210096, China; duyanjun@seu.edu.cn

⁴M.S Candidate, Institute of Geotechnical Engineering, Southeast University, Nanjing 210096, China;lhjinfei@163.com

ABSTRACT: Cement can be used as a binder for contaminated land remediation by reducing the leachability of contaminants. The contaminated soils can achieve a higher strength after cement solidification/stabilization process. However, contaminants in soils may interfere with the process of cement hydration, and lead to a more complicated strength development than conventional cemented soils. For soils contaminated by different types of heavy metals, the cement stabilized products may have different strength properties since heavy metals in the soils would influence the extent of chemical fixation among cement, soil, and contaminants mixtures. This paper presents an experimental study on the unconfined compressive strength of cement stabilized/solidified soils contaminated by lead, copper, and lead-copper mixture. The control samples (cement treated soils without any heavy metals) are also prepared for comparison purpose. The test results show that the presence of heavy metals in soils interferes with the cement hydration process, which is directly reflected by the variation in the strength development of samples. It is found that the types of heavy metal, the metal concentration, and the cement content are main factors which affect the cement hydration and strength.

INTRODUCTION

“Cement-based solidification/stabilization (S/S) is a chemical treatment process which aims to either bind or complex the compounds of a hazardous waste stream into a stable insoluble form (stabilization) or to entrap the waste within a solid cementitious matrix (solidification).” (Wiles, 1987). It can be applied as an in-situ or ex-situ technology for contaminated soil remediation with advantages of

relatively low cost, well-known material and technology, good long-term physical and chemical stability, good mechanical and structural characteristics, and so on (Conner, 1990; IABEA, 1993).

Soils contaminated by heavy metals could be treated by cement-based S/S technology through a number of complicated fixation mechanisms including (i) sorption (including physical adsorption and chemical adsorption), (ii) complexation, and (iii) precipitation (Yong et al., 1992). Cement treated contaminated soils could achieve an end product with higher strength than untreated soils, which can be reused as construction materials such as embankment fillings in the highway construction. Different heavy metals interact differently with cement and mineral components in soil, making the cementitious matrix present different physical or chemical properties (Hill et al., 1997; Yin et al., 2006; Qiao et al., 2007). The study on the effect of different heavy metals on the strength performance of S/S treated soils is required for engineering purpose.

The object of this study is to compare the influences of individual heavy metals and multi-heavy metals on the hydration of cemented soils. Unconfined compressive strength of cementitious matrix at different curing time is tested as a main assessment index for the extent of cement hydration.

EXPERIMENTAL

Materials

The soil used in this study was artificially prepared in the laboratory as a mixture of river sand and pulverized kaolin with a weight percentage of 85% and 15% respectively. The particle size of dry river sand is below 1 mm and the product grade of kaolin is 325 screen mesh. 10% moisture content was determined as the value of optimum water content based on the standard compaction test (ASTM D968-07) and was finally adopted as the designed water content of contaminated soil specimen.

The artificial heavy metal contaminated soils were prepared by mixing lead nitrate and copper nitrate as the source of pollutants into the soil. The nitrate was selected due to its high solubility and it does not inhibit S/S reactions (Boardman, 1999; Ouki, 2002). Three contents of heavy metal of 100 mg/kg, 500 mg/kg, 1000 mg/kg, and 10000 mg/kg (dry soil weight basis) were studied by simulating their concentration levels in the earth. Two designed cement contents of 5% and 7.5% by weight of dry soil were used. The control samples (cement treated soils without heavy metal) were also prepared for comparison. The detail of mix proportions of specimens are shown in Table 1.

Preparation and measurement of specimens

During sample preparation, cement agent was first mixed with the dry sand and kaolin to ensure homogeneous distribution of the cement in the soil. Then the deionized water which dissolving predetermined amount of lead nitrate or copper nitrate was added into the mixture. For control samples, the pure deionized water

was used directly with the designed quantity. It is found that the uniform wet mixture was obtained within 5-10 minutes of mixing due to the large proportion of sand in the mixture. After thorough mixing, soils were compacted in $\Phi 2.8\text{in} \times H 5.6\text{in}$ cylindrical moulds with designed optimum water content and maximum dry density. The specimen was initially cured for 2 hours, and then removed from the mould, sealed in the plastic to avoid water evaporation, and cured at 20°C for 1, 7, 14, 28, 56 and 90 days. Samples were all prepared in triplicate denoted MiCj, where i is the concentration of heavy metal M and j is the cement content. At designed curing time, unconfined compressive test for each specimen was conducted according to ASTM D2166-06.

Table 1. Mix proportions of specimens.

Specimen No.	Heavy metal		Cement content
	Type	Concentration	
Pb0.01C5	Lead	100 mg/kg (0.01%)	5%
Pb0.1C5		1000 mg/kg (0.1%)	
Pb1C5		10000 mg/kg (1%)	
Pb1C7.5		10000 mg/kg (1%)	
Cu0.01C5	Copper	100mg/kg (0.01%)	5%
Cu0.1C5		1000 mg/kg (0.1%)	
Cu1C5		10000 mg/kg (1%)	
Cu1C7.5		10000 mg/kg (1%)	
PbCu0.01C5	Lead and Copper	100mg/kg (0.01%) each	5%
PbCu0.05C5		500mg/kg (0.05%) each	
PbCu0.1C5		1000 mg/kg (0.1%)each	
BlankC5	No heavy metal	-	5%
BlankC7.5		-	7.5%

Note: The concentrations of heavy metal and cement contents are on the dry soil weight basis

RESULTS AND DISCUSSION

Unconfined compressive strength (UCS)

Figure 1 and Figure 2 show the influence of different heavy metal pollutants on the strength development of cement treated soils. The cement content of all specimens presented in Figs. 1 & 2 was 5%. It can be seen from Figure 1(a) that with the same heavy metal concentration in the soils, the specimen Pb0.01C5, PbCu0.01C5, and Cu0.01C5 have a very close strength development trend during the beginning 28 days curing time. The similar pattern is also found in Figure 1(b) for specimens under conditions of Pb0.1C5, PbCu0.05C5, PbCu0.1C5, and Cu0.1C5. After 28 days, Cu0.01C5 and Cu0.1C5 present respectively faster strength development than Pb0.01C5 and Pb0.1C5. It indicates that the late-age cement hydration process is different for cement treat soils contaminated by different heavy metals. Lead ions in soil cause a relatively more retarded or inhibited effect on the cement hydration as comparing with copper ions.

For the specimen containing lead-copper ions, the strength development at 90 days curing time follows the order of $Pb0.01C5 < PbCu0.01C5 < Cu0.01C5$, and $Pb0.1C5 < PbCu0.1C5 < Cu0.1C5 < PbCu0.05C5$. It means that when the soil is polluted by a lead-copper mixture at the concentration level of 100 mg/kg or 1000 mg/kg, the strength of these cemented two-heavy metals contained soils is between the values of corresponding single metal polluted soils. In this paper, the strength is relatively close to the value of copper-contaminated soils while considerably greater than that of lead-contaminated soils. As compared with $Cu0.01C5$ and $Cu0.1C5$, $PbCu0.01C5$ and $PbCu0.1C5$ contained additional 100 mg/kg and 1000 mg/kg lead ions; however, their strength values are closer to those of $Cu0.01C5$ and $Cu0.1C5$ respectively. It is implied that for a two-heavy metals contaminated soil, after treated by cement, its strength development is mainly controlled by the metal which has less retardation on the strength development. Similar observation was also found for the specimen of $PbCu0.05C5$. Comparing $PbCu0.05C5$ with $Cu0.1C5$, they contain an equal quantity of heavy metals, and there is 500 mg/kg lead in $PbCu0.05C5$. It seems that the strength of $Cu0.1C5$ should be higher than that of $PbCu0.05C5$, since lead could cause more retardation to cement hydration than copper. However, the strength of $PbCu0.05C5$ is obviously higher than that of $Cu0.1C5$.

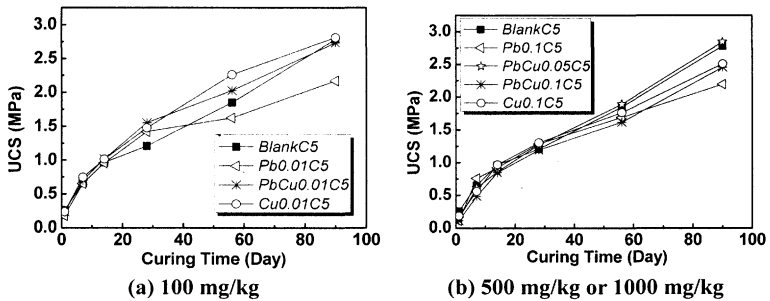


FIG. 1. Strength development of 5% cement treated contaminated soils with low heavy metal content (100 mg/kg-1000 mg/kg).

By comparing the control sample with heavy metal contaminated samples, the effects of heavy metals on the strength of cemented soils can be analyzed. In the early curing time, the specimens without heavy metals have the similar strength development to those containing lead or copper ions. In Figure 1(a), after 14 days curing, BlankC5's cement hydration is slower than that of other specimen leading to the lowest strength development at 28 days. Then, its cement hydration is accelerated. The 90 days strength of BlankC5 is close to those of $Cu0.01C5$ and $PbCu0.01C5$, and much higher than that of $Pb0.01C5$. In Figure 1(b), the strength of BlankC5 after 28 days curing is a little lower than that of $PbCu0.05C5$, but is higher than those of others.

Given that the heavy metal content of 1000 mg/kg or below is defined as a relatively low concentration level, which corresponds to a lightly polluted condition, 10000 mg/kg pollutant concentration is a more serious situation which is

also analyzed shown in Figure 2. The strength development of cement treated relatively highly polluted soils are very different with those of lightly polluted case. Cement hydration of Pb1C5 and Cu1C5 is seriously retarded or inhibited from the beginning of curing time when compared with that of BlankC5. The strength development follows the order of BlankC5 > Pb1C5 > Cu1C5. Though the strength of copper contaminated specimen is higher than that of lead contaminated specimen at low concentration level as discussed in Figure 1, the strength of Pb1C5 is much higher than that of Cu1C5 which appears to have no significant strength improvement with the curing time. It indicates that the strength of cement treated heavy metal soils depends not only on the type of metals, but also on their concentration. The trends may be reversed as the heavy metal concentration increases.

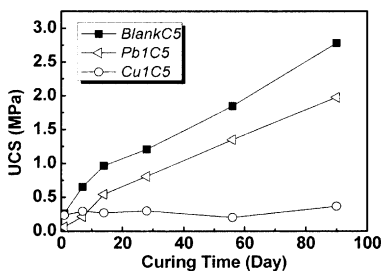


FIG. 2. Strength development of 5% cement treated contaminated soils with a high heavy metal content (10000 mg/kg).

The effect of heavy metal content on the UCS

To investigate the effect of heavy metal content on the strength of specimen, a normalized strength index was used for comparison purpose. The normalized UCS is identified as the strength value of cement treated heavy metal contaminated specimen divided by the value of control sample at the same curing time. The results are shown in Figure 3. Dash horizontal line with the normalized UCS equal to 1 is highlighted in Figure 3 to check whether the presence of heavy metals in soil improves or inhibits the cement hydration of cemented soils.

As shown in Figure 3, the strength of cement treated heavy metal soils with relatively low metal concentration (100 mg/kg, 1000 mg/kg) is higher than that of soils with a relatively high metal concentration (10000 mg/kg). Compared with the control sample, the cement hydration of specimens with a low metal concentration is retarded at the early age. Then it is accelerated, resulting in 20% to 30% increases in strength at 28 days. After that, the cement hydration slows down again, causing a 20% decrease in strength at 90 days for Pb contained specimens. The strength for PbCu contained and Cu contained specimens at 90 days is close to that of control sample.

The strength of cement treated heavy metal soils with a high metal concentration is much lower than that of control sample due to the significant

retardation or inhibition effect on cement hydration. However, Pb1C5 has the similar trend to the control sample. It means the interference effect of high concentration pollutant on the cement hydration diminished with the curing time. Oppositely, the strength difference between Cu1C5 and control sample considerably increased with the curing time, since cement hydration was seriously inhibited for Cu1C5 but kept developing for the control sample.

It is also shown in Figure 3 that for cement treated heavy metal contaminated soils, strength at 28 days of curing time should be cautiously applied to the field design as the conventional cemented soils without heavy metals. This is because the strength development of the former is much complicated. Long-term strength development of cement treated heavy metal contaminated soils is required for the further investigation.

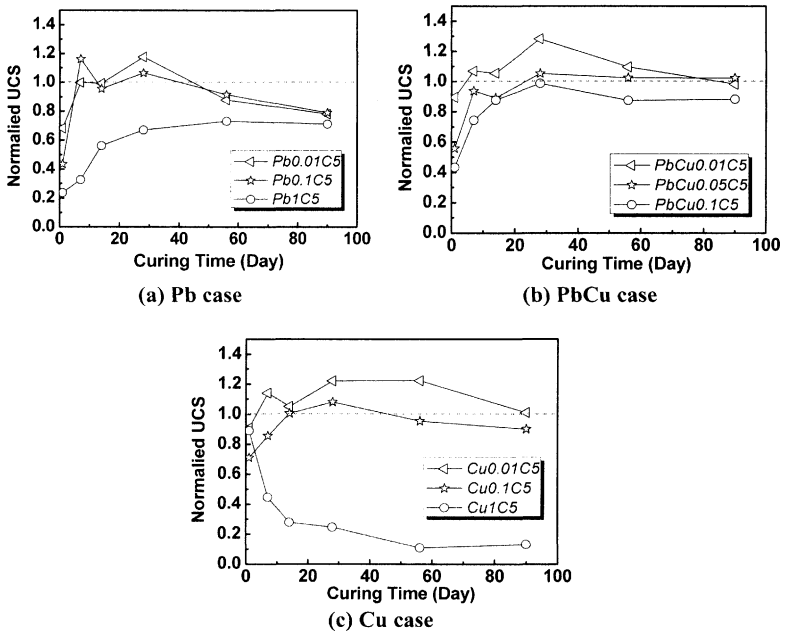


FIG. 3. Normalized strength of cement treated contaminated soils.

The effect of cement content on the UCS

Though the presence of heavy metals in soils could interfere with the cement hydration and finally impact the strength development of cemented soils, cement content is another main factor contributing to the strength development. Figure 4 compares the difference of strength between specimens treated with 5% and 7.5% cement.

As shown in Figure 4(a), the strength of BlankC5 is much higher than that of Pb1C5. When treated with 7.5% cement, the strength of Pb1C7.5 and BlankC7.5 is very close except for the case of 90 days, which exhibits a little difference. In Figure 4(b), Cu1C5 almost has no strength development as compared with BlankC5. After treated by 7.5% cement, Cu1C7.5 shows a significant strength increase although it is still slower than BlankC7.5. It indicates that though heavy metals may retard or inhibit the cement hydration in cemented soil, increasing the cement content can diminish this interference effect, and promote the strength development of heavily polluted soils.

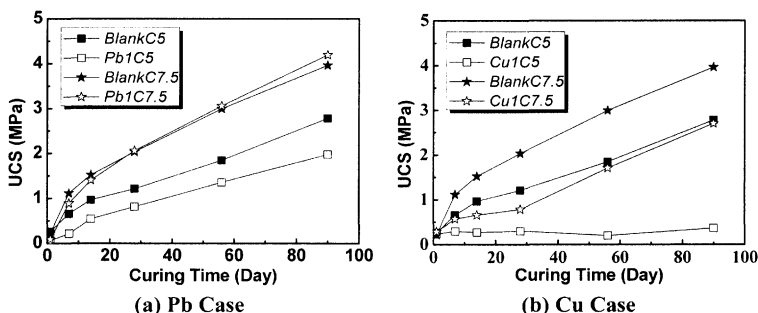


FIG. 4. Strength development of cement treated heavy metal contaminated soils with different cement contents.

CONCLUSIONS

Based on the laboratory tests, following conclusions can be drawn:

1) The types of heavy metals, the metal concentration, and the cement content are three main factors which interfere with the cement hydration and strength development.

2) For cement treated soils contaminated by heavy metals, strength at 28 days should be cautiously used as the characteristic strength for conventional cemented soils without the presence of heavy metals, because the strength development with the curing time of the former soil is much complicated.

3) The cement hydration process is different for cement treat soils polluted by different heavy metals. For soils with relatively low concentration of heavy metals, the strength development follows the order of Cu0.01C5>Pb0.01C5, and Cu0.1C5>Pb0.1C5. For the soil with relatively high concentrations, the corresponding strength development follows the order of Pb1C5>Cu1C5.

4) For two-heavy metals contaminated soils, after treated by cement, its strength development is mainly controlled by the corresponding single metal which has less retardation on strength development. In this study, copper is the dominant metal for the case of low concentrations of lead-copper contaminated soils.

5) The strength of cement treated heavy metal soils with low metal

concentrations (100 mg/kg, 1000 mg/kg) is higher than that of soils with a high metal concentration (10000 mg/kg).

6) The strength of cement treated heavy metal soils with a high metal concentration is much lower than a control sample due to the retardation on cement hydration. The strength difference between control samples and heavy metal contaminated samples decreases or increases with the curing time depending on the type of metals. However, the interference decreases with an increase in the cement content.

ACKNOWLEDGMENTS

The authors appreciate the support of Specialized Research Fund for the Doctoral Program of Higher Education of China under Grant No. 20060286031, the National Natural Science Foundation of China under Grant No. 50878052 and Grant No. 40972173, and the Foundation of Key Laboratory of Geotechnical and Underground Engineering (Tongji University) by the Ministry of Education under Grant No.KLE-TJGE-0801. The anonymous reviewers are highly appreciated for their suggestive comments.

REFERENCES

- Boardman, D.J. (1999). "Lime stabilization: clay-metal-lime interactions." Ph.D. Thesis, Civil and Building Engineering, Loughborough University, United Kingdom.
- Conner, J. R. (1990). "Chemical fixation and solidification of hazardous wastes." Van Nostrand Reinhold, New York.
- Hills, C.D., and Pollard, S.J.T. (1997). "Influence of interferences effect on the mechanical, microstructural and fixation characteristics of cementsolidified hazardous waste forms." *Journal of Hazardous Materials*, Vol. 52: 171–191.
- IABEA (1993). "Improved cement solidification of low and intermediate level radioactive wastes." *Technical Report Series No. 350*, International Atomic Energy Agency, Vienna.
- Ouki, S.K., and Hills, C.D. (2002). "Microstructure of Portland cement pastes containing metal nitrate salts." *Waste Management*, Vol. 22: 147-151.
- Qiao, X.C., Poon, C.S., and Cheeseman, C.R. (2007), "Investigation into the stabilization /solidification performance of Portland cement through cement clinker phases." *Journal of Hazardous Materials*, Vol. 139: 238–243.
- Wiles, C.C. (1987). "A review of solidification/stabilization technology." *Journal of Hazardous Materials*, Vol. 14: 5-21.
- Yin, C.Y., Mahmud, H.B., and Shaaban, M.G. (2006), "Stabilization /solidification of lead-contaminated soil using cement and rice husk ash." *Journal of Hazardous Materials*, Vol. 137:1758–1764.
- Yong, R.N., Mohamed, A.M.O., and Warkentin, B.P. (1992). *Principles of Contaminant Transport in Soils*. Elsevier, Amsterdam.

Geotechnical Properties of Zinc/Lead Mine Tailings from Tara Mines, Ireland

Michael E. Quille¹ and Brendan C. O'Kelly²

¹Research Assistant, Department of Civil, Structural and Environmental Engineering, Trinity College Dublin, Ireland; quillem@tcd.ie

²Lecturer, Department of Civil, Structural and Environmental Engineering, Trinity College Dublin, Ireland; bokelly@tcd.ie

ABSTRACT: This paper presents the geotechnical properties of the zinc/lead mine tailings from Tara Mines in County Meath, Ireland. The coarser and finer materials from the mechanical crushing and grinding processes were classified as slightly sandy silt and clayey silt, with high specific gravity of solids values of 2.78 and 2.82, and bulk density values of 2.01 and 2.08 tonne/m³, respectively. Chemical analysis indicated that the tailings comprised high proportions of calcium and magnesium (derived from the limestone ore body), with high residual concentrations of zinc and lead. The materials in the tailings pond were in a loose to medium dense state, with low to very low hydraulic conductivity of the order of 10⁻⁶–10⁻⁸m/s, and values of effective angle of shearing resistance of 37° (coarse) and 32° (fine). An indicative inert capping layer is presented that will form part of the rehabilitation works towards reintegrating the tailings pond into the surrounding landscape when its storage capacity is reached.

INTRODUCTION

Mine tailings consist of the pulverized rock that remains after the mechanical and chemical processes that are used to extract the metal ores from the ore body. The disposal and management of tailings storage facilities are fundamental concerns for the mining industry, owing to the large volume and chemical composition of these spoil materials. At present, most tailings are retained in slurry form behind dams, embankments or other surface impoundments. Tailings disposal is subject to stringent regulations (e.g. European Union Directive on the Management of Waste from Extractive Industries, 2006) in order to prevent environmental impacts that include, for example, the leaching of heavy metal pollutants into surrounding watercourses.

Tara Mines is operated by the New Boliden Group and is currently one of the largest zinc mines in Europe, and the fifth largest in the world, producing about 2.7 million

tonnes of zinc and lead concentrates annually. The ores are extracted from the limestone rock using the mechanical and chemical processes of crushing and grinding; froth floatation; dewatering; and cycloning (Vick, 1990). The mechanical crushing and grinding processes generate two material types that are distinguished by their particle size distribution, namely coarser and finer tailings. At Tara Mines, about half of the coarser tailings are separated by cycloning; mixed with cement at a ratio of 15:1 to 30:1; and used as mine slope backfill. The remaining tailings are mixed with the process wastewater and pumped about 5 km to the Randalstown tailings impoundment, where they are discharged into the tailings beaches, via a series of 200 mm spigots, located at 80 m intervals around the perimeter of the earthfill dams. The tailings pond covers an area of about 160 ha and the earthfill dams are up to 12.5 m high, with side slopes of one vertical to two horizontal. The hydraulic deposition process produces heterogeneous tailings deposits, with the denser particles settling out first. Water ponded over the tailings surface prevents wind erosion of the tailings dust. Groundwater from the tailings pond is controlled by a horizontal seepage system, and along with the supernatant water, is collected and re-circulated back to the mine, where it is reused in the ore extraction process.

The geotechnical properties of the mine tailings must be understood in order to construct more environmentally-friendly tailing ponds, and to further improve the efficiency of these disposal methods. In this paper, the geotechnical properties of the coarser and finer tailings from the tailings ponds at Tara Mines were studied, along with the development of an indicative inert capping layer that will form part of the rehabilitation works towards reintegrating the tailings pond into the surrounding landscape.

GEOTECHNICAL PROPERTIES

Bulk tailing samples were sourced from shallow depths at the Randalstown tailings impoundment and stored, prior to testing, in plastic drums at ambient laboratory temperature. The geotechnical properties were determined using standard laboratory tests to BS 1377 (1990).

INDEX AND PHYSIOCHEMICAL PROPERTIES

Table 1 lists some index and physical properties of the grayish-black tailings.

Table 1. Index and physical properties of the mine tailings.

Parameter	Coarse	Fine	Parameter	Coarse	Fine
Liquid limit (%)	–	75	Max void ratio	0.71	0.64
Plastic limit (%)	–	60	Min void ratio	0.47	0.43
Effective size, D_{10} (mm)	0.008	<0.002	Bulk density (tonne/m ³)	2.01	2.08
Specific gravity of solids	2.78	2.82	Dry density (tonne/m ³)	1.78	1.83
In situ water content (%)	15	20	Max dry unit weight (tonne/m ³)	1.89	1.97
In situ void ratio	0.63	0.61	Min dry unit weight (tonne/m ³)	1.62	1.71

Figure 1 shows the particle size distribution of the materials that were determined from a wet-sieve analysis. The coarser and finer tailings were classified as slightly sandy silt and clayey silt, respectively. The finer tailings had a liquid limit value of 75% (measured using the fall-cone penetrometer method); a plastic limit value of 60%; and hence a plasticity index value of 15. The specific gravity of solids was determined using the glass jar method, with high values of 2.78 (coarse) and 2.82 (fine). High concentrations of residual zinc and lead are generally contained in the finer tailings (Vick, 1990), which accounts for its slightly higher specific gravity of solids value. Values of bulk density of 2.01–2.08 tonnes/m³ and dry density of 1.78–1.83 tonnes/m³ were measured over the water content range 6%–30%.

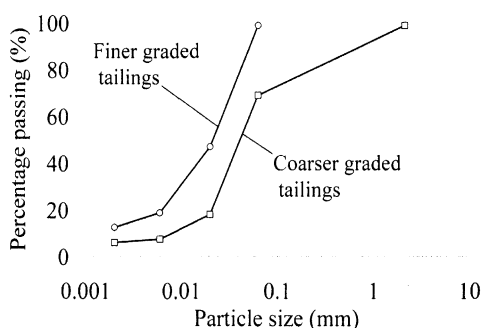


FIG. 1. Particle size distribution of the tailings.

CHEMICAL PROPERTIES

The chemical composition of the tailings reflects the chemistry of the ore body, the mineralogy and the metallurgical processes. The tailings were slightly alkaline and comprised high proportions of calcium and magnesium, which were derived from the limestone ore body, along with high residual concentrations of zinc and lead (Table 2).

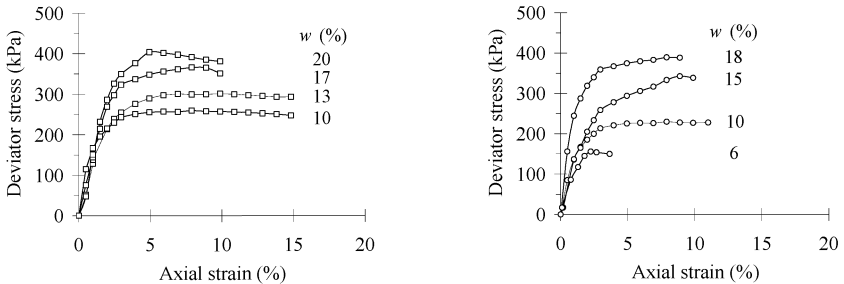
Table 2. Chemical composition of the tailings.

Parameter	Range	Parameter	Range	Parameter	Range	Parameter	Range
pH	7.0–7.9	Mercury	<0.5–0.9	Chromium	40–310	Sulfide	3.0%–5.5%
Aluminum	445–11488	Molybdenum	<25	Cobalt	15–26	Tellurium	<5–7
Arsenic	90–600	Nickel	47–100	Copper	30–171	Thallium	17–43
Barium	118–288	Potassium	333–10000	Iron	26.0–69.5	Tin	<5–212
Boron	<5–16	Silver	<5–18	Lead	1.4–2.9	Titanium	5–900
Cadmium	12.5–39.1	Sodium	647–1100	Magnesium	11.5–73.0	Uranium	<5
Calcium	22%–44%	Sulfate	0.19%–6.59%	Manganese	1.4–2.3	Zinc	3912–11169

Note: Values are given in mg/kg (i.e. parts per million) dry mass basis, unless otherwise stated. Data are mean values for coarser and finer tailings (Tara Mines Ltd., 1995).

SHEAR STRENGTH TRIAXIAL COMPRESSION

Quick-undrained triaxial compression tests were conducted on standard Proctor compacted specimens, 100 mm in diameter and 200 mm high, over the water content range 6%–20%. A cell confining pressure of 100 kPa was applied to the triaxial specimens, which were sheared quickly at a rate of 2% axial strain/min. Figure 2 shows data for the deviator stress against axial strain.



(a) Coarser tailings.

(b) Finer tailings.

FIG. 2. Deviator stress against strain data (w , water content).

SHEARBOX

Shearbox tests were conducted on saturated specimens, 60 mm square by 20 mm deep, which were sheared at a rate of 0.6 mm/min; sufficiently slow to allow full dissipation of the pore water pressures to occur throughout the specimens under the applied normal stresses of 50, 100 and 200 kPa (Figs. 3 and 4). The values of effective angle of shearing resistance of 37° (coarse) and 32° (fine) were determined from the data of shear stress at failure against normal stress (Fig. 5). As expected, the coarser tailings gave higher shear stress values at similar applied normal stresses, and hence a higher effective angle of shearing resistance value.

HYDRAULIC CONDUCTIVITY

The hydraulic conductivity was determined using falling-head permeability tests to BS 1377 (1990). The tailings specimens, 100 mm in diameter and 160 mm high, were loosely poured into the permeameter, with typical values of relative density of 0.33 (coarse) and 0.18 (fine), simulating *insitu* conditions. Values of hydraulic conductivity of 6.0×10^{-6} m/s (coarse) and 2.0×10^{-8} m/s (fine) were measured at ambient laboratory temperature of 20°C .

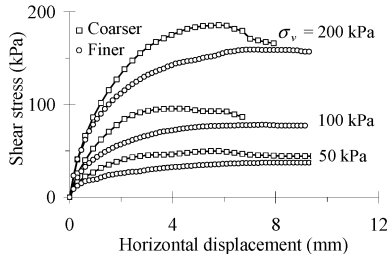


FIG. 3. Shear stress against horizontal displacement.

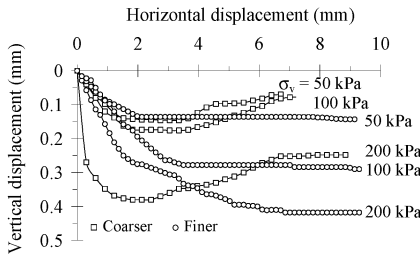


FIG. 4. Vertical displacement against horizontal displacement.

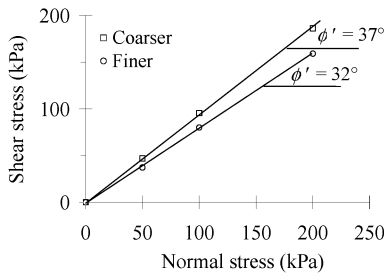


FIG. 5. Shear stress against normal stress (ϕ' effective angle of shearing resistance).

COMPRESSION

The compression behavior was determined using oedometer tests, with two-way specimen drainage to atmosphere, over the applied stress range 6–400 kPa. The test specimens, 76.2 mm in diameter and 18 mm high, were taken direct from the tailings pond, simulating *insitu* conditions. The coarser and finer tailings consolidated quickly,

although with small load strains of 3%–9% measured under the final compression stage at 400 kPa. Figure 6 shows the data of void ratio against effective stress, with a compression index value of only 0.09 for the finer tailings, determined from the gradient of its e -log σ_v' curve.

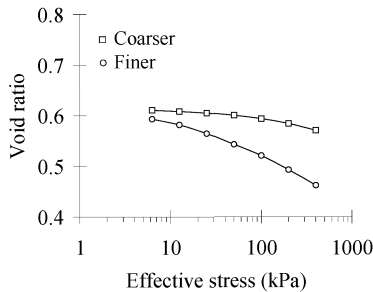


FIG. 6. Void ratio against effective stress.

CAPPING LAYER

An inert capping layer, comprising topsoil; subsoil; Terram non-woven geotextile; and inert rockfill layer; will be constructed above the tailings pond at full height (Fig. 7), in order to encourage the growth of vegetation and to reintegrate the tailings pond into the surrounding landscape. The geotextile layer will prevent the upward migration of fines from the tailings pond into the capping subsoil and topsoil layers, while the inert rockfill will act as a drainage layer, and will also serve as a working platform to facilitate the capping layer construction.

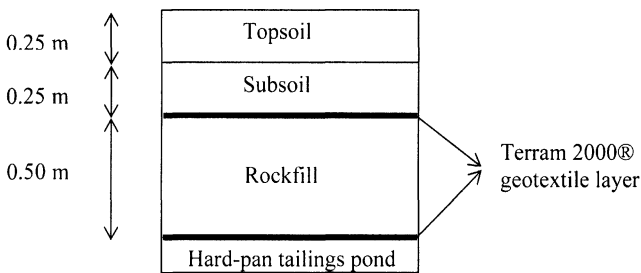


FIG. 7. Proposed capping layer with indicative dimensions.

SUMMARY AND CONCLUSIONS

The coarser and finer tailings from Tara Mines were classified as slightly sandy silt and clayey silt respectively, and contained high proportions of calcium and magnesium from the limestone ore body, with specific gravity of solids of 2.78 (coarse) and 2.82 (fine).

The higher value of the latter was due to its higher concentration of residual zinc and lead. The values of bulk and dry density were high, although in line with the high values of specific gravity of solids. The values of effective angle of shearing resistance were 37° (coarse) and 32° (fine), with values of hydraulic conductivity for the coarse and fine tailings in the loose to medium dense state of 6.0×10^{-6} m/s and 2.0×10^{-8} m/s, respectively. The tailings consolidated quickly, with small cumulative strains of 3%–9% measured during the oedometer tests under applied stresses of up to 400 kPa. An indicative inert capping layer was presented that will form part of the rehabilitation works towards reintegrating the tailings pond into the surrounding landscape.

ACKNOWLEDGMENTS

The authors acknowledge the work of Martin Carney and Aaron Kelly in performing some of the tests on the tailings materials at the geotechnical laboratory, Trinity College Dublin. In addition, the authors would like to thank the Environmental Department at New Boliden Tara Mines for their assistance during this study. Michael Quille would like to acknowledge funding received through postgraduate research awards from Trinity College Dublin and the Geotechnical Trust Fund of Engineers Ireland.

REFERENCES

- BS 1377 (1990). "Methods of Test for Soils for Civil Engineering Purposes." British Standards Institution, London.
- Council of the European Union (2006). "The Management of Waste from Extractive Industries." *Official Journal of the European Communities*, L3102/15: 1–19.
- Tara Mines Ltd. (1995). "Environmental Impact Statement." Tara Mines Publications, Navan, Ireland.
- Vick, S.G. (1990). "Planning, Design, and Analysis of Tailings Dams." BiTech Publishers, Vancouver.

Experimental Study of Cemented Soil under Na₂SO₄ Corrosive Condition

Pengju Han¹ and Xiaohong Bai²

¹ Lecturer , Doctor, College of Architecture and Civil Engineering of Taiyuan University of Technology, Yingze West Road, Taiyuan, 030024. E-mail: hanpengju1013@163.com

² Professor, College of Architecture and Civil Engineering of Taiyuan University of Technology, Yingze West Road, Taiyuan, 030024. E-mail: bxhong@tyut.edu.cn

ABSTRACT: The Na⁺ and SO₄²⁻ in the surrounding environment of cement-soil piles may affect the mechanical properties of cemented soil, which may cause some serious damage to structures. In order to simulate and study the erosion effect process, a series of unconfined compressive tests were conducted on the cemented soil blocks which were cured in the Na₂SO₄ solutions with various concentrations and ages. For comparison purposes, photos of the blocks were taken and the Na⁺ and SO₄²⁻ concentration of the Na₂SO₄ solution were recorded after the curing process. The testing results show that the Na₂SO₄ solution does make the cement-soil block change, and the influence of Na₂SO₄ to the blocks is increasing with the concentration of Na₂SO₄ and curing time increasing. The unconfined compressive strength of cemented soil block is decreased with the increasing of solution concentration, increased with the curing time. A coefficient α is put forward to predict the modification of the compressive strength of cemented soil in various concentration of Na₂SO₄ solution. The Na⁺ and SO₄²⁻ concentrations of the solutions decrease with the corrosive time. Chemical analysis indicates that the corrosion of Na₂SO₄ solution to cemented soil is a composite action including dissolving and crystallizing corrosions. Finally, a strength model of cemented soil is set up based on the relationship of compressive strength and Na⁺ and SO₄²⁻ concentrations, and its limit is also described. The model may be used in practical design in the future based on the concentrations of Na⁺ and SO₄²⁻ of corrosive environment.

INTRODUCTION

The cemented soil technical is a method of mixing cement with the soil in situ in order to improve soil properties. Because of its material extensive source, convenient construction, cheaper price, cemented soil technique has been widely used in ground treatment and retaining projects. However cemented soil, sometimes, has to be worked in a sulfate and/or alkaline corrosive environment, when the groundwater is polluted or worked under the seawater such a corrosive environment inevitably erode the cemented soil affect its mechanical property. In turn, the reduction of mechanical property of cemented soil can cause some serious damage

to the structure supported by it, which should be considered in the practical project (Technical code for ground treatment of buildings, 2002, Pei and Yang, 2000).

Many researchers have paid much affection to the influences study of the sulfate or alkaline environment on the cemented soil property (Zhang et al., 2003). Zhang's study shows that the influence of Na_2SO_4 on the cemented soil mainly presents the diffusions of Na^+ and SO_4^{2-} and their chemical reaction to $\text{Ca}(\text{OH})_2$ existed in cemented soil, the chemical reaction causes the cemented soil decomposed and broken, so makes its strength decrease. Jiao et al. (2005) analyzed the influencing factors of cement-soil strength in acid environment. Ning et al. (2005, 2006) investigated the behaviors of cemented soil under various environmental conditions and made the conclusion that the environmental erosion had little effects on fracturing process in contrast to evident influence on mechanical strength. Huang et al. (2005) designed laboratory experiments on anticorrosion ability of cement soil and provides feasible directions. Rolling (1999), Bai et al. (2007) and Dong et al. (2007) tested mechanical property and electrical resistance of cement-soil polluted by H_2SO_4 . In order to further simulate and study the erosion effect process in sulfate and/or alkaline corrosive environment, a series of tests including unconfined compressive tests were conducted on the cemented soil blocks which were cured in the Na_2SO_4 solutions with different concentrations, meanwhile, the appearance change of the block were taken photos, the Na^+ and SO_4^{2-} concentrations of Na_2SO_4 solutions were measured too, after curing the blocks. Chemical analysis indicates that the corrosion of Na_2SO_4 solution to cemented soil is a composite action including dissolving and crystallizing corrosions. Finally, a multiple linear regression model was set up to state and to predict strength of the cemented soil eroded by various concentration of Na_2SO_4 solution, and its limit is also described, which could be used in practical design in the future.

MATERIALS AND METHODS

Preparations of test blocks

The air dried silt soil was used in the tests with 8.1 plasticity index (I_p), taken from a building site in Taiyuan, China. The cement used was ordinary Portland cement (OPC), brand 32.5#, produced in Taiyuan SHITOU Cement Co. LTD. Soil, cement and water were mixed a HJW-30 blender, rotating speed 48 round/min with certain proportion shown in table 1. After well mixing, the mixture was put into a steel mold to form a cemented soil block. After molding 24 hours, the blocks were taken out from the molds, cured in a standard conservative box to cure for 7 days. Then the cemented soil blocks were cured in the Na_2SO_4 solutions with various concentrations prepared in advance.

Table 1 The Formula of Cemented Soil.

Air dried soil (g)	Cement (g)	Water (g)
100	15	50

Preparations of Na_2SO_4 solution

The Na_2SO_4 concentrations of the solution used in this experiment were 1.5g/L, 4.5g/L, 9.0g/L and 18.0g/L, respectively. The selection of this based on “Code for investigation of geotechnical engineering (GB 50021-2001, 2002)” and “Code for anticorrosion design of industrial constructions (GB 50046-95, 1995)”. The Na^+ and SO_4^{2-} concentrations of Na_2SO_4 solution and corrosive evaluation are listed in table 2, which the grade of circumstance can be marked as B, according to “Code for investigation of geotechnical engineering”, 2002.

Table 2 The chemical ingredients of solutions and corrosive evaluation.

Concentration (g/L)	Na^+		SO_4^{2-}	
	(mg/L)	Corrosive evaluation	(mg/L)	Corrosive evaluation
1.5	521.46	no	1001.20	weak
4.5	1198.35	no	2300.84	medium
9.0	1461.40	no	2805.88	medium
18.0	1670.53	no	3207.41	strong

Testing procedure

In order to simulate the erosion process and study the erosion mechanism, following test procedures were adopted:

Step 1: make cemented-soil blocks, described in above section, 60 blocks were made in total.

Step 2: cure the blocks in Na_2SO_4 solutions with 5 concentrations of Na_2SO_4 , such as 0, 1.5, 4.5, 9.0 and 18.0 g/L respectively.

Step 3: take photos for every block at certain curing time, like 3, 7, 14 and 28 days, respectively, in order to observe the appearance changing during the erosion process.

Step 4: take the unconfined compress tests for the blocks at same curing times as step 3, 3, 7, 14, and 28 days. At each curing time, 3 blocks were tested in parallel for one concentration of the solution. The average value of the three testing results is used as the block strength.

Step 5: measure the SO_4^{2-} concentrations of the solutions immediately after the blocks were taken out, in turn, the Na^+ concentrations of the solutions were calculated.

RESULTS AND DISCUSSION

Block appearance change

Figures 1 and 2 give the photos of the appearance of the blocks curing in the solutions for 7 days, and 28 days, respectively. Comparing the 8 photos, it can be clearly seen that Na_2SO_4 solution does make the cement-soil block change, mainly representing as the block appearance peeling off, the block size reducing, even the block cracking. The influence of Na_2SO_4 to the blocks is increasing with the concentration of Na_2SO_4 and curing time increasing.

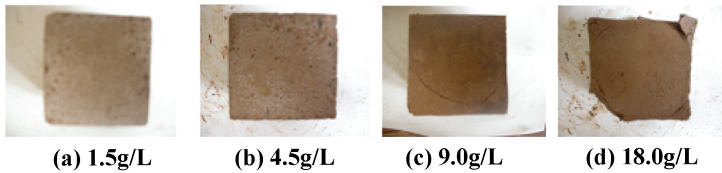


Fig.1. Photos of cemented soil blocks cured 7 days.

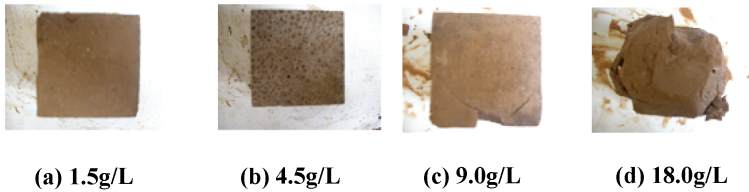


Fig.2. Photos of cemented soil blocks cured 28 days.

Unconfined compressive test results

The unconfined compression strength of the cemented soil blocks are listed in the table 3, from which equation 1 can be put forward:

$$f'_{cu} = \alpha f_{cu} \tag{1}$$

Where f'_{cu} is compression strength of the block which cured in Na_2SO_4 solutions,
 α is modified coefficient (table 4), expressing blocks corrosive degree,
 f_{cu} is compression strength of the block which cured in pure water.

Table 3. The compressive strength of cemented soil (MPa).

Time (d)	Na_2SO_4 solution concentration (g/L)				
	0	1.5	4.5	9.0	18.0
3	1.03	1.34	1.18	0.95	0.93
7	1.82	2.20	2.04	1.64	1.55
14	2.24	2.67	2.40	1.27	0.99
28	2.59	3.03	2.51	1.37	0.00

The unconfined compressive strength testing results show that the compression strength decreases with the increase of the corrosive solution concentration at the same erosion time, and that the corrosive degree increases with the corrosive time (Table 3 and fig. 3). From table 4, all the cemented soil strength modified coefficients are great than 1 for the 1.5 g/L solution environments, from which it may be drawn out that these environments are beneficial to the strength increasing of cemented soil. On the other hand, all of strength modified coefficients for the other solutions are less than 1, which may be indicated out that these environments are proposing the corrosion to the cemented soil, and cause the strength reduce. Therefore the working environmental condition of the cemented soil should be

taken into account when designing and calculating the foundation bearing capacity and settlement in order to optimize design, reduce the cost, adopt suitable measures, and assure the safety.

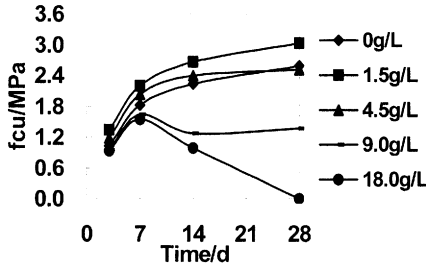


Fig. 3. Relationship between the compressive strength of cement soil and time.

Table 4. Compressive strengths modified coefficient of cemented soil.

Time (d)	Na ₂ SO ₄ solution concentration (g/L)				
	0	1.5	4.5	9.0	18.0
3	1	1.30	1.15	0.92	0.9
7	1	1.21	1.12	0.9	0.85
14	1	1.19	1.07	0.83	0.44
28	1	1.17	0.97	0.53	--

The results of Na⁺ and SO₄²⁻ concentration in Na₂SO₄ solution after curing the cemented soil blocks

Figs.4 and 5 give the relationships between the Na⁺ or SO₄²⁻ concentration and the curing time under various Na₂SO₄ solutions, respectively. The concentration of the Na⁺ or SO₄²⁻ decrease with the curing time, and the decreasing degree at the beginning, see before 7 days is higher than that at the later stage, ie after 7 days. Also, it can be seen that the concentration change of Na⁺ or SO₄²⁻ is very small at the Na₂SO₄ solution concentration of 1.5 g/L.

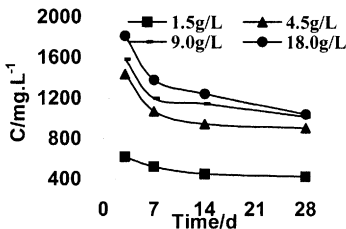


Fig. 4. Relationship between the Na⁺ concentration and time.

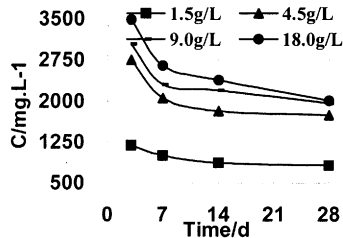
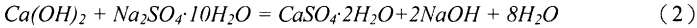


Fig. 5. Relationship between the SO₄²⁻ concentration and time.

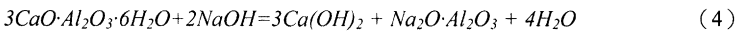
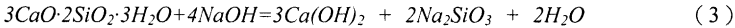
Corrosive chemical mechanism analysis

The main chemical reaction of cemented soil with Na_2SO_4 in Na_2SO_4 solution is as follow:



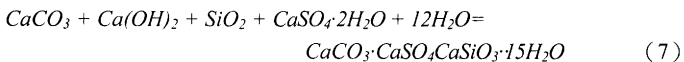
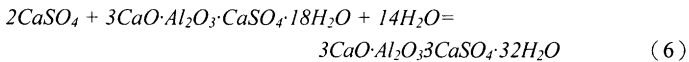
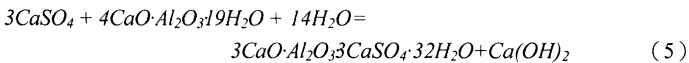
It is well known that the resultant volumes of $CaSO_4 \cdot 2H_2O$ is 2 times of $Ca(OH)_2$'s, so the new product $CaSO_4 \cdot 2H_2O$ may fill into the void in the cemented soil and be good for unconfined compressive strength of cemented soil, when the mass of Na_2SO_4 is suitable and the new reactant $CaSO_4 \cdot 2H_2O$ is small. But, the mass of $CaSO_4 \cdot 2H_2O$ will be great and may make the cemented soil block inflate in turn, block strength decrease when the mass of Na_2SO_4 is large enough. Therefore, this explain why the unconfined compressive strength of the cemented soil blocks cured in the low concentration Na_2SO_4 solutions (1.5 and 4.5 g/L) are greater than those cured in either pure water (0 g/L concentration) or higher concentration solutions.

As mentioned above, the main products are $CaSO_4 \cdot 2H_2O$ and $NaOH$ for reaction between cemented soil and Na_2SO_4 . Further, the new product $NaOH$ may take chemical reaction with $3CaO \cdot 2SiO_2 \cdot 3H_2O$ and $3CaO \cdot Al_2O_3 \cdot 6H_2O$, when the $NaOH$ is enough in the cemented soil, the chemical equations are given below:



For cemented soil, the $3CaO \cdot 2SiO_2 \cdot 3H_2O$ and $3CaO \cdot Al_2O_3 \cdot 6H_2O$ are acted as sticking materials, which make the soil particles stick together and are main providers of the strength of cemented soil. But, in the Na_2SO_4 solution, $NaOH$ takes chemical reactions with $3CaO \cdot 2SiO_2 \cdot 3H_2O$ and $3CaO \cdot Al_2O_3 \cdot 6H_2O$ and forms new reactants such as $2Na_2SiO_3$ and $Na_2O \cdot Al_2O_3$, which are poor coagulation and easy to produce an unsteady structure, in turn, making the strength of cemented soil reduce. Therefore the Na^+ corrosion to cemented soil is a sort of dissolving corrosion.

Meanwhile, the $CaSO_4$ takes chemical reaction with the cemented soil, as equations 5, 6 and 7, products the $3CaO \cdot Al_2O_3 \cdot 3CaSO_4 \cdot 32H_2O$ and $CaCO_3 \cdot CaSO_4 \cdot CaSiO_3 \cdot 15H_2O$ crystallizing resultants. When such crystallizing resultants are large enough, the inflating force would be greater than the sticking force within the cemented soil, so cracks may bring about in the cemented soil block and the strength would be reduced. Therefore, the SO_4^{2-} corrosion to cemented soil is a sort of crystallizing corrosion.



The Multiple Linear Regression Strength Model of cemented soil

From the above discussion conclusion it is concluded that compressive strength is closely related with Na^+ and SO_4^{2-} contains of Na_2SO_4 corrosive environment for

cemented soil. After analyzing the data and regression, a compression strength forecasting model is set up. The math expression of the strength model is given as following:

$$f_{cu} = 3.36 - 3.6N + 1.11S \quad (8)$$

Where f_{cu} is strength of cement soil,

N is Na^+ concentration, 400~2000 mg/L,

S is the SO_4^{2-} concentration, 500~3000 mg/L.

Table 5. Predicted values (P) and measured values (M).

C/ g·L ⁻¹	3 d			7 d			14 d			28d		
	M /MPa	P /MPa	Error /%									
1.5	1.34	1.34	0.00	2.20	2.59	17.73	2.67	2.69	0.75	3.03	2.73	10.0
4.5	1.18	1.24	5.08	2.04	1.78	12.75	2.40	1.97	17.92	2.51	2.02	20.0
9.0	0.95	1.02	7.37	1.64	1.59	3.05	1.27	1.64	29.50	1.37	1.86	36.0
18.0	0.93	0.79	15.81	1.55	1.33	14.19	0.99	1.53	-	-	-	-

The predicted and measured values are listed in the table 5. From the table 5, the range of error is from 0 to 36%, and the predicted values and measured values are rather close so that the model, based on the concentrations of Na^+ and SO_4^{2-} of corrosive environment, could be used in practical design in the future.

CONCLUSIONS

The Na_2SO_4 solution does make the cement-soil block change, mainly representing as the block appearance peeling off, the block size reducing, even the block cracking. The influence of Na_2SO_4 to the blocks is increasing with the increment both of the concentration of Na_2SO_4 and curing time.

The unconfined compressive strength of cemented soil block is decreased with the increasing of Na_2SO_4 solution concentration, increased with the curing time development and a coefficient α is put forward to predict the modification of the compressive strength of cemented soil in various concentration of Na_2SO_4 solution.

Chemical analysis of corrosive environment indicates that the Na^+ and SO_4^{2-} concentration decreases with the corrosive time. The Na^+ corrosive type is dissolving type and SO_4^{2-} corrosive type is crystallizing type, so the Na_2SO_4 solution to cemented soil corrosive type is a composite type of dissolving and crystallizing combination.

A strength model of cement soil is set up based on the relationship of compressive strength and Na^+ and SO_4^{2-} concentrations, and the limit for the model is also described. The predicted and measured values agree well so that the accuracy of the formula is rather high and the model may be used in practical design in the future based on the concentrations of Na^+ and SO_4^{2-} in corrosive environment.

ACKNOWLEDGMENTS

Financial support from Shanxi Province Foundation for Returnees No. 2006-26 and the Ph.D. Programs Foundation of Ministry of Education of China No. 20070112003.

REFERENCES

- Jiao, Z.B., Liu, H.L. and Cai Z.Y. (2005). "Experimental study on cement soil strength in mucky-acid soil." *Rock and Soil Mechanics*. Vol. 26(5): 57-60.
- Chinese Stand JGJ 79-2002 (2002). "Technical code for ground treatment of buildings." *China building industry Press*. Beijing.
- Pei, X.J., Yang, G.C. (2000). "Research on preventing cement erosion in marine soil." *Journal of Changchun Institute of Technology*. Vol. 15(1): 12-14.
- Zhang, Y., Jiang L.X., Zhang, W.P. and Qu, W.J. (2003) "Durability of concrete structures." *Shanghai technology press*. Shanghai.
- Huang, H.S., Yan, T.N. and Lan K. (2005). "Laboratory, Experiment of the Anticorrosion of Cement Stabilized Soft in Deep Mixing Pile." *Geological Science and Technology Information*. Vol.23(7): 85-88.
- Ning, B.K. Chen, S.L. and Liu, B. (2005). "Fracturing behaviors of cemented soil under environmental erosion." *Chinese Journal of Rock and Mechanics and Engineering*. Vol. 24(10): 1778-1782.
- Ning, B.K. Jin, S.J. and , Chen, S.L. (2006). "Influence of erosive on mechanical properties of cemented soil." *Chinese Journal of Shenyang University of Technology*. Vol. 28(2): 178-181.
- Rolling, R.S. (1999). "Sulfate attach on cement stabilized sand." *Journal of Geotechnical and environmental Engineering*. Vol. 121(5): 364-372.
- Bai, X.H. Zhao, Y.Q. and Han, P.J. et al. (2007). "Experimental study on mechanical property of cemented soil under environmental contaminations." *Chinese Journal of Geotechnical Engineering*. Vol. 29 (8): 1260-1263.
- Dong, X.Q., Bai, X.H. and Zhao, Y.Q. (2007). "Study on electrical resistance of soil-cement polluted by Na_2SO_4 ." *Chinese Journal of Rock and Soil Mechanics*. Vol. 28 (7): 1453-1548.
- Chinese Stand GB/50021-2001. (2001). "Code for investigation of geotechnical engineering." *China building industry Press*. Beijing.
- Chinese Stand GB/50046-2008. (2008). "Code for anticorrosion design of industrial constructions." *China project Press*. Beijing.
- Chinese Stand GB/T50123-1999. (1999). "Standard for soil test method." *China project Press*. Beijing.
- HAN P.-J. (2009). "Experimental study and durability assessment of inorganic compound corrosive action on cemented soil and slit soil." [D]. Taiyuan: 2009.6.

Influence of Heavy Metal Contaminants on the Compressibility of Reconstituted Kaolinite

Liu¹, X.F., Saiyouri², N. and Hicher³, P.Y.

¹PhD student, Research Institute of Civil and Mechanical Engineering (GeM), Ecole Centrale de Nantes, 1 Rue de la Noë, BP 92101, Nantes, France; Xianfeng.liu@ec-nantes.fr

²Associate professor, Ecole Centrale de Nantes; nadia.saiyouri@ec-nantes.fr

³Professor, Ecole Centrale de Nantes; Pierre-yves.hicher@ec-nantes.fr

ABSTRACT: The study aims to investigate the influence of heavy metal contaminants on the compressibility of clays. Two one-dimensional consolidation tests were performed on reconstituted kaolinite samples with two types of pore fluids: distilled water and 2 mM Cu (NO₃)₂ solution. The influence of the heavy metal contaminants on compressibility (C_c , C_{s1} , C_{ae}) was then examined. In order to investigate heavy metal ions interaction with the kaolinite used, a series of batch tests were conducted. In addition, prior to consolidation, the clay samples were tested for their microstructure by using scanning electron microscope observation (SEM) and mercury intrusion pore size distribution measurements (MIP). Furthermore, the permeability coefficient of the specimens can be estimated using Terzaghi's one-dimensional consolidation theory. The first results tend to indicate that the permeability and compressibility of kaolinite were slightly affected when using the diluted Cu (NO₃)₂ solution.

INTRODUCTION

Over the past forty decades, the effect of pore fluid chemistry on engineering properties of clays has been of significant interest to geotechnical engineers. Many studies have been performed to understand the compressibility changes of clays as induced by the presence of chemical compounds in pore fluids, such as Bolt 1956; Olson and Mesri 1970; Sridharan and Rao 1973; Maio 1996; Chen *et al.* 2000 etc. Accordingly, the compressibility of clays is related to the fabric of the clays and the pore fluid chemistry. The composition of fluid affects electrostatic forces developed in the interlayer spaces between contiguous clay particles as well as the equilibrium between internal and external forces. Furthermore, among all the studied chemical compounds, the transport of contaminants was also shown to induce dramatic changes of the permeability of clays (Shackelford *et al.* 2000, etc).

In the literature, there is a lack of data concerning the effect of heavy metal compounds on the permeability and compressibility of clays. Ouhadi *et al.* (2006) and Souli (2006) studied the influence of heavy metals (Pb, Zn and Cr) on the compressibility and hydraulic conductivity of reconstituted clays. Despite their

relatively high hydraulic conductivity, kaolinite clays have been widely used as clay barrier materials because of their greater chemical resistance, better workability, and less susceptibility to desiccation-induced cracking (Chen 2000). Therefore, the purpose of this paper is to present the first results concerning the influence of heavy metals on the compressibility of reconstituted kaolinite from macro and micro point of view.

MATERIALS AND METHODS

Kaolinite

In this study, we used Speswhite kaolin. Its mineral composition is 94 % kaolinite, 4 % Mica, 1 % Montmorillonite, and 1 % Feldspar and quartz. The CEC is 4-5 meq/100 g at pH 7, and exchangeable ions are Na⁺, Ca²⁺, Mg²⁺, K⁺ (Wu 2000). Its specific gravity and surface area (BET) are 2.6 and 14 m²/g, respectively (Imerys Minerals Ltd. UK).

Batch test procedures

According to the ASTM-D4319 norm, the batch tests were conducted with kaolinite and copper nitrate (Cu(NO₃)₂•2H₂O) solutions. Six solutions with concentrations varying from 0.1 to 10 mM were prepared. Their pH was adjusted to 5 by adding HCl and/or NaOH. Samples were prepared by mixing 2 g of air-dried kaolinite powders with 20 ml of every single prepared solution. The equilibration time was tested in preliminary experiments and was found close to 48 hours while the samples were gently agitated. Once equilibrated, samples were centrifuged for 20 min at 2000 g to separate the solid from the dissolved phases. Cu concentrations in the dissolved phase were finally analyzed using an atomic adsorption spectrophotometer (Shimadzu AA-6300).

Consolidation test procedures

Consolidation test were conducted according to the ASTM-D2435 norm. Two kaolinite suspensions (1:1 of soil:liquid ratio) were prepared by mixing air-dried kaolinite powders with (i) distilled water and (ii) 2 mM of Cu(NO₃)₂ solutions. The suspensions were slowly poured into a consolidameter (30 cm height x 10 cm diameter). The preconsolidation lasted about five days under a vertical pressure of 40 kPa and double drainage condition until the steady vertical settlement was achieved. Following the completion of preconsolidation, samples were carefully trimmed into a suitable size for conventional oedometer tests (19 mm height x 70 mm diameter). The tests were performed by applying incremental loading from 5 kPa to 800 kPa. The successive loading was twice of previous one and each loading lasted for 24 h. Since the stability of unloading is quickly achieved, each unloading lasted for 12 h.

MIP test

Samples for MIP were carefully trimmed into small cubes (10 × 10 × 10 mm) after preconsolidation and 1D oedometer tests. In order to prevent the capillary shrinkage, the samples were freeze-dried. The MIP device is a Micromeritics

AutoPore 9500 with a maximum intrusion pressure of 210 MPa and permit to determine the distribution of radii from 3 nm to 360 μm .

SEM observation

Fresh fragments produced by breaking carefully the (pre)consolidated samples were directly analyzed for their microstructure by using an environmental SEM.

EXPERIMENTAL RESULTS AND DISCUSSION

Heavy metals (HMs) and kaolinite physicochemical interaction

The results of the batch tests provided information about the evolution of Cu bound to the kaolinite suspension as a function of the added Cu concentrations. An initial linear increase of the sorbed Cu indicated the presence of unoccupied sorption sites up to 150 mg/L of added Cu. Beyond this value, the sorbed content remains relatively unchanged. This suggests that almost the totality of the sorption sites is saturated with Cu.

Consolidation and compressibility behaviour of HMs contaminated kaolinite

The consolidation parameters are presented in Table 1, including the compression index (C_c), the swelling index (C_s) and secondary compression index (C_{ae}). In the absence of Cu, the C_c displayed the highest value. Under small vertical effective pressure, Cu contributed to decrease the void ratio, which is consistent to the double layer theory. Accordingly, the thickness of the double layers decreases due to the decrease of interlayer repulsive forces while exchanging Cu ions with the Na^+ and K^+ ions within kaolinite. That is confirmed by the results of SEM imaging for two tested samples before consolidation. At higher vertical effective pressures, however, the importance of double layers effects on the void ratios tend to fade out. Besides, the relative smaller void ratio for Cu sample can also be interpreted in terms of osmotic compressibility (Di Maio 1996 and Ouhadi 2006). The increase of the concentration of Cu in the diffuse double layers induces an increase of osmotic pressure of the clay system and subsequently smaller void ratio of the samples.

Table 1 Consolidation and compressibility parameters of tested samples

Parameter	Distilled water sample			Cu solution sample		
	17 kPa	94 kPa	768 kPa	17 kPa	94 kPa	768 kPa
C_c	0.481			0.423		
C_s	0.103			0.103		
C_{ae}	0,00210	0,0074	0,0093	0,00259	0,0080	0,0073
C_{ae}/C_c	0,00436	0,0154	0,0193	0,00612	0,0189	0,0173

Considering the swelling of the tested samples, C_s remained unchanged. This indicates that tested Cu concentration did not affect the swelling of reconstituted kaolinite. That is in agreement with the results of Chen 2000 stating that the swelling of kaolinite is primarily controlled by mechanical factors such as rebound

of bent particles, rather than swelling of double layers (Mesri and Olson 1970, Chen 2000).

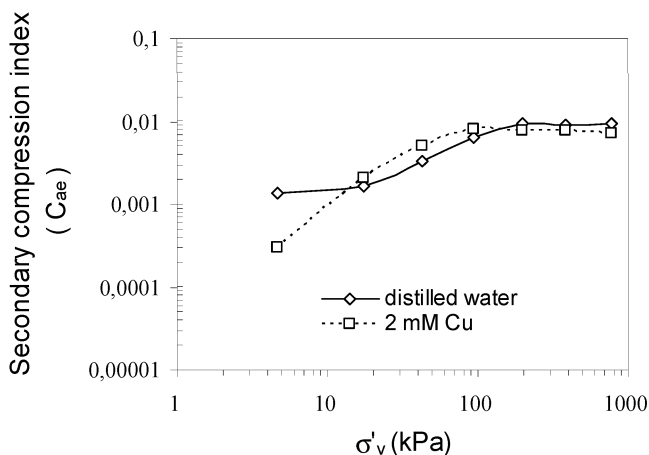


FIG. 1. $C_{\alpha\epsilon}$ versus σ'_v of kaolinite with distilled water and 2.0 mM $\text{Cu}(\text{NO}_3)_2$ solution.

The relationships between secondary compression index ($C_{\alpha\epsilon}$) and vertical effective pressure of the samples are presented in Fig. 1. The evolution tendencies of $C_{\alpha\epsilon}$ with an increase of σ'_v were similar for the tested samples. $C_{\alpha\epsilon}$ of the sample contaminated by Cu is little larger than that of no-contaminated one while the loading is less than 94 kPa, which is the successive loading of approximate preconsolidation pressure; beyond this loading, it becomes little smaller. The change of $C_{\alpha\epsilon}$ due to Cu contamination is supposed to be interpreted in terms of the findings reported by Wang 2007. It has been proved that secondary consolidation processes as primary consolidation preferentially occur in the larger and weaker inter-aggregated pores instead of in the smaller and stronger intra-aggregate pores. As mentioned above, the double-layers are compressed by the presence of Cu in pore fluid. Consequently, the particle size of kaolinite is enlarged, and the inter-aggregate size becomes simultaneously larger. In other words, the contaminated sample has more large inter-aggregate pores for same void ratio. This is confirmed by the fact that the increase of permeability of kaolinite was induced by the presence of Cu in pore fluid, presented in Fig. 2. When the loading is less than 94 kPa, which is the first loading larger than preconsolidation pressure, secondary compression is dominated by the collapse of the larger and weaker inter-aggregate pores within samples. Subsequently, most of them collapse with a rearrangement of kaolinite particles under relative high pressure. As a result, secondary compression is dominated by the smaller and stronger intra-aggregate pores. Consequently, the sample becomes less compressible during the secondary compression, thus $C_{\alpha\epsilon}$ was almost unchanged for the tested samples under high vertical applied pressure (more than 94 kPa). During these high loading stages, the no-contaminated sample has little larger $C_{\alpha\epsilon}$, this can be interpreted for two

reasons: (i) For same void ratio, while the contaminated sample has more large inter-aggregate pores, it should have less intra-aggregate pores. (ii) Due to the presence of Cu exchanged within the kaolinite particles, the adsorbed water layer surrounding the particles is fixed more strongly within the contaminated sample. These deduced interpretations will be further confirmed by using the results of MIP and SEM.

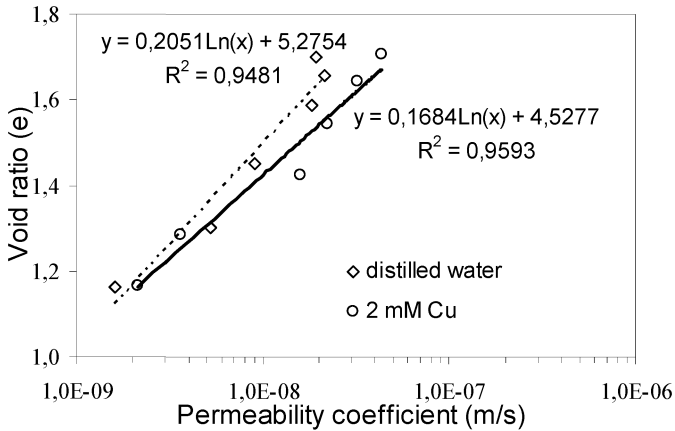


FIG. 2. Void ratio (e) versus permeability coefficient for kaolinite with distilled water and 2.0 mM $\text{Cu}(\text{NO}_3)_2$ solution, respectively.

Evolution of pore size distribution due to HMs contamination

The pore size distribution of the sample with 2 mM Cu before consolidation obtained by MIP shows that the PSD of the sample with Cu is bimodal with a peak located at about $0.1 \mu\text{m}$ and a minor peak located at $0.015 \mu\text{m}$. These pores belong to the range of large intra-aggregate pore space classified by Wang 2006. However, the inter-aggregate pores did not appear in the tested sample, likely because of the too small sample which is not representative for the testing.

CONCLUSION

By comparing the compressibility and consolidation behaviors of reconstituted kaolinite samples with and without Cu contamination, some interesting findings were obtained as follows:

- (1) The presence of Cu in pore fluid affected the compressibility and consolidation properties of reconstituted kaolinite, but did not affect their swelling properties.
- (2) The presence of Cu in pore fluid also induced a slight increase of permeability of reconstituted kaolinite.

ACKNOWLEDGMENTS

The authors appreciate much the help of Zhenyu YIN for his suggestions, the help of Pierre MOUNANGA for SEM imaging, the help of Emmanuel Rozière for MIP test, and the help of Bogdan Muresan for the correction of manuscript.

REFERENCES

- Bolt, G.H. (1956). "Physico-chemical analysis of the compressibility of pure clays." *Géotechnique*, Vol. 6 (2): 86-93.
- Chen, J., Anandarajah, A., and Inyang, H. (2000). "Pore Fluid Properties and Compressibility of Kaolinite." *J. Geotechnical & Geoenv. Engrg.*, Vol. 126 (9): 798-807.
- Di Maio, C. (1996). "Exposure of bentonite to salt solution: osmotic and mechanical effects." *Géotechnique*, Vol. 46 (4) : 695-707.
- Olson, R.E. and Mesri, G. (1970). "Mechanisms Controlling Compressibility of Clays." *J. Soil Mech. Found Div. (ASCE)*, Vol. 96 (6): 1863-1878.
- Ouhadi, V.R., Yong, R.N. and Sedighi, M. (2006). "Influence of heavy metal contaminants at variable pH regimes on rheological behavior of bentonite." *Applied Clay Science*, Vol. 32 (3-4): 217-231.
- Sridharan, A. and Rao, G.V. (1973). "Mechnisms controlling volume change of saturated clays and the role of the effective stress concept." *Géotechnique*, Vol. 23 (3): 359-382.
- Shackelford, C.D., Benson, C.H., Katsumi, T., Edil, T.B. and Lin, L. (2000). "Evaluating the hydraulic conductivity of GCLs permeated with non-standard liquids." *Geotextiles and Geomembranes*, Vol. 18 (2-4): 133-161.
- Souli, H. (2006). "Etudes hydromécanique et physico-chimique de deux argiles en présence de cations métalliques." *Doctoral dissertation of Ecole Centrale Paris*.
- Wang, Y. H. and Xu, D. (2007). "Dual Porosity and Secondary Consolidation." *J. Geotechnical & Geoenv. Engrg.*, Vol. 133 (7): 793-801.
- Wu, J., West, L.J. and Stewart, D.I. (2001). "Copper(II) humate mobility in kaolinite soil." *Engineering Geology*, Vol. 60 (1-4): 275-284.

Beneficial Reuse of Corrugated Board in Slurry Applications

James L. Hanson¹, M. ASCE, Nazli Yesiller², A.M. ASCE, Jagjit Singh³, Greg M. Stone, S.M. ASCE⁴, and Adam Stephens⁵

¹Professor, Civil and Environmental Engineering Department, California Polytechnic State University, San Luis Obispo, CA 93407; jahanson@calpoly.edu

²Interim Director, Global Waste Research Institute, California Polytechnic State University, San Luis Obispo, CA 93407; nyesiller@gmail.com

³Associate Professor, Industrial Technology, Orfalea College of Business, California Polytechnic State University, San Luis Obispo, CA 93407; jsingh@calpoly.edu

⁴Research Assistant, Civil and Environmental Engineering Department, California Polytechnic State University, San Luis Obispo, CA 93407; gstone@calpoly.edu

⁵Laboratory Coordinator, Orfalea College of Business, Industrial Technology, California Polytechnic State University, San Luis Obispo, CA 93407; astephe@calpoly.edu

ABSTRACT: Use of virgin and post-consumer corrugated board as a replacement for bentonite in slurry mixes was investigated. The effectiveness of the slurry mixes was assessed using typical tests including Marsh funnel viscosity, density, and filtrate loss. Filter cake permeability was also determined. Corrugated board was fiberized for the test program. Test results indicated that corrugated board could be used to replace 9 to 27% (0.5 to 1.5% corrugate content) of bentonite in slurry mixes with a total solids content of 5.5%. Slurry applications provide a new and viable beneficial reuse alternative for paper/paperboard products, which constitute the largest weight and volume fraction of municipal solid waste generated and disposed of in the U.S.

INTRODUCTION

Bentonite slurries are used in construction of vertical cutoff walls for geotechnical and geoenvironmental applications. The construction of cutoff walls typically is a step-by-step process, where a trench is excavated, filled first with slurry, and then backfill. The slurry covers the inside walls of the trench forming a low permeability filter cake layer. The slurry also provides hydrostatic pressure to keep the trench open prior to placement of the backfill. Typical slurries consist of 4 to 7% bentonite and 93 to 96% water by weight (Boyes 1975). Paper and paperboard constitute the highest fraction by both weight and volume of municipal solid waste generated (32.7% by weight) and disposed of (22.3% by weight) in the U.S. The amount of paper and paperboard generated and disposed of was 83 million and 37.8 million tons in 2007, respectively (USEPA 2009). The use of recovered paper in manufacturing containerboard has remained stable at approximately 16 million tons since 1997 (Paper Industry Association Council 2008). An economical limit for incorporating

waste papers into containerboard has been reached. Some corrugated board is not suitable for conventional recycling due to presence of contamination. Pizza boxes are a common example, which comprise nearly 1% of the total annual production of 313 million m² of corrugated board (Flaherty 2009). Residue on pizza boxes is problematic for recycling as grease prevents absorption of moisture, proper pulping of paper fiber, and quality of binding of fibers in recycled paper (RecycleBank 2009). Innovative recycling options (beyond the packaging industry) need to be investigated to promote beneficial reuse of paper products. This study has been conducted to evaluate reuse of paper and paperboard in civil engineering applications. Results from the portion of the study with use of corrugated board in slurry applications are presented herein.

EXPERIMENTAL TEST PROGRAM

Tests were conducted to assess the feasibility of using corrugated board in slurry mixtures. Bentonite was replaced by corrugated board at varying ratios. Properties of bentonite-board-water mixes were compared to baseline bentonite-water mixes to evaluate the influence and practical limits of corrugated board addition.

Materials

A commercially available standard powder bentonite was used in the test program. Baroid AQUAGEL is a finely ground, premium-grade Wyoming sodium bentonite that meets the American Petroleum Institute (API) Specification 13A, section 4 requirement. The bentonite had a liquid limit = 539, plastic limit = 82, and specific gravity = 2.65. Corrugated board was selected as the paper/paperboard product due to the significant quantities available for reuse. Tests were conducted on non-waxed products. Two types of corrugated board were used in the test program: conventional box material (c-flute corrugated board) and pizza boxes. Identical products for virgin (V) and post-consumer (PC) corrugated board were tested to determine potential effects of use on the properties of corrugated board in slurry applications. The c-flute corrugated board was subjected to standardized laboratory conditioning as prescribed by ISTA (2009) to provide post-consumer status. The post consumer pizza boxes were collected from a garbage bin and contained representative amounts of food product (i.e., grease and food remains) residue. The corrugated board samples were fiberized by mixing with water in a Waring cb 15 stainless steel 4-L capacity blender that contained a specially fabricated blade adhering to the specifications outlined by White and Kendrick (2009).

Corrugated Board Tests

Tests (summarized in Table 1) were conducted on virgin and post-consumer corrugated board to determine material properties. The corrugated board properties are presented in Table 2. The edge crush and water absorption tests on corrugated board provided indication of the fiberization potential and shredding of the corrugated board for the proposed slurry application.

Table 1. Corrugated Board Tests

Test Name	Standard Designation	Description of Test
Grammage of paper and paperboard (weight per unit area)	TAPPI T 410 om-02	Weight per 92.90 m ² of all three containerboard components of a single wall corrugated fiberboard is determined after conditioning for 24 hours at 21±1°C temperature and 52±0.5% RH.
Bursting strength of corrugated and solid fiberboard	TAPPI T810 om-06	Square corrugated fiberboard samples with dimension 31.50±0.03 mm are tested by distending an expansible diaphragm under a pressure of 690 kPa to 4825 kPa.
Edgewise compressive strength of corrugated fiberboard	TAPPI T839 om-02	A test specimen with length 50.8±0.8 mm and height 25.4±0.4 mm is compressed vertically (load parallel to flutes) to failure at the rate of 111±22 N/s.
Water absorptiveness of corrugated fiberboard (Cobb test)	TAPPI T441 om-04	A sample with a diameter of 11.28±0.02 cm is exposed to 100 mL of water (23±1°C) and a head of 1±0.1 cm for 120 seconds.

Table 2. Corrugated Board Properties

Material	Weight/Unit Area (g/m ²)	Burst Strength (kPa)	Edge Crush (N)	Cobb Test (g/m ²)
V c-flute box	579	1350	162	78.3
PC c-flute box	588	1140	146	89.0
V pizza box	447	900	155	94.3
PC pizza box	493	1025	165	99.0

Slurry Tests

Slurry mixes were prepared using bentonite and water and also using bentonite, fiberized corrugated board, and water. Visual comparison was made for the solids suspension / sedimentation behavior of the bentonite and fiberized corrugated board by allowing mixtures to settle in hydrometer jars and by centrifugation. Example photographs of the slurries are presented in Fig. 1. The centrifuge was run at 1500 rpm for 1 minute to assess segregation and sedimentation in the mixtures. At high fiber ratios, the homogeneity of the slurries was decreased as flocculation and segregation of the fibers occurred (presence of clear water within the grab samples and at the top of the centrifuge samples). Bentonite dispersed in water and remained in suspension for extended periods of time, whereas the paper fibers alone flocculated in the presence of water and became segregated from the bentonite with time. In addition, high corrugate content mixtures exhibited gas production within 5-6 days of mixing, which remained entrapped within the fiber matrix. Overall, fiber-only and low-bentonite content mixes (<2.5% bentonite) were deemed inappropriate to provide effective slurry behavior. Solids remained in suspension for slurry mixtures that contained both fibers and sufficient amounts of bentonite. The specific mixtures tested for slurry behavior were based on these observations.

All mix ratios are provided on weight basis (Table 3). Tap water was used for all slurry mixes. The water was conditioned to a pH of 8.5 ± 0.12 using small amounts of soda ash before solids were added to the slurry mixtures. Pure bentonite slurries were mixed in a blender on low speed for 2 minutes prior to testing. For slurries containing corrugated board, water and corrugated board were mixed on low speed

for a 2-minute period to allow corrugate to be pulped into fibers, then mixed again after the addition of bentonite for an additional 2 minutes. The post-consumer corrugated board was more difficult to pulp than the virgin corrugated board. The original pulping period of 2 minutes was increased to 5 minutes for post-consumer corrugated board samples in subsequent tests to investigate the effect of increased pulping duration on the engineering properties of the slurry mixtures.

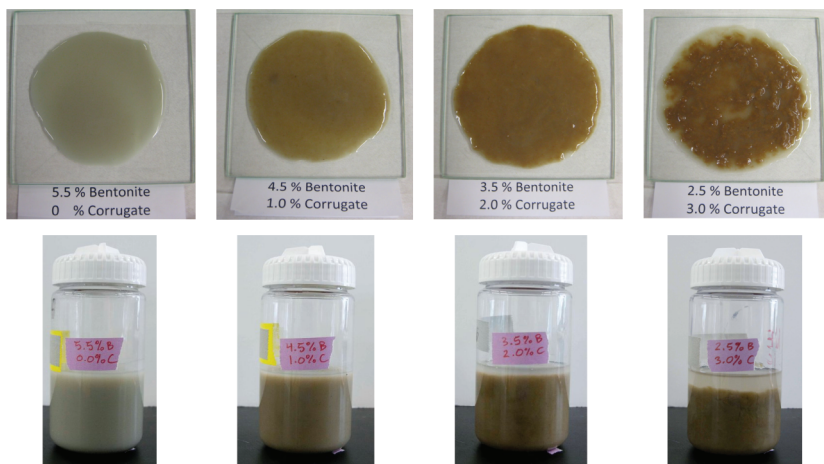


Figure 1. Comparison of Slurry Mixtures (grab and centrifuge samples)

Table 3. Slurry Mix Ratios

Mix Number	Corrugate Type	Bentonite (%)	Corrugated Board (%)	Water (%)
B5.0	None	5.0	0	95
B5.5	None	5.5	0	94.5
B6.0	None	6.0	0	94
V0.5	Virgin	5.0	0.5	94.5
V1.0	Virgin	4.5	1.0	94.5
V1.5	Virgin	4.0	1.5	94.5
V2.0	Virgin	3.5	2.0	94.5
V2.5	Virgin	3.0	2.5	94.5
V3.0	Virgin	2.5	3.0	94.5
PC0.5	Post-consumer	5.0	0.5	94.5
PC1.0	Post-consumer	4.5	1.0	94.5
PC1.5	Post-consumer	4.0	1.5	94.5
PC2.0	Post-consumer	3.5	2.0	94.5
PC2.5	Post-consumer	3.0	2.5	94.5
PC3.0	Post-consumer	2.5	3.0	94.5

Typical slurry tests (D’Appolonia 1980, USEPA 1984) were used in the experimental program: Marsh funnel viscosity (ASTM D 6910); mud balance (ASTM

D 4380); filter press (API Recommended Practice 13B); and filter cake permeability (conducted in conjunction with / immediately following API Recommended Practice 13B). Standardized test methods were generally followed. In order to prevent segregation of paper fibers from the slurries, the mixtures containing fibers were not poured through the attached funnel screen in Marsh funnel testing. The thickness of the filter cake was measured by averaging values determined at three locations on the cake using a pair of digital calipers. Thickness of the filter cake was measured after permeability tests had been conducted to minimize damage and disturbance to the filter cake. Separate tests were conducted to verify that filter cake thickness did not change during the permeability stage of the experiments. The permeability tests were conducted using a pressure differential of 140 kPa. The hydraulic gradient varied depending on the thickness of the filter cake and was on the order of 5,000.

RESULTS AND DISCUSSION

The results of the slurry tests are provided in Table 4. The Marsh funnel viscosity of the bentonite-water slurry mix was equal to 40.5 s for the 5.5% solids content and this mixture was established as the baseline mixture for the tests. The total solids content of the mixes containing both bentonite and corrugated board was set to 5.5%. The viscosity of the mixture with 5% bentonite was in general similar to the baseline mix, whereas the 6% bentonite mix had higher viscosity and density and lower filter cake thickness than the baseline mix. For mixes containing bentonite, corrugated board, and water, viscosity, filter loss, filter cake thickness, and filter permeability generally increased with increasing corrugate content. Mud balance density generally decreased with increasing corrugate content.

Acceptable slurry mix properties were established as: Marsh funnel viscosity of approximately 40 s (up to 50 s was deemed acceptable for this test program); density of 1010-1040 kg/m³; and filtrate loss of less than 30 ml based on specifications provided in USEPA (1984) and Ryan and Day (2003). The variations of Marsh funnel viscosity, density, filtrate loss, and permeability as a function of corrugate content are presented in Fig. 2. Shaded regions in the plots in Fig. 2 represent areas that are outside acceptable limits for Marsh funnel viscosity, mud balance density, and filtrate loss. In general, mixtures up to approximately 1.5% corrugate content (baseline, V mixes up to 1.5%, PC mixes up to 1.0%, and PC(+) mixes up to 2% corrugate content, Table 4) maintain acceptable engineering properties. The corrugated board can be used to replace 9 to 27% (0.5 to 1.5% corrugate content in a 5.5% mixture) of the bentonite used in the slurry mixes. In addition, the PC2.0-P(+) slurry (2% corrugate) and other 2% corrugate slurry mixtures were close to the acceptable range and may be used based on specific site and construction conditions. Significant amount of this natural resource (i.e., bentonite) can be saved using the corrugated board, in consideration to large-scale construction projects.

The differences between virgin and post-consumer board were not significant with regard to performance in slurry mixes. The changes in engineering properties of the slurries with added corrugate content were attributed to the fibrous structure of the corrugate. Specifically, a fibrous matrix developed with sufficient addition of corrugate, which promoted more viscous, less cohesive behavior. This resulted in an

increase in Marsh funnel viscosity (up to 2.5 corrugate content beyond which Marsh funnel readings could not be obtained due to excessive bridging of the fibers in the testing device); a decrease in mud balance density (due to replacement of bentonite with the lighter fibers); and increase in filtrate loss and permeability (attributed to presence of sufficient fiber content to provide preferential pathways for flow).

Table 4. Slurry Test Results

Corrugate Type	Mix	MFV (s)	MB (kg/m ³)	FL (mL)	CT (mm)	k/t (s ⁻¹)	k (cm/s)
None	B5.0	38.3	1030	19	2.4	4.68 x 10 ⁻⁸	1.12 x 10 ⁻⁸
	B5.5	40.5	1030	16	2.7	4.89 x 10 ⁻⁸	1.33 x 10 ⁻⁸
	B6.0	49.2	1035	14	1.8	3.24 x 10 ⁻⁸	5.93 x 10 ⁻⁸
C-flute box	V0.5-C	42.4	1025	19	3.8	4.20 x 10 ⁻⁸	1.58 x 10 ⁻⁸
	V1.0-C	41.8	1010	17	3.1	4.74 x 10 ⁻⁸	1.46 x 10 ⁻⁸
	V1.5-C	47.1	1010	22.8	3.2	4.30 x 10 ⁻⁸	1.36 x 10 ⁻⁸
	V2.0-C	57.0	1010	26.3	4.8	5.14 x 10 ⁻⁸	2.48 x 10 ⁻⁸
	V2.5-C	NM	1015	32.8	8.3	4.71 x 10 ⁻⁸	3.91 x 10 ⁻⁸
	V3.0-C	NM	1010	39.8	10.8	6.92 x 10 ⁻⁸	7.48 x 10 ⁻⁸
	PC0.5-C	47.3	1025	20.6	3.2	3.80 x 10 ⁻⁸	1.22 x 10 ⁻⁸
	PC1.0-C	49.7	1020	20.1	3.5	4.38 x 10 ⁻⁸	1.53 x 10 ⁻⁸
	PC1.5-C	52.7	1010	21.6	3.6	3.72 x 10 ⁻⁸	1.36 x 10 ⁻⁸
	PC2.0-C	58.0	1010	26.2	4.2	5.02 x 10 ⁻⁸	2.09 x 10 ⁻⁸
	PC2.5-C	NM	1015	32.1	9.1	6.53 x 10 ⁻⁸	5.92 x 10 ⁻⁸
	PC3.0-C	NM	1015	36	11.0	8.00 x 10 ⁻⁸	8.83 x 10 ⁻⁸
	PC0.5-C(+)	46.5	1025	19	4.0	3.75 x 10 ⁻⁸	1.49 x 10 ⁻⁸
	PC1.0-C(+)	49.0	1015	20.7	3.0	4.08 x 10 ⁻⁸	1.23 x 10 ⁻⁸
	PC1.5-C(+)	49.4	1010	19.6	3.7	3.41 x 10 ⁻⁸	1.26 x 10 ⁻⁸
	PC2.0-C(+)	56.8	1010	25	5.5	4.25 x 10 ⁻⁸	2.33 x 10 ⁻⁸
	PC2.5-C(+)	79.1	1010	27.8	5.1	3.42 x 10 ⁻⁸	1.74 x 10 ⁻⁸
PC3.0-C(+)	NM	1005	32.9	11.4	4.90 x 10 ⁻⁸	5.58 x 10 ⁻⁸	
Pizza box	V0.5-P	44.44	1025	18.8	3.2	4.27 x 10 ⁻⁸	1.35 x 10 ⁻⁸
	V1.0-P	47.7	1020	20.1	4.0	4.07 x 10 ⁻⁸	1.62 x 10 ⁻⁸
	V1.5-P	49.0	1015	22.6	4.1	4.38 x 10 ⁻⁸	1.80 x 10 ⁻⁸
	V2.0-P	56.4	1010	24.6	5.7	4.80 x 10 ⁻⁸	2.73 x 10 ⁻⁸
	V2.5-P	NM	1010	31	8.0	6.19 x 10 ⁻⁸	4.89 x 10 ⁻⁸
	V3.0-P	NM	1010	33.6	10.5	7.48 x 10 ⁻⁸	7.83 x 10 ⁻⁸
	PC0.5-P	46.4	1025	20.1	3.1	4.13 x 10 ⁻⁸	1.27 x 10 ⁻⁸
	PC1.0-P	47.1	1020	21.1	3.4	4.02 x 10 ⁻⁸	1.35 x 10 ⁻⁸
	PC1.5-P	52.0	1010	23.2	4.4	4.61 x 10 ⁻⁸	2.03 x 10 ⁻⁸
	PC2.0-P	55.2	1010	24.6	6.2	3.22 x 10 ⁻⁸	1.98 x 10 ⁻⁸
	PC2.5-P	70.2	1015	28.7	8.2	4.37 x 10 ⁻⁸	3.58 x 10 ⁻⁸
	PC3.0-P	NM	1015	34.3	6.2	4.83 x 10 ⁻⁸	3.00 x 10 ⁻⁸
	PC0.5-P(+)	39.4	1025	16.8	2.2	3.44 x 10 ⁻⁸	7.60 x 10 ⁻⁹
	PC1.0-P(+)	38.5	1020	17.5	1.5	3.55 x 10 ⁻⁸	5.23 x 10 ⁻⁹
	PC1.5-P(+)	40.6	1010	18.8	2.7	3.65 x 10 ⁻⁸	9.91 x 10 ⁻⁹
	PC2.0-P(+)	48.1	1000	24	4.0	4.82 x 10 ⁻⁸	1.93 x 10 ⁻⁸
	PC2.5-P(+)	65.1	1015	30.2	8.0	6.96 x 10 ⁻⁸	5.54 x 10 ⁻⁸
PC3.0-P(+)	NM	1015	31	10.7	7.66 x 10 ⁻⁸	8.17 x 10 ⁻⁸	

MFV – Marsh funnel viscosity, MB – Mud balance density, FL – Filtrate loss, CT – Thickness of filter cake (t), k/t – Quotient of permeability of filter cake and thickness of filter cake, k – permeability of filter cake, “-C” – C-flute corrugated box, “-P” – Pizza box, “(+)”– sample subjected to additional blending time, NM – Not measurable due to flocculation and bridging in the Marsh funnel device.

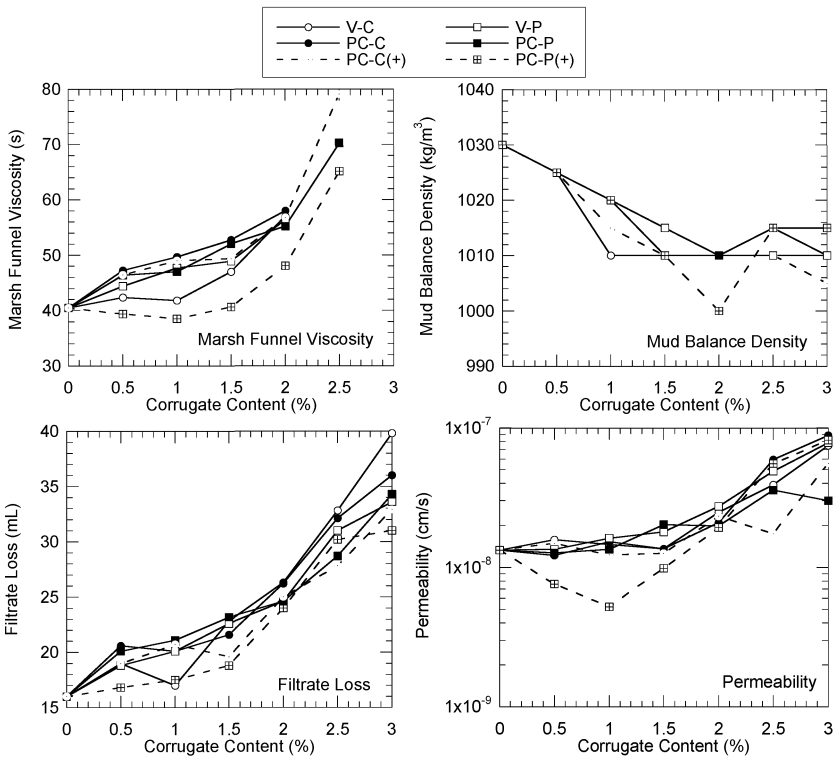


Fig. 2. Engineering Properties of Slurries

The additional blending time for the post-consumer samples had a more pronounced effect on engineering properties of the slurries containing pizza box fibers than the c-flute box fibers. The greater differences were attributed to the breakdown of greasy film on the pizza box allowing access to water and softening during the extended blending. In comparison, the c-flute fibers had already sufficiently broken down after 2 min. of blending and additional blending did not change the behavior significantly.

CONCLUSIONS

Tests were conducted to assess the feasibility of using corrugated board in slurry applications. Bentonite used in typical slurry mixtures was replaced by fiberized corrugated board at varying ratios. Properties of bentonite-corrugated board-water mixes were compared to baseline bentonite-water slurry mixes to evaluate the influence and practical limits of corrugated board addition to the mixes. The results indicated that the corrugated board could be used to replace 9 to 27% (corresponding to 0.5 to 1.5% corrugate content in a 5.5% mixture) of the bentonite used in the slurry

mixes based on Marsh funnel viscosity, density, and filtrate loss tests. Corrugated board may be used to replace up to 36% of bentonite (2.0% corrugate in a 5.5% mixture) for specific site and construction conditions requiring high MFV. In addition, permeability of the mixes with corrugated board was similar to baseline bentonite-water mix permeability. The differences in engineering properties of the slurries containing corrugate content were attributed to the presence of a fibrous matrix that influenced viscosity and flow characteristics. Overall, slurry applications provide a new and viable beneficial reuse alternative for paper / paperboard products, which constitute the largest weight and volume fraction of municipal solid waste generated and disposed of in the U.S. as well as other countries.

ACKNOWLEDGMENTS

This study was partially supported by Office of Naval Research (Award No. N00014-08-1-0855). Mr. Timothy Kershaw and Mr. Matthew Anderson assisted with laboratory testing.

REFERENCES

- Boyes, R. G. H. (1975). *Structural and Cut-off Diaphragm Walls*, Applied Science Publishers Ltd., London, England.
- D'Appolonia, D. J., "Soil-Bentonite Slurry Trench Cutoffs," *Journal of the Geotechnical Engineering Division*, ASCE, 106, GT4, 399-417.
- Flaherty, R. (2009). *Personal communication*, President, International Corrugated Packaging Foundation, December 19, 2009.
- ISTA (2009). International Safe Transit Association, "ISTA 2 Series Partial Simulation Performance Test Procedure," <http://www.ista.org/forms/IAoverview.pdf>, last accessed December 26, 2009.
- Paper Industry Association Council (2008). "2007 Recovered Paper Annual Statistics," <http://stats.paperrecycles.org/>, Paper Industry Association Council, last accessed May 6, 2008.
- RecycleBank (2009). "The Pizza Box Recycling Mystery," <http://www.recyclebank.com/recycling/recycling-101/330-the-pizza-box-recycling-mystery>, last accessed December 17, 2009.
- Ryan and Day (2003). "Soil-Bentonite Slurry Wall Specifications," *Proceedings, Soil and Rock America 2003, 12th Panamerican Conference on Soil Mechanics and Geotechnical Engineering*, P. J. Culligan, H. H. Einstein, and A. J. Whittle, Eds.
- White, A. and Kendrick, J. (2009). Recycling Paper Food Packaging with Corrugated Cardboard: A Proposal for a New Recyclability and Repulpability Protocol and Preliminary Test Results for Fiber-Based Hot Cups, Global Green USA's Coalition for Resource Recovery, New York.
- USEPA (2009). "Municipal Solid Waste in the United States – 2007 Facts and Figures." <http://www.epa.gov/epawaste/nonhaz/municipal/pubs/msw07-rpt.pdf>, last accessed August 26, 2009.
- USEPA (1984). *Slurry Trench Construction for Pollution Migration Control*, EPA-540/2-84-001, Washington D.C.

Analysis on Tensile Force of Liner System with the Variation of Location of Roller Compactor in Landfill

Sifa Xu¹, Zhe Wang² and Hao Zhao³

¹ College of Civil Engineering and Architecture, Zhejiang University of Technology, Hangzhou 310032, China; xusifa@zjut.edu.cn

² College of Civil Engineering and Architecture, Zhejiang University of Technology, Hangzhou 310032, China; wangzsd@163.com

³ College of Civil Engineering and Architecture, Zhejiang University of Technology, Hangzhou 310032, China; zhanghao@zjut.edu.cn

ABSTRACT: A liner system is installed on the bottom and the side slope of a waste landfill. Tensile forces can occur due to waste compaction which is transferred into the geosynthetics by friction. The long term design strength of the liner system placed on side slope in landfill may be determined by creep rupture strength, so it is very important to estimate the amount of tensile force created in the liner system, especially on the shoulder of liner system in the course of filling. In this research, centrifugal model experiments and FEM analyses are conducted to study the variation of tensile force created at the shoulder of liner system with the variation of roller compactor's location.

INTRODUCTION

Waste landfill should be designed that no leachate that may include hazardous materials flows into the surrounding ground and water over its design life. A liner system is installed on the bottom and the side slope of a waste landfill to prevent the leachate from infiltrating into surrounding ground and polluting groundwater (Wang and Wang 2004). The liner system is considered to experience various forces, such as tensile force induced by settlement of base ground (Knipschild. 1984), thermal stress due to decrease of temperature (Imaizumi et al. 1999), lifting force by the wind (Zornberg and Giroud 1997), tensile force by compaction work of disposed waste (Xu and Imaizumi 2003). The long term design strengths of the liner system are usually controlled by creep rupture within the design life. Creep strain would occur if the tensile forces of the liner system remain constant over a sufficiently long period of time, and it can lead to creep rupture if the strain exceeds the limit strain (Ingold et al. 1994), so it is very important for the design of the liner system to determine the tensile force induced in components of the liner system, especially on the shoulder of HDPE geomembrane with the location of roller compactor (Hullings and Sansou 1997). But it is not clearly

understood how the tensile force acting on the liner system due to the compaction work varies with the location of the roller compactor in landfill. In this paper, the variations of tensile force created at the shoulder of the liner system with the location of roller compactor are studied.

INTERFACE FRICTION CHARACTERISTICS

The characteristics of the studied geosynthetic materials at 20°C are listed in Table 1. Incinerated ash from municipal waste is used to represent disposed waste in landfill, its cohesion and friction angle are 8 kPa and 36.5°, respectively. Water content of the incinerated ash is 41%.

Table 1. Mechanical Properties of Geosynthetics.

Material	Thickness (mm)	Tensile strength (MPa)	Elastic modulus (MPa)
HDPE geomembrane	1.5	35.3	484
Non-woven geotextile	10	1.4	6.5

The interface friction angles between the incinerated ash and non-woven geotextile, HDPE geomembrane and non-woven geotextile are 12.5° and 19.7°, respectively.

CENTRIFUGAL MODEL TESTS

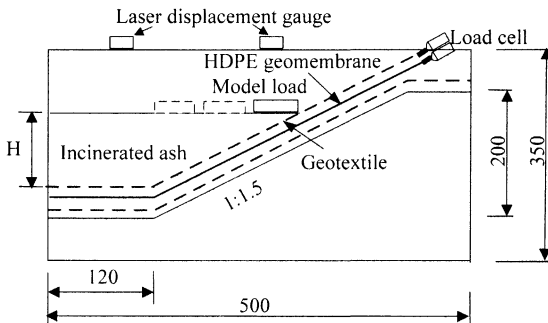


FIG.1. Configuration of the centrifugal model.

The model landfill as shown in Fig.1 is placed in a steel container having a length of 500 mm, a width of 260 mm and a depth of 350 mm. The foundation and slope of the model landfill are made of gypsum. The slope of the model landfill is 1:1.5(V:H) with a height of 200 mm. Non-woven geotextile is then glued to the surface of the model landfill which is then covered by an HDPE geomembrane with a thickness of 1.5 mm. A

protective layer of non-woven geotextile is spread over the HDPE geomembrane which is then covered on the surface by incinerated ash. The model is accelerated to about 37 g in the centrifuge. The tensile forces induced within the top non-woven geotextile and HDPE geomembrane are measured through load transducers of 196 N and 490 N which are fixed at the top of the slope.

Incinerated ash is poured into the model landfill. Its wet density is approximately 820 kg/m³. Acceleration of the centrifuge is increased at a rate of 5 g/min to a maximum of 37 g (g is gravitational acceleration and equals to 9.8m/s²), a 150 mm height in the model is equivalent with a 5 m height of waste landfill in the prototype. The tensile forces of HDPE geomembrane and non-woven geotextile and the acceleration are recorded by computer at each 5 g interval in acceleration.

To evaluate the influence of the location of roller compactor on tensile force of liner system for constant height of incinerated ash, the model load of 47.4 kPa (37g) is applied on the surface of incinerated ash to simulate the roller compactor. The distance from the model load to the slope liner system is also varied at 0, 70, 140 mm.

RESULTS OF TESTS

The measured tensile forces created at the shoulder of HDPE geomembrane and non-woven geotextile with model load applied on the surface of incinerated ash are shown in Fig.2 and Fig.3. It is found that the tensile forces of HDPE geomembrane and non-woven geotextile increase significantly, and as the distance from model load to slope liner system becomes larger, the tensile forces of HDPE geomembrane and non-woven geotextile decrease. For example, the tensile force of HDPE geomembrane increases from 0.26 kN/m to 0.72 kN/m when the model load is applied on the surface of incinerated ash, the increment of tensile force is larger than that of tensile force created by incinerated ash. The tensile force of non-woven geotextile also increases from 0.25 kN/m to 0.47 kN/m. But the tensile forces of HDPE geomembrane decrease from 0.72 kN/m to 0.63 kN/m when the distance increases from 0 mm to 140 mm.

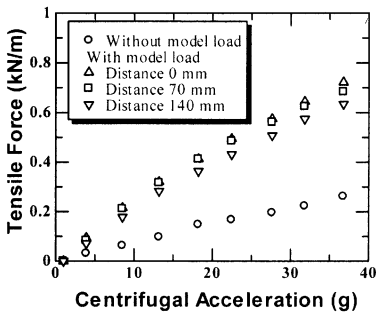


FIG. 2. Measured tensile force. (geomembrane).

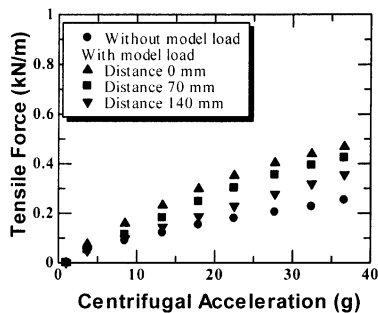


FIG. 3. Measured tensile force. (geotextile).

FEM ANALYSIS

The finite element meshes and boundary conditions are shown in Fig.4. It is possible to displace freely between incinerated ash and steel container in the vertical direction, and the HDPE geomembrane and non-woven geotextile at the shoulder are fixed. The quadrilateral element and triangle element are used to model the incinerated ash, and the geosynthetics were modeled by quadrilateral element. The interfaces between different materials are modeled by joint element to simulate the transfer of frictional stresses through them.

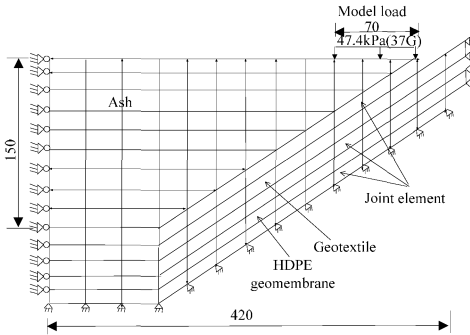


FIG. 4. Finite element mesh.

The stress-strain response of the incinerated ash is modeled by Duncan-Chang model (Duncan and Chang 1970). The tangential modulus can be expressed

$$E_t = \left(1 - \frac{R_f (1 - \sin \phi) (\sigma_1 - \sigma_3)}{2c \cos \phi + 2\sigma_3 \sin \phi} \right)^2 k P_a \left(\frac{\sigma_3}{P_a} \right)^n \quad (1)$$

Where σ_1 and σ_3 are maximum and minimum principal stresses, respectively; R_f is failure ratio; c and ϕ are cohesion and friction angle, respectively; P_a is atmospheric pressure; k and n are experimentally determined constants according to direct shear tests. The friction angle and cohesion of the incinerated ash are 19.7° and 1.3 kPa , respectively.

The HDPE geomembrane and non-woven geotextile are treated as a linear elastic materials and secant modulus at a strain of 1% (Table 1) is applied in the analysis.

The shear stiffness K_{st} of interface ahead of the peak shear stress can be expressed as follows

$$K_{st} = \left(1 - R_f \frac{\tau}{\tau_f} \right)^2 k \gamma_w \left(\frac{\sigma_n}{P_a} \right)^n \quad (2)$$

Where, τ and σ_n is shear stress and normal stress at the interface; τ_f is shear stress at failure; γ_w is unit weight of water.

The interface shear strength τ_f can be expressed as a function of the normal stress by Mohr-Coulomb failure criterion.

Beyond peak value, the interface shear stress is assumed to be constant. The parameters of interfaces used in the analysis are shown in Table 2.

Table 2. Analysis Parameters.

Interface or materials	k	n	R_f
Incinerated ash-geotextile	11.65	1.06	0.82
HDPE geomembrane-geotextile	3.90	0.84	0.78
Incinerated ash	63.2	0.83	0.81

The calculated tensile forces of HDPE geomembrane and non-woven geotextile are shown in Fig.5. Irrespective of distance from model load to slope liner system, the calculated values of HDPE geomembrane are smaller than the test values, about 0.76-0.90 of the test values.

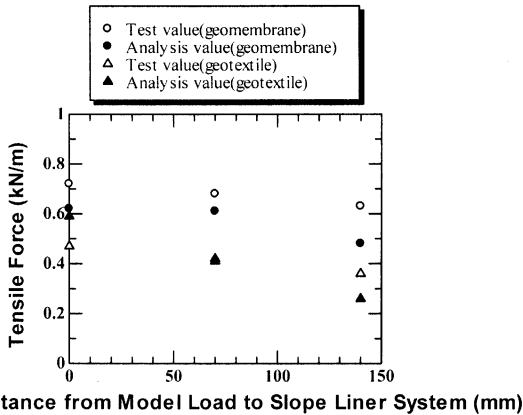


FIG. 5. Relationship between calculation and test values.

The relationship between temperature t and secant modulus $E_{1\%}$ of HDPE geomembrane can be expressed as:

$$E_{1\%} = 784 \cdot 10^{-0.0102t} \tag{3}$$

The elastic modulus of HDPE geomembrane used for FEM analysis is data of 20°C, but the test temperature is 14°C, so the elastic modulus of HDPE geomembrane used is smaller than the test value, the deviation between calculated values and test values is generated.

The calculated values of non-woven geotextile are about 0.72-1.25 of the test values.

The test values are larger than the calculated values except at 0 mm distance of model load to slope liner system.

CONCLUSIONS

This paper describes the influence of the location of roller compactor on tensile force creating at the shoulder of liner system. As the distance from model load to slope liner system becomes larger, the tensile forces of HDPE geomembrane and non-woven geotextile decreased. Effects of model load on the tensile forces of HDPE geomembrane and non-woven geotextile are significantly. The tensile forces of HDPE geomembrane and non-woven geotextile analyzed by FEM are consistent with those obtained by centrifugal model test in general. The calculated values of HDPE geomembrane are smaller than the test values, about 0.76-0.90 of the test values. The calculated values of non-woven geotextile are about 0.72-1.25 of the test values.

REFERENCES

- Wang, X. and Wang, J. (2004). "Development and application of geomembrane liner system in solid waste landfills." *Environmental protection science*. Vol. 30(2):24-26 (in Chinese) .
- Knipschild, F.W. (1984). "Selected Aspects of Dimensioning Geomembrane for Groundwater Protection Applications. " *Proc.of the Int.Conf. on Geomembranes*. 439-443.
- Imaizumi, S., Kawamata, K. and Tsuboi, M. (1999). "Study on Termal Stress within the Geomembrane Liner Induced by Temperature Decrease. " *Proc.of the 7th International Landfill Symposium*.115-122.
- Xu, S. and Imaizumi, S. (2003). "The drag force evaluation of the liner sheet with a change of slope angle. " *Geosynetics Engineering Journal*. 49-54(in Japanese).
- Ingold, T.S., Montaneui, F. And Rimoldi, P. (1994). "Extrapolation Techniques for Long Term Strengths of Polymeric Geogrids. " *Fifth International Conference on Geotextiles, Geomembranes and Related Products*, Singapore, Vol.3,1117-1120.
- Hullings, D.F. and Sansone, L.J. (1997). "Design Concerns and Performance of Geomembrane Anchor Trenches. " *Geotextiles and Geomembranes*. Vol.15 (4):403-417.
- Duncan, J.M. and Chang, C.Y. (1970). "Nonlinear Analysis of Stress and Strain in Soil. " *Journal of the Soil Mechanics and Foundations Division*. ASCE, 1970, Vol. 96(SM5): 1629~1654.

pH Changes in Solidified Dredged Materials

Gan Zhao¹, Wei Zhu², Lei Li³, Chun-Lei Zhang⁴

¹PhD student, Geotechnical Research Institute, Hohai University, Nanjing, 210098, China; zhaogan@hhu.edu.cn

²Professor, College of Environmental Science and Engineering, Hohai University, Nanjing, 210098, China; weizhu863@126.com

³Doctor, National Engineering Research Center of Water Resources Efficient Utilization Engineering Safety, Hohai University, Nanjing, 210098, China; dr.lilei@163.com

⁴Doctor, Research Academy, Hohai University, Nanjing, 210098, China; chunleizhang@hhu.edu.cn

ABSTRACT: The cement-based solidification is recently considered as an alternative option to reuse the dredged materials as engineering fills. As the solidification involves hydration reactions, the pH value of the solidified soil can change which may affect the surrounding environment after its placement. Thus the pH value of the solidified dredged material is one of the key factors which govern its suitability as fill materials. In this study, the effects of the type of additive, curing method and curing time on the change in pH value of a solidified dredged material were investigated. Four different additives (cement, fly ash, gypsum and rice straw powder) were used. The solidified samples were cured under either humidity controlled or exposed conditions. The curing period ranges from 1 to 60 days. The test results show that among the four additives used in the study, cement gives a more substantial increase in the pH value than the other three additives. Regarding the curing conditions, samples cured under humidity controlled condition exhibit higher pH value than those cured under exposed condition.

INTRODUCTION

Dredging is commonly employed to improve water quality of rivers and lakes and ensure the ability of river for flood discharge and navigation. As a result huge amount of high water content and low strength dredged materials are produced (LUO Qing ji et al., 2005). Land and ocean disposal are the traditional methods for treating the dredged materials in China. Besides the disposal methods, cement-based solidification is recently considered as an alternative option to reuse the dredged materials as engineering fills (Zhu Wei et al., 2005). As the solidification involves hydration reactions, the pH value of the solidified soil can change which may affect the surrounding environment after its placement. Besides, the leachability of heavy metals (if any) entrapped in the solidified soil is significantly affected by the soil pH value (Sanchez et al., 2005). Thus the pH value of the solidified dredged material is one of the key factors which govern its suitability as fill materials.

Previous studies show that the additive was an important factor affecting the pH of mixture materials (M. Kimura et al., 2000; C.Q. Wang et al., 2004). Curing method, such as curing sealed or curing exposed to air, also affected the pH change of materials (R.E.H. Sweeney et al., 1999). In this study the effects of the type of additive, curing method and curing time on the change in pH value of a solidified dredged material were investigated. Four different additives (cement, fly ash, gypsum and rice straw powder) were used. The treated samples were cured under either humidity controlled or exposed conditions. The curing period ranged from 1 to 60 days. The objective of the study is, through the laboratory tests, to provide a scientific basis for controlling the pH of solidified soil used in practical engineering.

MATERIALS AND METHODS

Materials

The dredged material was taken from Taihu Lake, China and its main physical properties are summarized in Table 1. Four additives were used: Ordinary Portland cement (OPC), fly ash, semi-hydrated gypsum and rice straw material (drying below 60°C and grinding into powder).

Table 1. Physical properties of dredged material

Water content (%)	Density (g/cm ³)	Specific gravity	Void ratio	Organic matter content (%)	Plastic limit (W _p) (%)	Liquid limit (W _L) (%)	Plasticity index (I _p)	pH
104	1.48	2.64	2.7	4.7	18	33	15	6.89

pH test

First, the dredged material and additives were mixed thoroughly inside a mixer. Then some mixtures were sealed by polyethylene bags and cured at temperature around 20°C and humidity greater than 90%. The other mixtures were placed on the plexiglass plates and exposed to air. After curing for the target time, the pH of solidified soil was measured according to the methods specified by (ISO 10309: 2005). The mixture samples were first dried in an oven at 40°C, and pulverized to pass through a 2mm sieve. Then the powder samples were extracted at a liquid to solid (L/S) ratio of 5 ml/g in capped polypropylene bottles, stirred for 60 min, and the pH was measured by using a PHS-3C pH meter.

RESULTS AND DISCUSSION

Effect of additives

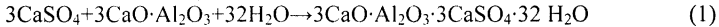
(1) OPC

Fig.1 (a) shows the change in pH for the OPC solidified samples. The pH increases with increasing OPC content. It is found that the pH varies slightly for OPC content less than 8%, beyond which it increases substantially. Hydration and pozzolanic reactions occur when the cement reacts with the dredged materials. The resultant hydration products are calcium silicate hydrates ($3\text{CaO}\cdot 2\text{SiO}_2\cdot 2.5\text{H}_2\text{O}$, C-S-H), calcium hydroxide ($\text{Ca}(\text{OH})_2$), calcium aluminate hydrates ($4\text{CaO}\cdot \text{Al}_2\text{O}_3\cdot 13\text{H}_2\text{O}$, C-A-H), etc. These hydration products have high pH value (Stegemann JA et al., 2002), such as the pH of C-S-H ranges from 9.9 to 12.3, the pH of calcium hydroxide pH ranges from 10.5 to 12.0, and the pH of C-A-H ranges from 9.8 to 12.8. The amount of hydration products increases with increasing OPC content, thus the pH of solidified samples also increases with increasing OPC content.

(2) Composite additives

(i) OPC and gypsum

OPC (5% content by weight of dredged material) and semi-hydrated gypsum (5 - 30% by weight of dredged material) were mixed with the dredged material and cured for 7 days inside a humidity-controlled chamber. Fig.1 (b) shows the change in pH of the OPC and gypsum solidified samples. For a given OPC content (5%), the pH changes slightly with gypsum content. When gypsum and OPC were added into the dredged material, the main ingredients of gypsum, calcium sulfate, and the calcium aluminates in cement react with water in the dredged material, which produce ettringite (Huang Xin et al., 1998), as shown in Equation (1).



Equation (1) shows that the amount of ettringite in the solidified samples increases with gypsum content, but some calcium aluminates in the OPC are also consumed. Thus the amount of hydration product is reduced. Equation (1) also shows that the amount of produced ettringite is similar to the amount of consumed calcium aluminates. Therefore, the pH of the solidified samples changes slightly with gypsum content.

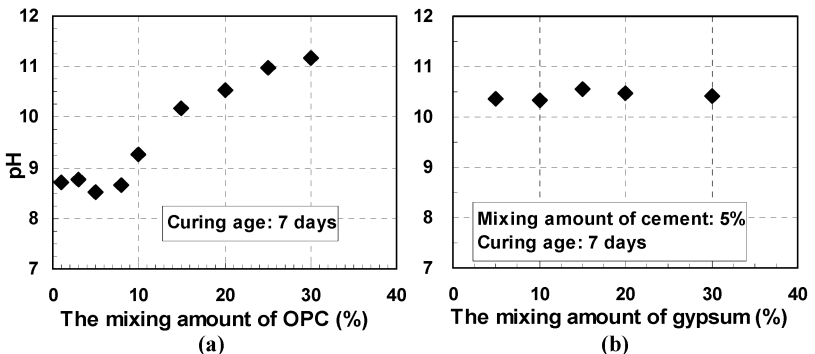
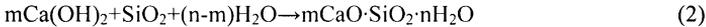


Fig.1. Change in pH for (a) OPC solidified samples; (b) OPC and gypsum

solidified samples.

(ii) OPC and fly ash

OPC (5% content by weight of dredged material) and fly ash (1 - 3.5 times of weight of OPC) were mixed with the dredged material and cured for 7 days inside a humidity-controlled chamber. Fig. 2 (a) shows the change in pH of the OPC and fly ash solidified samples. For a given OPC content (5%), the pH increases slightly with increasing fly ash content. Thus, the influence of fly ash on the pH of solidified samples is less significant. Fly ash contains active ingredient, SiO₂ and Al₂O₃, which can react with the hydration product of OPC, calcium hydroxide (Ca(OH)₂), which forms calcium silicate hydrates and calcium aluminate hydrates (Zhang Chunlei, 2003), as shown in Equations (2) and (3).



From Equations (2) and (3), the amounts of resultant C-S-H and C-A-H are similar to the amounts of consumed calcium hydroxide in solidified samples. Therefore, the pH of solidified samples increases slightly with increasing fly ash content.

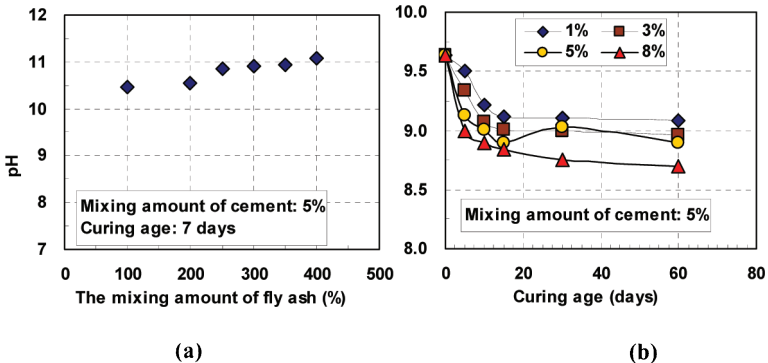


Fig. 2. (a) Change in pH for OPC and fly ash solidified samples; (b) Relationship between pH and curing time for OPC and rice straw powder solidified samples.

(iii) OPC and rice straw powder

Among the previous three additives used in the study, OPC solidified samples exhibit the highest pH value, ranging from 10.5 to 11.0. To this end, rice straw powder is chosen as an additional additive to regulate the pH of solidified soil. Fig. 2 (a) shows the effect of rice straw powder content and curing time on the OPC (5% by weight) solidified samples. The figure shows that the pH of solidified samples decreases with increasing rice straw powder content. The rice straw powder is an organic material, which is rich in a variety of physiologically active substances and nutrients (Gao Yong

heng et al., 2005). It is the process of degradation that produces CO₂, organic acids and inorganic acids and other substances and the consequence is the reduction of the pH of treated samples. Fig. 2 (b) also shows that the pH of solidified samples decreases rapidly during the initial 15 days of curing, beyond which the rate of reduction reaches a steady value. It is mainly due to the rapid rate of degradation of the rice straw powder during the early stage of curing and the amounts of CO₂ and acid produced are greater in this stage. As a result, the pH of solidified samples decreases rapidly in the early stage of curing. As time passes, the amount of rice straw powder left in the samples reduces and the decomposition has been largely completed. Thus, the decomposed rate of remaining material is more slowly and a low rate of reduction for the pH is expected.

Effect of curing time

Fig. 3 (a) shows the change in pH with curing days for OPC solidified samples. The samples were cured under exposed condition. The figure shows that the pH of the solidified samples increases to a peak value around a curing time of 3 days, beyond which the pH decreases with increasing curing time and reaches a steady value around a curing time of 28 days. The reason is that at the initial stage, with the ongoing of hydration reaction of cement, lots of hydration products with high pH value are produced. Thus the pH of solidified samples increases with time. As time passes, the hydration reaction is completed and the quantities of hydration products remain unchanged. When the solidified samples are cured under exposed condition, carbonation occurs between CO₂ and hydration product, calcium hydroxide and the quantity of hydration products is deduced (Fernández Bertos et al., 2004). Over time, a sealing layer is formed on the surface of solidified samples by carbonation to protect them from any further carbonation and the pH value can maintain a steady value.

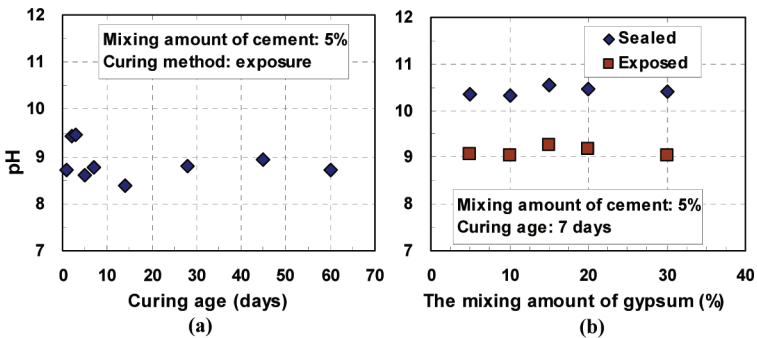


Fig. 3. (a) Change in pH with curing days for OPC solidified samples; (b) Effect of curing methods on OPC and gypsum solidified samples.

Effect of curing method

Fig. 3 (b) shows the effect of curing methods (under humidity-controlled and exposed conditions) on the OPC and gypsum solidified samples. It is seen from the figure that the pH of solidified samples cured under exposed condition is significantly lower than that cured under humid condition. A large proportion of water is lost when the samples are cured under exposed condition, thus the amount of hydration products is lower than that cured under humid condition. In addition, some hydration products are consumed by carbonation occurred between CO_2 and calcium hydroxide in the solidified samples. As a result, less amount of hydration products is left and a lower value of pH for solidified samples cured under exposed condition is expected.

CONCLUSIONS

The following conditions can be drawn from the study:

(1) The pH of cement-solidified soil is determined by the amounts of hydration products generated between the cement and water in the dredged materials. As the amount of hydration products in solidified soil increases with increasing cement content and curing time, a higher pH of solidified soil is expected.

(2) For soil treated by composite additives, the pH of solidified soil only increases slightly with the fly ash and semi-hydrated gypsum content. Hence, the composite additives may be chosen in practical engineering to control the pH of solidified soil.

(3) The pH value of solidified soil can be reduced effectively by adding rice straw powder. It is because lots of organic and inorganic acid are produced by the decomposition of rice straw powder.

(4) The pH value of solidified soil cured under exposed air condition is lower than that cured under humid condition. It is suggested that the solidified soil should be exposed to air as much as possible to reduce its pH.

REFERENCES

- Wang, C.Q., Xie, T.D., Li, B., Li, H.X., Li, T.X. and Li, S.C. (2004). "Studies on Dynamic Change of pH to Different Composition Ratio of Slope Nutrition Layer Materials." *Journal of Soil and Water Conservation*. Vol. 18 No. 6.
- Sanchez, F., Gervais, C., Garrabrants, A.C., Barna, R. and Kosson, D.S. (2002). "Leaching of inorganic contaminants from cement-based waste materials as a result of carbonation during intermittent wetting." *Waste Manage.* Vol.22: 249–260.
- Gao, Y.H. and Sun J.X. (2004). "Effects of soil amendment on the physical and chemical properties of soil for turf." *Grassland and Turf (Quarterly)*, No. 2.
- Huang, X. and Hu, T. (1998). "On stabilization of soft soil with waste gypsum and cement." *Chinese Journal of Geotechnical Engineering*. Vol.20, No.5: 72-76.
- ISO 10390: 2005. "Soil quality Determination of pH."
- Luo, Q.J. and Shi J.Z. (2005). "Silt and Ecological Dredging of the Wulihu Lake." *The Administration and Technique of Environmental Monitoring*. 15 (1) : 27-29.
- Kimura, M., Nishizawa, T., Kotera, H. And Katakura, N. (2000). "Improvement of soft ground using solidified coal ash and its effects on the marine environment." *Journal of Hazardous Materials*. 76: 285–299.

- Bertos, M.F., Simons, S.J.R. and Hills, C.D. (2004). "A review of accelerated carbonation technology in the treatment of cement-based materials and sequestration of CO₂." *Journal of Hazardous Materials*. B112193-205.
- Sweeney, R.E.H., Hills, C.D. and Buenfeld, N.R. (1999). "Acid Neutralisation Capacity of Carbonated Solidified Waste." *Imperial College of Science Technology and Medicine*. London.
- Stegemann, J.A. and Buenfeld, N. R. (2002). "Prediction of leachate pH for cement paste containing pure metal compounds." *Journal of Hazardous Materials*. B90:169-188.
- Zhang, C.L. (2003). "Research on the Mechanical Properties and Solidification Mechanism of Solidified Silt." *Master thesis*.
- Zhu, W. and Zhang, C.L. (2005). "Fundamental mechanical properties of solidified dredged marine sediment." *Journal of Zhejiang University (Engineering Science)*. Vol.39 No.10:1561-1565.

Recent Developments in Modelling THCM Behaviour of Geoenvironmental Problems

Philip Vardon¹ and Hywel Thomas²

¹Research Fellow, Geoenvironmental Research Centre, Cardiff University, The Parade, Cardiff, CF24 3AA, UK; VardonPJ@Cardiff.ac.uk

²Director, Geoenvironmental Research Centre, Cardiff University, The Parade, Cardiff, CF24 3AA, UK; ThomasHR@Cardiff.ac.uk

ABSTRACT: As part of continuing research into the Thermo-Hydro-Chemo-Mechanical (THCM) processes in porous media, a number of recent developments, undertaken at the Geoenvironmental Research Centre (GRC) at Cardiff University, are presented in this paper. These processes are of particular importance in a number of geoenvironmental problems, for example, high-level nuclear waste repositories, landfill leachate transport and carbon dioxide sequestration. In particular, the numerical modeling of large field-scale phenomena has been undertaken, with a High Performance Computing (HPC) algorithm developed to take advantage of current computational facilities, hence allowing larger and more detailed models to be undertaken in realistic timescales; a geochemical model has been included into the multi-species reactive transport THCM model. In addition, a first attempt to include biological reactions has been made. These developments are placed within the context of increasing overall understanding, building predictive capacity and impact upon assessing the overall system performance.

INTRODUCTION

Geoenvironmental problems are wide ranging and in all cases based upon flow conditions through soils and/or chemical reactions. Well known examples are high-level nuclear waste disposal, where the hydration process of the buffer material is of importance as is the long term performance of the clay barrier, in terms of containing the waste and retarding the release; landfill leachate, where reactive chemical transport processes are effected by heat, water flow, chemistry and biological processes; and carbon dioxide sequestration, where the flow of CO₂ through rocks/soils and chemical processes are key for well capacity and long term stability. In all of these examples a lack of proper understanding and management could lead to damage in the health of a human population, from the small scale of a small landfill site to global in the case of carbon dioxide sequestration. In addition, all of the examples have long timescales, from years to millennia, and are large in space, over 100m scale. A large volume of work exists internationally in this field, e.g. Thomas (2006).

Thermo-hydro-chemo-mechanical (THCM) processes have been developed into a theoretical formulation and incorporated into the numerical code COMPASS, a bespoke transient finite-element code developed at the Geoenvironmental Research Centre (GRC), at Cardiff University, and used to model a number of problems (e.g. Thomas et al., 2003, 2009a, 2009b, 2009c, Thomas and Rees, 2009). This paper describes some recent advances in the simulation of THCM phenomena.

LARGE-SCALE MODELLING

A number of geoenvironmental problems are large-scale, in both time and space as described in the introduction. In addition, the complexity of the problems considered may be high, e.g. the granitic rock that some nuclear waste repositories are likely to be located may be highly fractured, leading to preferential flowpaths; and the consideration of many chemical and biological species leads to a large number of degrees-of-freedom within a system. The numerical simulation of such problems leads to a number of problems from domain, mesh and results creation and visualisation to undertaking the analyses. Large-scale analyses may take a significant amount of time and computer memory storage requirements become large.

HIGH PERFORMANCE COMPUTING

In computationally expensive applications, such as complex or large-scale models, the investment in code development to optimise and reduce time is worthwhile. It is worth noting that computational programming techniques reflect advances and trends in computational hardware. Specifically the respective rates of change in various components affect the overall performance. In recent times, processors have become, on average, over 50% faster than the previous year, whereas interconnect bandwidth increased by approximately 25% (Hennessy and Patterson, 2007). Further to this multi-core processors are now more common and adding extra cores to processors has replaced the increase in clock-speed to increase overall processor speed (Intel, 2006).

The numerical code COMPASS is formed of two main sections which take the majority of the runtime: *the matrix build*, where the current variables are used to define the system matrices; and the *solver*, where the solution to the model variables is found. *The matrix build* section was found easy to parallelise with communication of system matrix fragments only needed at the end of the section. Good efficiencies were found in this section up to over 32 processors, depending upon the analysis size.

The *solver* section is more difficult to parallelise. There are two types of solver available in general, direct and iterative. Direct solvers are more easily parallelisable, but iterative solvers are faster in serial and require significantly lower memory, which is critical in large-scale simulations (Barrett et al., 1995). Iterative solvers demand knowledge of vectors throughout each iteration of the solver making the design of a parallel scheme more challenging (Duff and van der Vorst, 1999). The Krylov subspace type of iterative solvers are implemented for COMPASS with the BiCG variant used for THM and THCM simulations due to the non-symmetric nature of the system matrix.

A previous parallel implementation was found to be ineffective on modern HPC systems (Vardon et al., 2008) and this was determined to be due to the relative increase in speed of the processors over the latency and bandwidth of the interconnect. The most

common modern HPC machine architecture comprises a number of individual nodes connected together with a high performance interconnect with individual nodes made up from a number of multi-core processors with access to a single block of memory. Reflecting this, a new HPC algorithm was proposed. Recognising the Krylov subspace solvers are formed from a number of vector-vector operations, usually dot-products, and either one or two matrix-vector multiplications, the new algorithm formulates the vector-vector operations to be parallelised ‘on-node’ using the memory as shared-memory, thereby eliminating communication costs. The matrix-vector multiplications were split across nodes, using a multi-threaded operation on-node and message-passing across nodes, reducing the communication required in proportion to the number of processing cores.

Results are presented, in figure 1, for two example THM problems with 100,000 and 350,000 elements undertaken on the Merlin HPC system located at Cardiff University, based upon 3.0GHz Intel quad core processors, arranged with two per node, and a 20Gb InfiniBand interconnect. The results show good performance increase as the number of cores increases. With 100,000 elements the communication effects can be seen clearly when moving from lines representing fewer nodes to those representing more. In the 350,000 element problem (Figure 1b) some effects of shared-bus saturation are seen making the pattern slightly more complex, although with the same overall trends of increasing cores and reducing time. Further details are provided in Vardon et al. (2009) and Vardon (2009).

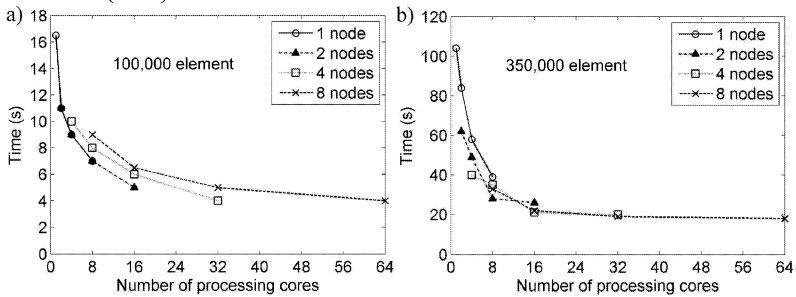


FIG. 1. Results from example THM simulations using the new parallel implementation undertaken on the Merlin HPC system.

SIMULATION OF THE PROTOTYPE REPOSITORY PROJECT

The Prototype Repository Project (PRP) is a real-scale mock-up of a High Level Nuclear Waste (HLW) repository, featuring all aspects of the KBS-3 (SKB, 2003) conceptual design, with the exception of the HLW whose effect is simulated by the use of heaters embedded within the canisters. The PRP comprises a repository tunnel, six deposition-holes split into two sections. Copper canisters with heaters embedded are installed into the deposition-holes with a highly-compacted bentonite clay buffer surrounding them. The repository tunnel is then backfilled with a mixture of crushed spoil rock and bentonite. A large quantity of data has been collected at various stages. The PRP, as many countries intend for the final repositories, is situated in highly fractured granitic rock. This may, as in the case of the PRP, cause highly anisotropic

flow conditions, and along with the repository shape and processes occurring are implicitly three-dimensional.

Two main phases have been simulated, the pre-placement stage, where the tunnel and deposition-holes have been excavated and the post-placement phase where the canisters and buffer material has been installed. The pre-placement stage is useful to see if the rock domain and modelling techniques are able to simulate the flow condition and the post-placement stage includes the buffer material whose saturation behaviour is critical to the performance of the engineered barrier system and overall repository safety.

The rock domain has been formed from an effective continuum model, including a number of deterministic fractures, with idealised shapes, that were found during hydraulic borehole tests. Two major fractures, radius 20m, and six minor fractures, radius 2m, were included. Some calibration was undertaken and the results were found to be able to represent recorded inflow results, both into the deposition-holes and along the tunnel, which a continuum model without deterministic fractures was not able to do. The inflow results along the tunnel length are shown in figure 2 highlighting the model ability to simulate anisotropic flow conditions. The post-placement conditions have also been simulated and the anisotropic flow conditions in the rock domain allow the differing rate of buffer saturation in separate deposition-holes is able to be simulated. The backfill is also saturated in a similar time to the experimental results, which is not the case if using an effective continuum. More results and details can be found in Vardon (2009).

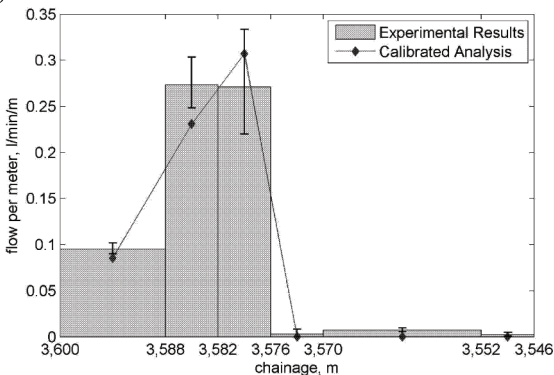


FIG. 2. Numerical and experimental inflow results into the PRP along the tunnel length including the range of experimental results.

GEOCHEMICAL AND BIOLOGICAL PROCESSES

Geochemical and biological processes affect the transport of chemicals and stability and the host geomaterial. For example, landfill leachate introduces chemicals into the surrounding geomaterial which react with this material and in general conservative transport equations are unable to predict chemical breakthrough. Geochemical and biological processes are also important in CO₂ sequestration where the carbon can be sorbed geochemically to soil minerals. Geochemical processes are included into the COMPASS and a first attempt at the inclusion of biological processes has been made.

The inclusion of geochemical and biological processes into the existing THCM model is undertaken following the algorithm presented in figure 3. The conservative transport equation formulation inclusive of a sink/source term to allow for adsorption and precipitation/dissolution and the impact of biological processes. A geochemical model, namely MINTEQA2 (Allison et al., 1991), has been linked to the THCM model and is able to calculate equilibrium reactions among dissolved, solid and gas phases and incorporates a large thermodynamic database. The integration of the chemical and geochemical model to COMPASS is described by Cleall et al. (2007).

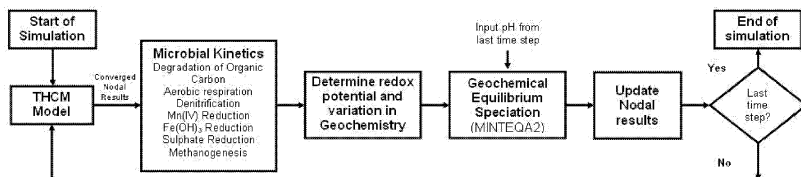


FIG. 3. The COMPASS THCM algorithm.

Microbial activity is treated, as a first estimate, as a macroscopically averaged quantity. A supply of dissolved organic carbon is required as is an appropriate redox pair. Two half-step reactions have been employed, with the first, the biological reaction, limiting the rate of reaction and the second based on inorganic equilibrium. The resultant chemical change from microbial activity is calculated post the conservative THCM calculation and prior to geochemical equilibrium. Further details of the biological model can be found in Thomas and Seetharam (2009).

CONCLUSIONS

To extend the ability to simulate Thermo-Hydro-Chemical-Mechanical (THCM) processes a number of advancements have been made. A High Performance Computing (HPC) algorithm has been designed and implemented to enable large-scale modelling, in scale, time and complexity to be undertaken. An example of the Prototype Repository Project has been shown to highlight the importance of this ability. In addition, geochemical soil interactions have been included and a first estimate of the geobiological processes has been included within the model.

ACKNOWLEDGMENTS

The support of Dr Suresh Seetharam and Dr Peter Cleall throughout much of this work is gratefully acknowledged. Access to high quality experimental results from SKB's large scale experiments was very gratefully received and the use of High Performance Computing facilities at the Advanced Research Computing @ Cardiff (ARCCA) department of Cardiff University is recognised.

REFERENCES

Allison, J.D., Brown, D.S. and Novo-Gradac, K.J. (1991). *MINTEQA2/PRODEFA2, A geochemical assessment model for environmental systems: version 3.0 user's manual.*

Environmental Research Laboratory, US EPA, Georgia.

- Barrett, R., Berry, M., Chan, T., Demmel, T., Donato, J., Dongraa, L., Eijkhout, V., Pozo, R., Romine, C., and Van der Vorst, H. (1995). *Templates, for the solution of linear systems: building blocks for iterative methods*. John Wiley Press, New York.
- Cleall, P.J., Seetharam, S.C. and Thomas, H.R. (2007). "Inclusion of some aspects of chemical behaviour of unsaturated soil in thermo/hydro/chemical/mechanical models. I: Model development." *ASCE Journal of Engineering Mechanics*, Vol. 133 (3): 338-347.
- Duff, I. S., and van der Vorst, H. A. (1999). *Developments and trends in the parallel solution of Linear Systems*. CERFACS, Technical Report TR/PA/99/10.
- Hennessy, J. and Patterson, D. (2007). *Computer Architecture: A Quantitative Approach*, 4th edition, Morgan Kaufman, San Francisco.
- Intel. (2006). *White paper - Intel architecture and silicon cadence. The catalyst for industry innovation*.
- SKB (2003). *Deep repository for spent nuclear fuel*. SKB, Stockholm.
- Thomas, H.R. (ed.) (2006). *5th ICEG Environmental Geotechnics, opportunities, challenges and responsibilities for environmental geotechnics*. Thomas Telford, London, 823 p.
- Thomas, H.R., Cleall, P.J., Chandler, N., Dixon, D. and Mitchell, H.P. (2003). "Water infiltration into a large scale in-situ experiment in an underground research laboratory - physical measurements and numerical simulation." *Géotechnique*, Vol. 53 (2): 207-224.
- Thomas, H.R., Cleall, P.J., Dixon, D. and Mitchell, H.P. (2009a). "The Coupled Thermal-Hydraulic-Mechanical Behaviour of a Large Scale In-Situ Heating Experiment." *Géotechnique*, Vol. 59 (4): 401-413.
- Thomas, H.R., Cleall, P.J., Li, Y., Harris, C. and Kern-Luetschg, M. (2009b) "Modelling of cryogenic processes in permafrost and seasonally frozen soils." *Géotechnique*, Vol. 59(3): 173-184.
- Thomas, H.R. and Seetharam, S.C. (2009). "On the inclusion of some biological impacts and influences in coupled transport phenomena in unsaturated soil." *Proceedings of the 12th International Conference of the International Association for Computer Methods and Advances in Geomechanics*, Goa, 2172-2180.
- Thomas, H.R. and Rees, S.W. (2009) "Measured and simulated heat transfer to foundation soils." *Géotechnique*, Vol. 59(4): 365-375.
- Thomas, H. R., Siddiqua, S., and Seetharam, S. C. (2009c) "Inclusion of higher temperature effects in a soil behaviour model." *Géotechnique*, Vol. 53(3): 279-282.
- Vardon, P.J. (2009). *A three-dimensional numerical investigation of the thermo-hydro-mechanical behaviour of a large-scale prototype repository*. Ph.D. thesis, Cardiff School of Engineering, Cardiff University, UK.
- Vardon, P.J., Cleall, P.J., Thomas, H.R. and Philp, R. (2008). "Three-dimensional field-scale coupled thermo-hydro-mechanical modelling." *Proceedings of the 12th International Conference of the International Association for Computer Methods and Advances in Geomechanics*, Goa, 2419-2425.
- Vardon, P.J., Banicescu, I., Cleall, P.J., Thomas, H.R. and Philp, R.N. (2009). "Coupled thermo-hydro-mechanical modelling: A new parallel approach." *Proceedings of the PDSEC-09 workshop of IEEE IPDPS 2009 conference, Rome*.

Field Test of a Geothermal System in HafenCity Hamburg

X. Ma¹, J. Grabe²

¹Institute for Geotechnics and Construction Management, Hamburg University of Technology, Harburger Schlosstr. 20, 21079 Hamburg, Germany; xiaolong.ma@tuhh.de

²Director of Institute for Geotechnics and Construction Management, Hamburg University of Technology, Harburger Schlosstr. 20, 21079 Hamburg, Germany; grabe@tuhh.de

ABSTRACT: Geothermal Energy is available all over the world and plays an increasing role in the renewable energy supplies, especially in the space heating and cooling sector. Within a research project of Hamburg University of Technology, a shallow geothermal energy system is combined with a desiccant assisted air conditioning system. In this research project, 3 borehole exchangers and 5 energy piles were built in Hamburg's harbor area and supply heating and cooling for the new air conditioning system. Numerical modeling and analytical method was used to estimate the extraction rate of the energy piles. The results of field test in the summer 2009 will be shown in this paper.

INTRODUCTION

In Germany, the temperatures of soils and groundwater up to 100 m are constantly between 8.5 °C and 12 °C. As this temperature is relatively stable over the whole year, it gives rise to the opportunity of heat extraction for environmental and economical heating and cooling. Several variations of heat exchangers in the ground such as ground heat collectors, borehole heat exchangers and thermo-active ground structures have been installed worldwide over the past 20 years (Lund et al., 2004). In a research project of the Hamburg University of Technology, a pilot plant of shallow geothermal energy and desiccant assisted air conditioning has been built and will be tested in 2009 and 2010.

The test site has a base area of 460 m². It is equipped with 8 soil heat exchangers consisting of 5 energy piles and 3 borehole heat exchangers. Energy piles are one of the most commonly employed thermo-active underground structures (Bandl, 2006 and Katzenbach et al., 2008). Piles, which are required as building foundations, are assembled with plastic U-tubes (seldomly with metallic tubes) and then filled with a heat transfer medium. During circulation of the heat transfer medium in the U-tubes, heat can be extracted or discharged from/into the ground. The double usage of piles enables a cost reduction during manufacturing. Borehole heat exchangers are not statically required and are therefore flexible in performance.

CONSTRUCTION OF THE GEOTHERMAL SYSTEM

The pilot plant is located in a newly created metropolitan area, the “HafenCity Hamburg”, near the center of Hamburg. The geothermal system comprising 8 soil heat exchangers supplies cooling energy for the desiccant air conditioning system. Above the ground level, there are 7 construction containers in three of which the air conditioning system and the cold and heat distribution system are installed. The other four containers act as office space, which is cooled by the geothermal energy. The office containers are constructed to keep the standard of the German regulation for energy savings in buildings and building systems (DIN 4108-2).

Four of the five energy piles are arranged under the corner points of the containers (FIG. 1). The other one is located at the center.

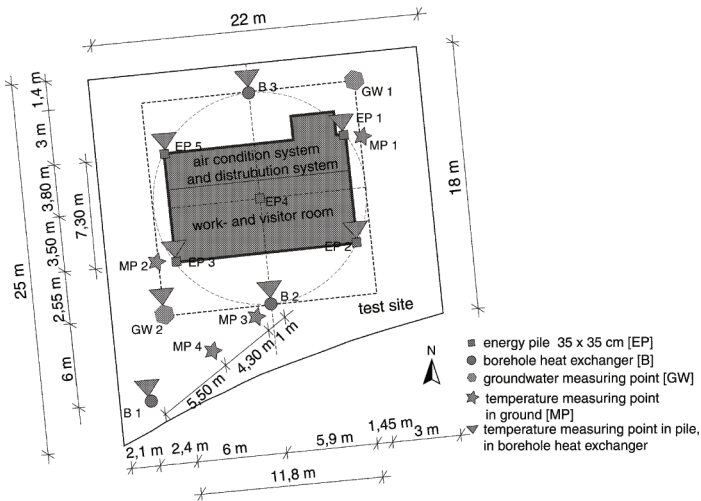


FIG. 1. Site plan of the geothermal system.

The energy piles are precast concrete piles. The U-tubes as well as the temperature probes are fixed directly onto the reinforcement cage. Around these a 4 cm concrete covering protects both the reinforcement cage and the U-tubes. After being concreted they were transported to the test site and driven into underground.

In a standard energy pile 2 loops of U-tubes are assembled. As a variation 3 loops of U-Tubes are embedded into two of the five test energy piles (Table 1).

Both the beginning of the feeding tube and the end of the return tube, between which the maximum temperature difference exists, stand at the top of the piles. In order to reduce the undesirable heat transfer between these, thermal insulation is installed on the last meter of the return tubes.

The advantage of a precast concrete pile is that the quality of the pile can be guaranteed, especially at the pre-installation of U-tubes and temperature probes. The

disadvantage is the potential noise and swinging emissions during pile-driving.

The holes for the borehole heat exchangers were drilled using hydraulic-circulation drilling method. Double-U-tubes are plugged, after that the final depth of the borehole is attained. To avoid undesired heat transfer between the U-tubes, spacers are used every 2-3 meters. The boreholes are filled with a cement-clay mixture, which has a thermal conductivity of 2 W/(m·K).

Table 1: Configuration of the 5 energy piles

Pile number	Number of U-tube loops	Thermal insulation on U-tubes at the pile head	Temperature measurement
1	2	Yes	-0.5, -4.5, -12.5 m
2	3	No	-0.5, -4.5, -8.5, 12.5 m
3	3	Yes	-0.5, -8.5 m
4	2	No	No
5	2	No	-0.5, -4.5, -8.5, -12.5 m

CALCULATED AND ESTIMATED SPECIFIC COOLING CAPACITY

Heat transport of the installed energy piles has been calculated using the finite-element- method to obtain the specific cooling capacity (Ma and Grabe, 2009). The subsoil in the numerical models was assumed to be homogenous and to have a thermal conductivity of 2.53 W/(m·°C) and an undisturbed temperature of 10 C. FIG. 2 shows the calculated time-dependent specific cooling capacity (P_s) of one energy pile over a period of 90 days. The specific cooling capacity is large at the beginning of the operation and tends to a constant value of ca. 37 W/m after 90 days, which can be regarded as the quasi steady-state value. The average specific cooling capacity amounts to 42 W/m.

The specific cooling capacity at a steady-flux state can also be calculated analytically with the equation:

$$P_s = (T_f - T_m) \times R_{sf}, \tag{1}$$

where T_f is the average fluid temperature and T_m is the average ground temperature. The steady-flux thermal resistance for a double U-tube soil heat exchanger is defined (Hellström, 1991) as:

$$R_{sf} = \frac{1}{2\pi\lambda} \left[\ln\left(\frac{r_1}{r_{po}}\right) - \frac{3}{4} - b^2 - \frac{1}{4} \ln(1 - b^8) - \frac{1}{2} \ln\left(\frac{\sqrt{r}br_1}{r_{po}}\right) - \frac{1}{4} \ln\left(\frac{2br_1}{r_{po}}\right) \right] + \frac{R_b}{4}, \tag{2}$$

$$R_{po} \ll r_1 \quad B_u > 3r_{po} \quad r_{po} < (1 - b)r_1$$

where r_1 is the radius of ground region affected by soil heat exchanger, r_{po} is the outer tube radius, B_u is the distance between tubes and λ is the thermal conductivity of the soil. The eccentricity parameter b is given by:

$$b = \frac{B_u}{2r_1}. \tag{3}$$

The fluid-to-ground thermal resistance R_b of a tube consists of three parts:

- convective heat transfer resistance R_{fc} between the bulk fluid and the inner surface of the tube,

- thermal resistance R_p' of the tube wall and
- contact resistance R_c at the interface between the tube and the surrounding soil.

So R_b can be written as:

$$R_b = R_{fc} + R_p' + R_c \tag{4}$$

$$= \frac{1}{\pi \lambda_f Nu} + \frac{1}{2\pi \lambda_p} \ln\left(\frac{r_{po}}{r_{pi}}\right) + \frac{1}{2\pi \lambda_s} \frac{\delta_s}{r_{po}}$$

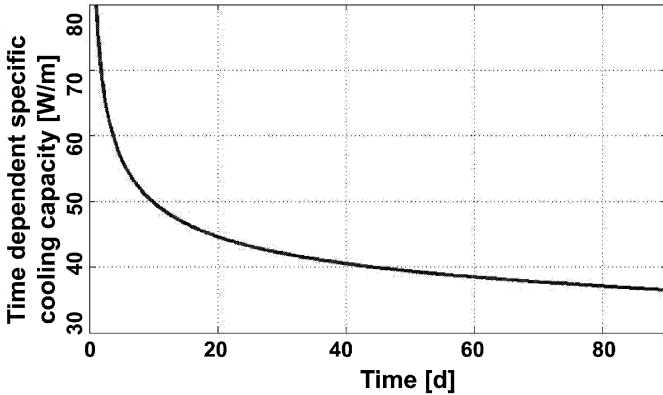


FIG. 2. Numerically calculated time-dependent specific cooling capacity over a period of 90 days.

Here, λ_f , λ_p and λ_s are the thermal conductivities of the heat transfer fluid, tube wall and material that fills the gap between the tube and the surrounding soil. The characteristic width of the gap is denoted δ_s , r_{po} and r_{pi} are the outer and inner radius of the tube. The Nusselt's number Nu is defined by:

$$Nu = \frac{\alpha \cdot 2r_{pi}}{\lambda_f} \tag{5}$$

where α is the heat transfer coefficient ($W/m^2 \cdot K$). Flow in the tube is assumed laminar giving rise to a Nusselt's number of 4.36 for uniform surface heat flux (Incropera and DeWitt, 2002).

Table 2: Analytical calculation of specific cooling capacity of energy piles

Parameter		Value	Unit
Radius of affected soil	r_l	5	m
Outer radius of tube	r_{po}	0.01	m
Inner radius of tube	r_{pi}	0.0081	m
Distance between tubes	B_u	0.025	m
Thermal conductivity of fluid	λ_f	0.5	W/(m·K)
Thermal conductivity of tube	λ_p	0.4	W/(m·K)

Thermal conductivity of gap	λ_s	∞	W/(m·K)
Thermal conductivity of soil	λ	2.53	W/(m·K)
Average fluid temperature	T_f	19.5	°C
Average soil temperature	T_m	12	°C
Fluid-to-ground thermal resistance	R_b	0.157	(m·K)/W
Steady-flux thermal resistance	R_{sf}	0.228	(m·K)/W
Specific cooling capacity	P_s	33	W/m

According to analytical calculation the specific cooling capacity at steady-flux-state amounts to 33 W/m, which matches the quasi steady-state value of numerical simulation (37 W/m) very well.

The specific cooling capacity for borehole heat exchangers is estimated according to VDI-Guideline (VDI 4640-2, 2001) and the survey of the test site (FIG. 3).

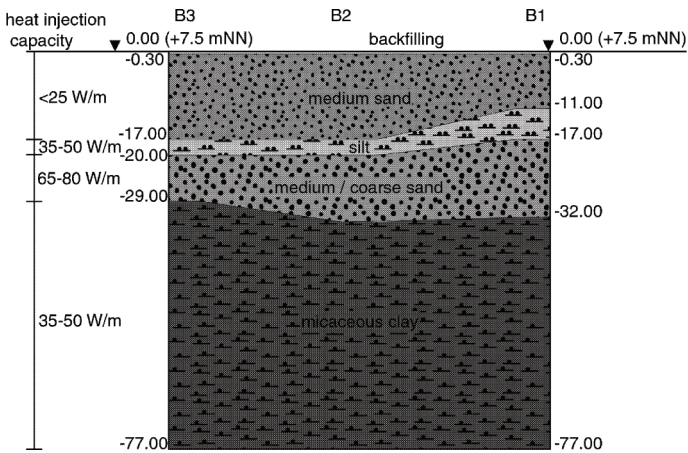


FIG. 3. Soil buildup of the test site and specific cooling capacity of borehole heat exchangers according to VDI 4640-2 (cross section B1-B2-B3).

MEASUREMENT RESULTS

The injected heat into the underground (E) is calculated using the difference between inlet and outlet temperatures (ϑ_i, ϑ_o) of the heat transfer medium:

$$E = \int \rho_{htm} A v_{htm} c_{htm} (\vartheta_i - \vartheta_o(t)) dt \tag{6}$$

where A is the inner cross section of the U-tubes, ρ_{htm} , v_{htm} , and c_{htm} are the density, flow velocity and specific heat capacity of heat transfer medium. The analyzed specific cooling capacity (SCC) of each soil heat exchanger is a daily average, since it is considered to be a better indicator of the long-term evolution than instantaneous values (Wood et al., 2009).

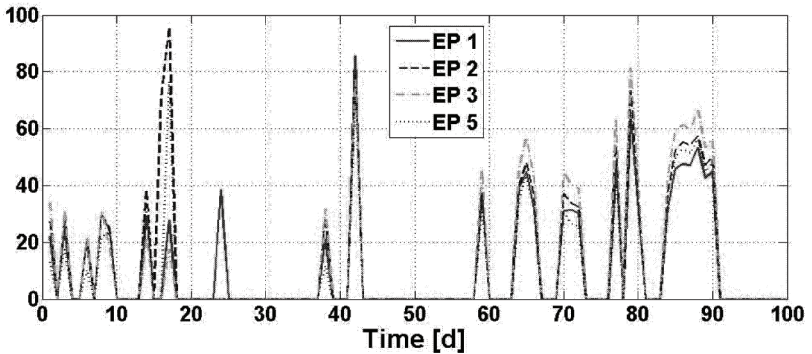


FIG. 4. Daily specific cooling capacity of energy piles (EP).

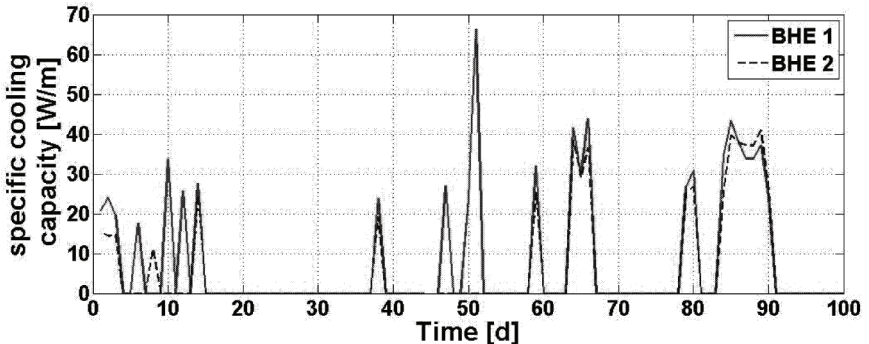


FIG. 5. Daily specific cooling capacity of borehole heat exchangers (BHE).

FIG. 4 and 5 show the daily average specific cooling capacity (SCC) of energy piles (EP) and borehole heat exchangers (BHE) from July 01. to Oct. 04. 2009. BHE 3 was not in use this summer since the heat load was not very high. The daily SCC is heavily dependent on the operational parameters, (such as daily operation time, heat load of the building, mass flow rate and inlet temperature of heat transfer medium) and is therefore not constant during the operation. The peak capacity of EP and BHE can be over 90 and 60 W/m respectively. Because of irregular maintenance and optimization work the pilot plant has only been in use for several days. The total operation time of EP and BHE only amounts to about 90 and 70 hours (Table 3). The injected energy is insufficient for overheating of the subsoil to occur. As a result a reduction of specific cooling capacity with time was not detected.

The average SCC of EP over the whole operation time is about 40 W/m, which compares to the numerically calculated value of 42 W/m very well (Table 3). The borehole heat exchangers have a relative lower SCC value of about 30 W/m, which is even lower than the recommended specific heat capacity (SHC) in clay (35-50 W/m). The reason for the low SCC value may be attributed to the low average flow velocity of

the heat transfer medium in the U-tubes (0.22 m/s, Table 3) and the small horizontal distance between each tube.

Table 3: Summarization of the energy piles and borehole heat exchangers

heat exchanger	EP 1	EP 2	EP 3	EP 4	EP 5	BHE 1	BHE 2
flow velocity of HTM (m/s)	0.31	0.31	0.31	0.32	0.31	0.22	0.22
injected energy [kWh]	46.2	53.7	56.3	55.5	44.7	167.8	155.7
energy consume of pumps [kWh]	2.5	2.8	2.8	2.8	2.1	1.6	1.4
total operation time [h]	94.3	93.5	93	92	92.8	74.7	70.7
length of heat exchanger [m]	14	14	14	14	14	75	75
injection capacity [kW]	0.49	0.57	0.61	0.60	0.48	2.25	2.20
specific injection capacity [W/m]	35.0	41.0	43.2	43.1	34.4	30.0	29.4
cooling performance factor (CPF) [-]	18.4	19.4	20.4	19.8	21.7	107.8	110.2

It can be seen, that EP 2 and 3 have a larger SCC than that of EP 1 and 5. The reason being that in EP 2 and 3 three loops of U-tube were installed, which increase the heat transfer area between heat transfer medium and the subsoil and therefore the heat transfer velocity. EP 4 also has a high SCC value, which can be ascribed to its beneficial location. It lies in the shade of the office container and its top most meters are least affected by the temperature change of the atmosphere, which is higher than the temperature of the subsoil in summer.

In EP 1 and 3 the last meter of the tubes is heat insulated. Compared with EP 5 and EP 2, their SCC is larger. Although the increasing factor only amounts to 1.7% for EP 1 and 5.4% for EP 3 and can thus be neglected.

The geothermal energy is available all over the world, but it is not free for use. In our system, circulation pumps are needed to transfer the heat from the air conditioning system to the subsoil. Heat can then be injected into the underground, while pumps simultaneously consume electrical energy. To evaluate the efficiency of the geothermal system the cooling performance factor (CPF), analogous to the seasonal performance factor of the heat pump, is introduced in this paper. It is defined as:

$$CPF = \frac{\text{injected energy through geothermal system}}{\text{energy consumption of circulation pump}} \tag{7}$$

The CPF of energy piles is about 20. Borehole heat exchangers obviously have a higher CPF value of about 110. This means that the BHE only need about 1/5 of the energy for the same energy output of EP. The reason being, that the U-tubes in BHE have a larger diameter (40 mm) than those in EP (20 mm) and therefore the hydraulic resistance in BHE is correspondingly smaller leading to a smaller SCC value.

CONCLUSIONS AND OUTLOOKS

The specific cooling capacity of soil heat exchangers depends on several parameters and is not trivial to estimate accurately. The measurements in HafenCity Hamburg show

that EP can supply an average SCC value of about 40 W/m which matches the numerically calculated value very well. The installation of the third U-tube loop in EP can increase the heat transfer of the EP system and therefore the SCC up to 23%. Heat insulation in the final meter of U-tubes in EP has not proven advantageous. The BHE point a lower SCC but a better CPF value compared to EP.

The measurements will be continued this winter and next summer. More variations will be carried out to get detailed information about the relationship between SCC and its dependent parameters. The long term temperature development of the subsoil around the soil heat exchangers will also be investigated. Further, numerical simulations with in-situ soil characters and varied boundary conditions are planned to investigate the thermodynamic reaction of EP and BHE systems under other conditions.

REFERENCES

- Brandl, H. (2006). "Energy Foundations and Other Thermo-Active Ground Structures." *Géotechnique*, Vol. 56(2): 81-122.
- DIN 4108-2 (2003). "Thermal Protection and Energy Economy in Buildings Part 2: Minimum Requirements to Thermal Insulation." *German Institute for Standardization*.
- Hellström, G. (1991). "Thermal Analysis of Duct Storage Systems – I. Theory." *Ground Heat Storage*, University of Lund, Sweden.
- Incropera, F.P. and DeWitt, D.P. (2002). "Fundamentals of heat and mass transfer." 5th Edition, Wiley, New York.
- Katzenbach, R., Vogler, M. and Waberseck, T. (2008). "Large energy pile systems in urban areas." *Bauingenieur*, Vol. 83: 343-348.
- Lund, J., Sanner, B., Rybach, L., Curtis, R. and Hellström, G. (2004). "Geothermal (Ground-Source) Heat Pumps a World Overview." *GHC Bulletin*, Vol. 25(3).
- Ma, X. and Grabe, J. (2009). "Influence of groundwater flow on efficiency of energy Piles." *Proc. of Int. Conf. on Deep Foundations - CPRF and Energy Piles*, Frankfurt.
- VDI 4640-2. (2001). "Thermal Use of the Underground – Ground source heat pump systems." Part 2. VDI-Guideline.
- Wood, C.J., Liu, H. and Riffat, S.B. "Use of Energy piles in a Residential Building, and Effects on Ground Temperature and Heat Pump Efficiency." *Géotechnique*, Vol. 59(3): 287-290.

Bioremediation of Heavy Metals in Soil and Groundwater: Impact of Nitrate as an Inhibitor

Qiang He¹, and Jizhong Zhou²

¹Assistant Professor, Department of Civil and Environmental Engineering, University of Tennessee, Knoxville, TN 37996; qianghe@utk.edu

²Professor, Department of Botany and Microbiology, University of Oklahoma, Norman, OK 73019; zhouj@ou.edu

ABSTRACT: Sulfate-reducing bacteria are studied for their potential in heavy metal bioremediation. However, the occurrence of elevated nitrate in contaminated environments has been shown to inhibit sulfate reduction activity. While the inhibition has been suggested to result from competition with nitrate-reducing bacteria, the possibility of direct inhibition of sulfate reducers by elevated nitrate needs to be explored. Using *Desulfovibrio vulgaris* as a model sulfate-reducing bacterium, functional genomics analysis reveals that osmotic stress contributed to growth inhibition by nitrate as demonstrated by the up-regulation of the glycine/betaine transporter genes and the relief of nitrate inhibition by osmoprotectant. The observation that significant growth inhibition was effected by 70 mM NaNO₃ but not 70 mM NaCl suggests the presence of inhibitory mechanisms in addition to osmotic stress. The differential expression of genes characteristic of nitrite stress responses under nitrate stress condition further indicates that nitrate stress response by *D. vulgaris* was linked to components of both osmotic and nitrite stress responses. The involvement of the oxidative stress response pathway, however, might be the result of a more general stress response. Given the low similarities between the response profiles to nitrate and other stresses, less defined stress response pathways could also be important in nitrate stress, which might involve the shift in energy metabolism.

INTRODUCTION

Exploiting microbially-mediated reduction of redox-sensitive metals has been proposed as a promising strategy to remediate metal-contaminated subsurface environments *in situ* (Gadd and White 1993; Valls and de Lorenzo 2002). With the ability to reduce and accumulate heavy metals and radionuclides (Chardin et al. 2002; Jones et al. 1976; Lovley et al. 1993a), sulfate-reducing bacteria (SRB) have drawn particular attention for potential applications in heavy metal immobilization. It has been well documented that SRB can reductively precipitate redox metals through enzymatic pathways (Abdelouas et al. 1998; Lovley and Phillips 1992a; Lovley and

Phillips 1992b) or can simply precipitate metals as metallic sulfides. Enzymatic reduction of soluble metal oxyanions to insoluble forms has been specifically demonstrated for *Desulfovibrio* spp. (Lloyd et al. 1999; Lovley and Phillips 1992b; Lovley et al. 1993b; Payne et al. 2002), which are the model SRB most extensively studied for their bioremediation capacity. More importantly, SRB populations are also found to be significant members of microbial communities involved in such metal reduction and are ubiquitous even in extreme environments (Bagwell et al. 2006; Chang et al. 2001; Fields et al. 2006; Gillan et al. 2005; Odom 1993; Widdle 1988). Therefore, stimulation of SRB activities has been considered as a useful approach for the immobilization of heavy metals and radionuclides (Landa 2005; Lloyd and Lovley 2001; Lloyd and Renshaw 2005; Wang et al. 2003).

To exploit SRB effectively for the remediation of heavy metal and radionuclide contaminated sites, it is important to understand the microbial responses to adverse environmental factors commonly encountered in these subsurface environments. One such factor is the high nitrate concentration of many contaminated sites at the U.S. nuclear weapon complexes managed by the Department of Energy (NABIR 2003; Riley and Zachara 1992). The presence of nitrate may pose a specific stress to SRB as nitrate has been observed to suppress sulfate reduction activity *in situ* (Davidova et al. 2001; Jenneman et al. 1986). Thus, it is important to examine the responses of sulfate-reducing microorganisms in metabolic and regulatory pathways following nitrate exposure to understand their defense mechanisms. Such knowledge would facilitate the development of strategies to monitor and predict the performance of these microorganisms in bioremediation (Hazen and Stahl 2006).

In this report, we used *Desulfovibrio vulgaris* Hildenborough as a model organism to investigate the inhibition of sulfate reduction by nitrate as compared to other related stress conditions. This bacterium lacks the ability to reduce nitrate which makes an inhibition by nitrate obscure. Our results from functional genomics analyses indicate the presence of inhibitory mechanisms in addition to the expected osmotic stress responses.

MATERIALS AND METHODS

Monitoring of cell growth under stress conditions

The growth response of *D. vulgaris* cells to various concentrations of sodium nitrate (NaNO_3) or sodium chloride (NaCl) were monitored using the Phenotype MicroArray™ platform (Biolog Inc., Hayward, CA). Culture handling and instrument operation were carried out in an anaerobic chamber with an atmosphere of 5% CO_2 , 5% H_2 , and 90% N_2 . Mid-log phase *D. vulgaris* cultures were obtained as inocula by growing *D. vulgaris* cells in a defined lactate-sulfate (LS4D) medium (Mukhopadhyay et al. 2006) at 30°C to an OD_{600} of 0.3-0.4, corresponding to approximately 10^8 cells/ml. Growth monitoring and culture incubation at 30°C was performed by the OmniLog instrument.

Biomass production for molecular analysis

Cultures for biomass production were initiated with 10 % (v/v) inocula from stocks of *D. vulgaris* frozen at -80° C (fully grown cells in LS4D with 10% (v/v) glycerol)

into LS4D medium (Mukhopadhyay et al. 2006). Absence of obvious contaminants was verified by microscopic inspection and lack of fast growing aerobes by spreading samples on aerobic tryptic soy agar plates at 30°C when the subcultures reached mid-log phase. Subsequently, 2-liter production cultures were inoculated with 10% (v/v) active subculture. All production cultures were grown in triplicate (three control cultures and three stressed cultures). When the production cultures reached an OD₆₀₀ of 0.3, 50 ml were taken from each replicate culture as the T0 samples. Once the T0 samples were taken, degassed NaNO₃ solution was immediately added to the three treatment cultures to a final concentration of 105 mM (6500 ppm nitrate, which was shown to inhibit the growth rate of the log-phase cultures by approximately 50%), and an equivalent volume of sterile, distilled, degassed water was added to each control culture.

Microarray transcriptomic analysis

A previously described whole-genome oligonucleotide DNA microarray (He et al. 2006), covering more than 98.6% of the annotated protein-coding sequences of the *D. vulgaris* genome, was used for global transcriptional analysis of nitrate stress response. The accuracy of the microarrays in global transcriptional profiling has been extensively tested and validated in previous studies on stress response pathways in *D. vulgaris* (Clark et al. 2006; He et al. 2006). All microarray procedures including the extraction and labeling of nucleic acids, microarray hybridization and washing, and data analysis were performed using previously published protocols (He et al. 2006; Mukhopadhyay et al. 2006). Pairwise correlation coefficients between any two transcriptional profiles were computed with the centered Pearson correlation using the entire transcriptional expression profiles obtained by the *D. vulgaris* microarray. Color heat map representations comparing gene expression under various growth conditions were generated using the software JColorGrid (Joachimiak et al. 2006).

RESULTS

Growth inhibition of *D. vulgaris* by nitrate

The inhibitory effect of nitrate was evaluated by monitoring the growth of *D. vulgaris* in the presence of various concentrations of sodium nitrate. While a slow-growth phase (with no detectable growth) of approximately 20 hours was observed in control cultures without nitrate addition, an extended phase of slow growth followed by normal growth was observed with increasing concentrations of nitrate in the culture medium, indicative of a moderate inhibitory effect (Figure 1A). A more severe inhibition pattern, characterized by a sharp decrease in growth rate accompanied by an increasingly longer slow-growth phase, was apparent when the nitrate concentration reached 70 mM, as indicated by the reduced slope of the growth curve (Figure 1A).

Since sodium nitrate is an ionic solute, high concentrations of nitrate are expected to result in osmotic stress as a non-specific inhibitory mechanism. To identify any inhibitory effects specific to nitrate, a comparison was made between the growth responses of *D. vulgaris* to sodium nitrate versus sodium chloride, known to cause osmotic stress. In sharp contrast to the 70 mM sodium nitrate addition needed for growth inhibition, a significant decrease in the growth rate of *D. vulgaris* was

observed only when 200 mM sodium chloride was added into the LS4D medium (Figure 1B). These results suggest that sodium nitrate inhibition results from at least some interactions specific to nitrate and not simply from a salt-induced osmotic effect.

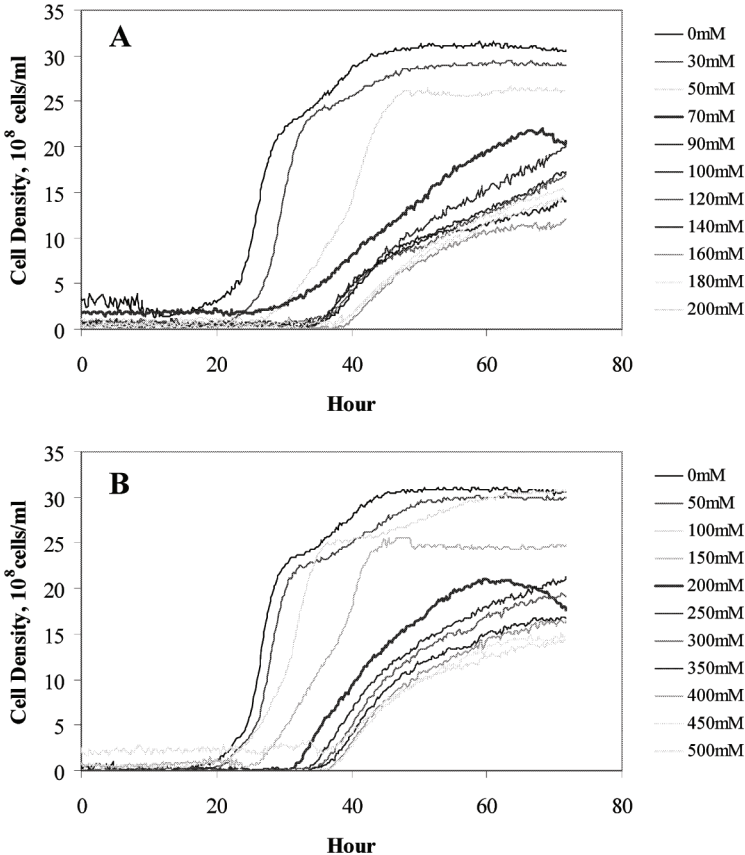


FIG. 1. Growth response of *Desulfovibrio vulgaris* to varying concentrations of (A) NaNO₃ or (B) NaCl.

Global transcriptomic analysis of nitrate stress

To understand the mechanisms of nitrate inhibition and the potential response pathways used by *D. vulgaris* cells to alleviate nitrate stress, microarray experiments were carried out to compare global gene expression profiles between nitrate-stressed *D. vulgaris* cultures and control cultures without nitrate exposure. *D. vulgaris* cells were challenged by a nitrate level of 105 mM, which was effective in inhibiting, but

not eliminating, cell growth in log-phase cultures.

Changes in the gene expression profile were observed at 30 min following nitrate exposure and peaked at 120 min, with 298 genes being differentially expressed, either up or down, greater than two fold (Figure 2). A similar number of genes (288) remained differentially regulated at 240 min. It is noted that the number of genes with reduced expression level considerably exceeded the number of genes with increased expression at 30, 60, and 120 min, consistent with the inhibitory effect of nitrate observed in the growth study (Fig. 1). As the number of down-regulated genes peaked at 120 min, the number of up-regulated genes, however, continued to rise throughout the duration of the experiment, indicative of an active response to nitrate treatment following the initial inhibition.

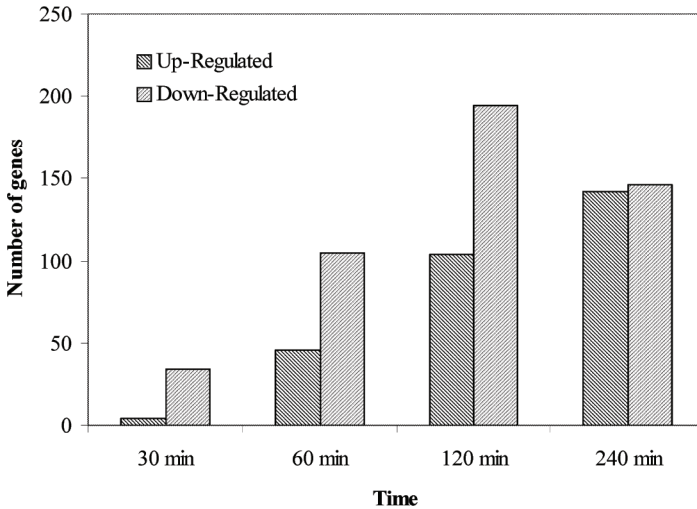


FIG. 2. Distribution of up- and down-regulated genes in *D. vulgaris* as a function of time upon exposure to 105 mM sodium nitrate. Only genes with $Z > 2$ (absolute value) and $\log_2 R < -1$ (down-regulation) or $\log_2 R > 1$ (up-regulation) were included in the plot.

Effects of osmoprotectant on growth inhibition by nitrate

Given the presence of osmotic stress at high nitrate concentrations, indications of osmotic stress response following nitrate exposure were examined. Indeed, transcriptional profiling showed an increase in the gene expression of the periplasmic-binding protein of the glycine/betaine/proline ABC transporter (DVU2297; $\log_2 R = 1.6$ at 240 min), although not the putative permease or ATP binding protein. Since glycine betaine is a known osmoprotectant (Cayley and Record 2003) and has been shown to relieve osmotic stress in *D. vulgaris* (Mukhopadhyay et al. 2006), the up-regulation of this gene supports the expected overlap between osmotic stress and nitrate stress. To further confirm that nitrate inhibition is associated with osmotic

stress, growth was monitored following the addition of glycine betaine as an osmoprotectant into *D. vulgaris* cultures in nitrate-supplemented defined medium (Figure 3).

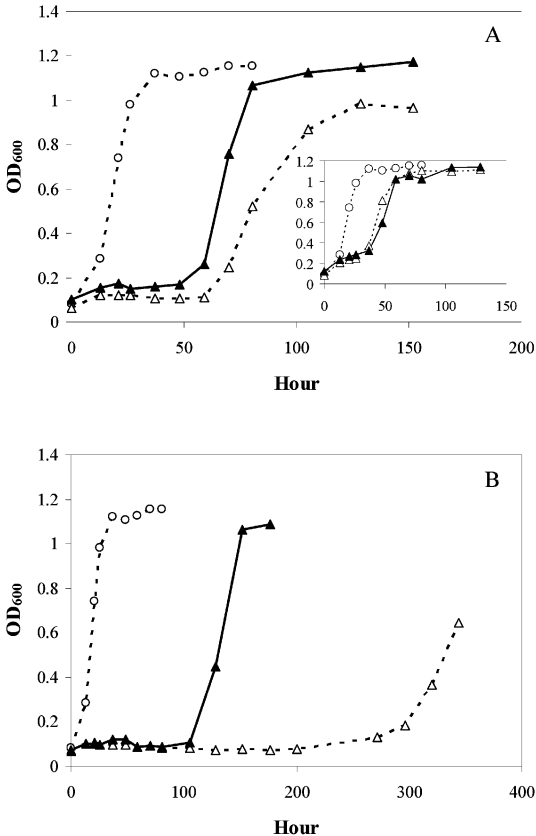


FIG. 3. Impact of glycine betaine on the growth of *D. vulgaris* exposed to 100 mM (A) and 200 mM (B) sodium nitrate. The inset in panel A shows the growth of *D. vulgaris* when 2 mM sodium nitrite was in place of sodium nitrate. *D. vulgaris* cultures were inoculated to a defined medium (Control, open circles), medium supplemented with sodium nitrate / nitrite only (open triangles), or medium supplemented with sodium nitrate / nitrite plus 2 mM glycine betaine as an osmoprotectant (closed triangles). Note different time scales on graphs.

Similar to stress-inducing concentrations of NaCl, elevated NaNO₃ concentrations resulted in a prolonged lag phase and significantly reduced final cell density. The addition of glycine betaine led to the complete recovery of the final cell density in *D.*

vulgaris cultures exposed to 100 mM NaNO₃; but provided only a 16% reduction of the lag phase (Figure 3A), which is in contrast to the near complete reversal of growth inhibition by glycine betaine in NaCl stress (Mukhopadhyay et al. 2006). The inability of glycine betaine to relieve nitrate stress entirely indicates that osmotic stress does not account for all the inhibition of cellular activities by nitrate stress.

On the other hand, growth inhibition by 200 mM NaNO₃ was more significantly relieved by the inclusion of glycine betaine in the medium, with the lag phase shortened from approximately 300 h to 100 h (Figure 3B). This observation was likely the result of the increasing importance of osmotic stress with higher levels of nitrate. Nonetheless, only partial relief of nitrate stress was provided by the addition of osmoprotectant, further suggesting the presence of additional sources of growth inhibition that were specific to nitrate stress, but not osmotic stress.

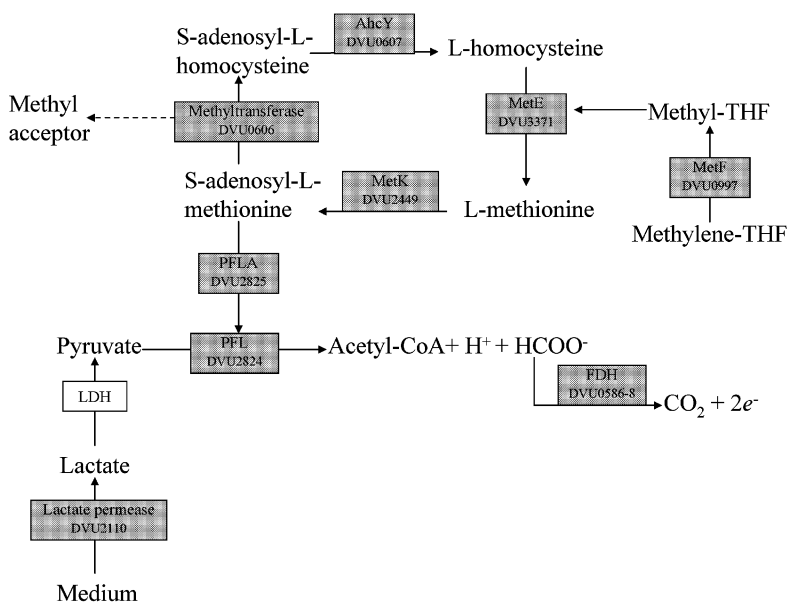


FIG. 4. Differential expression of genes involved in pathways of methyl metabolism and formate formation in response to nitrates stress. PFL: pyruvate formate-lyase; PFLA: pyruvate formate-lyase activating enzyme; FDH: formate dehydrogenase; LDH: lactate dehydrogenase. Red: up-regulation.

Genes involved in methyl/SAM metabolism

In nitrate-stressed *D. vulgaris*, a group of genes involved in the methyl metabolism were among those with the greatest increases in expression, including *metF* (DVU0997), *metE* (DVU3371), and *ahcY* (DVU0607). All these genes have functions in the metabolism of methionine and regeneration of *S*-adenosylmethionine (SAM), a

major methyl-donor in various cellular processes (Wang and Frey 2007). A careful examination of the genes up-regulated under nitrate stress further revealed the increased expression of the gene encoding another key enzyme in SAM biosynthesis, *S*-adenosylmethionine synthetase MetK (DVU2449; $\log_2R = 1.7$). From the co-expression patterns of all these genes (Figure 4), scattered across the genome, we infer the presence of a regulatory mechanism that might be involved in the increased turnover of SAM.

Interestingly, the enzyme activating the pyruvate formate-lyase (DVU2825), which was also among the most up-regulated genes under nitrate stress (Table 1), has been shown to require the methyl-donor SAM in other bacteria (Chase and Rabinowitz 1968; Knappe and Schmitt 1976), providing a potential link between energy metabolism and methyl/SAM metabolism (Figure 4).

Genes involved in energy metabolism

Nitrate does not support growth of *D. vulgaris* as an electron acceptor or nitrogen source (Haveman et al. 2004; Haveman et al. 2005). However, in many other anaerobes nitrate metabolism is directly linked to energy metabolism via multiple redox reactions (Moura et al. 1997). Thus, the involvement of genes in energy metabolism was investigated when elevated nitrate constituted a stress condition. Transcriptional analysis indicated that a small number of genes with functions in energy metabolism were among those highly up-regulated under nitrate stress, such as the genes related to the catabolism of pyruvate as a key metabolic intermediate: a pyruvate formate-lyase (DVU2824) and its activating enzyme (DVU2825). These two genes form an operon with two other genes encoding a TRAP dicarboxylate transporter (DVU2822-2825). In addition, a formate dehydrogenase gene cluster (DVU0586-0588) had increased expression under nitrate stress (data not shown). The composite of these differentially expressed genes appears to be consistent with an increased flow of reducing equivalent cycling through formate as a metabolic intermediate, as suggested under certain growth conditions (He et al. 2006; Pereira et al. 2008).

The gene encoding the hybrid cluster protein (DVU2543), which was suggested to be involved in the response to reactive nitrogen species generated in nitrate metabolism in other microorganisms (van den Berg et al. 2000; Wolfe et al. 2002), was also up-regulated ($\log_2R = 1.8$). It is noted that this gene was among the most highly up-regulated ($\log_2R = 6.4$) under nitrite stress (Haveman et al. 2004; He et al. 2006). The iron-sulfur cluster-binding protein, predicted to be encoded promoter distal in the same operon (DVU2544), was also increased in expression ($\log_2R = 1.9$), representing a shared response to nitrate and nitrite stress. Nonetheless, the differential expression of the hybrid cluster protein operon was much weaker in response to nitrate than that to nitrite. No significant changes in gene expression were observed in other known genes participating in nitrogen metabolism.

Another highly up-regulated gene with annotated functions in energy metabolism encodes a putative rubrerythrin (DVU2318), which is predicted to be under the regulation of the Peroxide-Responsive Regulator (PerR) (Rodionov et al. 2004). A survey of the gene expression profile indicated that all genes in the predicted PerR regulon had increased expression to various extents under nitrate stress. However,

comparison of gene expression profiles found that the PerR regulon was consistently up-regulated throughout different stress conditions (Chhabra et al. 2006; He et al. 2006; Mukhopadhyay et al. 2006; Mukhopadhyay et al. 2007), indicating that the increased expression of the PerR regulon was likely a part of the general stress response.

DISCUSSION

Nitrate is a common co-contaminant in subsurface environments impacted by radionuclides and heavy metals (Brooks 2001). Nitrate inhibition of metal-reducing microbial populations, such as the sulfate-reducing bacteria, hinders bioremediation efforts exploiting these microbial biocatalysts (Abdelouas et al. 1998; Finneran et al. 2002; Istok et al. 2004; Nyman et al. 2006). However, the persistence of sulfate-reducing bacteria at contaminated sites with high nitrate levels suggested the presence of potential resistance mechanisms (Bagwell et al. 2006; Fields et al. 2006; Gu et al. 2005), which were explored in this study using physiological and genomics approaches.

Growth inhibition by nitrate in the form of osmotic stress was demonstrated by the up-regulation of the glycine/betaine transporter genes and the relief of nitrate inhibition by osmoprotectant (Figure 3). However, osmotic stress response is not likely the only pathway contributing to the inhibitory effect of nitrate, given the minimal similarity in the transcriptional profiles between nitrate stress and NaCl stress. Indeed, the finding that *D. vulgaris* cells were significantly more sensitive to NaNO₃ than NaCl (Figure 1) indicates the involvement of inhibitory mechanisms in addition to the osmotic stress resulting from elevated nitrate concentrations. Presumably, the more severe growth inhibition under nitrate stress (Figure 1A) could be attributed to the presence of the nitrate ions, as compared to chloride ions.

Differing from Cl⁻, in some bacteria, the nitrate ion is redox active and can serve as a terminal electron acceptor in energy metabolism or as a source of nitrogen for biosynthesis, both requiring the reduction of nitrate coupled with electron transfer. However, nitrate-dependent growth of *D. vulgaris* has not been observed, which is consistent with the absence of nitrate reductase genes in the sequenced genome of *D. vulgaris* (Haveman et al. 2004; Heidelberg et al. 2004; Moura et al. 1997). Thus, it is unlikely that copious amounts of nitrogenous intermediates would be generated as toxic intermediates from nitrate reduction in *D. vulgaris*. It is suggested, however, that small amounts of nitrite, and subsequently other reactive nitrogen species, could be produced from non-specific reduction of nitrate by low potential reductases in *D. vulgaris* cells, such as the multiheme *c*-type cytochromes (Wall et al. 2007). Due to the specificity of nitrite toxicity to sulfate reduction (Greene et al. 2003; Haveman et al. 2004), nitrite derived from nitrate could represent a major stress condition for *D. vulgaris*. It appears that the significant up-regulation of the hybrid cluster protein genes (DVU2543-2544) upon nitrate exposure, which resembled a similar response pattern specific to nitrite stress (Greene et al. 2003; Haveman et al. 2004; He et al. 2006), would support the suggestion that nitrite stress is a result of nitrate exposure. However, direct evidence for the significance of low levels of nitrite under nitrate stress is still lacking. It is also possible that the up-regulation of certain genes

responsive to nitrite under nitrate stress was fortuitous, or the result of mechanisms yet to be understood.

Aside from components of salt stress and nitrite stress, involvement of oxidative stress response was also implicated during nitrate stress in *D. vulgaris*, with the up-regulation of the genes in the PerR regulon, which is known to be responsive to oxidative stress (Rodionov et al. 2004). However, examination of the responses of *D. vulgaris* to other stress conditions reveals that the up-regulation of the Per-R regulon under not only oxygen stress (Mukhopadhyay et al. 2007), but also nitrite (He et al. 2006), salt (Mukhopadhyay et al. 2006), and heat (Chhabra et al. 2006) stress, suggesting the response of the PerR regulon may not be specifically linked to nitrate. The same non-specific response could also be suggested for several other genes responsive to nitrate stress. For example, the gene for the phage shock protein A (DVU2988) was up-regulated in nitrate stress. However, this gene was also up-regulated under conditions of salt (Mukhopadhyay et al. 2006), heat (Chhabra et al. 2006), and oxygen (Mukhopadhyay et al. 2007) stress, suggesting that this response was not directly related to nitrate stress, rather a form of general stress response.

On the other hand, energetic consequences of nitrate stress could be considered as potential mechanisms contributing to the inhibition of *D. vulgaris* by nitrate. Indeed, our results indicate that a number of genes with functions in energy metabolism were among those highly up-regulated under nitrate stress, such as an operon consisting of genes related to the catabolism of pyruvate as a key metabolic intermediate, a pyruvate formate-lyase (DVU2824) and its activating enzyme (DVU2825), as well as another operon encoding a formate dehydrogenase (DVU0586-0588). These regulatory events implicate a shift in energy metabolism to the increased flow of reducing equivalents through formate as a metabolic intermediate during nitrate stress. Notably, the activation of the pyruvate formate-lyase (DVU2824), a key enzyme in the generation of formate from the central metabolite pyruvate, has been shown to require the methyl-donor SAM in other bacteria (Chase and Rabinowitz 1968; Knappe and Schmitt 1976). Interestingly, genes involved in methyl/SAM metabolism were among the most responsive to nitrate stress in *D. vulgaris*, thus linking the methyl/SAM metabolic pathway to the shift in energy metabolism (Figure 4). However, a definitive relationship between the shift in energy metabolism and nitrate inhibition could not be established, given the limited scope of this study. Future work should be focused on the elucidation of the roles of the energy metabolism in nitrate stress.

Therefore, the response to nitrate stress by *D. vulgaris* was shown to be linked to components of both osmotic and nitrite stress responses. The involvement of the oxidative stress response pathway, however, might be the result of a more general stress response. Given the low similarities between the response profiles to nitrate and other stresses, less defined stress response pathways could also be important in nitrate stress, which might involve the shift in energy metabolism.

ACKNOWLEDGMENTS

This work is support in part by the College of Engineering at the University of Tennessee, Knoxville.

REFERENCES

- Abdelouas, A., Lu, Y.M., Lutze, W., and Nuttall, H.E. (1998). "Reduction of U(VI) by indigenous bacteria in contaminated ground water." *J Contam Hydrol*, 35, 217-233.
- Bagwell, C.E., Liu, X., Wu, L., and Zhou, J. (2006). "Effects of legacy nuclear waste on the compositional diversity and distributions of sulfate-reducing bacteria in a terrestrial subsurface aquifer." *FEMS Microbiol Ecol*, 55, 424-431.
- Brooks, S.C. (2001). *Waste characteristics of the former S-3 ponds and outline of uranium chemistry relevant to NABIR Field Research Center studies ORNL/TM-2001/27*, NABIR Field Research Center, Oak Ridge, TN.
- Cayley, S., and Record, M.T., Jr. (2003). "Roles of cytoplasmic osmolytes, water, and crowding in the response of *Escherichia coli* to osmotic stress: biophysical basis of osmoprotection by glycine betaine." *Biochemistry*, 42, 12596-12609.
- Chang, Y.-J., Peacock, A.D., Long, P.E., Stephen, J.R., McKinley, J.P., MacNaughton, S.J., Hussain, A.K.M.A., Saxton, A.M., and White, D.C. (2001). "Diversity and characterization of sulfate-reducing bacteria in groundwater at a uranium mill tailings site." *Appl Environ Microbiol*, 67, 3149-3160.
- Chardin, B., Dolla, A., Chaspoul, F., Fardeau, M.L., Gallice, P., and Bruschi, M. (2002). "Bioremediation of chromate: thermodynamic analysis of the effects of Cr(VI) on sulfate-reducing bacteria." *Appl Environ Microbiol*, 60, 352-360.
- Chase, T., and Rabinowitz, J.C. (1968). "Role of pyruvate and S-adenosylmethionine in activating the pyruvate formate-lyase of *Escherichia coli*." *J Bacteriol*, 96, 1065-1078.
- Chhabra, S.R., He, Q., Huang, K.H., Gaucher, S.P., Alm, E.J., He, Z., Hadi, M.Z., Hazen, T.C., Wall, J.D., Zhou, J., Arkin, A.P., and Singh, A.K. (2006). "Global analysis of heat shock response in *Desulfovibrio vulgaris* Hildenborough." *J Bacteriol*, 188, 1817-1828.
- Clark, M.E., He, Q., He, Z., Huang, K.H., Alm, E.J., Wan, X.-F., Hazen, T.C., Arkin, A.P., Wall, J.D., Zhou, J.-Z., and Fields, M.W. (2006). "Temporal transcriptomic analysis as *Desulfovibrio vulgaris* Hildenborough transitions into stationary phase during electron donor depletion." *Appl Environ Microbiol*, 72, 5578-5588.
- Davidova, I., Hicks, M. , Fedorak, P.M., and Sufliya, J.M. (2001). "The influence of nitrate on microbial processes in oil industry production waters." *J Ind Microbiol Biotechnol*, 27, 80-86.
- Fields, M.W., Bagwell, C.E., Carroll, S.L., Yan, T., Liu, X., Watson, D.B., Jardine, P.M., Criddle, C.S., Hazen, T.C., and Zhou, J. (2006). "Phylogenetic and functional biomarkers as indicators of bacterial community responses to mixed-waste contamination." *Environ Sci Technol*, 40, 2601-2607.
- Finneran, K.T., Housewright, M.E., and Lovley, D.R. (2002). "Multiple influences of nitrate on uranium solubility during bioremediation of uranium-contaminated subsurface sediments." *Environ Microbiol*, 4, 510-516.
- Gadd, G.M., and White, C. (1993). "Microbial treatment of metal pollution - a working biotechnology?" *Trends Biotechnol*, 11, 353-359.
- Gillan, D.C., Danis, B., Pernet, P., Joly, G., and Dubois, P. (2005). "Structure of sediment-associated microbial communities along a heavy metal contaminated

- gradient in the marine environment." *Appl Environ Microbiol*, 71, 679-690.
- Greene, E.A., Hubert, C., Nemati, M., Jenneman, G.E., and Voordouw, G. (2003). "Nitrite reductase activity of sulfate-reducing bacteria prevents their inhibition by nitrate-reducing, sulfide-oxidizing bacteria." *Environ Microbiol*, 5(7), 607-617.
- Gu, B., Wu, W.-M., Ginder-Vogel, M.A., Yan, H., Fields, M.W., Zhou, J., Fendorf, S., Criddle, C.S., and Jardine, P.M. (2005). "Bioreduction of uranium in a contaminated soil column." *Environ Sci Technol*, 39, 4841-4847.
- Haveman, S.A., Greene, E.A., Stilwell, C.P., Voordouw, J.K., and Voordouw, G. (2004). "Physiological and gene expression analysis of inhibition of *Desulfovibrio vulgaris* Hildenborough by nitrite." *J Bacteriol*, 186, 7944-7950.
- Haveman, S.A., Greene, E.A., and Voordouw, G. (2005). "Gene expression analysis of the mechanism of inhibition of *Desulfovibrio vulgaris* Hildenborough by nitrate-reducing, sulfide-oxidizing bacteria." *Environ Microbiol*, 7, 1461-1465.
- Hazen, T.C., and Stahl, D.A. (2006). "Using the stress response to monitor process control: pathways to more effective bioremediation." *Curr Opin Biotechnol*, 17, 285-290.
- He, Q., Huang, K.H., He, Z., Alm, E.J., Fields, M.W., Hazen, T.C., Arkin, A.P., Wall, J.D., and Zhou, J. (2006). "Energetic consequences of nitrite stress in *Desulfovibrio vulgaris* Hildenborough, inferred from global transcriptional analysis." *Appl Environ Microbiol*, 72, 4370-4381.
- Heidelberg, J.F., Seshadri, R., Haveman, S.A., Hemme, C.L., Paulsen, I.T., Kolonay, J.F., Eisen, J.A., Ward, N., Methe, B., Brinkac, L.M., Daugherty, S.C., Deboy, R.T., Dodson, R.J., Durkin, A.S., Madupu, R., Nelson, W.C., Sullivan, S.A., Fouts, D., Haft, D.H., Selengut, J., Peterson, J.D., Davidsen, T.M., Zafar, N., Zhou, L., Radune, D., Dimitrov, G., Hance, M., Tran, K., Khouri, H., Gill, J., Utterback, T.R., Feldblyum, T.V., Wall, J.D., Voordouw, G., and Fraser, C.M. (2004). "The genome sequence of the anaerobic, sulfate-reducing bacterium *Desulfovibrio vulgaris* Hildenborough." *Nature Biotechnol*, 22, 554-559.
- Istok, J.D., Senko, J.M., Krumholz, L.R., Watson, D., Bogle, M.A., Peacock, A., Chang, Y.-J., and White, D.C. (2004). "In situ bioreduction of technetium and uranium in a nitrate-contaminated aquifer." *Environ Sci Technol*, 38, 468-475.
- Jenneman, G.E., McInerney, M.J., and Knapp, R.M. (1986). "Effect of nitrate on biogenic sulfide production." *Appl Environ Microbiol*, 51, 1205-1211.
- Joachimiak, M.P., Weissman, J.L., and May, B. C.H. (2006). "JColorGrid: software for the visualization of biological measurements." *BMC Bioinformatics*, 7, 225.
- Jones, H.E., Trudinger, P.A., Chambers, L.A., and Pylotis, N.A. (1976). "Metal accumulation by bacteria with particular reference to dissimilatory sulfate-reducing bacteria." *Z Allg Mikrobiol*, 16, 425-435.
- Knappe, J., and Schmitt, T. (1976). "A novel reaction of *S*-adenosyl-L-methionine correlated with the activation of pyruvate formate-lyase." *Biochem Biophys Res Commun*, 71, 1110-1117.
- Landa, E.R. (2005). "Microbial biogeochemistry of uranium mill tailings." *Adv Appl Microbiol*, 57, 113-130.
- Lloyd, J.R., and Lovley, D.R. (2001). "Microbial detoxification of metals and radionuclides." *Curr Opin Biotechnol*, 12, 248-253.
- Lloyd, J.R., and Renshaw, J.C. (2005). "Bioremediation of radioactive waste:

- radionuclide-microbe interactions in laboratory and field-scale studies." *Curr Opin Biotechnol*, 16, 254-260.
- Lloyd, J.R., Ridley, J., Khizniak, T., Lyalikova, N.N., and Macaskie, L.E. (1999). "Reduction of technetium by *Desulfovibrio desulfuricans*: biocatalyst characterization and use in a flowthrough bioreactor." *Appl Environ Microbiol*, 65, 2691-2696.
- Lovley, D.R., and Phillips, E.J.P. (1992a). "Bioremediation of uranium contamination with enzymatic uranium reduction." *Environ Sci Technol*, 26, 2228-2234.
- Lovley, D.R., and Phillips, E.J.P. (1992b). "Reduction of uranium by *Desulfovibrio desulfuricans*." *Appl Environ Microbiol*, 58, 850-856.
- Lovley, D.R., Roden, E.E., Phillips, E.J.P., and Woodward, J.C. (1993a). "Enzymatic iron and uranium reduction by sulfate-reducing bacteria." *Marine Geol*, 113, 41-53.
- Lovley, D.R., Widman, P.K., Woodward, J.C., and Phillips, E.J.P. (1993b). "Reduction of uranium by cytochrome c_3 of *Desulfovibrio vulgaris*." *Appl Environ Microbiol*, 59, 3572-3576.
- Moura, I., Bursakov, S., Costa, C., and Moura, J.J.G. (1997). "Nitrate and nitrite utilization in sulfate-reducing bacteria." *Anaerobe*, 3, 279-290.
- Mukhopadhyay, A., He, Z., Alm, E.J., Arkin, A.P., Baidoo, E.E., Borglin, S.C., Chen, W., Hazen, T.C., He, Q., Holman, H.-Y., Huang, K., Huang, R., Joyner, D.C., Katz, N., Keller, M., Oeller, P., Redding, A., Sun, J., Wall, J., Wei, J., Yang, Z., Yen, H.-C., Zhou, J., and Keasling, J.D. (2006). "Salt stress in *Desulfovibrio vulgaris* Hildenborough: an integrated genomics approach." *J Bacteriol*, 188, 4068-4078.
- Mukhopadhyay, A., Redding, A.M., Joachimiak, M.P., Arkin, A.P., Borglin, S.E., Dehal, P.S., Chakraborty, R., Geller, J.T., Hazen, T.C., He, Q., Joyner, D.C., Martin, V.J.J., Wall, J.D., Yang, Z.K., Zhou, J., and Keasling, J.D. (2007). "Cell-wide responses to low-oxygen exposure in *Desulfovibrio vulgaris* Hildenborough." *J Bacteriol*, 189(16), 5996-6010.
- NABIR. (2003). "Bioremediation of metals and radionuclides: what it is and how it works." NABIR primer, 2nd ed, T.C. Hazen, S.M. Benson, F.B. Metting, B. Faison, A.C. Palmisano, and J. McCullough, eds., Lawrence Berkeley National Laboratory, Berkeley, California, 1-78.
- Nyman, J.L., Marsh, T.L., Ginder-Vogel, M.A., Gentile, M., Fendorf, S., and Criddle, C. (2006). "Heterogeneous response to biostimulation for U(VI) reduction in replicated sediment microcosms." *Biodegradation*, 17, 303-316.
- Odom, J.M. (1993). "Industrial and environmental activities of sulfate-reducing bacteria." The sulfate-reducing bacteria: contemporary perspectives, J. M. Odom and R. Singelton, Jr., eds., Springer-Verlag, Inc., New York, N. Y., 189-210.
- Payne, R.B., Gentry, D.A., Rapp-Giles, B.J., Casalot, L., and Wall, J.D. (2002). "Uranium reduction by *Desulfovibrio desulfuricans* strain G20 and a cytochrome c_3 mutant." *Appl Environ Microbiol*, 68, 3129-3132.
- Pereira, P.M., He, Q., Valente, F.M.A., Xavier, A.V., Zhou, J., Pereira, I.A.C., and Louro, R.O. (2008). "Energy metabolism in *Desulfovibrio vulgaris* Hildenborough: insights from transcriptome analysis." *Antonie van Leeuwenhoek*, 93, 347-362.

- Riley, R.G., and Zachara, J.M. (1992). *Chemical contaminants on DOE lands and selection of contaminant mixtures for subsurface science research DOE/ER-0547T. U.S. Department of Energy, Washington, D. C.*
- Rodionov, D.A., Dubchak, I., Arkin, A.P., Alm, E., and Gelfand, M.S. (2004). "Reconstruction of regulatory and metabolic pathways in metal-reducing δ -Proteobacteria." *Genome Biol*, 5, R90.
- Valls, M., and de Lorenzo, V. (2002). "Exploiting the genetic and biochemical capacities of bacteria for the remediation of heavy metal pollution." *FEMS Microbiol Rev*, 26, 327-338.
- van den Berg, W.A.M., Hagen, W.R., and van Dongen, W.M.A.M. (2000). "The hybrid-cluster protein ("prismane protein") from *Escherichia coli*: characterization of the hybrid-cluster protein, redox properties of the [2Fe-2S] and [4Fe-2S-2O] clusters and identification of an associated NADH oxidoreductase containing FAD and [2Fe-2S]." *Eur J Biochem*, 267, 666-676.
- Wall, J.D., Yen, H.-C.B., and Drury, E.C. (2007). "Evaluation of stress response in sulphate-reducing bacteria through genome analysis." *Sulphate-reducing bacteria: Environmental and engineered systems*, L. L. Barton and W. A. Hamilton, eds., Cambridge University Press, Cambridge, UK, 141-165.
- Wang, S., Jaffe, P.R., Li, G., Wang, S.W., and Rabitz, H.A. (2003). "Simulating bioremediation of uranium-contaminated aquifers; uncertainty assessment of model parameters." *J Contam Hydrol*, 64, 283-307.
- Wang, S.C., and Frey, P.A. (2007). "*S*-adenosylmethionine as an oxidant: the radical SAM superfamily." *Trends Biochem Sci*, 32, 101-110.
- Widdle, F. (1988). "Microbiology and ecology of sulfate- and sulfur-reducing bacteria." *Biology of anaerobic microorganisms*, A.J.B. Zehnder, ed., John Wiley and Sons, Inc., New York, N. Y., 469-485.
- Wolfe, M.T., Heo, J., Garavelli, J.S., and Ludden, P.W. (2002). "Hydroxylamine reductase activity of the hybrid cluster protein from *Escherichia coli*." *J Bacteriol*, 184, 5898-5902.

Simulation of Groundwater Composition Change due to Deposition of Uranium Minerals in Dolomite Gravel Fill

Fan Zhang¹, Jack C. Parker², David B. Watson³, Debra Phillips⁴ and Philip M. Jardine⁵

¹ Corresponding author: Institute of Tibetan Plateau Research, Chinese Academy of Sciences, P.O.Box 2871, Beijing, 100085, China. Email: zhangfan@itpcas.ac.cn

² Department of Civil and Environmental Engineering, University of Tennessee, Knoxville, TN 37996, USA. Email: jparker@utk.edu

³ Environmental Sciences Division, Oak Ridge National Laboratory, Oak Ridge, TN 37831, USA. Email: watsondb@ornl.gov

⁴ Environmental Engineering Research Centre, School of Planning, Architecture, and Civil Engineering, Queen's University of Belfast, Belfast BT9 5AG, Northern Ireland, UK. Email: d.phillips@qub.ac.uk

⁵ Biosystems Engineering and Soil Science Department, University of Tennessee Knoxville, TN 37996, USA. Email: pjardine@utk.edu

ABSTRACT: A large plume of uranium contaminated groundwater has been formed as a consequence of historical weapons processing and waste disposal at the former U.S. Department of Energy (DOE) S-3 ponds site located at the Y-12 National Security Center in Oak Ridge Tennessee. Measurements of groundwater samples from the site showed much higher pH values and lower concentrations of uranium and aluminum in carbonate gravel fill than in the underlying lower pH saprolite. Field and laboratory studies demonstrate that precipitates with high U content (> 19%) form when acidic U and Al containing groundwater contacts high pH carbonate gravel. Lab morphology and mineralogy analyses reveal that uranyl carbonates and amorphous basalumnite occur as coatings on dolomite gravel and as detached individual precipitates (Phillips et al. 2008). This study employs a new method that integrates the field measurements, the past laboratory analyses, and numerical modeling to determine physical and geochemical processes that are critical to explain the groundwater composition changes. The resulting numerical simulations indicate that significant reductions in aqueous U concentrations occur due to reactions with high pH carbonate gravel. Insights from the numerical modeling on the formation and stability of U precipitates are important to determine U transport properties and the effectiveness of U remediation strategies.

INTRODUCTION

Historical weapons processing and waste disposal practices has produced significant subsurface radionuclide contamination at U.S. Department of Energy (DOE) weapons processing plants. Uranium (U) is the most frequently detected radionuclide in contaminated groundwater and sediments at these DOE facilities

(Riley and Zachara 1992). At the DOE S-3 Pond site at the Y-12 National Security Center in Oak Ridge, Tennessee, a large plume of contaminated groundwater has been formed as a result of historical weapons production and U-bearing waste disposal activities (ORNL 1984; Watson et al. 2005). The DOE Field Research Center located at the site has been the host for a number of studies examining the fate, transport and removal of U from groundwater (Phillips et al. 2000; Gu et al. 2003; Istok et al. 2004; Luo et al. 2006; Wu et al. 2007; Zhang et al. 2008). Insights into how U precipitates and adsorbs onto subsurface geological materials are important to identify possible means of controlling the mobility of U in groundwater and model the fate and transport of U (Phillips et al. 2008).

The S-3 Ponds site is underlain by shale and carbonate bedrock that has been weathered to depths of 15 m to a clay rich saprolite (Watson et al. 2005). At approximately 60 m from the former S-3 disposal ponds, the native saprolite material was excavated and backfilled with dolomite gravel to construct a foundation for storage tanks. The gravel fill intercepts about the top meter of the water table of the shallow groundwater contaminant plume. The highly permeable gravel preferentially diverts some of the groundwater flow toward nearby Bear Creek (Watson et al. 2005). The high pH carbonate gravel removed significant quantities of U from the acidic Al^{3+} and SO_4^{2-} rich groundwater infiltrating from the underlying saprolite (Phillips et al. 2008). Examination of the U containing precipitates shows that uranyl carbonates are present with amorphous basalumnite $\text{Al}_4(\text{SO}_4)(\text{OH})_{10}\cdot 4\text{H}_2\text{O}$ as coatings on the dolomite gravel and as individual precipitates (Phillips et al. 2008).

The objectives of this study are: (1) to determine physical and geochemical processes that are critical to explain the groundwater composition changes using a new methodology that integrates the field measurements, the past laboratory analyses, and modeling studies, and (2) to develop geochemical reaction models to simulate U removal when acidic contaminated groundwater contacts carbonate gravel. Improved ability to predict field behavior of U will facilitate the assessment of contamination risk under ambient conditions and will facilitate the design of remediation measured to control exposure.

GROUNDWATER ANALYSIS

Since 2004, groundwater has been sampled from a multilevel well (FW410) screened within the gravel fill (~2.74 to 4.22 m depth) and in underlying saprolite (~7.22 to 8.39 m depth). Groundwater pH and solution composition measurements are summarized in Table 1. Higher pH values and sulfate concentrations, and lower U, Al, Ca, Mg, K and Na concentrations occur in the gravel fill than in underlying saprolite.

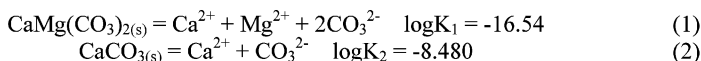
X-ray absorption near edge structure spectroscopy (XANES) and extended X-ray absorption fine structure spectroscopy (EXAFS) of over 80 sampled regions for gravel fill material shows that the uranyl carbonate and amorphous basalumnite $\text{Al}_4(\text{SO}_4)(\text{OH})_{10}\cdot 4\text{H}_2\text{O}$ occur as coatings on dolomite gravel and as individual precipitates (Phillips et al. 2008). The uranyl carbonate structure is heterogeneous with some regions similar to grimselite $\text{K}_3(\text{UO}_2)(\text{CO}_3)_3\cdot \text{H}_2\text{O}$ and other regions more like liebigite $\text{Ca}_2(\text{UO}_2)(\text{CO}_3)_3\cdot 11\text{H}_2\text{O}$ or andersonite $\text{Na}_2\text{CaUO}_2(\text{CO}_3)_3\cdot 6\text{H}_2\text{O}$.

Table 1. Groundwater pH and major reactive composition in mg/L (ORIFRC 2009)

Parameter	In saprolite	In gravel fill
pH	3.20 ~3.44	6.16 ~6.65
U	22.20 ~ 39.87	0.66 ~ 0.99
Al	225.65 ~ 882.90	0.04 ~ 0.87
Ca	134.36 ~ 475.87	111.35 ~ 149.95
Mg	80.07 ~ 315.89	18.67 ~ 30.93
K	56.51 ~ 118.72	3.71 ~7.03
Na	213.10 ~ 421.08	9.44 ~ 25.69
SO ₄ ²⁻	2.51 ~ 30.30	84.88 ~ 113.00

Integration of field groundwater geochemistry observations, laboratory morphology and mineralogy analyses, and numerical modeling indicate the following physical and geochemical processes are significant to explain groundwater composition changes:

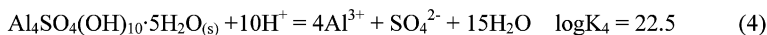
a) dissolution of dolomite and calcite, the major components of the gravel minerals that results in the higher groundwater pH and higher Ca and Mg concentrations in the gravel fill (Stumm and Morgan 1996)



b) precipitation of uranyl carbonates that removes uranium from groundwater (Phillips et al. 2008)



c) precipitation of basalumnite that reduces groundwater Al and sulfate concentrations (Gundersen and Beier 1988)



d) weathering of pyrite (FeS₂) inclusions in the gravel layer (Phillips et al. 2008) that produces elevated SO₄²⁻ concentrations in the gravel fill; and

e) acidic contaminated groundwater from the saprolite that flows into the gravel fill and mixes with the higher pH groundwater. Assuming one volume of contaminated groundwater from the saprolite mixes with x volume of gravel solution, contaminants are diluted by a factor $f = 1/(1+x)$.

GEOCHEMICAL MODELING

The computer code HydroGeoChem v5.0 (HGC5) (Yeh et al. 2004) was used to model geochemical reactions. HGC5 is designed to handle generic biogeochemical reaction networks, which may include equilibrium and kinetic reactions with user specified formulations. HGC5 was coupled with the nonlinear inversion code PEST

(Doherty 2004) to enable estimation of specified model coefficients by calibrating simulation results to measured data.

An equilibrium geochemical reaction model including aqueous complexation reactions of carbonate, sulfate, K, Na, Ca, Mg, Al (Stumm and Morgan 1996) and U (Guillaumont et al. 2003) and mineral precipitation/dissolution reactions (Equations 1~4) was used to simulate the the major composition of groundwater in gravel fill mixed with acidic contaminated groundwater from underlying saprolite. According to previous studies, oxic groundwater conditions prevail at the site (Gu et al. 2003). As a consequence, hexavalent uranium in the form of uranyl (UO_2^{2+}) is expected in the groundwater. However, because of relatively high concentrations of sulfate and carbonate, uranyl may also be present as uranyl carbonates [e.g., UO_2CO_3^0 and $\text{UO}_2(\text{CO}_3)_2^-$] and/or uranyl sulfates [e.g., UO_2SO_4^0 and $\text{UO}_2(\text{SO}_4)_2^-$] etc (Guillaumont et al. 2003).

Scanning electron microscopy (SEM) microprobe analyses show U ranging from 1.6-19.8% within coatings. Highest concentrations are present at the interface of dolomite fragments where $\text{K}_4\text{UO}_2(\text{CO}_3)_3\cdot\text{H}_2\text{O}$ is generally observed as a thin surface coating. Both $\text{K}_4\text{UO}_2(\text{CO}_3)_3\cdot\text{H}_2\text{O}$ and $\text{Ca}_2(\text{UO}_2)(\text{CO}_3)_3\cdot 11\text{H}_2\text{O}/\text{Na}_2\text{Ca}(\text{UO}_2)(\text{CO}_3)_3\cdot 6\text{H}_2\text{O}$ are present in the individual precipitates in the fine fraction and in coatings further away from the interface (Phillips et al. 2008). The dominant mineral phase, $\text{K}_4\text{UO}_2(\text{CO}_3)_3\cdot\text{H}_2\text{O}$, was considered in the model.

The geochemistry modeling process is summarized in Figure 1. One volume of groundwater from the saprolite is mixed with x volume of gravel solution in equilibrium with dolomite, the major mineral phase of the gravel.

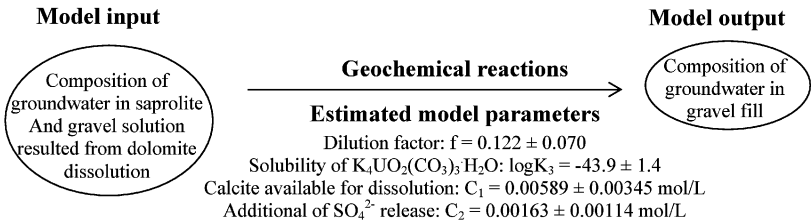


FIG. 1. Illustration of geochemistry modeling process and parameter estimates.

Four model parameters were estimated through calibration of the simulation results to the observed groundwater composition for samples taken from the gravel fill on four dates. The parameters were determined by simultaneously fitting to data for all dates. Final parameter estimates and their standard errors are shown in Figure 1. Simulation results are compared with groundwater measurements in Figure 2. The simulation closely captures the pH increase and Al and U removal, which is due mainly to precipitation of uranyl carbonate, $\text{K}_4\text{UO}_2(\text{CO}_3)_3\cdot\text{H}_2\text{O}$, and basalumnite, $\text{Al}_4\text{SO}_4(\text{OH})_{10}\cdot 5\text{H}_2\text{O}$, when acidic contaminated groundwater is mixed with high pH carbonate gravel.

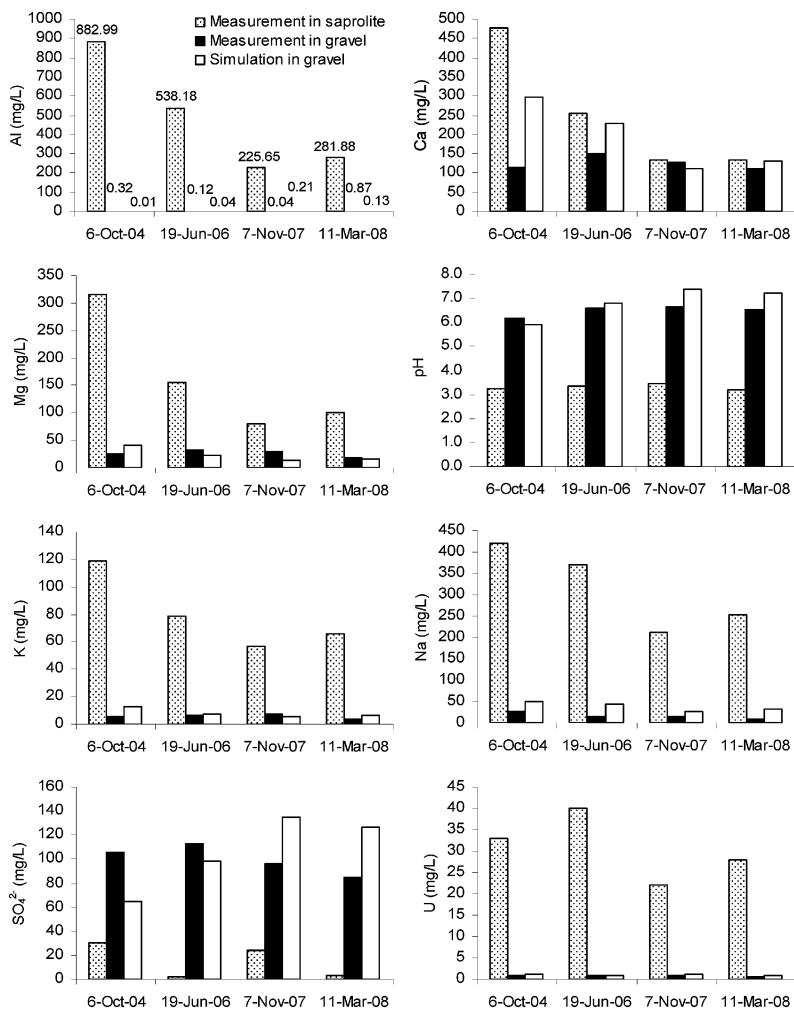


Fig. 2. Observed and simulated major groundwater composition

COMCLUSIONS

Uranium-containing carbonate precipitates associated with amorphous basaluminite have been observed in a dolomitic gravel fill near the U.S. DOE former S-3 Pond waste disposal site as a result of mixing with influent acidic (pH 3.20 to 3.44) groundwater contaminated with U (22.2 to 39.9 mg/L) and Al (225.6–882.9 mg/L), etc. Morphologic and mineralogy analyses of the U-containing precipitates reveal that the U is hexavalent and the uranyl is coordinated with carbonate. Laboratory and field data were used to develop a geochemical model to estimate groundwater composition due to contaminated groundwater seeping into gravel fill. Modeling results indicate that uranium removal from the aqueous phase can be largely attributed to precipitation of $K_4UO_2(CO_3)_3 \cdot H_2O$.

ACKNOWLEDGEMENTS

This research was funded by the U.S. Department of Energy, Office of Science, Biological and Environmental Research Programs. Oak Ridge National Laboratory is managed by UT- Battelle, LLC, for the U.S. Department of Energy under Contract DE-AC05-00OR22725.

REFERENCES

- Doherty, J., ed. (2004). *PEST: Model Independent Parameter Estimation*: Watermark Numerical Computing.
- Gu, B, Brooks, S.C., Roh, Y., and Jardine, P.M. (2003). Geochemical reactions and dynamics during titration of a contaminated groundwater with high uranium, aluminum and calcium. *Geochim. Cosmochim. Acta*. Vol. 67:2749-2761.
- Guillaumont, R, Fanghanel, T., Neck, V., Fuger, J., Palmer, D. A., Grenthe, I., and Rand, M. H. (2003). *Update on the Chemical Thermodynamics of Uranium, Neptunium, Plutonium, Americium, and Technetium*: Elsevier.
- Gundersen, P., and Beier, C. (1988). Aluminium sulphate solubility in acid forest soils in Denmark. *Water, Air, & Soil Pollution* Vol. 39 (3-4):247-261.
- Istok, J. D., Senko, J. M., Krumholz, L. R., Watson, D., Bogle, M. A., Peacock, A., Chang, Y. J., and White, D. C. . (2004). In situ bioreduction of technetium and uranium in a nitrate-contaminated aquifer. *Environ. Sci. Technol.* Vol. 38:468-475.
- Luo, J., Wu, W-M., Fienen, M.N., Jardine, P.M., Mehlhorn, T.L., Watson, D.B., Cirpka, O.A., Criddle, C.S., and Kitanidis, P.K. . (2006). A nested cell approach for in situ remediation. *Ground water* Vol. 44:266-274.
- ORIFRC. 2009. 2009 [cited May 13 2009]. Available from <http://public.ornl.gov/orifc/dataqueryparam.cfm>.
- ORNL. (1984). *The Chemical and Radiological Characterization of the S-3 Ponds*. Oak Ridge, TN: Oak Ridge National Laboratory.
- Phillips, D. H., Watson, D. B., Kelly, S. D., Ravel, B., and Kemner, K. M. (2008). Deposition of Uranium Precipitates in Dolomitic Gravel Fill. *Environ. Sci. Technol.* Vol. 42 (19):7104-7110.
- Phillips, D.H., Gu, B., Watson, D.B., Roh, Y., Liang, L., and Lee, S.Y. . (2000). Performance evaluation of a zerovalent iron reactive barrier: Mineralogical characteristics. . *Environ. Sci. Technol.* Vol. 34: 4169-4176.

- Riley, R.G., and Zachara, J.M. (1992). *Chemical Contaminants on DOE Lands and Selection of Contaminant Mixtures for Subsurface Science Research*: DOE/ER-0547T.
- Stumm, W, and Morgan, J. J. (1996). *Aquatic chemistry*. third ed. New York: John Wiley and Sons.
- Watson, D.B., Doll, W.E., Gamey, T.J., Sheehan, J.R., and Jardine, P.M. . (2005). Plume and lithological profiling with surface resistivity and seismic tomography. *Ground water* Vol. 43:169-177.
- Wu, W., Carley, J., Luo, J., Ginder-Vogel, M. A., Cardenas, E., Leigh, M. B., Hwang, C., Kelly, S.D., Ruan, C., Wu, L., Van Nostrand, J., Gentry, T., Lowe, K., Mehlhorn, T., Carroll, S., Lou, W., Fields, W., Gu, B., Watson, D., Kemner, K.M., Marsh, T., Tiedje, J., Zhou, J., Fendorf, S., Kitanidis, P.K., Jardine, P.M., and Criddle, C.S. . (2007). In-situ bioreduction of uranium (VI) to submicromolar levels and reoxidation by dissolved oxygen. *Environ. Sci. Technol.* Vol. 41:5716-5723.
- Yeh, G.-T., Sun, J. T., Jardine, P. M., Burgos, W. D., Fang, Y. L., Li, M. H., and Siegel, M. D. . (2004). *HydroGeoChem 5.0: A three-dimensional model of coupled fluid flow, thermal transport, and hydrogeochemical transport through variable saturated conditions - Version 5.0*: Oak Ridge National Laboratory.
- Zhang, F., Luo, W., Parker, J. C., Spalding, B. P., Brooks, S. C., Watson, D. B., Jardine, P. M., and Gu, B. (2008). Geochemical Modeling of Reactions and Partitioning of Trace Metals and Radionuclides during Titration of Contaminated Acidic Sediments. *Environ. Sci. Technol* Vol. 42 (21):8007-8013.

“Kriging Assistant”: A Geostatistical Analysis and Evaluation Tool

Alessandro Mazzella¹, UNICA and Antonio Mazzella², UNICA

¹PhD Student, Department of GeoEngineering and Environmental Technologies, University of Cagliari, Piazza D’Armi 19, 09123; amazzella@unica.it

²Associate Professor, Department of GeoEngineering and Environmental Technologies, University of Cagliari, Piazza D’Armi 19, 09123; mazzella@unica.it

ABSTRACT: The definition of the investigation area border line, the choice of the proper sampling mesh and exploration technique, the correct analysis of the collected data, represent the most important steps of each environmental research project. The “Krige’s Diagram” demonstrates that the evaluation quality depends on the accuracy by which each of these phases has been performed. This paper introduces an innovative geostatistics-based software for environmental data analysis and evaluation, called “Kriging Assistant” (KA). This new tool, developed within the Department of Geoengineering and Environmental Technologies – University of Cagliari (Italy), is able to work both in 2D and 3D dimensions and, moreover, it is able to solve the complex problem of the experimental semivariogram fitting through an innovative and automatic modeling procedure. In this way the estimation errors deriving from the evaluator modeling process are avoided.

INTRODUCTION

All the environmental-applied researches focus on the *outliers* identification and on the anomaly variation (i.e. space and/or time) modeling inside an investigated area. For this reason, every researcher has to proceed with a statistical treatment and analysis of data deriving from chemical analysis of collected samples. This step represents only the last phase of a large series of operations (e.g. samples collection, samples size/mass reduction for laboratory analysis, samples multi-element analysis, statistic treatment of chemical analysis results, etc). Each single step is important and influences the final estimation quality. Unfortunately the evaluation goodness can be measured only at the end of project, because only from that moment the real values become known.

A posteriori control of the evaluation integrity is possible through the “Krige’s Diagram” (shown in fig.1). This diagram allows to compare, for each sample, the estimated value with the real measured data (Mazzella An. et al., 1984): the estimation will be perfect only if the estimated-real pairs are aligned along the regression line.

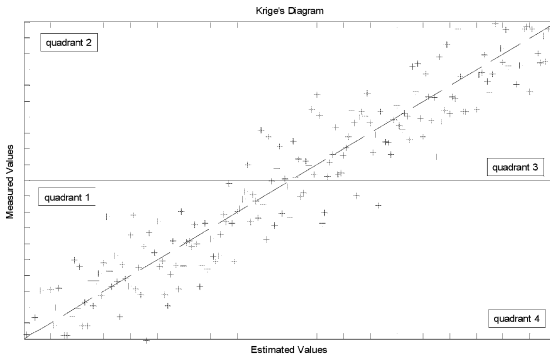


FIG. 1. An example of Kriging’s Diagram: the red crosses represent the estimated-real values of each sample, blue line represents the regression line (Mazzella An. et al., 1984).

Obviously the operative step during which is possible to commit the most serious mistakes is the phases of analysis and processing of collected data. For this reason our team has been working since ‘80s in the development of innovative geostatistics-based technologies able to assist the researcher during the evaluation of the environmental data. This paper introduces a new tool for the environmental data analysis and evaluation, called “Kriging Assistant” (KA). This new software, developed within the Department of Geoenvironment and Environmental Technologies – University of Cagliari, is based exclusively on open source technologies and represents a powerful and user-friendly *automatic* geostatistical analysis tool.

KRIGING ASSISTANT DESCRIPTION

KA core is based upon the experiences of: FGAM (fig.2), a simple tool for calculate the experimental semivariogram of a dataset, and JCBLOK (fig.2), a simple tool for the subsequent interpolation through Kriging (Carr J.R. and Mela K., 1998).



FIG. 2. Main windows of “FGAM” and “JCBLOK” tools (Carr J.R. and Mela K., 1998).

KA (whose main window is shown in fig.3) represents an evolution of Carr & Mela's work; in fact it has been written in Microsoft Visual Basic 6, using the GeoLIBS libraries (Deutsch C. and Journel A., 1992) and it gathers the *FGAM* and *JCBLOK* characteristics, but it has been rewritten and implemented in order to be more powerful, user-friendly and efficient.

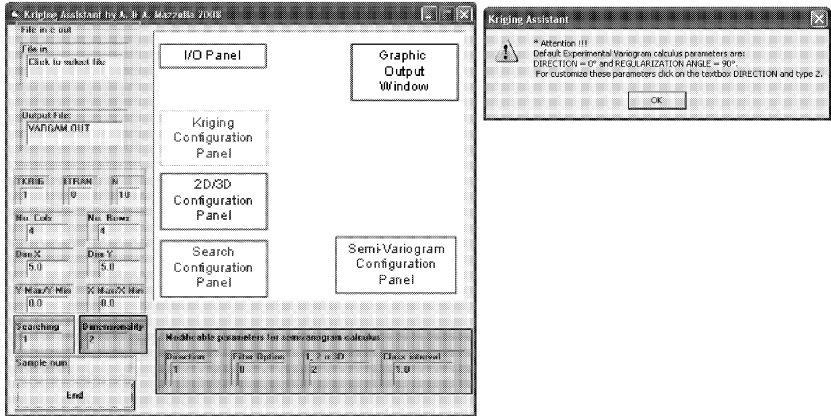


FIG. 3. On the left, the control panels forming KA main windows are shown. On the right, it is shown the alert message that informs the user about the default parameters used for experimental semivariogram calculus.

Once the user starts KA (by clicking twice on its desktop icon), the software alert window is shown. The message informs the user about the default condition for semivariogram calculus and the instruction to customize them (fig.3). Regarding the correct datafile management and the accurate semivariogram calculus the most important parameters are "*dimensionality*" and "*1, 2 or 3D*" (fig.4).

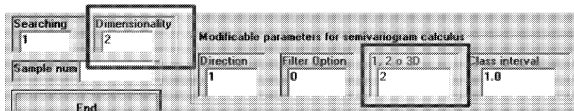


FIG. 4. Localization of the "*dimensionality*" and "*1, 2 or 3D*" customization panels.

Through the customization of these two parameters KA will know the sampling mesh features (sampling made along a line, along a gallery, along a bore hole, etc) and will calculate a mono-, bi- or three-dimensional semivariogram. In particular, the first

parameter regards the datafile reading procedure whereas the second one deals with the calculation algorithm. After these parameters customization KA is ready to import the data and to proceed to the geostatistical esteem. The current KA version (v2.0/2009) is able to read only two different datafile standards: geoas datafile, csv datafile. The first one is a dataset introduced since 1991 by the program GEOEAS (Geostatistical Environmental Assessment Software) which represents a *de facto* standard now. This standard features are (fig.5): the first line is reserved for the title of the project; the second row indicates the number of variables stored in the datafile; many rows as number of variables indicating the name and format (according to the FORTRAN syntax) of the data; the sequence of data separated by white space. The other supported standard is a classic "comma delimited".

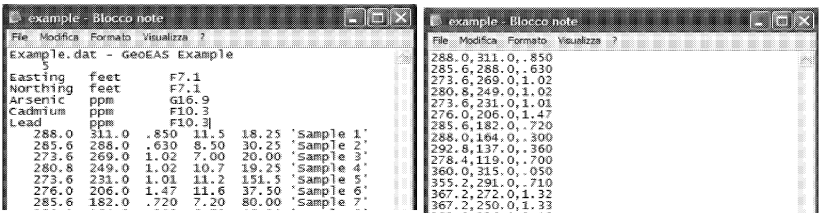


FIG. 5. Comparison between “GeoEAS” and “Comma Separated Values” formatted datafiles.

A DATA ANALYSIS SESSION WITH KRIGING ASSISTANT

Once the datafile has been imported within KA, the *sample map* is automatically generated (fig.6). The average time required for the map generation is approximately 0.2 seconds every 4000 records.

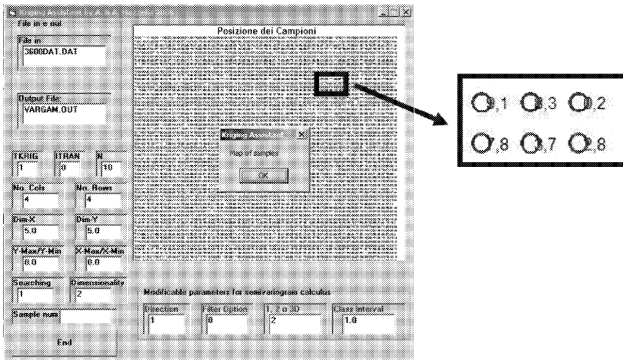


FIG. 6. An example of KA sample map.

The KA *sample map* represents the position (indicated by red circles) and the measured values (on the right of each red circle) of each sample. Naturally in the case of a large amount of samples, KA adjusts the map scale for prevent the display overlapping of values. This simple representation allows the user to perform a quick visual inspection of the mesh sampling integrity. At this point KA proceeds automatically with the experimental semivariogram calculus (the result is shown in fig.7) and, subsequently, with the semivariogram curve modelling and interpretation. This step is primary for the calculus of the parameters needed for the next phase of data kriging.

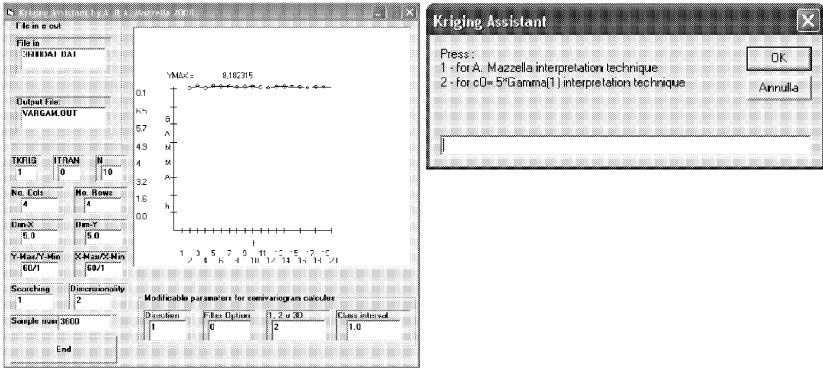


FIG. 7. On the left, it is shown the experimental semivariogram calculus result. On the right, it is shown the panel for the automatic interpretation technique selection.

Once the user selects the technique for the semivariogram modelling (Mazzella Al. et al., 2009), KA shows the graphical representation for the theoretical models (in the graphical output window) and the calculated values of “Nugget Effect”, “Range” and “Sill” (in the kriging configuration panel). At this point the kriging procedure starts clicking on the *KRG* button of the kriging configuration panel (fig.8); the data kriging can be initiated with the KA-calculated parameter or with a user-customized set. At the end of the interpolation step KA automatically generates two different kind of graphical results representation shown in fig.9.

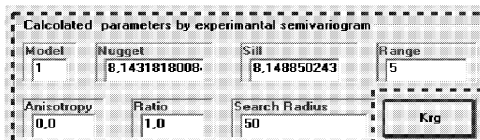


FIG. 8. The KA kriging configuration panel with the numerical results of the interpretation and, in blue, the kriging starting button.

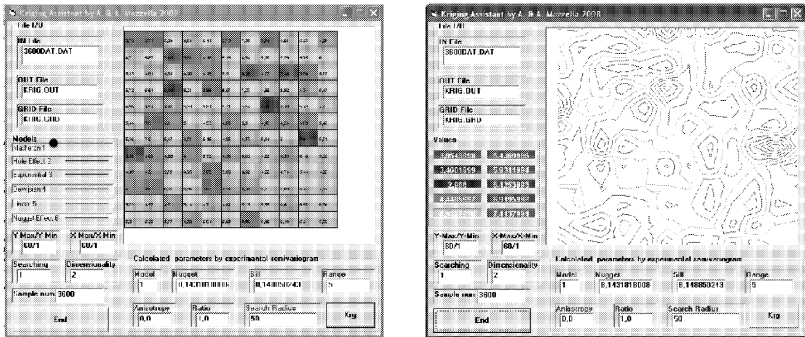


FIG. 9. KA evaluation graphical results: on the left the “block map”, on the right the “contour map”.

CONCLUSIONS

Thanks to the VB6 power and the capabilities of the GeoLIBs (Deutsch C. and Journel A., 1992), the current version of KA (v2.0/2009) is an efficient, powerful and user-friendly tool for the geostatistical esteem of any kind of environmental data. As underlined in the paper, the strength of KA compared to the other most famous data treatment software (e.g. Surfer) is that in KA there are no default settings and/or parameters for data interpolation: in fact KA bases the data interpolation upon the parameters calculated on the data. This features, obviously, allows also unskilled users to obtain accurate estimates. Our research team is still working mainly along the following directions: the first one focuses to improve the KA kriging variants (actually only *Point Kriging* is supported) meanwhile, the second one focuses to develop specific routines for linking the KA engine with a GIS environment.

REFERENCES

Mazzella, An. Pretti, S. and Valera, R. (1984). “Valutazione dei Giacimenti e Geostatistica. Risultati e prospettive.” *Industria Mineraria*, n. 6: 23-27.

Deutsch, C. and Journel, A. (1992). “Geostatistical Software Library and User's Guide.” *Oxford University Press*.

Carr, J.R. and Mela, K. (1998). “FGAM and JCBLOK Visual Basic Programs for One, Two, or Three-Dimensional Geostatistical Analysis.” *Computers & Geosciences*, n. 24: 531-536.

Mazzella, Al. Mazzella, An. and Valera, P. (2009). “Kriging Assistant: an innovative and automatic procedure for geostatistical analysis of environmental data.” *Proceedings of European Congress on Regional Geoscientific Cartography and Information Systems* Vol. 1: 85-88.

The Wells Simulator: Analytical Solutions for Groundwater Flow Using Modified Streamfunction Contouring

Holzbecher Ekkehard¹, Sauter Martin¹

¹Georg-August University Göttingen, GZG, Goldschmidtstr. 3, 37077 Göttingen; cholzbe@gwdg.de

ABSTRACT: The Wells Simulator is a groundwater modeling software that is especially designed for the simulation of groundwater well systems, with applications concerning pumping systems of water works, doublette systems for geothermal energy utilization, pump and treat systems for aquifer restoration, and water drainage systems for open pits. The advantage of its user-friendly graphical user interface (GUI) is that it can be applied by users, which are not familiar with the common modeling software. It is also an appropriate tool in a class-room for students, or for demonstration purposes.

INTRODUCTION

There are several application fields, in which knowledge concerning the interaction of groundwater wells is relevant. There are well galleries of water works. These usually consist of multiple pumping wells only, but sometimes these are combined with infiltration wells, in order to utilize water for artificial groundwater recharge. Such a combination of wells may be necessary for the entire water balance, in order to keep real groundwater extraction low. It may also be important in order to keep groundwater tables high and prevent strong drawdown in the cones of depression of pumping wells.

Another application field of increasing importance is geothermics, i.e. to utilize geothermal energy, which is CO₂-neutral, sustainable and renewable. Geothermal facilities are increasingly utilized for energy production, as well for heat as for power supply. A doublette, consisting of a pumping and an infiltration well, is a classical set-up, by which water of increased temperature is extracted from a near-surface or deep subsurface formation, and after heat utilization the cooled fluid is returned into the same aquifer horizon.

With the increased exploitation of heat stored in subsurface formations the installed systems become competitive and influence each other. The productivity and also the

lifetime of a single doublette may be drastically reduced by nearby further installations. Thus it is a severe challenge for decision makers and technicians, already in the planning phase, that hydraulic interactions of several systems are investigated.

A third field of application is the aquifer restoration technology. Polluted groundwater is pumped out at one location, treated in some ex-situ facility and pumped back after treatment into the aquifer at another location. The doublette system can be found here again again, in practice, however, often several pumping and recharging wells are combined. These may be arranged as systems of doublettes, but in practice the constellation of wells is irregular, based on appropriate conditions for well drilling and other circumstances.

A fourth application field is for pumping systems keeping a construction site or excavation pit drained. The problem is, to find optimal locations for pumping wells with which pumping rate have to be placed in order to keep a pit dry. This is a relevant task not only in the building, but also in the mining industry.

The *Wells Simulator* software is designed to assist in the planning phase of a well system before the installation and during operation of such systems. The program is equipped with a graphical user interface (GUI) that allows user-friendly input of parameters and visual output of results. The software is implemented in MATLAB and can be used directly from the command window, but main envisaged application is as a stand-alone executable.

The program can be used in classes for students, and by students in exercises. It is suitable as part of a demonstration task to explore the properties of a well system. Last not least it can be used as a first check, if conditions at a specific site are appropriate or not. The tool may serve for the decision maker, who has to compare several alternative sites; or for the technician in the field as well, who aims to find the optimal position of a well or well gallery.

To use the Wells Simulator requires less skill, than using a groundwater program – which is the common technique to be applied for such a purpose. For that reason it can be applied not only by groundwater specialists, but also by technicians in the field on the laptop, or by decision makers in non-technical departments of concerned companies.

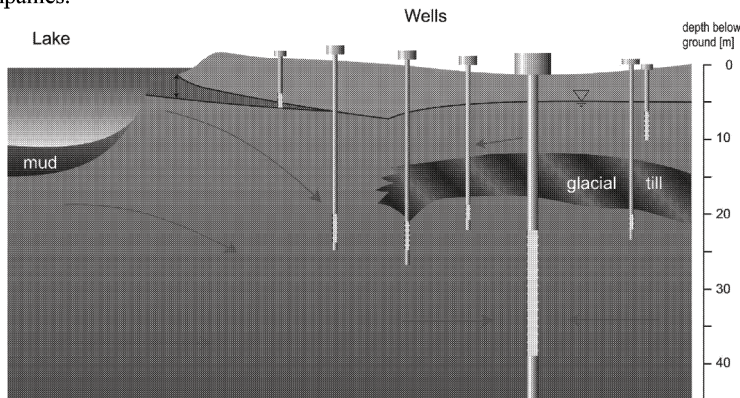


FIG. 1. A typical well gallery – cross-sectional view

The Well Simulator is implemented in MATLAB. Some more details concerning the programming are given by Holzbecher (2008), for a version tailored for the modeling of well systems for bank filtration. With reference to a first version the current working name is: Wells Designer, version 2. Some of the features mentioned in the following are currently tested, in order to present the final version at the conference.

In comparison to numerical methods analytical solutions have the advantage that they can be computed much faster and more accurately. The latter is due to the fact there are no numerical approximations involved. However, analytical solutions are available for specific situations only and can not compete with the flexibility of numerical methods concerning dimensions, boundary conditions, inhomogeneities, etc (Holzbecher & Sorek 2005).

In comparison to other software packages using analytical solutions (GFLOW, see: Haitjema 1995; TWODAN, see: Diodato 1998) the Wells Simulator stands out due to direct use of the streamfunction for the visualization of flowpath patterns. Details are outlined below.

DIFFERENTIAL EQUATIONS AND ANALYTICAL SOLUTIONS

The mathematical algorithms are implemented using analytical solutions based on potential theory. We give a brief outline of the details. The reader, who is interested in the background, will find them in the classical textbook of O. Strack (1989).

Groundwater flow modelling is based on Darcy's Law, given by the formula

$$\mathbf{v} = -K\nabla h \quad (1)$$

Equation (1) is an empirical relationship, that is well established for groundwater flow (Bear 1976, Holzbecher 1997). It states the proportionality between filtration (or Darcy-) velocity \mathbf{v} and dynamic pressure, here represented by hydraulic head h . The proportionality constant is the material parameter K , the so called hydraulic conductivity. K depends on the porous medium of the aquifer, but also on the density and viscosity of the fluid.

Two types of aquifers can be distinguished concerning the upper surface of the water bearing pore space, which may be either free or confined by an impermeable layer. The hydrogeologist speaks of an unconfined or phreatic aquifer in the first situation and of a confined aquifer in the second. The principle of mass conservation leads to variants of the continuity equation

$$\left. \begin{array}{l} \nabla \cdot H\mathbf{v} = 0 \\ \nabla \cdot h\mathbf{v} = 0 \end{array} \right\} \text{for } \begin{cases} \text{confined situations} \\ \text{unconfined situations} \end{cases} \quad (2)$$

where H denotes the aquifer thickness of the confined aquifer. Hydraulic head h is measured with respect to the aquifer basis. Combination of equations (1) and (2) yields partial differential equations for the unknown variable h :

$$\left. \begin{array}{l} \nabla \cdot HK\nabla h = 0 \\ \nabla \cdot hK\nabla h = 0 \end{array} \right\} \text{for } \begin{cases} \text{confined situations} \\ \text{unconfined situations} \end{cases} \quad (3)$$

Equation (3) is linear for the confined situation and nonlinear for the unconfined case.

Aquifer modeling in 2D is usually based on these differential equations. An alternative formulation is based on the hydraulic potential φ

$$\varphi = \begin{cases} K \cdot H \cdot h - \frac{1}{2} K \cdot H^2 + \varphi_0 \\ \frac{1}{2} K \cdot h^2 + \varphi_0 \end{cases} \text{ for } \begin{cases} \text{confined situations} \\ \text{unconfined situations} \end{cases} \quad (4)$$

for which the classical *potential equation* (or *Laplace equation*) holds

$$\nabla^2 \varphi = 0, \quad \text{in 2D: } \frac{\partial^2 \varphi(x, y)}{\partial x^2} + \frac{\partial^2 \varphi(x, y)}{\partial y^2} = 0 \quad (5)$$

(Strack 1989, Holzbecher 2007). The potential φ has the physical unit of [m³/s]. The constant φ_0 has to be chosen appropriately. In the Wells Simulator it is chosen to fulfil a point condition. In the implementation we utilize the complex potential $\Phi = \varphi + i\psi$ with imaginary unit i and streamfunction ψ .

The solution for a single well with pumping or recharge rate Q_{well} at the position z_{well} is given by:

$$\Phi = \frac{Q_{well}}{2\pi} \log(z - z_{well}) \quad (6)$$

Note that we apply the complex logarithm here, which is a generalization usual logarithm for complex numbers. Moreover the values of the complex logarithm are complex numbers also. The complex logarithm $\log(z)$ is well-defined on each simply connected part of the complex plane. It is not defined for $z=0$, and usually the negative real axis is used as a boundary, at which the function has a discontinuity. For details see textbooks on complex analysis, for example Krantz (2008).

In addition baseflow can be considered (that feature is not yet implemented in the current version). The analytic solution for a regional 1D flow field is:

$$\Phi = \bar{Q}_0 z \quad (7)$$

with baseflow discharge vector Q_0 , given by a complex number.

According to the principle of superposition, solutions for generic situations can be summed up as *analytical elements*, to obtain a solution for a specific situation. For a system of N wells and baseflow one can generally write the solution as:

$$\Phi(z) = \bar{Q}_0 z + \frac{1}{2\pi} \sum_{j=1}^N Q_{well}^j \log(z - z_{well}^j) \quad (8)$$

Streamline patterns are visualized as contour lines of the streamfunction ψ . For that purpose we identify the model region with a part of the complex plane, represented by the variable $z=x+iy$. The above mentioned discontinuity of the complex logarithm is cause of some problems in the visualization of the streamline pattern. Additional horizontal lines between the well positions and the left model boundary appear, if the contouring algorithm is applied in a straightforward manner. Holzbecher (2009) describes how this unrealistic feature can be avoided by a modification of the contouring procedure. A demonstration is depicted in FIG. 2.

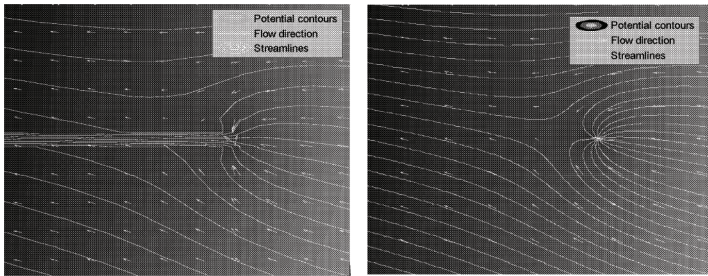


FIG. 2. Flow pattern in the vicinity of a single well, obtained by straight forward contouring (left) and modified contouring (right)

THE GRAPHICAL USER INTERFACE (GUI)

The program is equipped with a graphical user interface that is easy to handle. As the software is designed mainly for users which are not familiar with groundwater software, the software must be easy to understand and use.

The GUI is divided in several panels, most of which concern input values:

- Graphical output options
- Output parameters (2D)
- Aquifer characteristics
- Well system specification
- Gridding
- Numerical output

Optional graphical output is for: head contours, streamlines, velocity vectors, travelttime markers, and separatrices (limiting streamlines).

Aquifer parameters are: thickness, hydraulic conductivity, base flow, reference head and porosity.

The well system is three by vectors: one for the x-coordinates of the well locations, another for the y-coordinates and a third for the pumping rates. Pumping wells have positive pumping rate, recharging wells negative.

Note that gridding is used for plotting, not for the calculation of the solution – in contrast to numerical methods. The grid in x- and y-axis has to be specified by the user. The simplest way is to specify the minimum and the maximum values and a grid spacing for both coordinate directions.

Moreover the GUI has radio-buttons for optional graphical output in a separate figure, and for the additional graphical output as a surface or piezometric head as a surface above the model regime, i.e. as a 3D graphic. After setting all options the graphical output is initiated by using the 'Plot'-button. A help system can also be used in order to become familiar with the basic terms and handing of the program.

The graphical user interface (GUI) of the Wells Simulator is depicted in FIG. 3. Input and output are gathered in a single panel, as default. There is the option to obtain the graphical output in a separate window. An example input and output-view of the GUI is shown in FIG. 3.

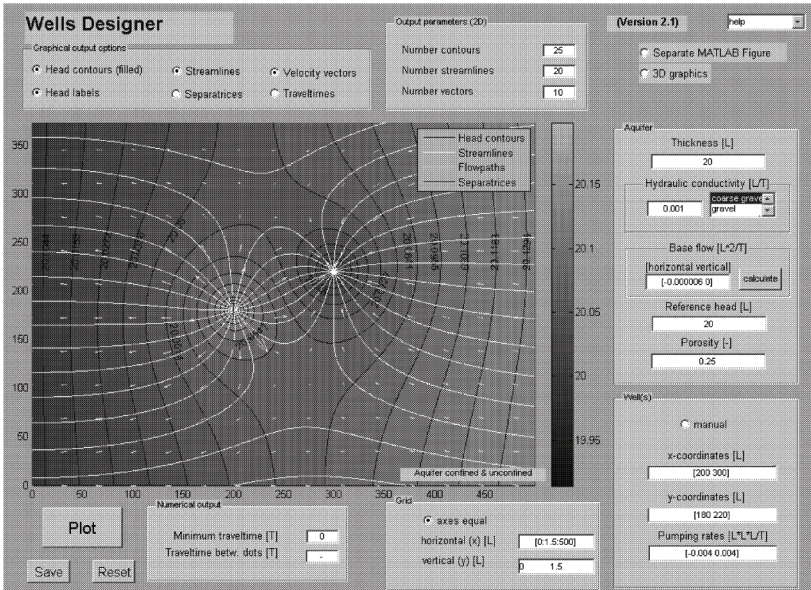


FIG. 3. The Wells Simulator Graphical User Interface; showing panels for numerical input and option selection, and the graphical result for a single doublet

EXAMPLE

One of the most generic situation concerns a single doublet within a constant ambient flow field. DaCosta and Bennett (1960) examined such constellations systematically for different angles of the background flow and for different ratios of ambient flow and pumping rate.

FIG. 4 provides a series of visualizations concerning the interaction of a pumping and a recharging well within baseflow at different angles between the doublet axis and groundwater flow direction. The figures depict flow patterns for angles of 0°, 55.5°, 90° and 180°. In the 0° case the flow comes from the left, in the 180° case from the right. For all scenarios the pumping rate Q_1 and the background discharge Q_0 are chosen to fulfill the following equation for the dimensionless ratio:

$$\frac{Q_1}{\pi d Q_0} = 1.27 \tag{9}$$

where d denotes the half distance between the doublet wells. The figure demonstrates clearly that the angle has a significant effect on resulting flow pattern. There is no connection between the wells if flow comes from the left (top left subfigure), i.e. if the pumping well is located upstream. If the infiltrating well is located upstream, a circulating system results that is closed against the ambient flow

around it (lower right subfigure).

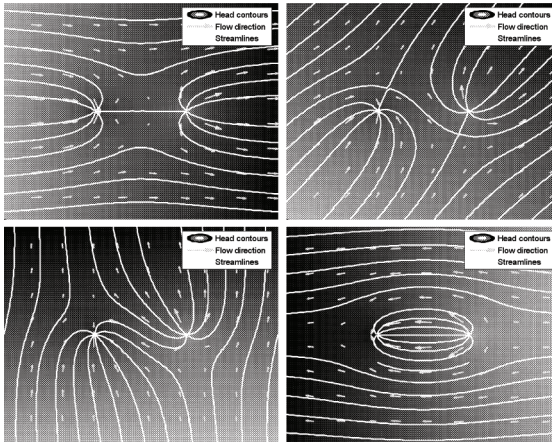


FIG. 4. Doublette flow connected with baseflow of different angles

At the conference the change of the solution with the angle between the doublette axis and groundwater flow direction will be demonstrated as a video! For a single doublette the video depicts the stagnation points and separatrices (limit streamlines) also.

CONCLUSIONS

Commercial groundwater modeling codes are almost all based numerical methods are given the preference. Common numerical codes based on numerical methods allow irregular boundaries, general boundary conditions, inhomogeneities, transient effects, and 3D patterns – just to mention a few points. All these are not taken into account in the Wells Simulator. The purpose of this software is the evaluation of generic situations of well systems. The Wells Simulator is designed to be used

- if a numerical model is not envisaged,
- in order to support a decision whether the set-up of a numerical model is necessary or not, or
- before a numerical groundwater model effort is undertaken.

The use of the analytical solution has several advantages, in comparison to numerical solutions. The solutions given by equation (8) are grid independent. They can thus be computed **quickly** and **accurately** for the visualization. Moreover it is not necessary to specify a boundary of the model region and boundary conditions.

ACKNOWLEDGMENTS

The authors appreciate the support of 'Niedersächsisches Ministerium für Wissenschaft und Kultur' and 'Baker Hughes' within the GeBo G7 project.

REFERENCES

- Bear, J. (1976). "Hydraulics of groundwater", Mc Graw Hill, New York, 569p.
- DaCosta, J.A. and Bennett, R.R. (1960). "The pattern of flow in the vicinity of a recharging and discharging pair of wells in an aquifer having a real parallel flow"; in: IUGG Gen. Ass. of Helsinki, IAHS Publ., No. 52, 524-536.
- Diodato D.M. (1998). "Software Spotlight", *Groundwater*, Vol. 36(3), 389-390.
- Haitjema H.M. (1995). "Analytic Element Modeling of Groundwater Flow", Academic Press, San Diego.
- Holzbecher, E. (1997). "Modellierung dynamischer Prozesse in der Hydrologie: Grundwasser und ungesättigte Zone", Textbook incl. Software on CD-ROM, Springer Publ., Heidelberg.
- Holzbecher, E. (2007). "Environmental Modeling – using MATLAB", Springer Publ., Heidelberg, 392p.
- Holzbecher, E. (2009). "Streamline visualization for potential flow with singularities – with applications in groundwater flow", submitted.
- Holzbecher, E., Grützmacher, G., Amy, G., Wiese, B., Sharma, S. (2008). "The Bank Filtration Simulator - a MATLAB GUI"; in: Möller, A., Page, B., Schreiber, M. (eds), *EnviroInfo08: Environmental Informatics and Industrial Ecology*, Shaker Publ., 359-365.
- Holzbecher, E., Sorek S. (2005). "Numerical Models of Groundwater Flow and Transport"; in: Anderson M. (ed.) *Encyclopaedia of Hydrological Sciences*, Wiley, Vol. 4, Part 13, Art. 155, 2401-2414.
- Krantz, S.G. (2008). "Complex variables – a physical approach with applications and MATLAB", Chapman & Hall, Boca Raton, 421p.
- Strack, O.D.L (1989). "Groundwater mechanics", Prentice Hall, Englewood Cliffs, 732p.

Rapid Drawdown of Water Table in Layered Soil Column

Hong Yang¹, Harianto Rahardjo², and Daping Xiao³

¹Parsons Brinckerhoff, 303 2nd St, 700N, San Francisco, CA 94107, USA; yangh@pbworld.com

²School of Civil and Environmental Engineering, Nanyang Technological University, Singapore; chrahardjo@ntu.edu.sg

³Institute of Foundation Engineering, China Academy of Building Research, Beijing, China; xiaodaping1234@yahoo.com.cn

ABSTRACT: Tests of rapid drawdown of water table were performed in two one-meter-high soil columns of finer- over coarser-grained soils. The columns were instrumented with tensiometers for pore-water pressure measurements. The test was started from a saturated, hydrostatic condition and after drawdown the final water table was stabilized at the bottom. The test results show that a segregation of pore pressures across the finer-coarser soil interface began immediately after the drawdown was started. An isolated zone with positive pore pressures formed in the finer layer and the pore pressures dissipated in a relatively slow rate. At the same time, a new water table formed in the coarser layer and dropped to the bottom rapidly. The entire column reached a new hydrostatic condition after several days. The observed behavior was due to the sharp contrast in soil hydraulic properties across the soil interface.

INTRODUCTION

Vertical infiltration in layered soils under unsaturated conditions has always been of interest due to the contrast in soil hydraulic properties across the soil interface and the subject has been studied by a number of researchers (e.g., Ross, 1990; Stormont and Anderson, 1999; Morbidelli et al., 2008). The infiltration process involved in these studies was generally a downward water flow caused by applying a flux from the top. These studies show that pore-water pressures changed drastically across the soil interface during infiltration. However, vertical drawdown of water table in layered soils, especially under a rapid drawdown condition, has not been widely reported in the literature. On the other hand, many geotechnical problems involve infiltration under a drawdown condition, such as soil slope stability (Duncan et al., 1990; Lane and Griffiths, 2000; Viratjandr and Michalowski, 2006). Therefore, detailed information about drawdown infiltration may be helpful for a better understanding of the associated geotechnical problems. In this paper, two rapid drawdown tests were performed in two instrumented soil columns of finer- over coarser-grained soils in the laboratory and the results are presented and discussed.

TEST METHOD

The drawdown tests were conducted in one-meter-high soil columns constructed in transparent acrylic cylinders with an internal diameter of 190 mm. The soil columns were instrumented with a tensiometer-transducer system together with a data logger to automatically measure pore-water pressures along the column. Schematic of the soil column is illustrated in Fig. 1. Details of the column set-up have been documented by Yang et al. (2004). Transient infiltration behavior observed in soil columns using the set-up by applying a flux on the top has also been reported by Yang et al. (2006).

Two soil columns (A and B) were constructed as summarized in Table 1. The soils were placed and compacted in 100 mm lifts to ensure soil homogeneity. Basic properties of the soils in the soil columns are also summarized in Table 1, and the grain size distributions of the soils are presented in Fig. 2. The saturated permeability (k_s) of the Medium Sand and the Fine Sand were investigated using the constant head method. The k_s values of the Clayey Sand and the Silty Sand were calculated from the saturated upward infiltration tests (the results are not presented in this paper) in the respective soil columns.

After the soil column was constructed, the column was first saturated by filling it with water from the bottom at a very small hydraulic gradient in order to minimize the disturbance to the soil structure. Then a rapid drawdown test was carried out. The top of the soil column (elevation $z = 1.00$ m) was always covered to prevent evaporation. The water table was maintained constant at the bottom of the soil column (elevation $z = 0$). Drainage was collected through an outlet at the bottom and was weighed periodically to obtain the drainage rate during the test. The position of the outlet was also always kept exactly at the bottom of the soil column.

Table 1. Summary of the Soil Columns, Tests and Basic Soil Properties.

Soil Column	Column A		Column B	
Drawdown Test	Test A		Tests B	
Soil Layer	Finer (upper)	Coarser (lower)	Finer (upper)	Coarser (lower)
Layer thickness (mm)	650	350	600	400
Soil Name	Clayey Sand	Medium Sand	Silty Sand	Fine Sand
Unified Soil Classification	SC	SP	SM	SP
Specific gravity	2.64	2.60	2.59	2.65
Liquid limit	31%	–	48%	–
Plasticity index	10	–	21	–
Dry density (kN/m^3)	17.2	16.9	14.7	15.6
Void ratio	0.535	0.538	0.762	0.699
Porosity	0.348	0.350	0.432	0.411
Water content at saturation	20.3%	20.7%	29.4%	26.4%
Permeability, k_s (m/s)	1.5×10^{-6}	2.0×10^{-4}	8.8×10^{-7}	2.7×10^{-4}

A rapid drawdown test began with a saturated, hydrostatic condition with the water table being located at the top ($z = 1.00$ m). The valve at the bottom of the soil column was suddenly and swiftly opened to its maximum position. Water immediately started to flow out. The pore-water pressures at different elevations along the soil column and the cumulative drainage were measured during the entire test. The test ended when the soil column reached a new hydrostatic condition with the final, stable water table at the bottom (elevation $z = 0$).

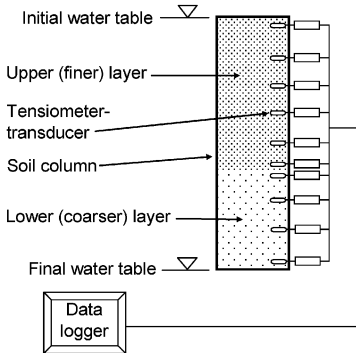


FIG. 1. Schematic of soil column.

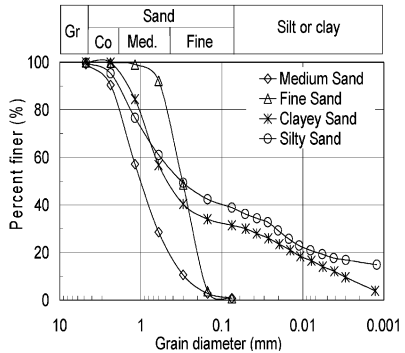


FIG. 2. Soil grain size distributions.

TEST RESULTS AND DISCUSSIONS

Drawdown in Clayey Sand over Medium Sand (Test A). The pore pressure versus time in Test A is presented in Fig. 3 which shows the general process of the test. The pore pressures decreased immediately and became negative shortly after commencement of the drawdown test. As time elapsed, the negative pore pressures developed steadily at different elevations. The entire soil column reached a new hydrostatic condition about 16 days after the drawdown when there was essentially no further decrease in the pore pressures. Corresponding to the changes in pore pressures, the changes in the drainage rate (Fig. 4) also reflected the entire process of the drawdown. The drainage rate was relatively large at the beginning and became smaller and smaller as time elapsed. At the end of the test, the drainage rate was on the order of 10^{-9} m/s which is very low.

A close examination of the drawdown process indicates that the developments of the pore pressures in the finer soil layer and the coarser soil layer were totally different (Figs. 5 and 6). The pore pressures dropped from positive to completely negative values in less than 4 minutes in the coarser soil layer but in about one hour in the finer soil layer (Fig. 6). In addition, the decrease of the pore pressures in the finer soil layer started from the lower portion of the layer (i.e., near the soil interface) first, then gradually extended to the upper portion of the layer. These observations indicate that the distinct difference in the hydraulic properties of the two soils across the soil interface resulted in an extremely non-uniform distribution and development of pore pressures across the soil interface. There was an apparent pore pressure segregation

between the two soils across the soil interface. This distinct difference gradually diminished at the later stage of the test when the pore pressure approached hydrostatic conditions. When hydrostatic pressure was reached, there were no further changes in the pore pressures as the total head along the soil column was constant and the hydraulic gradient was zero at all locations.

The drawdown process can be further examined by the changes in water tables that are indicated by the zero pore pressures (Fig. 7). In the coarser soil layer, the segregation of the pore pressure across the soil interface shortly after the rapid drawdown resulted in the emergence of a temporary, new water table (point of zero pore pressure). The new water table was first recorded at the elevation of $z = 0.34$ m (which was immediately below the soil interface $z = 0.35$ m) at an elapsed time of

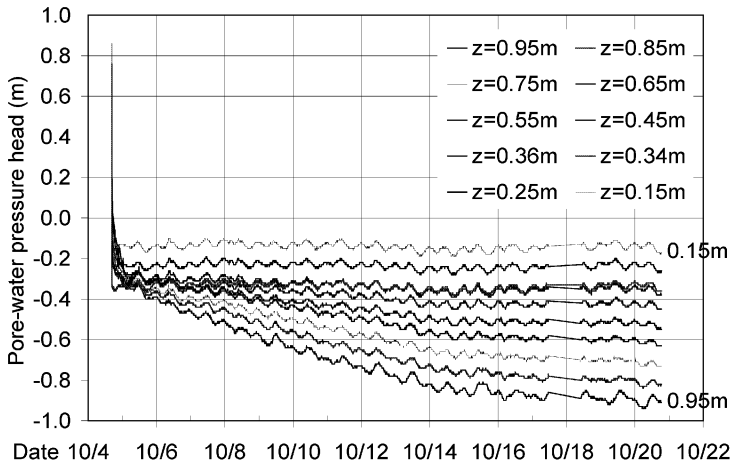


FIG. 3. Pore pressure vs time in Test A (Clayey Sand over Medium Sand).

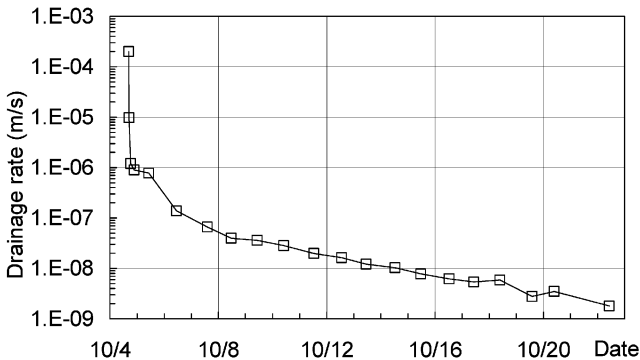


FIG. 4. Drainage rate vs time in Test A (Clayey Sand over Medium Sand).

about $t = 38$ s (Fig. 6). The new water table continuously moved down and reached the bottom of the soil column at about $t = 4$ min (Fig. 7).

In the finer soil layer, following the downward movement of the initial water table (at $z = 1.00$ m), a new and lower free water surface (or a “down-hang” water table, which had zero pore pressure) formed just above the soil interface (Figs. 6 and 7) and gradually moved upward. Between the two water tables is an isolated zone with excess pore pressures. However, the excess pore pressures dissipated in about one hour ($t = 1$ h) when the initial water table and the new water table converged at the elevation of

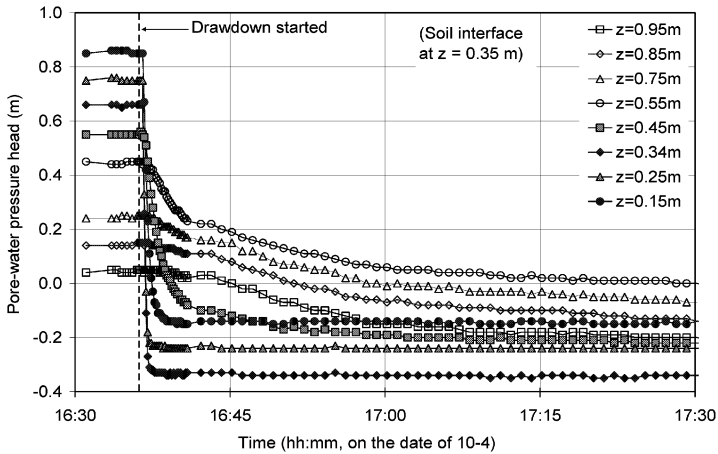


FIG. 5. Detailed pore pressure vs time in Test A (Clayey Sand over Medium Sand).

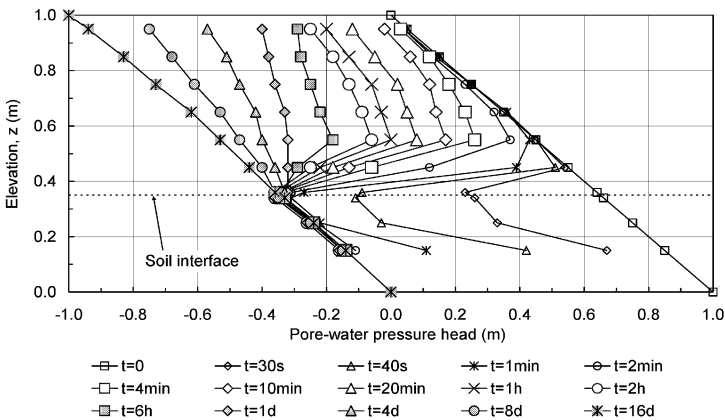


FIG. 6. Pore pressure head profiles in Test A (Clayey Sand over Medium Sand).

$z = 0.55$ m. Thus, all water tables disappeared and the pore pressures became negative along the entire soil column. The water tables in the finer soil layer changed at a much smaller rate as compared to that in the coarser soil layer due to the much lower soil permeability of the finer soil layer.

Drawdown in the Silty Sand over the Fine Sand (Test B). A rapid drawdown test (Test B) that was similar to Test A was conducted in the soil column of the Silty Sand over the Fine Sand. The test was also started from a saturated hydrostatic condition with an initial water table located at the top of the soil column ($z = 1.00$ m) and the final water table was maintained at the bottom of the soil column ($z = 0$). The results are shown in Figs. 8, 9 and 10. In general, the process of change in pore pressure in

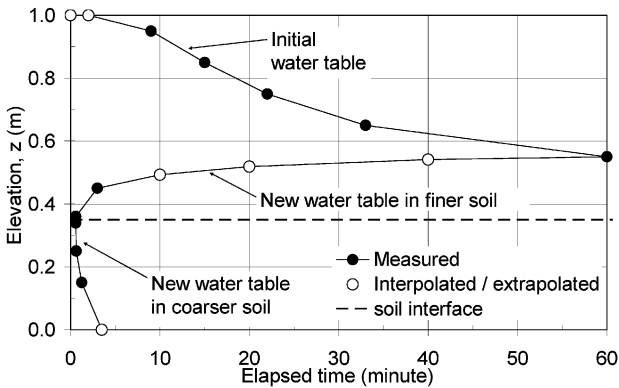


FIG. 7. Change in zero pore pressures in Test A (Clayey Sand over Medium Sand).

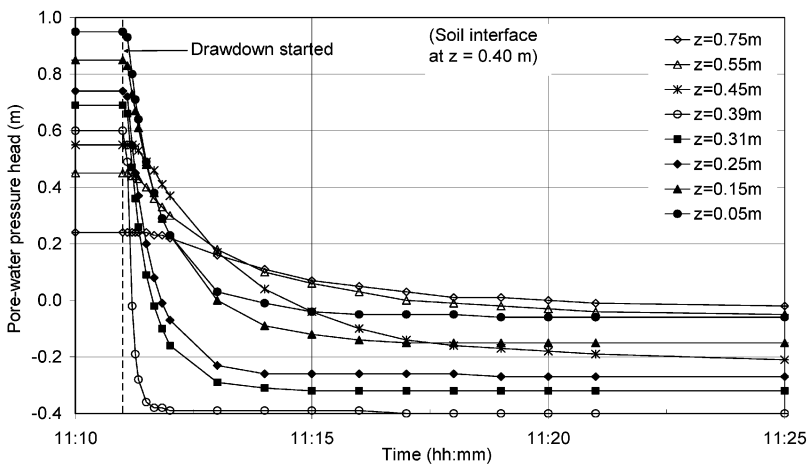


FIG. 8. Detailed pore pressure head vs time in Test B (Silty Sand over Fine Sand).

Test B was similar to that in Test A. The segregation of pore pressures across the soil interface ($z = 0.40$ m) was apparent due to the large contrast of the soil hydraulic properties. The pore pressures dropped to zero in less than 4 min in the coarser soil layer but in about 27 min in the finer soil layer. An isolated zone with excess pore pressure formed in the finer soil layer shortly after the drawdown was started (Fig. 10). The entire soil column reached a new hydrostatic condition in 4.5 days (Fig. 9).

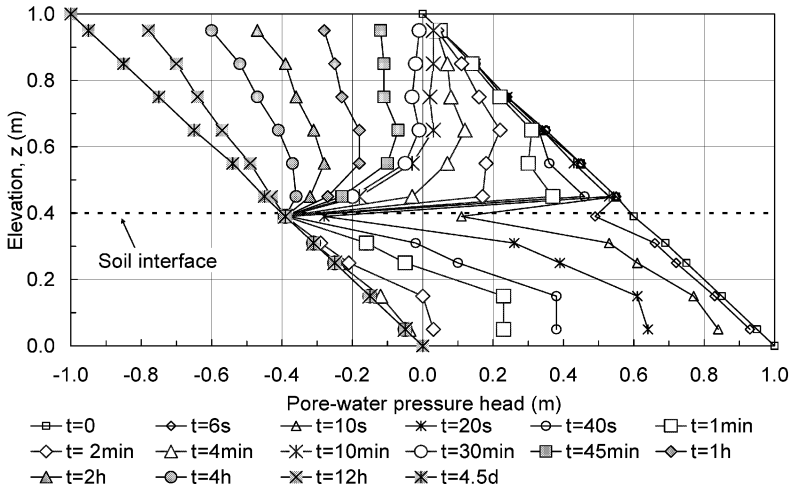


FIG. 9. Pore-water pressure head profiles in Test B (Silty Sand over Fine Sand).

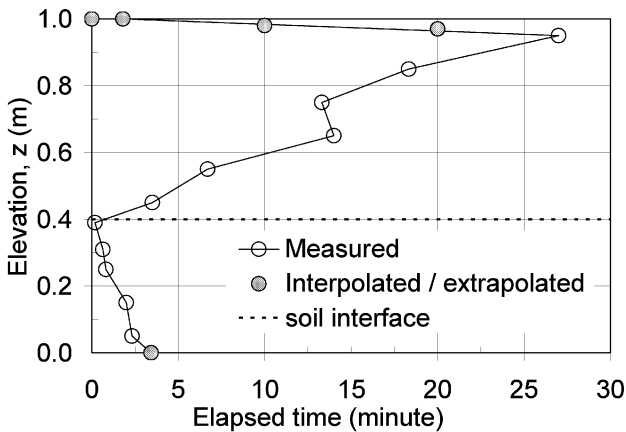


FIG. 10. Development of zero pore pressures in Test B (Silty Sand over Fine Sand).

CONCLUSIONS

The tests of rapid drawdown of water table conducted in the soil columns of finer-over coarser-grained soils show that the pore pressures changed drastically across the soil interface shortly after the water table drawdown was started from the top to the bottom of the soil column. A new water table developed in the coarser soil layer and dropped to the bottom of the soil column rapidly, while an isolated zone with excess pore pressures formed in the finer soil layer and the pore pressures dissipated at a relatively slow rate. The entire soil column reached a new hydrostatic condition with the final water table being located at the bottom of the soil column.

ACKNOWLEDGMENTS

The first author is grateful to Nanyang Technological University, Singapore for the Master's degree research scholarship granted between 2000 and 2002, and to colleagues at Parsons Brinckerhoff for their insightful review comments.

REFERENCES

- Duncan, J.M., Wright, S.G., and Wong, K.S. (1990). "Slope stability during rapid drawdown", in *H. Bolton Seed Symposium*, Vol. 2, University of California at Berkeley, 253-272.
- Lane, P.A. and Griffiths, D.A. (2000). "Assessment of stability of slopes under drawdown conditions", *Journal of Geotechnical and Geoenvironmental Engineering*, ASCE, 126(5): 443-450.
- Morbideilli, R., Govindaraju, R.S., Corradini, C., Saltalippi, C. and Flammini, A. (2008). "A preliminary analysis of field-scale infiltration into layered soils". In *Proceedings of the World Environmental and Water Resources Congress*, edited by R.W. Babcock and R. Walton. May 12-16, Honolulu, Hawaii.
- Ross, B. (1990). "The diversion capacity of capillary barriers." *Water Resource Research*, 26(10): 2625-2629.
- Stormont, J.C. and Anderson, C.E. (1999). "Capillary barrier effect from underlying coarse soil layer". *Journal of Geotechnical and Geoenvironmental Engineering*, ASCE, 125(8): 641-648.
- Viratjandr, C. and Michalowski, R.L. (2006). "Limit analysis of submerged slopes subjected to water drawdown". *Canadian Geotechnical Journal*, 43, 802-814.
- Yang, H., Rahardjo, H., and Leong, E.C. (2006). "Behavior of unsaturated layered soil columns during infiltration". *Journal of Hydrologic Engineering*, ASCE, 11(4): 329-337.
- Yang, H., Rahardjo, H., Wibawa, B., and Leong, E.C. (2004). "A soil column apparatus for laboratory infiltration study". *Geotechnical Testing Journal*, ASTM, 27 (4): 347-355.

The Effect of Clay Content on Filter-Cake Formation in Highly Permeable Gravel

Fan-Lu Min¹, Wei Zhu², Xiao-Rui Han³, Xiao-Chun Zhong⁴

¹PhD student, Geotechnical Research Institute, Hohai University, Nanjing, P.R. China, 210098; minfanlu@126.com

²Professor, College of Environmental Science and Technology, Hohai University, Nanjing, P.R. China, 210098; National Engineering Research Center of Water Resources Efficient Utilization Engineering Safety, Hohai University, Nanjing, P.R. China, 210098; weizhu863@126.com

³Master, Geotechnical Research Institute, Hohai University, Nanjing, P.R. China, 210098; hanxiaorui123@126.com

⁴Doctor, College of Civil Engineering, Hohai University, Nanjing, P.R. China, 210098; xchzhong@tom.com

ABSTRACT: Yangtze River tunnel in Nanjing, China, was constructed by slurry shield tunnelling method. Along the 3020m tunnel, one of the construction difficulties is to pass through a gravelly sand stratum. As this stratum is highly permeable subjected to an elevated water pressure, one of the key issues is the formation of filter cake for a stable cutting face during tunnel excavation. To solve this specific engineering problem, a series of permeability tests were carried out on samples taken from the gravelly sand stratum and slurry materials used in the Yangtze River tunnel project. A new apparatus was developed to simulate the filter cake formation on the surface of the gravelly sand under elevated pressure, through which the quantities of the discharged water were measured. The effects of clay content of the slurry on the thickness and permeability of filter cake were studied. The test results indicated that the clay content of the slurry played an important role in the filter cake formation. The amount of seepage through the gravelly sand and the thickness of the filter cake decreased with the increasing of the clay content in slurry.

INTRODUCTION

Slurry type shield tunnelling is widely used in tunnel construction in saturated, granular and highly permeable ground. One of the key issues for its successful

operation is how to form a filter-cake to protect the working face (Anagnostou et al., 1994; Koyama et al., 2003; Li et al., 2009). However, there are too many influencing factors of it, such as the permeability of the ground, the setting of mud pressure, the properties of the slurry (density, viscosity, stability, grain size distribution etc.), etc. (Piers et al., 1982; Zhang et al., 2004). As the permeability of the ground is inherent, and the setting of the mud pressure is also at a small range, it is important to study the effect of the properties of slurry on filter-cake formation, especially in highly permeable ground.

Past studies on the formation of filter-cakes were focused on the model tests in the laboratory. Cheng (2001) conducted laboratory model tests for pure bentonite suspensions in medium coarse sand, and the results showed that the density and viscosity of suspensions had a great impact on the filter cake formation. Fritz (2007) developed an apparatus for measuring the support pressure of slurry and conducted the support pressure tests to evaluate the best combination of additives such as polymer, sand and vermiculite (0.7~4mm). The successful excavation of Zimmerberg Base Tunnel proved the validity of the laboratory tests. Han and Zhu (2008) evaluated the factors that controlling the filter cake formation based on some tests conducted by a modified permeameter. This study indicated that the higher the viscosity of the slurry was, the denser the resultant filter cake would be.

Recently the slurry shield mode of the TBM was used to construct the Yangtze River tunnel in Nanjing, one of the three Yangtze River tunnels in China. Its diameter was approximately 14.93 m. Along the 3020 m tunnel, one of the construction difficulties was to pass through a highly permeable gravel stratum (its permeability coefficient was about 3×10^{-4} m/s) under elevated water pressure. Therefore, it was a key issue whether filter-cakes can be formed to maintain the stability of cutting face during tunnel excavation. FIG. 1 shows the grain size distribution of the gravel samples. 40% of the particles are coarser than 2 mm and the clay content was less than 5%. A laboratory testing program was conducted to study the effect of clay content on the physical stability of the slurry and formation of filter cake in highly permeable ground.

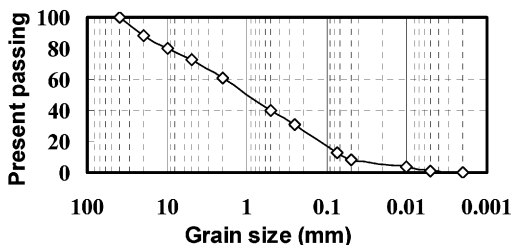


FIG. 1. Grain size distribution of the gravel samples.

LABORATORY EXPERIMENTS

Five groups of slurries with different clay content but similar viscosity and density were prepared from the slurry materials used in the Nanjing Yangtze River tunnel project. The basic properties of the slurries are summarized in Table 1 and the grain size distribution curves are shown in FIG. 2.

Table 1. Basic properties of the five groups of slurries

Sample no.	Clay content* (%)	Silt content (%)	Funnel viscosity (s)	Density (g/cm ³)
1	47.32	52.2	23	1.18
2	38.43	58.6	22.4	1.18
3	31.75	60.3	22.5	1.18
4	19.2	68.8	22.9	1.18
5	6.83	65.2	22.7	1.18

* grain size smaller than 5 μ m.

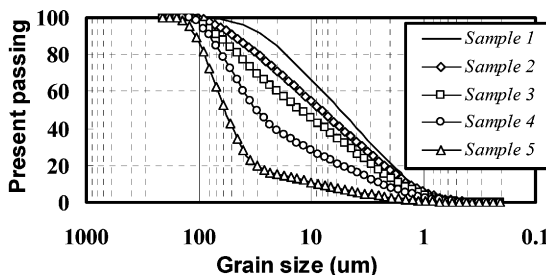


FIG. 2. Grain size contribution curve of the slurry samples.

FIG. 3 shows the schematic layout of the testing apparatus for evaluating the water discharge through the slurry under a constant hydraulic pressure and the thickness of the filter cake formed on the gravelly soil. First a Perspex tube (8 cm diameter and with calibration on it) was filled with a filter bed and gravel which was saturated with water from below. Then the slurry was added and the tube was closed by a piston. Subsequently a vertical pressure was applied at the top of the piston. The slurry seeped through the gravel layer and the amount of water expelled into the container was measured. Meanwhile, the thickness of the formed filter cake can be measured by the calibration on the plastic tube. The tests were conducted at applied pressure ranging from 0 to 0.3 MPa. Both the penetration depth into the gravel layer and the volume of discharged water increased with the increasing applied pressure. When the changing speed of water discharge became steadily, the corresponding time

was the formation time of the filter cake.

INTERPRETATION OF TEST RESULTS

FIG. 4 shows permeability test results of the five different slurry samples used in the study. As the volume of the discharged water reaches a steady value, the filter cake is formed on the surface of the gravel layer. The figure also shows that the volume of discharged water increases with decreasing clay content. In particular the volume of discharged water for slurry sample 5 (clay content of 6.83%) reaches a value about 350 ml. The greater the volume of discharged water is, the poorer the corresponding filter-cake formation will be. As more discharged water can lead to more loss of the slurry and may reduce the stability of the working face during the tunnel excavation. The volume of discharged water is a possible parameter for evaluating the quality of filter-cake formation. For slurry shield tunnelling in the gravel deposit, one of the key problems is the high permeability of the stratum, which causes a significant loss of slurry and the required support pressure cannot be built up at the working face of the excavation. One of the essential evaluating parameters is the permeability coefficient (PC) of the resultant filter cake.

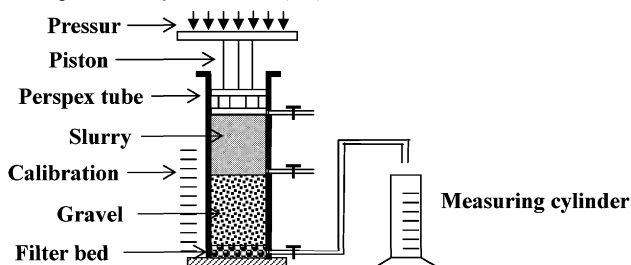


FIG. 3. Apparatus for measuring volume of water discharged and thickness of filter cake.

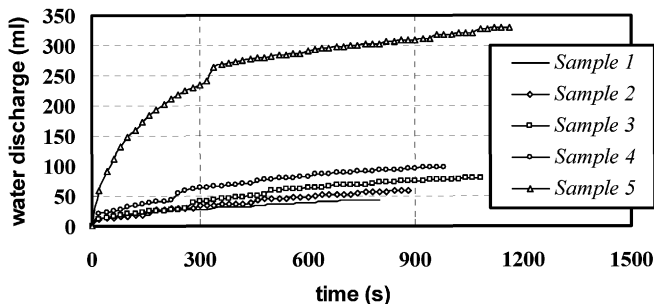


FIG. 4. Results of permeability tests of the slurry samples.

FIG. 5 shows the relationship between the thicknesses of filter-cakes and the clay content of the slurries. It is obvious that with the increasing clay content in the slurry, the thickness of the corresponding filter-cake becomes thinner. Based on the volume of discharged water (in FIG. 4) and these thicknesses of filter-cakes, the PC of the filter cake can be obtained by the Darcy's Law. FIG. 6 shows that the PC of the filter cakes and they decrease with the increasing clay content of the slurry. When the clay content is 47%, the PC of the filter cake is 2.96×10^{-7} cm/s, which is nearly two orders of magnitude lower than that for 6% clay content. Thus, the higher the clay content is, the denser the resultant filter cake will be, and the better its quality is.

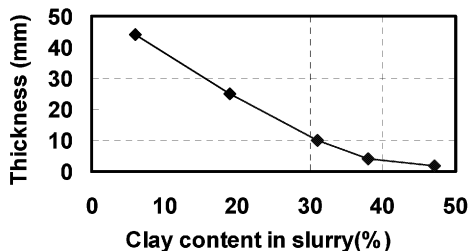


FIG. 5. Relationship between thickness of filter-cakes and clay content of slurry.

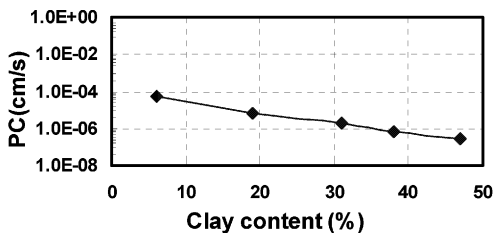


FIG. 6. Relationship between coefficient of permeability of filter cake and clay content of slurry.

Besides the PC of the filter cake, the formation time is another parameter for evaluating the quality of the filter cake. During the field excavation, the filter cake formation is a dynamic process, i.e. it is formed and destroyed. Therefore, the formation time of the filter cake should be very short. The formation time of the filter cake for the slurry sample 5 is nearly 300s (see FIG. 4), which was very dangerous for slurry shield tunnel projects. On the other hand, for slurry samples 1 to 4, the formation time is within several seconds.

CONCLUSIONS

The following conclusions are drawn from this study:

1. The permeability coefficient (PC) and formation time of the filter cake are two important parameters for evaluating the quality of filter cakes. The lower the PC is and the faster the filter cake forms, the better the quality of the filter cake will be.
2. As has a great impact on the formation of filter cakes in gravel deposit, the clay content of slurries can be an indicator of adjustment during the advancing of slurry shields. For a given density and viscosity, the higher the clay content of slurry is, the easier the filter cake will be formed and the denser the filter cake is.

ACKNOWLEDGMENTS

The research project was conducted with funding provided by the National Natural Science Foundation of China through Grant No.50908075. The authors also deeply appreciate the help of Dr Abraham C.F. Chiu, Hohai University.

REFERENCES

- Anagnostou, G. and Kovári, K., (1994). "The face stability of slurry shield driven tunnels." *Tunnelling and Underground Space Technology*, Vol. 9 (2):165-174.
- Cheng, Z.L., Wu, Z.M. and Xu, Y.Y. (2001). "Experimental Study on Stability of Excavation Face of Slurry Shield Tunnel Construction in Sandy Ground." *Journal of Chang Jiang Academy*, Vol.18 (5):53-55. [In Chinese]
- Fritz, P. (2007). "Additives for slurry shields in highly permeable ground." *Rock Mechanics and Rock Engineering*, Vol.40(1): 81 - 95.
- Han, X.R. and Zhu, W. (2008). "Influence of slurry property on filter cake quality on working face of slurry shield." *Rock and Soil Mechanics*, Vol. 29 (Supp):288-292. [In Chinese]
- Koyama, Y. (2003). "Present status and technology of shield tunnelling method in Japan." *Tunneling and Underground Space Technology*, Vol.18(2): 145-159
- Li, Y., Emeriault, F., Kastner, R. and Zhang, Z.X. (2009). "Stability analysis of large slurry shield-driven tunnel in soft clay." *Tunnelling and Underground Space Technology*, Vol. 24, 472-481.
- Piers, G., Harding. (1982). "High density slurry shield extends Japanese technology." *Tunnels & Tunnelling*, January/February: 55-56.
- Zhang, F.X, Zhu, H.H and Fu, D.M. (2004). "Shield Tunnel." Beijing People's Communication Press. [In Chinese].

Remote Sensing and GIS for Groundwater Mapping and Identification of Artificial Recharge Sites

Rajat C. Mishra¹, Biju Chandrasekhar², and Ranjitsinh D. Naik³

¹Sr. Engineer, Multit Mantech International Pvt. Ltd., Ahmedabad, India; rajat122@yahoo.co.in

²Member Technical Staff, Geomatics Solution Development Group - Center for Development of Advanced Computing (CDAC), Pune, India; c.biju@yahoo.co.in

³Retd. Geologist, Ground Water Survey and Development Agency, Pune, India; ranjitsinhnaik@gmail.com

ABSTRACT: Groundwater exploration is based upon terrain characteristic along with geology, structure, geomorphology, landuse and other parameters. These thematic information's generated using remote sensing and GIS technique can be used for evaluation of groundwater resources. In order to achieve the objective it is essential to systematically organize the database and check out every possibility of inter thematic and interclass dependencies and variability operating in nature. In the present study an attempt has been made to use Multi Criteria Evaluation technique to evaluate the interclass and intermap dependencies for ground water resource evaluation in a mini-watershed of Bhima River. The individual class weights and map scores were determined through Satty's Analytical Hierarchy Technique. These weights were applied in linear summation equation to obtain a unified weight map containing due weights of all input variables, which was further reclassified to arrive at groundwater potential zone map based on which the sites were selected for artificial recharge structures and the type of structure thereof are proposed.

INTRODUCTION

The occurrence of groundwater in hard-rock terrain is confined to joint, fractured and weathered portions. In India, about 65 per cent of the total geographical area is covered by hard-rock formations. Efficient management of surface water resources and groundwater development is required in such formations. Remote sensing data provide accurate spatial information and can be economically utilized over conventional techniques of groundwater studies.

GIS techniques involve the integrated and conjunctive analysis of huge volumes of multidisciplinary data, both spatial and non-spatial, within the same geo-referencing scheme. Through integration of these two spatial data management technologies,

groundwater development by water harvesting and artificial recharge can be well organized.

The present study is carried out through the preparation of hydrogeomorphological, drainage and other relevant thematic maps.

LOCATION OF STUDY AREA

The study area is bounded by latitude from $18^{\circ} 15' 10''$ N to $18^{\circ} 24' 30''$ N and longitude from $74^{\circ} 16' 10''$ E to $74^{\circ} 25' 00''$ E. The longest axis, along the highest to lowest elevation is in NW-SE direction and is approximately 21 km. Along the east-west direction, the average linear spread of the miniwatershed is about 8 km, while the average linear spread along the north-south direction is approximately 12 km. Thus the total area covered is approximately 87.74 sq km. The area is thinly populated and economically backward. There are in all 9 villages and 13 small hamlets with total population of about 12421 persons as per 2001 census.

MATERIALS AND METHODS

The methodology of the present study consists of the following four steps: in the first stage the main tasks were the collection of data (maps and reports, ground water data), downloading and preparation of satellite data. The methodology to be used was prepared during this stage. The second stage involved the import of data to the ERDAS IMAGINE software, geometric correction (Projection: UTM, Zone 43, WGS84). The following processes were performed in the third stage:

- Visual Image Interpretation classification of the Landsat-ETM Path-147, Row-047 Date: 14th November 1999 image for land use classification.
- Digitization of the drainage network, geologic and geomorphologic and soil maps and ground water fluctuation and recuperation map

In the final fourth step, the thematic maps were processed in GIS software (ArcGIS) and its extension, Spatial Analysis was used after the class ranking and calculation of different weights.

The Analytical Hierarchical Process (AHP) was deployed as it is suitable for complex decisions which involve the comparison of decision elements which are difficult to quantify. AHP is designated to aid decision makers (DMS) in making multi-attribute decisions. It consists of the following steps:

1. Development of hierarchy with an objective, alternatives and criteria.
2. Ranking and judgment of all criteria importance by comparing their priorities using pair wise comparison judgment matrix (PCJM) and a 9-point scale.
3. Calculation of weights and computation of consistency ratio (CR), which is considered consistent if it is less or equal to 10 %.

RESULTS AND DISCUSSION

Thematic Maps

Geomorphology: All the watersheds in Pune district have been classified into three categories viz. A, B and C. According to this classification, the study area falls in B-category, moderately dissected plateau (recharge zone). The Geomorphology Map of the study area shows that most of the area falls in the MDP-C zone, which characterises the area with thick weathered zone and moderate soil cover. The major portion is favourable from groundwater occurrence point of view. Also the southeastern part falls in the HDP-A to MDP-B zones, which is characterized by thin to negligible soil cover or exposed rock (**Fig. 1**).

Drainage: The Drainage Map of the study area (**Fig. 2**) shows that the area is drained mainly by centrally flowing major stream and its tributaries, which flow northwest to southeast direction within the watershed and occupy major part of the area. The major streams in the watershed exhibit considerably straight drainage course and abrupt change in flow direction, which indicates local structural control over the drainage course.

Geology: The area is part of the Deccan Volcanic Province comprising of hard rock formations. It is characterized by Deccan Volcanic Basalt. The Geology Map shows that simple flows are exposed higher up in the miniwatershed. These have greater thickness and consist of two major basaltic units i.e. upper vesicular-zeolitic basalt and lower massive basalt. The study of these basaltic units reveals that, the weathered, jointed and fractured zone, contact zones constitute the main water bearing zones (**Fig. 3**).

Soil: The soil thickness is more along the bank of river; The soil depth indicates the zone, which support a good growth of plants. The area comprises of shallow loamy calcareous soil and coarse shallow to medium black soil (**Fig. 4**).

Land Use: It is seen that the cultivable area is about 68 % of the total area of the miniwatershed. The irrigated areas are limited to the banks of streams and tributaries. The irrigation is completely based on the groundwater source. The hill slopes towards the north and northeastern part of the watershed are barren. The settlements are mainly located along the streams. (**Fig. 5**).

Water Level Fluctuation Map: In the study area total 405 observation wells have been identified for monitoring the groundwater levels. The observation well data indicates that the pre-monsoon and the post-monsoon water level trends are falling.

The Water Level Fluctuation Map generated for the study area is shown in (**Fig 6**). The areas with higher groundwater fluctuation, of the order of above 4 m indicate poor development of aquifer space. In the rest of the area, annual groundwater fluctuation ranges from 1 to 4m, indicating good aerial extent and development of aquifer space.

Well Recuperation Map: The recuperation of the water levels as observed in the observation wells has been studied and the recuperation rate map has been generated.

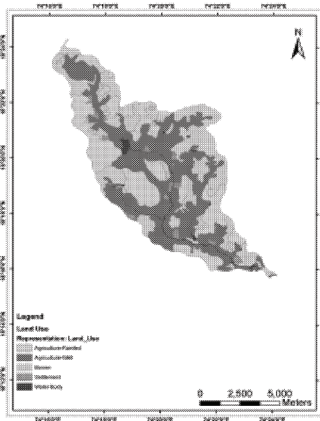


FIG. 5. Land Use Map.

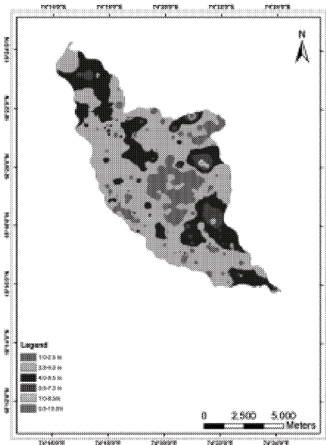


FIG. 6. Water Level Fluctuation Map.

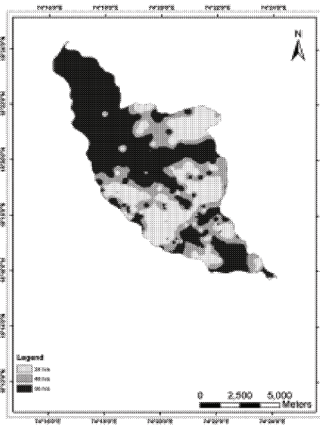


FIG. 7. Well Recuperation Map.

SUITABILITY ANALYSIS

Table 1 shows the different ranks assigned to different classes and the normalized weights of different combinations

Table 1. Pairwise Comparison of All Thematic layers.

	Geol-ogy	Geomor-phology	Soil	Fluctu-ation	Recuper-ation	Landuse	Weight	Nor. Wt.
Geology	1.00	2.00	4.00	6.00	8.00	1.00	0.04	4
Geomorphology	0.50	1.00	2.00	4.00	6.00	0.50	0.14	14
Soil	0.25	0.50	1.00	2.00	4.00	0.25	0.07	7
Fluctuation	0.17	0.25	0.50	1.00	2.00	0.17	0.32	32
Recovery	0.13	0.17	0.25	0.50	1.00	0.13	0.19	19
Landuse	1.00	2.00	4.00	6.00	8.00	1.00	0.25	25

These weights were fed into the multicriteria analysis of ArcINFO 9.3 software and a ground water recharge potential map was prepared using Weighted Overlay Process to identifying four classes namely high potential, moderately potential, low potential and poor potential. The resulting potential areas map is illustrated in **Fig 8**.

CONCLUSION

The areas where there is need for ground water and there is potential for recharge were classified into four zones, through the suitability analysis process, from which a site suitability map was prepared which gives 7.15 % of total area as high potential zone, 39.59 % of area as moderate potential zone, 47.70 % area as low potential zone and 5.50 % area does not have any potential or doesnot need recharge because of high water table. The presented methodology could serve as an effective method for groundwater development in arid environments. Thus, the classical methods such as geophysical works and interpretation of aerial photographs are better to be enhanced by a prior suitability analysis.

The sites identified provide a measure of the recharge potential of the location, for taking up the water conservation measure through the construction of artificial recharge structures such as check dams, percolation tanks, gabions structures, recharge wells / pits etc. The areas selected are overlaid with the drainage map of the watershed and water conservation and recharge structure are planned depending upon the catchment area, slope, underlying geology, soil permeability and other local factors **Fig 9**.

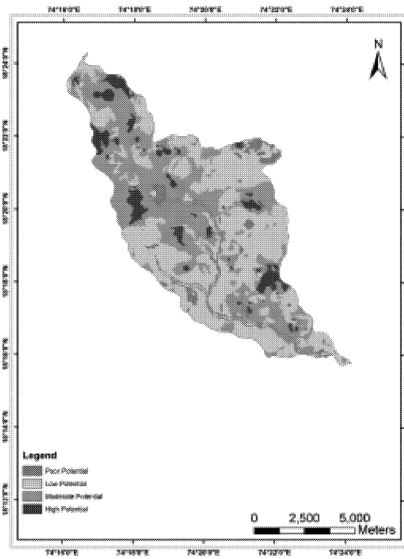


FIG. 8. Map showing potential recharge zones.

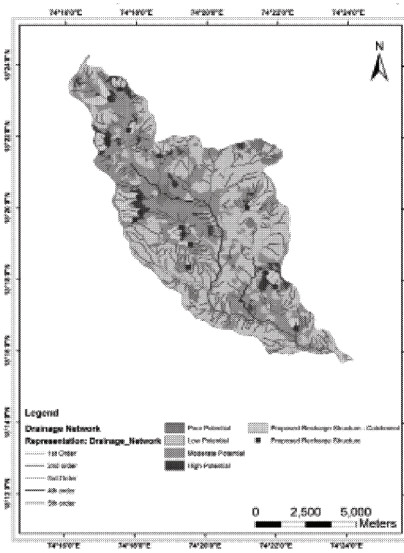


FIG. 9. Map showing potential recharge zones along with recharge structures.

REFERENCES

- Dinesh Kumar P. K. and Gopinath G (2007), *Application of Remote Sensing and GIS for the Demarcation of Groundwater Potential Zones of a river basin in Kerala, Southwest Coast of India*, International Journal of Remote Sensing, Vol. 28, No. 24, 20 December 2007, 5583–5601
- H. Vijith (2007), *Groundwater Potential In Hard Rock Terrain Of Western Ghats: A Case Study From Kottayam District, Kerala Using Resourcesat (IRS-P6) Data And GIS Techniques*, Journal of Indian Society of Remote Sensing, Vol. 35, No. 2, 2007. 164-171.
- Advanced Center for Water Resources Development and Management (2005), *Rapid Hydrogeological Study of Pondhe Watershed, Purandar Taluka, Pune District, Maharashtra*, August 2005.
- Ahmedou Ould Cherif A., R. Nagasawa and K. Hattori, Analytical Hierarchical Process, *Remote Sensing and GIS Integration for Groundwater Development*
- Debasish Das, *Integrated Remote Sensing and Geographical Information System Based Approach Towards Groundwater Development Through Artificial Recharge in Hard-Rock Terrain*.
- Dhiman S.C (2007), *Artificial Recharge of Ground water Aquifers and Ground Water Regulations*, National Ground Water Congress-Technical papers, September 2007, New Delhi.

Development of Discharge Capacity Testing Apparatus and Numerical Analyses of Test Results

Nam-Jae Yoo¹, Dong-Gun Kim², Dong-Won Lee³, and Sang-Hyun Jun⁴

¹Professor, Dept. of Civil Engineering, Kangwon National University, Korea; njyoo@kangwon.ac.kr

²Ph.D. course, Dept. of Civil Engineering, Kangwon National University, Korea; smap3d@kangwon.ac.kr

³MA course, Dept. of Civil Engineering, Kangwon National University, Korea; ldw1923@hanmail.net

⁴Full-time Lecturer, Dept. of Civil Engineering, Saekyung University, Korea; clays@saekyung.ac.kr

ABSTRACT: A discharge capacity testing apparatus able to reconstruct in the laboratory the condition of installing vertical drains in a field was built to investigate the discharge capacity of prefabricated vertical drains (PVD). The apparatus, with a mandrel, was designed to insert PVD into the ground. While changing the method of preparing the ground and installing drains, preliminary tests were carried out to investigate the discharge capacity of PVD in clay. Test results are discussed and analyzed with a numerical approach.

INTRODUCTION

Vertical drains have been used to improve soft clays since drains made from wood and cardboard material were introduced (Kjellman, 1948). The consolidation of thick clay deposits can be accelerated by installation of vertical drains. However, this is often delayed by formation of smear zones and the well resistance of the drains. For PVD, the discharge capacity of the drain is normally designed to be sufficiently large for the well resistance to be ignored. Various apparatuses and methods have been used for measuring the discharge capacity of vertical drains (Hansbo, 1983; Suits et al., 1986; Oostveen & Troost, 1990; Koerner & Lawrence, 1988; Bergado et al., 1996). As the value of discharge capacity is assessed, many factors influencing the discharge capacity, such as consolidation stress, deformation of the drain, time, clogging of the drain, hydraulic gradient and temperature, need to be considered (Bo, 2003). It is thus necessary to use an appropriate discharge capacity testing apparatus able to consider the dominant factors affecting the discharge capacity of PVD driven by a mandrel. Therefore, a newly designed apparatus able to reconstruct the condition of installing drains in a field is used in this

study.

APPARATUS AND MATERIALS USED

Fig. 1 shows a schematic of the discharge capacity testing apparatus. It is assembled with 5 stacked cylinders. Each cylinder is 25 cm in height and 50 cm in inner diameter. Loads are applied by air pressure via a rubber bag and a loading plate. A LVDT is mounted on a rod connected to the loading plate for measurement of the settlements. For given positions of inlet and outlet boxes, constant heads for supplying the flow through the PVD can be maintained. The volume of outflow is measured to estimate the discharge capacity of the PVD. Two pore pressure transducers are connected to a tube embedded in the soil so that excess pore pressures generated can be monitored. Fig. 2 represents details of the mandrel with the PVD and the air compressor system driving them into previously prepared ground. The mandrel driven by the hydraulic system is specially designed to fit into a slot located at the bottom of the cylinder and connected to the inlet valve.

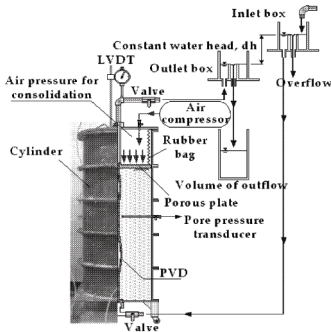


FIG. 1. Schematic of the apparatus

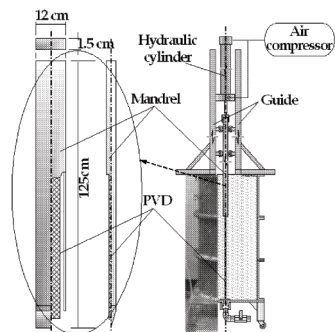


FIG. 2. Mandrel and driving system

The properties of the materials used in this study, soil and PVD, are summarized in Table 1. For modeling clay soil, bulk dry kaolinite in powder was purchased and used for tests.

TEST PROCEDURES

As a preliminary test for this study, two discharge capacity tests were performed while changing the way of installing the PVD, as presented in Table 2. For the case 1 test of driving the PVD with the mandrel, kaolinite in powder was mixed with water at an initial water content of 120 % (= 2 LL) and poured into the apparatus. Consolidation pressure in stages up to 20 kPa was applied during a period of 3 months. A rectangular shape of mandrel (12 cm×1.5 cm) was used to insert the PVD into the soil. The mandrel

was removed after the PVD had been installed. During the discharge capacity test, four stages of surcharge load including 50, 100, 150 and 200 kPa were applied after assembly of the loading system had been completed.

For the case 2 test, a slurry of kaolinite prepared at a water content of 90 % was poured into the cylinders where the PVD had been set up. The test conditions of applying the staged loads in the case 2 test were identical to those in the case 1 test.

Table 1. Description of materials used

Types	Property		Description
Soil	Specific Gravity		2.6
	Grain size distribution	< 0.074 mm, %	100 %
		USCS	CH
	Atterberg limit	LL, %	59.8
		PL, %	35
		PI, %	24.8
Preparation technique		Remolded in a slurry state	
PVD	Cross section, (mm × mm)		100 × 4
	Shape of core		Ribbed groove

Table 2. Contents of discharge capacity test

Procedure	PVD driven test (case 1)	PVD embedded test (case 2)
PVD installation method	- Driving with mandrel into Pre-consolidated ground	- Setting up PVD before ground preparation
Ground preparation	- Slurry state of $w_0=120\%$, $H_0=105$ cm - Pre-consolidation stress 20 kPa for 3 months resulting in $w_0=90\%$, $H_0=85$ cm	- Slurry state with $w_0=90\%$, $H_0=85$ cm
Discharge capacity test	- Consolidation: 50, 100, 150, 200 kPa (every 3 days) - Discharge capacity: Hydraulic gradient 0.5, performing every 2 hours	

TEST RESULTS AND DISCUSSION

Fig. 3 shows measured settlement curves with time during the discharge capacity test. For both cases 1 and 2, final settlements during the loading stages tend to decrease gradually with increasing of loading stage. Total settlements during each stage are very close to each other, except for the first stage of applying 50 kPa vertical stress. The ground for the case 1 test was prepared by applying a pre-consolidation pressure of 20 kPa so that it passed from an over-consolidated state to a normally consolidated state

during the first loading stage.

Fig. 4 shows the change of excess pore pressure with elapsed time, measured at distances 5 cm and 10 cm apart horizontally from the drain. It is seen that pore pressures at 5 cm apart dissipate faster than those at 10 cm apart. Excess pore pressure at a point closer to the drain boundary dissipates easily. Residual pore pressures are perceived to accumulate as the stages of loading proceed, especially the pore pressure at 10 cm.

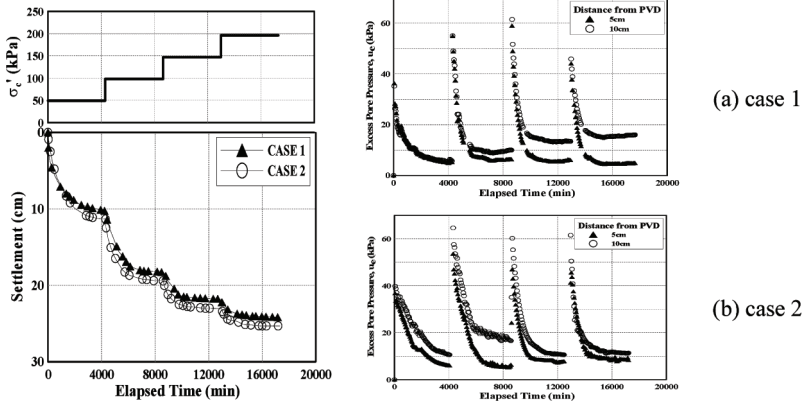


FIG. 3. Settlement curves with time FIG. 4. Changes of excess pore pressure with time

Fig. 5 represents the change of discharge capacity with time. Discharge capacity decreases drastically to the value of 11.5-12.3 cm³/sec until 1000 min. elapsed time, which is 24.2-38.1 % of the initial value. After that, it tends to decrease gradually. The discharge capacity of the drain decreases with increasing consolidation stress, due to reduction in the cross section of the drain as a result of the compressibility of the drain and penetration of the filter in the drain groove (Broms et al., 1994). Vertical strain at the elapsed time of 1000 min., showing a deflection point in terms of change of discharge capacity, is 9.8-10.3 % (8.3-8.8 cm of consolidation settlement). A discharge capacity decreased greatly in the range of settlement of 15-20 % of deposit thickness because of drain folding (Kremer et al., 1983). Reduction of discharge capacity to 14-66 % around 10 % of deformation strain was also reported (Bergado et al., 1993). Considering the results of this previous research, consolidation stress and deformation of the drain are expected to be dominant factors increasing well resistance at the elapsed time of 1000 min. For both cases 1 and 2, quite similar changes of discharge capacity with time are observed. Thus, ground disturbance due to insertion of the mandrel does not play an important role in reduction of discharge capacity. The smear zone, formed by insertion of the mandrel and expected to affect the cross-plane permeability of the drain, does not affect discharge capacity estimated from measuring in-plane flow. More experimental work is needed to

confirm the fact that the smear zone does not affect discharge capacity.

All kinds of deformation such as bending, twisting, folding and kinking, can be observed by cutting of the tested ground, as shown in Fig. 6. These are clearly the main causes of reduction of discharge capacity.

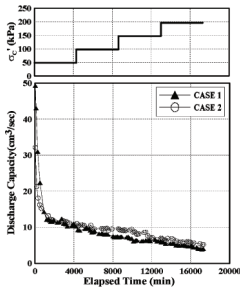
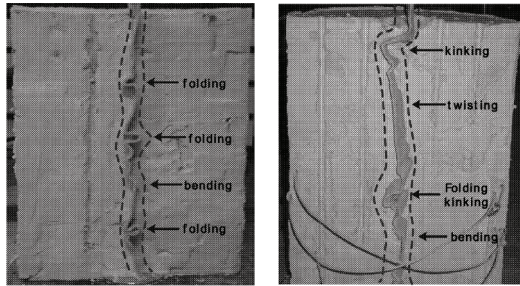


FIG. 5. Discharge capacity with time



(a) case 1 test (b) case 2 test
FIG. 6. Observed deformations of PVD

NUMERICAL ANALYSIS

Numerical analysis under 2-D plane strain condition with PLAXIS v8.2, a commercially available FEM software, was performed to investigate consolidation settlement of the ground. The layout of the drain is modified by transformed width (Tan & Tjahyono, 2006). The properties of the drain are assumed to be identical to those of soil, except for permeability, resulting in neglecting the stiffness of the drain. Based on the results of the discharge capacity test in Fig. 5, reduction of permeability of the drain with consolidation stress is simulated in terms of void ratio change. Input parameters for soil are summarized in Table 3. Most of these values were obtained from an oedometer test, except for the assumed value of permeability in the horizontal direction being equal to the measured value of permeability in the vertical direction because of the remolded soil being used. Conditions of equal strain loading with the rigid loading plate, being identical to the conditions of the discharge capacity test, were applied in the numerical analysis. For the smear zone, the width of the smear zone being 2 times the diameter of the mandrel was assumed. Settlement curves with time from the test and numerical results show that they are close to each other, as shown in Fig. 7.

CONCLUSIONS

A discharge capacity testing apparatus able to reconstruct in the laboratory the condition of installing vertical drains in a field was built to investigate the discharge capacity of PVD. From the results of two limited tests, while changing the method of preparing the ground and drains, consolidation stress and deformation of the drain are observed to be

dominant factors reducing the discharge capacity of the drain. The smear zone, formed by insertion of the mandrel, may not affect discharge capacity. More experimental work is needed to ascertain details of the crucial factors influencing the discharge capacity of PVD driven into soil. From the results of 2-D numerical analyses with a modified Cam-clay model, test results for settlement are found to be in good agreement with analytical results.

Table 3. Input parameters for numerical analysis

Model	Modified Cam-clay
γ_{sat} (kN/m ³)	14.478
k_h (m/day)	1.28×10^{-4}
k_v (m/day)	1.49×10^{-4}
e_0	2.236
C_c	0.663
C_s	0.112

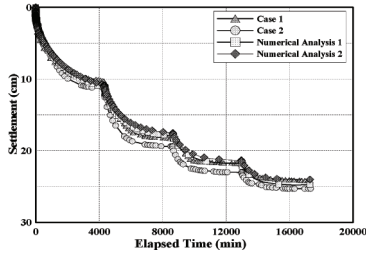


FIG. 7. Settlement curves with time from test and numerical results

REFERENCES

Bergado, D.T., Alfaro, M.C. and Balasubramaniam, A.S. (1993). "Improvement of soft Bangkok clay using vertical drains." *Geotextiles and Geomembranes*, 615-663.

Bergado, D.T., Manivannan, R. and Balasubramaniam, A.S. (1996). "Proposed criteria for discharge capacity of prefabricated vertical drains." *Geotextiles and Geomembranes*, Vol. 14, 481-505.

Broms, B.B., Chu, J. and Choa, V. (1994). "Measuring the discharge capacity of band drains by a new drain tester." *Proceedings of the 5th International Conference on Geotextiles, Geomembranes and Related Products*, Singapore, Vol. 3, 803-806.

Bo, M.W. (2003). "Soil improvement: Prefabricated vertical drain techniques." Thomson, Singapore, 5-23.

Hansbo, S. (1983). "How to evaluate the properties of prefabricated drains." *Proceedings of the 8th European Conference on Soil Mechanics and Foundation Engineering*, Helsinki, Vol. 2, 623-626.

Kjellman, w. (1948). "Accelerating consolidation of fine-grained soils by means of cardboard wicks." *Proceedings of the 2nd International Conference on Soil mechanics and Foundation Engineering*, Rotterdam, 302-305.

Koerner, C.M. and Lawrence, C.A. (1988). "Flow behavior of kinked strip drains." *Proceedings of ASCE Symposium on Geosynthetics for Soil Improvement*, Nashville, Tenn., Geotechnical special publication, No. 18.

Kremer, R.R.H.J., Oostveen, J.P., Van Wee, A.F., Dejager, W.F.J. and Meyvogel, I.J. (1983). "The quality of vertical drainage." *Proceedings of the 8th European Conference*

- on Soil Mechanics and Foundation Engineering*, Helsinki, Vol. 2, 721-726.
- Oostveen, J.P. and Troost, G.H. (1990). "Discharge index tests on vertical drains." *Geotextiles, Geomembranes and Related Products*, 345-350.
- Suits, L.D., Gemme, R.L. and Masi, J.J. (1986). "Effectiveness of prefabricated drains on laboratory consolidation of remolded soils." *Consolidation of soils: Testing and Evaluation*, ASTM, 663-683.
- Tan, S.A. and Tjahyono, S. (2006), "Practical modeling of stone column reinforced ground." *K.G.S. Fall Conference*, Vol. 2006, 291-311.

An Aquifer Analogue Study of High Resolution Aquifer Characterization Based on Hydraulic Tomography

Rui Hu¹, Wei Zhao², and Ralf Brauchler¹

¹University of Goettingen, Geosciences Centre, Goldschmidtstr.3, D-37077 Goettingen, Germany, rhu@gwdg.de

²University of Augsburg, Department of Computer Science, Universitätsstr. 6a, D-86159 Augsburg, Germany, garyswd@gmail.com

ABSTRACT: Hydraulic tomography is an efficient method for characterizing the subsurface heterogeneity of hydraulic parameters. In this paper we introduce a hydraulic tomographic travel time based inversion procedure showing the advantageous of the inversion of data subsets. The results demonstrate that the proposed inversion scheme is competent for the reconstruction of individual architectural elements as well as their hydraulic properties with a higher resolution in contrast to conventional hydraulic and geological investigation methods.

INTRODUCTION

Rarely is it possible to draw a significant conclusion about the geometry and the properties of geological structures of the subsurface using the information, which is typically obtained from boreholes, since soil exploration is only representative of the position where the soil sample is taken from. Conventional aquifer investigation methods like pumping tests can provide hydraulic properties of a larger area; however, they lead to integral information. This information is insufficient for the analysis of a wide variety of engineering, geotechnical and hydrogeological problems, e.g. contaminant transport models, which require information about the spatial distribution of the hydraulic properties of the subsurface. The tomographical method are hence applied to solve this problem and provide this information. The application of geophysical tomography has been well established for years. However, the geophysical methods such as radar, seismic or electrical tomography yield a geophysical parameter distribution that does not necessarily have to be in accordance with hydraulic properties of the subsurface, since no general relationship between geophysical and hydraulic parameters is expected yet (Hyndman and Tronicke, 2005).

In contrast to geophysical methods, hydraulic tomography allows us to determine the hydraulic properties directly (Yeh and Liu, 2000) and has the potential to yield information on spatial variation of hydraulic conductivity (k), specific storage (S_s)

and diffusivity (D) between wells. It consists of a series of short term pumping or slug tests performed in a tomographic array. Varying the location of the source stress (pumping or slug interval, usually separated by packers) and the receivers (pressure transducers) generates streamline patterns that are comparable to the crossed ray paths of a seismic tomography experiment (Butler et al., 1999). With such a vast amount of relevant information from the series of tests, inverse models with different strategies can thus capture the detailed three-dimensional hydraulic heterogeneity of the subsurface (e.g. Bohling, 2002; Gottlieb and Dietrich, 1995; Butler et al., 1999; Yeh and Liu, 2000; Zhu and Yeh, 2006; Brauchler et al., 2007; Illman et al., 2008). The hydraulic tomographic approach we introduce here relates the hydraulic diffusivity with hydraulic travel time inversion, which is based on the transformation of the transient groundwater flow equation into the eikonal equation using an asymptotic approach (Virieux et al., 1994). The eikonal equation can be solved with ray tracing techniques, which allow the calculation of pressure propagation along trajectories (Vasco et al., 2000; Brauchler et al., 2003). The hydraulic diffusivity is a key parameter for the groundwater contaminant transport models. Since D is the quotient of k to S_s , k for the zonation with constant D could be determined through other tomographical approaches, after which the S_s of each zone could be calculated from the k and S_s estimates (Bohling et al., 2007).

The groundwork of this study is the aquifer-analogue study from Bayer (1999), in which six parallel profiles of a natural sedimentary body with a size of $16 \times 10 \times 7 \text{ m}^3$ were mapped in high resolution with respect to structural and hydraulic parameters. Based on these results and using geostatistical interpolation methods, Maji and Sudicky (2008) designed a three dimensional hydraulic model with a resolution of $5 \times 5 \times 5 \text{ cm}^3$. Based on this data we simulated a large number of short term pumping tests in a tomographical array and inverted the travel times which derived from the tests, two- and three-dimensionally. The developed inversion strategy is based on the inversion of data subsets. Since the structure of the investigated aquifer analogue data set shows horizontally a larger extent than vertically, we have developed an inversion strategy which is adapted to the reconstruction of relatively thin and horizontally arranged sediment layers, which is typical for fluvio deposits.

AQUIFER ANALOGUE OUTCROP STUDY

The model domain is based on an aquifer analogue outcrop study in a braided river environment, consisting mainly of layers of poorly to well sorted sand and gravel (Bayer, 1999). During a period of six months, a series of photographs were taken as a gravel quarry was excavated. The excavation was performed in a sequential fashion as the quarry face was moved back 9 m. High resolution photographs of the exposed face, yielding six parallel images, were taken every 1-2 m as the face was moved back. Using sediment size, texture information, and GPR (Ground Penetrating Radar) surveys along with consideration of the sedimentological processes as constraints, the outcrop photographs were then carefully interpreted to yield maps of lithology. For each representative lithological unit, measurements were performed in the laboratory, providing porosity as well as hydraulic conductivity (hydrofacies classification). Maji and Sudicky (2008) performed an interpolation between the six profiles

by using geostatistical methods and translated the gathered information into a three-dimensional hydraulic parameter distribution. The three-dimensional (3D) realistic characterization of the aquifer makes the developed parameter distribution unique. This unique and perfectly suitable 3D parameter field with a resolution of $5 \times 5 \times 5 \text{ cm}^3$ is used for our groundwater model with simulation of short term pumping tests.

Groundwater model domain

This dataset was used in MODFLOW (Harbaugh and McDonald, 1996) to set up a groundwater model. The centre of the model is based on the aquifer analogue data set with a volume of $16 \times 10 \times 7 \text{ m}^3$, comprising cells with the size of $10 \times 10 \times 10 \text{ cm}^3$. Outside of the centre the model is extended for more than 1200 m in order to avoid boundary effects (in our case a constant head boundary). The hydraulic parameters for the cells of the extended area are the mean values taken from the aquifer analogue data set. The initial head of the cells is 0.2 m above the aquifer top and the aquifer is always under confined condition during the simulation of pumping tests. For each simulation of the pumping tests we have used 6 stress periods consisting of 100 time steps over a simulation length of about 300 seconds for the drawdown phase. From the 100 time steps we had 80 steps for the first 3 seconds. In the centre of the model domain we built five 2"-wells, arranged in a five star configuration. Each of the four wells is 2.5 m from the centre well (Fig. 1A).

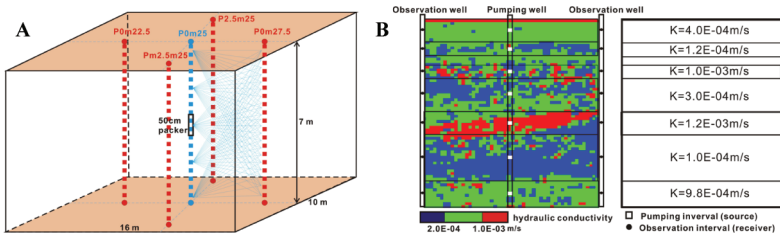


FIG. 1. (A) Centre area of the model and the thematic tomographical configuration of the sources and receivers during pumping tests; (B) Comparison between the *k* values of the aquifer analogue data set (left) and the derived *k* values (right), evaluated from simulated pumping tests with partial penetration.

Model verification

First, traditional pumping tests without packer system were simulated. The tests were analyzed with the analytical solution developed by Theis (1935). The evaluated values of the hydraulic parameters matched the corresponding mean values of the data set, which is a very good sign at the first place that the groundwater model could run well based on the analogue data set.

Subsequently we simulated the pumping tests with double packer system and evaluated them again. During each test the water was pumped out of a defined interval of the well in the middle and the hydraulic heads in the surrounding wells in the same depth were recorded. Since the fluvio aquifer with almost horizontally extended deposit has different layers with different hydraulic properties, we located the pumping and observation intervals in same depths of the aquifer for the characterization of each main layer. Fig. 1B shows the comparison between the K values of the

aquifer analogue data set and the K values estimated using the analytical solution developed by Theis (1935), taking partial penetration effects into account.

The results based on the analytical solution reflect the hydraulic properties of the different layers of the aquifer very well. This strongly supports the validity and plausibility of our numerical model.

TRAVEL TIME INVERSION

Vasco (2000) found that similar as in the seismic tomography, the diffusivity of an aquifer can also be determined through inversion of hydraulic travel time. Like the seismic wave the groundwater flows preferentially in the direction where the diffusivity is larger. The inversion strategy is based on the following line integral (Vasco et al., 2000, Kulkarni et al., 2001)

$$\sqrt{t_{\text{peak}}(t_2)} = \frac{1}{\sqrt{6}} \int_{t_1}^{t_2} \frac{dt}{\sqrt{D(t)}} \dots \tag{1}$$

where t_{peak} is the travel time of the peak of a Dirac signal from the point 1 (source) to the observation point 2 (receiver) and D is the diffusivity.

In the seismic travel time tomography, the following line integral relates the travel time t , which is recorded between source and receiver, with the spatial velocity v distribution of an investigated area.

$$t = \int_{x_1}^{x_2} \frac{ds}{v(s)} \dots \tag{2}$$

The similarity between the two inversions allows us to use the same application software GeoTom3D, which is based on the Bureau of Mines tomography program 3DTOM (Jackson and Tweeton, 1996) and developed originally for seismic tomography, to solve hydraulic tomographic problems. The travel time integral was solved with SIRT (Simultaneous Iterative Reconstruction Technique). In our case the travel time based inversion procedure was used to choose a diffusivity distribution which minimizes the functional J in equation (3), where t_i^e and t_i^m are the estimated and measured travel time for the i th measurement and n is the number of measurements. In Fig. 2 we show the overall residual $S^{0.5}$ (equation (4)) for 15 iteration steps of a 2D inversion. The $S^{0.5}$ decreases in a quasi exponential manner and fluctuates after 8 steps. Based on this fact the following inversion results are conducted with 8 iteration steps and the inversion takes around 10 seconds on a 3.2 GHz Pentium CPU.

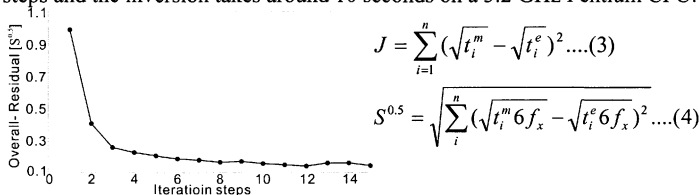


FIG. 2: Overall residual for 15 iteration steps of a 2D inversion.

DATA BASE OF THE TRAVEL TIME INVERSION

We simulated a large number of short term pumping tests in a tomographic array (Fig. 1a). During each test the water was pumped out of a defined section (the source) from a well with the help of the double packer isolation system. Meanwhile the resulting transient pressure changes in the surrounding observation wells in different depths (the receivers) were recorded. Subsequently the position of the source was varied and the whole test was repeated. With all possible combinations of source-receiver positions we recorded more than 700 pressure changes from different receivers during 56 simulated pumping tests which formed a dense net of source-receiver configurations.

As an example, Fig. 3A shows the drawdown curves recorded in one observation well (P2.5m25) from receivers located in different depths during a pumping test (pumping well: P0m25, pumping interval: 1.0-1.5 m under aquifer top). The pressure changes were recorded for each 10 centimetres over a depth of 7 meters. Note the travel time integral is just valid for an impulse source (Dirac pulse). For this reason we have to determine the first derivation of our pumping test signal in order to transform the Heaviside source into a Dirac pulse. The first derivation of the drawdown curves with logarithmic time scale show clearly the curves with different peak times, representing each corresponding receivers in different depths (Fig. 3B).

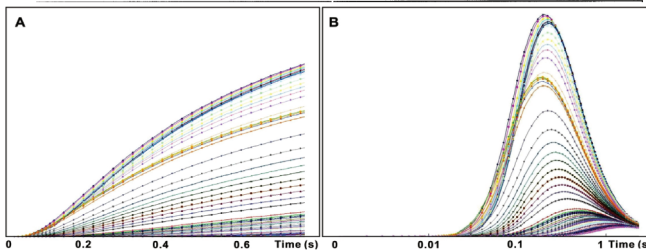


FIG. 3. (A) drawdown curves recorded in the observation well P2.5m25 (pumping interval: P0m25, 1.0-1.5m under aquifer top); (B) corresponding first derivatives of drawdown curves in (A).

The different peak times feature the characteristic properties of the aquifer in different depths. 70 recorded pressure curves should be able to help us to get a distribution of diffusivity with a very high resolution. However, it is very hard to monitor so many sections in one observation well in the real field. Hence we decided to record the pressure change for every 50 cm in the well. Based on those pressure changes we implemented different strategies of travel time inversion with data subsets.

In the end we applied the best strategy to a 3D inversion, i.e. to invert all the suitable pressure responses from all possible source-receiver combinations simultaneously to achieve a 3D distribution of the diffusivity values of the aquifer.

RESULTS

First we inverted all the travel times between every source and receiver with the above described travel time based inversion scheme to obtain the 2D distribution of

the diffusivity between wells. The second profile in Fig. 5 shows, as an example, the calculated diffusivity between the well P0m22.5 and P0m27.5. Compared with the first profile of the true values from the original data set, the inversion result based on the whole data set of travel time reflects the layered structure of the aquifer. However, due to the horizontal discontinuity, the reconstruction is still out of accord with the original data set, which might cause problems for some engineering case like a contaminant transport model.

In order to overcome the problem from above, we introduced the travel time inversion based on data subsets of specified source-receiver angle intervals in addition to the whole data set. As shown in the Fig. 4, hydraulic travel times, e.g. trajectory “a” with $\alpha=0^\circ$ (α defined as the angle between the horizontal and a straight line connecting the source and receiver), contain mainly information about vertical variations of the average velocity. Travel times of trajectories with larger source-receiver angles (e.g. trajectory “b”) indicate horizontal velocity changes and do not contribute much to the vertical resolution of the layered zones (Becht et al., 2004).

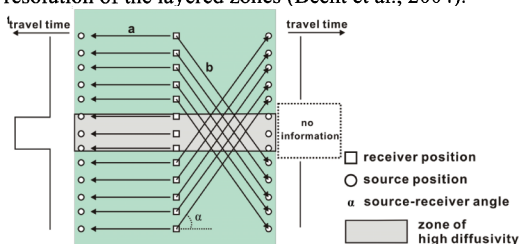


FIG. 4. Sketch of travel times based on different data subsets.

Inversion based on trajectories with too large source-receiver angles might add noise or artefacts in the horizontal direction. Hence we decide to invert the travel times with small source-receiver angles to enhance the vertical resolution and to investigate the continuity in the horizontal direction. Fig. 5 shows the comparison of inversion results using whole data set and different data subsets. Obviously the inversion result based on the trajectories with $|\alpha| < 20^\circ$ has the best match with the true values of original data set.

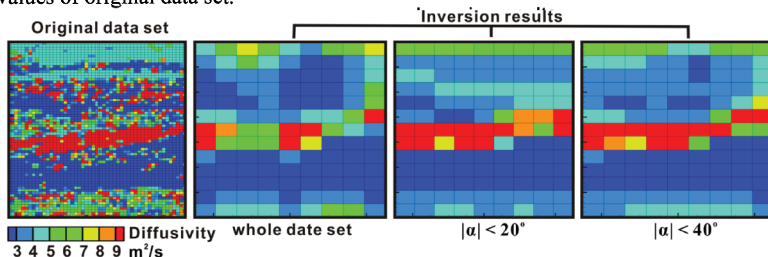


FIG. 5. Inversion results using whole dataset and different data subsets.

As introduced before and shown in the Fig. 6A, we changed the position of pumping wells and observations wells to repeat the simulations in order to get all possible source-receiver combinations in three dimensions. With the best inversion strategy

of data subsets for the 2D inversion, we inverted all of the possible travel times at the same time and acquired the 3D distribution of the diffusivity values (Fig. 6C). Comparing with the original data set in Fig. 6B, it is very easy to recognize the structure of the fluvio deposit and the individual layers and zones with different diffusivities.

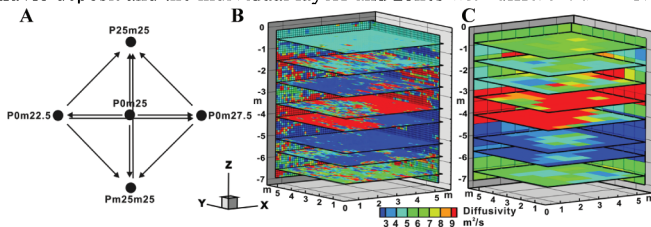


FIG. 6. (A) Sources and receivers (overlook) with arrows pointing from sources to receivers; (B) The original data set; (C) The result of 3D inversion.

CONCLUSIONS

As a new aquifer characterization method, hydraulic tomography based on travel time inversion shows great potential in reconstructing the aquifer with efficiency, flexibility and accuracy. In contrast to the traditional hydraulic field tests like pumping test, the determination of hydraulic travel time (peak time) required for the inversion, along with the inversion itself, add up to only several seconds. This will save us precious time in the field and contribute to the repeatability of research work. Based on the prior information and the inversion of data subsets, we could greatly enhance the resolution of results in the vertical direction and reduce the noise in the horizontal direction. In addition, this method can directly provide a 3D distribution of hydraulic diffusivity with a resolution at the magnitude of a few centimetres. This is very significant for many engineering purposes such as the setup of a groundwater contaminant transport model and the design of effective groundwater remediation systems, which require characterization of aquifer heterogeneity with higher resolution.

ACKNOWLEDGMENTS

The investigations were conducted with the financial support of the German Research Foundation within the project "High resolution aquifer characterization based on direct-push technology: An integrated approach coupling hydraulic and seismic tomography" (grant no. BR3379/1-2).

REFERENCES

- Bayer P. (1999). *Aquifer-Analog-Studium in grobklastischen braided river Ablagerungen: Sedimentäre/hydrogeologische Wandkartierung und Kalibrierung von Georadarmessungen*, Diplomkartierung, Universität Tübingen.
- Becht, A., Tronicke, J., Appel, E., and Dietrich P. (2004). "Inversion strategy in crosshole radar tomography using information of data subsets." *Geophysics*, 69:

222-230.

- Bohling, G.C., Butler Jr., J.J., Zhan, X., and Knoll, M.D. (2007). "A field assessment of the value of steady shape hydraulic tomography for characterization of aquifer heterogeneities." *Water Resources Research*, 43, W05430, p. 21.
- Bohling, G.C., Zhan, X., Butler Jr., J.J., and Zheng, L. (2002). "Steady shape analysis of tomographic pumping tests for characterization of aquifer heterogenous." *Water Resources Research*, 38(12): 1324.
- Brauchler, R., J. Cheng, M. Everette, B. Johnson, P. Dietrich, R. Liedl, M. Sauter (2007). "An integrated approach coupling hydraulic travel time tomography and amplitude inversion." *Journal of Hydrology*, doi:10.1016/j.jhydrol.2007.08.011.
- Brauchler, R., Liedl, R., Dietrich, P. (2003), A travel time based hydraulic tomographic approach, *Water Resources Research*, 39(12): 1370.
- Butler, Jr., J. J., C. D. McElwee and G. C. Bohling (1999). "Pumping tests in networks of multilevel sampling wells: Motivation and methodology." *Water Resources Research*, 35(11), 3553-3560.
- Gottlieb, J. and Dietrich, P. (1995). "Identification of the permeability distribution in soil by hydraulic tomography." *Inverse Problems*, 11: 353-360.
- Harbaugh, A.W., and McDonald, M.G. (1996). *User's documentation for MODFLOW-96*, an update to the U.S. Geological Survey modular finite-difference ground-water flow model. U.S. Geological Survey Open-File Report 96-485.
- Hyndman, D., Tronick, J. (2005). "Hydrogeophysical case studies at the local scale: the saturated zone." In: Rubin, Y., Hubbard, S. (Eds.), *Hydrogeophysics*. Springer, Berlin, ISBN 1-4020-3101-7, p. 522.
- Illman, W.A., Andrew J. C., and Liu, X. (2008). "Practical Issues in Imaging Hydraulic Conductivity through Hydraulic Tomography." *Ground Water*, Vol. 46 (1): 120-132.
- Jackson, M. J., and Tweeton, D.R. (1996). *3DTOM: Three-dimensional geophysical tomography*: U.S. Department of the Interior, Report of Investigations 9617, p. 84.
- Kulkarni, K. N., Datta-Gupta, A. and Vasco, D. W. (2001). "A Streamline Approach to Integrating Transient Pressure Data into High Resolution Reservoir Models." *SPE Journal*, 6(3): 273-282.
- Maji, R., and Sudicky, E. A. (2008). "Influence of mass transfer characteristics for DNAPL source depletion and contaminant flux in a highly characterized glaciofluvial aquifer." *Journal of Contaminant Hydrology*, Vol. 102 (1-2): 105-119.
- Theis, C.V. (1935). "The relation between the lowering of piezometric surface and the rate and duration of discharge of a well using ground-water storage." *Transactions American Geophysical Union*, Vol. 16: 519-524.
- Vasco D.W., Keers, H., and Karasaki, K. (2000). "Estimation of reservoir properties using transient pressure data: An asymptotic approach." *Water Resources Research*, 36 (12): 3447-3465.
- Virieux, J., Flores-Luna, C., and Gibert, D. (1994). "Asymptotic theory for diffusive electromagnetic imaging." *Geophysical Journal International*, 119, p857-868.
- Yeh, T.-C. J. and Liu, S. (2000). "Hydraulic tomography: Development of a new aquifer test method." *Water Resources Research*, 36 (8): 2095-2105.
- Zhu, J., and Yeh, T.-C. J. (2006). "Analysis of hydraulic tomography using temporal moments of drawdown recovery data." *Water Resources Research*, 42, W02403.

A Mathematical Model for Determination of the Critical Hydraulic Gradient in Soil Piping

Jian Zhou¹, Yan-Feng Bai² and Zhi-Xiong Yao³

¹Professor, Department of Geotechnical Engineering, Tongji University, Shanghai, China, 200092; tjuzj@vip.163.com

²PhD Student, Department of Geotechnical Engineering, Tongji University, Shanghai, China, 200092; b6y6f6@163.com

³Engineer, Fujian Communications Science Research Institute, Fuzhou, China, 350004; bearer@126.com

ABSTRACT: Piping erosion is one of the main causes responsible for dam and barrage failures. The issue of most important concern is to estimate the critical hydraulic gradient that triggers piping. Using the Kovacs's pore channels model, Darcy's law, Stoke's law and a critical tractive stress condition, a mathematical model was developed for the critical hydraulic gradient. The model was verified with lab tests, which means the model is effective and could be used to predict the critical hydraulic gradient with different parameters.

INTRODUCTION

The phenomenon of piping is commonly observed under dams and barrages. Piping is a form of seepage erosion and refers to the development of subsurface channels in which soil particles are transported through porous media. Piping begins at the land-facing side of the structure where the flow lines meet. High seepage pressure may force a slit to develop; then the process of erosion develops backward under the dam, and if the process continues, the structure may be undermined and collapse.

Bligh (1910) proposed empirical rules for preventing piping based on investigations on a large number of failures due to piping. Bligh's work is considered to be pioneering; however, limited attempts have been made to develop alternative models for piping. And no theoretical basis for Bligh's empirical rules has been forwarded since that. Meyer et al. (1994) stated that there was a distinct lack of models dealing with the piping phenomenon. Sellmeijer(1988) provided an equation for the critical head which should not be exceeded to avoid piping. Weijers and Sellmeijer (1993) proposed a modified equation for the critical head. Ojha et al (2003) gave two models to determine critical head in soil piping.

The objective of this study was to develop a critical hydraulic gradient model using Kovacs's pore channels model, Darcy's law, Stoke's law and Kozeny-Carman

equations.

MATHEMATICAL MODEL

Coarse particles of pore medium form a series of interpenetration pore channels. The channel can be treated as a conduit for water and particle flow. The cross sections of the channels vary in size due to the non-uniformity of soils in density. Kovacs(1981) assumed a uniform cross section for channels and the channels are parallel to the upright seepage way, as shown in Fig. 1, where d_1 is the maximum equivalent diameter of the pore channels, d_2 is the minimum equivalent diameter of the pore channels, and d_0 is the equivalent pore diameter.

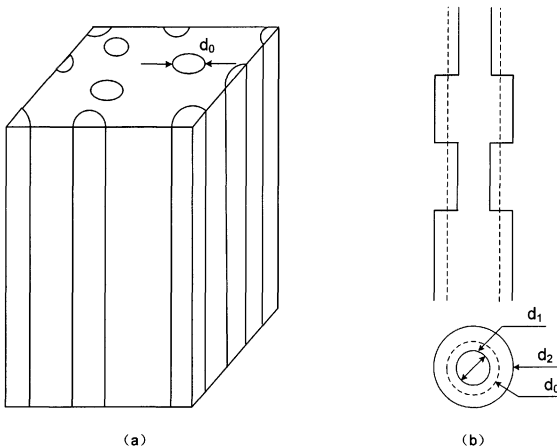


FIG. 1. Illustration of pore channels: (a) within typical filter element; (b) defining equivalent pore diameter, d_0 .

The objective of this study is to estimate the critical hydraulic condition at which fine particles begin to move. It is postulated that when the applied hydraulic gradient exceeds a critical value, the fine particles start to move under seepage force. A rational way of evaluating this hydraulic constraint is to establish the equilibrium between the external forces acting on a given particle within a pore channel, as shown in Fig. 2.

In Fig. 2, the following forces act on the particle, the seepage force $F_{\Delta p}$, the dragging force F_D , the weight of the particle G , the uplift force F and the friction force F_f .

At limit state,

$$F_{\Delta p} = (G - F) \sin \alpha + F_f - F_D \quad (1)$$

Using Dracy's law, the seepage force applied on particle corresponding to the mean hydraulic gradient (i) acting within the length δs is given by

$$F_{\Delta p} = i \cdot \gamma_w \cdot \delta s \cdot \frac{\pi d^2}{4} \quad (2)$$

Where γ_w is unit weight of water and d is the diameter of moving particles.

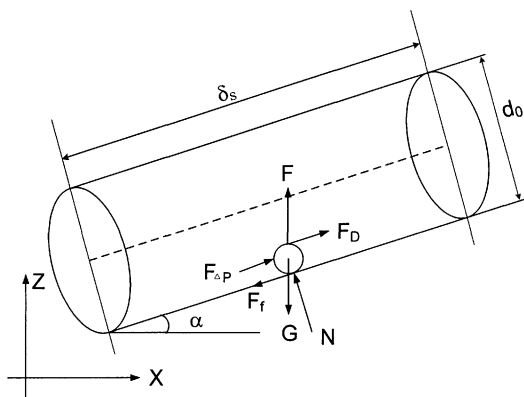


FIG. 2. Equilibrium of particle pore channels within typical element.

By Storke’s law, the dragging force is as follows,

$$F_D = 3\pi \cdot \mu_w \cdot d \cdot \frac{k}{n} \cdot i \tag{3}$$

Where coefficient of permeability k can be expressed by Kozeny-Carman equations as,

$$k = \frac{\beta}{180} \cdot \frac{d^2 n^3}{(1-n)^2} \cdot \frac{\gamma_w}{\mu_w} \tag{4}$$

The friction force between particles or particles and wall can be expressed as,

$$F_f = (G - F) \cos \alpha \cdot \tan \phi = \frac{4\pi r^3}{3} (\gamma_s - \gamma_w) \cos \alpha \cdot \tan \phi = \frac{\pi d^3}{6} (\gamma_s - \gamma_w) \cos \alpha \cdot \tan \phi \tag{5}$$

Where γ_s is unit weight of soil and ϕ is friction angle.

Using equation (2)-(5) in equation (1), the mean hydraulic gradient can be obtained,

$$i = \frac{\frac{\pi d^3}{6} (\gamma_s - \gamma_w) \cos \alpha \cdot \tan \phi + \frac{\pi d^3}{6} (\gamma_s - \gamma_w) \sin \alpha}{\gamma_w \delta_s \cdot \frac{\pi d^2}{4} + 3\pi \mu_w d \frac{k}{n}}$$

$$= \frac{\frac{\pi d^3}{6} (\gamma_s - \gamma_w) (\cos \alpha \cdot \tan \phi + \sin \alpha)}{\gamma_w d [\delta_s \cdot 0.25\pi d + 3\pi \frac{\beta}{180} \frac{\bar{d}^2 n^2}{(1-n)^2}]}$$

$$= \frac{2(\gamma_s - \gamma_w)}{3\gamma_w} \cdot \frac{d^2 (\cos \alpha \cdot \tan \phi + \sin \alpha)}{d \cdot \delta_s + \frac{\beta}{15} \frac{\bar{d}^2 n^2}{(1-n)^2}} \tag{6}$$

where \bar{d} is the average diameter of particles.

Assuming pore channel are the same in cross section and parallels with the upright seepage way which means $\alpha = 90^\circ$. When piping begins, the $\delta_s \approx d$, then the critical hydraulic gradient of piping can be simplified as,

$$i_{cr} = \frac{2(\gamma_s - \gamma_w)}{3\gamma_w} \cdot \frac{d^2}{d^2 + \frac{\beta}{15} \frac{\bar{d}^2 n^2}{(1-n)^2}} \quad (7)$$

COMPARISON WITH LABORATORY TESTS

To validate the model, a comparison with a series of laboratory tests is described.

A large-scale piping apparatus (500-mm long, 100-mm broad and 600-mm high) was constructed to investigate the piping phenomena. The tests described here employed a series of sands with 200-mm thickness. Gravel was placed, approximately 100-mm deep, as the flow buffer to ensure a uniform and avoid flow rushing sample to destroy. The base soil was placed and lightly compacted in 100-mm layers. Erosion was induced by a uniform upward flow of 0.2kPa/min. The experiment was repeated for different samples. The results are shown in Table 1, where d is obtained from the size of frame particles and \bar{d} is gained from the grading curve.

Table 1. Comparison of the critical hydraulic gradient of piping between calculation and experiments.

Sampl e	n	β	γ_s (kN/m ³)	γ_w (kN/m ³)	\bar{d} (mm)	d (mm)	i_{cr} calculate d	i_{cr} experimente d
P1	0.3 6	3. 5	25	10	1.31	0.25	0.33	0.31
P2	0.3 8	3. 5	25	10	1.28	0.25	0.30	0.28
P3	0.3 9	3. 5	25	10	1.26	0.25	0.29	0.26
P4	0.4 0	3. 5	25	10	1.29	0.25	0.27	0.25
P5	0.3 7	3. 5	25	10	1.32	0.25	0.31	0.27
P6	0.3 9	3. 5	25	10	1.34	0.25	0.27	0.29

RESULTS AND DISCUSSION

The results show that the model predicts similar values to those observed in the laboratory. The model is effective and could be used to predict the critical hydraulic gradient with different parameters.

Fig. 3 shows the relationship between critical hydraulic gradient and porosity when other parameters shown in Table 1. When porosity increases, the critical hydraulic gradient decreases linearly, this is well agreed with Ojha and Singh (2001).

When the diameter of moving particles increases and other parameters not change,

the critical hydraulic gradient increases linearly as shown in Fig. 4. However, the prediction is right only when the diameter of moving particles is smaller than the constriction size; otherwise, the fine particles can not move in the pore channel and may become part of the frame particles which means the seepage failure becomes flowing soil.

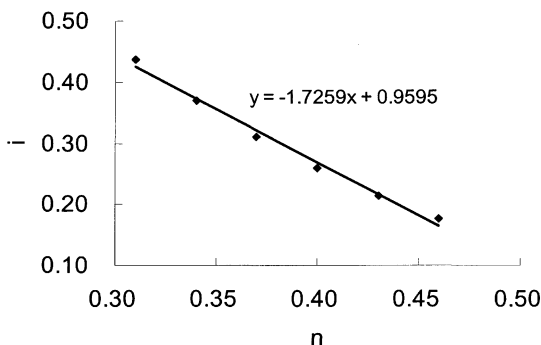


FIG. 3. Prediction of critical hydraulic gradient with different porosity.

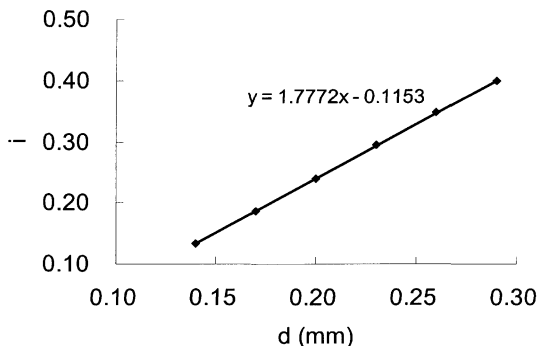


FIG. 4. Prediction of critical hydraulic gradient with different diameter of moving particles.

CONCLUSIONS

A physically based model for computing the critical hydraulic gradient is developed. The critical hydraulic gradient is found to depend on soil and fluid properties. The model takes on a form which supports the laboratory model tests findings. Then some useful conclusions are obtained. Highly porous soils have lower critical hydraulic

gradient in comparison to the less porous soils, and soils with larger particles have higher critical hydraulic gradient.

ACKNOWLEDGMENTS

The research is supported by the Chinese National Natural Science Foundation, Grant numbers 90815008 and 50379037. These supports are gratefully acknowledged.

REFERENCES

- Bligh, W. G. (1910). "Dams, barrages and weirs on porous foundations." *Eng. News*, Vol. 64 (12): 708.
- Ojha, C.S.P., and Singh, V.P. (2001). "Influence of Porosity on Piping Models of Levee Failure." *Journal of Geotechnical and Geoenvironmental Engineering*, Vol. 127 (12):1071-1074.
- Ojha, C.S.P., Singh, V.P., and Adrian, D.D. (2003). "Determination of critical head in soil piping." *Journal of hydraulic engineering*, ASCE, Vol. 129 (7): 511-518.
- Kovacs, G.(1981). "Seepage hydraulics." *Elsevier Scientific Publishers BV* (North Holland), Amsterdam, The Netherlands.
- Meyer, W., Schuster, R. L., and Sabol, M. A. (1994). "Potential for seep-age erosion of landslide dam." *J. Geotech. Eng.*, Vol. 120 (7): 1211–1229.
- Mindlin, R. D., and H. Deresiewicz. (1953). "Elastic spheres in contact under varying oblique forces." *J. Appl. Mech.*, Vol. 20, 327-344.
- Sellmeijer, J. B. (1988). "On the mechanism of piping under impervious structures." PhD thesis, Technical Univ., Delft, Netherlands.
- Skempton A., and Brogan J. (1994). "Experiments on piping in sandy gravels." *Geotechnique*, Vol. 44 (3):449-460.
- Sterpi D. (2003). "Effects of the erosion and transport of fine particles due to seepage flow." *Inter. J. of Geomech*, Vol. 3(1):111-122.
- Weijers, J. B. A., and Sellmeijer, J. B. (1993). "A new model to deal with piping mechanism." *Filters in geotechnical and hydraulic engineer-ing*, J. Brauns, M. Heibaum, and U. Schuler, eds., Balkema, Rotter-dam, Netherlands, 349–355.

Application of Natural Element Method in Solving Seepage Problem

S. Shahrokhbadi¹, M. M. Toufigh², R. Gholizadeh³

¹Department of Civil Engineering, Vali asr University of Rafsanjan, Iran; shahriar229@gmail.com

²Department of Civil Engineering, Shahid Bahonar University of Kerman, Iran

³Department of Civil Engineering, Shahid Bahonar University of Kerman, Iran

ABSTRACT: In recent years, with an increase in computer processing powers and the amount of memory available, numerical methods have seen a great improvement. Among variety of methods and algorithms, Finite Element Method (FEM) was the most successful algorithm used for solving diverse set of engineering problems, including boundary problems. Application of this method is limited in problems having large deformations due to the requirement for remeshing of the problem domain. According to this limitation, in recent years new methods which can work without the need for meshing of problem have been emerged. Natural Element Method (NEM) is a meshless method which has recently utilized as a tool for solving partial differential equations. The purpose of this research is to study the application of NEM in solving seepage problems. First, NEM is explained and its application in different 2D seepage problems is demonstrated. Finally, in order to justify the preciseness and convergence of proposed method, several numerical tests were conducted and results were compared with FEM using commercial software called PLAXIS. Results show the robustness of natural elements method in finding precise solutions.

INTRODUCTION

In Computational Mechanics, there are number of methods that give the exact or approximate results of differential equations. Finite Element Method (FEM) and Finite Difference Method (FDM) are common methods for solving boundary problems. The base of these methods is a particular part called mesh. Mesh generation needs special attention in order to keep connectivity on elements in domain of problem. In recent years, to tackle this problem, new methods in computational mechanics have been emerged, called as Meshless methods. In Meshless methods two conditions must be met (Idelsohn et al. 2002):

- 1- Definition of shape functions are only based on node position.

- 2- The evaluation of the nodes connectivity is bounded in time and it depends exclusively on the total number of nodes in the domain

Generally, the difference among Meshless methods is based on interpolation of scattered data techniques (Gonzalez et al. 2007). Some Meshless methods are: Smooth Particle Hydrodynamic (SPH), Partition of Unity Method (PUM) and Diffuse Element Method (DEM) (Alfaro et al. 2006). Some methods are formed from Moving Least Square technique (MLS) that in this technique shape functions don't possess kronecker delta property (Liu and GU, 2003).

Most of Meshless methods need background cells for the definition of numerical integration on domain of problem (Cho and Lee, 2007). But Liu has argued that the requirement for background cells makes this method not an ideal Meshless method. (Liu, 2002). Element Free Galerkin (EFG) is yet another method for interpolation of scattered data. Two properties are noticeable in EFG method (Liu 2003):

- 1- Non-element interpolation of field variable
- 2- Non-mesh integration of weak form

EFG has no kronecker delta property; hence, applying the essential boundary conditions might cause problems (Liu and GU, 2001). One way to overcome this shortfall is to use Point Interpolation Method (PIM). Although PIM is more accurate than MLS, it may cause the momentum matrix to become singular (Liu and GU, 2003). Matrix Triangularization Algorithm (MTA) is introduced to make up for this problem which MTA is an automatic process that assures the selected nodes in interpolation process are selected correctly (Liu and GU, 2003). Some Meshless methods consist of both weak and strong form of governing equation and when coupled together it is called Meshless Weak-Strong (MWS) form. This method has usually been used for modeling of stable and unstable incompressible flow (Liu, Wu, and Ding, 2004). There are also shortcomings related to the Meshless methods (Idelsohn et al. 2002):

- 1- In some methods, imposition of essential boundary conditions is complicated.
- 2- Many Gouse points are needed to assess the weak form of the problem.
- 3- Some methods have slow performance in interpolation of scattered data.

In this research, Natural Element Method (NEM) has been used in modeling of seepage problem. This method is based on Voronoi diagram and Delaunay tessellation that has been used as weak form for some mechanical problems (Sukumar, Moran, and Belytschko, 1998).

First, Voronoi diagram and Delaunay tessellation are explained. Then, the concept of natural neighbor and calculation of shape functions are discussed. In the third section, the weak form of seepage problem and its formulation using the Galerkin method is explained. Finally, the results from NEM and Plaxis8.0 software (which is based on FEM) are compared and discussed.

VORONOI DIAGRAM AND DELAUNAY TESSELLATION

Consider a set of discrete nodes in R^2 like $N = \{n_1, n_2, n_3, \dots, n_n\}$. The Voronoi diagram

(1st order Voronoi diagram) of set N is subdivided into regions T_i (closed, convex or unbounded), where each region T_i is associated with node n_i , that any point in region T_i is closer to point n_i than other points from other regions (Fig. 1(a)). (Sukumar, Moran, and Belytschko, 1998).

$$T_i = \{ x \in R^2 : d(x, x_i) < d(x, x_j) \forall J \neq I \} \tag{1}$$

Where $d(x_i, x_j)$ is the distance between x_i, x_j .

To compute the Voronoi diagram, there are other algorithms such as fuzzy Voronoi diagram. (Jooyandeh, Mohades, and Mirzakhani, 2009). Voronoi diagrams lead to Delaunay tessellation. Delaunay triangles are established by connecting nodes that have common boundaries (Fig. 2(b)). For Delaunay tessellation, Parallel Constrained Delaunay Mesh (PCDM) method is also available (Christos, 2009).



FIG. 1. Geometric Structure for set N of seven nodes: (a) 1st Voronoi Diagram of set N ; (b) Delaunay triangulation of set N DT(N).

SHAPE FUNCTION BASED ON NATURAL NIGHBOR CONCEPT

Finding the nearest neighbor for some points is an important task in many situations such as CAD/CAM programs and computational geometry. Elliptic Gabriel Graph (EGG) is a method developed in order to achieve this task (Lee et al. 2008). Sibson proposed natural coordinates which are restricted to convex hull of the sample point (Jooyandeh, Mohades, and Mirzakhani, 2009). To overcome the restriction mentioned above, extrapolation of natural neighbor interpolants are used on the basis of dynamic ghost points (Bobach and Farin, 2009).

Sibson has used empty circumcircle criterion which is a special property of Delaunay tessellation to define shape functions. If there are three nodes on circumcircle of each Delaunay triangle, then three edges will incinerate each other to form the center of a circumcircle (Fig. 2(a)) (Jooyandeh, Mohades, and Mirzakhani, 2009). Voronoi diagram is expandable, hence, 2nd-order of set N , can be constructed by subdividing of surface into

T_{IJ} cells. Each region of T_{IJ} with pair of (n_i, n_j) is the locus of cell points have n_i as the nearest neighbor, and n_j as the second nearest neighbor (Jooyandeh, Mohades, and Mirzakhani, 2009).

$$T_{IJ} = \{x \in R^2 : d(x, x_i) < d(x, x_j) < d(x, x_k), \forall K \neq I, J\} \tag{2}$$

If new point x , enters into set N , hence natural neighbor of x are the nodes that their circles include point x . 2nd Voronoi diagram can be introduced by this concept (Fig. 2(b)).



FIG. 2. Construction of Natural Neighbour Coordinates: (a) natural neighbour circumcircles; (b) 2nd-order Voronoi cells about x .

Shape functions are defined as follows:

$$\phi_I(x) = \frac{A_I(x)}{A(x)} \tag{3}$$

Where $A_I(x)$ is a surface related to node I and $A(x)$ is total surface of 2-st Voronoi diagram. Derivate of shape function is:

$$\phi_{I,j}(x) = \frac{A_{I,j} - \phi_I(x)A_{j,j}(x)}{A(x)} \quad (j = 1,2) \tag{4}$$

Where $A_{I,j}$ shows derivative of area function related to node I arbitrary to J.

WEAK FORMULATION FOR SEEPAGE

The governing equation to the porous material is the Laplace equation:

$$k\left(\frac{\partial^2 h}{\partial x^2} + \frac{\partial^2 h}{\partial y^2}\right) = 0 \tag{5}$$

Where h is potential head.

In Laplace equation (eq. 5), k is the conductivity factor which is constant in both x and y direction and the material is presumed to be homogeneous. In this research, definition of stiffness matrix and force matrix are based on weak form (Desai and Christian, 1977):

$$k_{ij} = \iint_{\Omega} \left(\frac{\partial \phi_i}{\partial x} \frac{\partial \phi_j}{\partial x} + \frac{\partial \phi_i}{\partial y} \frac{\partial \phi_j}{\partial y} \right) dx dy \tag{9}$$

$$f_j = \iint_s q \phi_j ds \tag{10}$$

Where K is the permeability matrix, F is the force matrix, q is internal head, Q is shape function based on eq.3 and eq. 4, I is the node shape function is calculated for and finally j is the neighboring node of i.

BOUNDARY CONDITION

Boundary conditions in seepage problems are divided into two categories: Essential boundary conditions and Natural boundary conditions.

Essential boundary conditions include Ω_3 (upstream head) and Ω_1 (downstream head).

Natural boundary conditions are defined wherever potential gradient $\left(\frac{\partial \phi}{\partial n}\right)$ is zero which means impermeable boundaries (Ω_2) (Fig. 3).

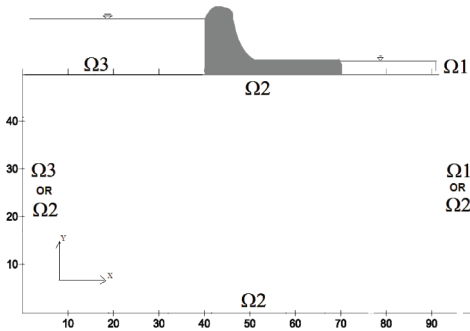


FIG. 3. Definition of boundary conditions in seepage problem.

Bedrock is an impermeable boundary in modeling of seepage problem and so velocity is always zero on that boundary.

In order to model left side and right side boundary conditions of dam, two different approaches are available:

- 1- Left side (near upstream) is assumed as a part of upstream (Ω_3) and right side (near downstream) as a part of downstream (Ω_1).
- 2- Right and left sides of a dam are assumed as an impermeable boundary (Ω_2) but both sides must be far enough from dam.

In this research the second method is used.

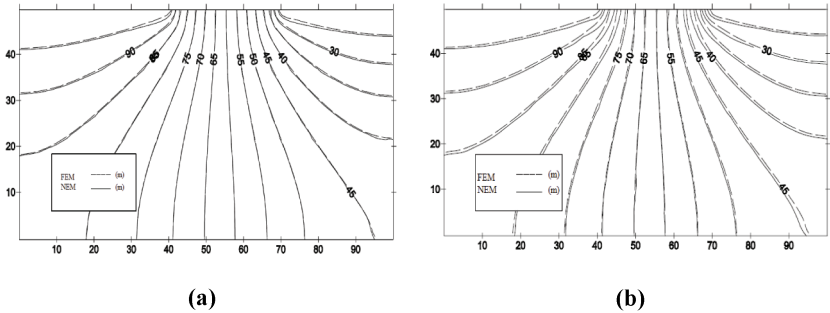


FIG. 4. Potential head on the domain of problem based on (a) regular distribution of nodes (b) irregular distribution.

SEEPAGE MODELLING WITH NEM

A concrete dam is modeled in order to investigate application of NEM in seepage problem. Upstream head is 100 m ($\Omega_3 = 100m$), downstream head is 20 m ($\Omega_1 = 20m$) and other boundaries are presumed as impermeable (Ω_2). In this approach both regular and irregular distribution of nodes has been used. 561, 861 and 1326 number of nodes have been used each time for modeling of soil and results have been assessed with 2389, 4441 and 8977 number of nodes in Plaxis8.0 software which is based on Finite Element Method. Fig. 4 shows potential head on the domain of problem in both regular and irregular distributions with 561 number of nodes.

A control node has been defined under the dam at (60, 50). Potential head from both NEM and FEM analysis has been calculated and results have been compared. Potential head in control node is showed in table 1 and in order to compare accuracy and convergence of methods, potential head values versus node numbers are plotted in Fig. 5. Considering the results at control node, some features of NEM are shown;

Table 1. Potential head at (60, 50) based on regular and irregular distributions.

NEM			FEM(Plaxis)		Difference	
Nodes	Result(reg.)	Result(irreg.)	Nodes	Result	regular	irregular
561	51.83269	54.8464	2389	51.7702	0.06249	3.0762
861	51.80913	53.1588	4441	51.7530	0.05613	1.4058
1326	51.83994	51.9259	8977	51.8617	0.02176	0.0642

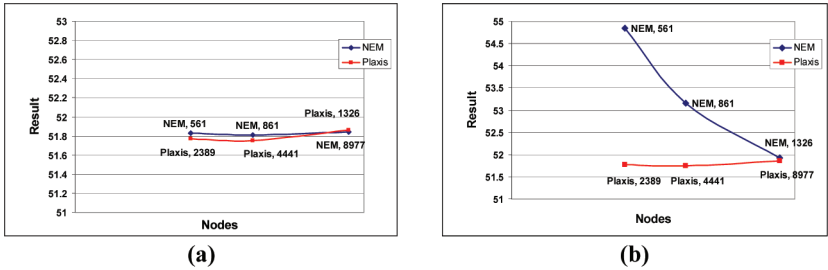


FIG. 5. Convergence and accuracy of Natural Element Method based on (a) regular distribution nodes; (b) irregular distribution nodes.

Regular distribution of nodes provide enough accuracy to achieve suitable results. NEM shows the results by 1326 nodes and three Gouse point in each Delaunay triangulation. On the other hand, FEM shows the same results by 8977 nodes and 15 Gouse points in each element. Convergence to suitable results grows up when irregular distribution of the number of nodes in domain increases, however, in regular distribution of nodes, there is little difference in results between 561 and 1326 number of nodes. Convergence when considering irregular distribution of nodes depends on influence of circumcircle of natural neighbors, in other words, radius of circles for shape functions may be too big to include some nodes that are not required to be in shape functions form.

CONCLUSIONS

In this research, Natural Element Method (NEM) has been investigated in order to solve the seepage problem. Laplace equation is a governing equation on the domain of problem and is used as a weak form method. Results show the robustness and applicability of this method in solving the seepage problem.

Irregular distribution of nodes is much less accurate than regular distribution of nodes in domain of problem. Convergence and accuracy in irregular distribution of nodes strongly depend on the number of nodes in domain of problem. Shape functions in NEM are smoother than FEM and also they have some important properties such as partition of unity and kronocker delta, hence imposition of essential boundary conditions is so simple. Empty circle criterion is a strong process to find neighbor nodes that form a shape function. But this method is time consuming because each node must be evaluated as a neighbor for the whole domain in each step.

REFERENCES

Alfaro, I., Yvonnet, J., Cueto, E., and Doblare, M. (2006). "Meshless methods with application to metal forming." *J. Comput Appl. Mech. Engrg.* Vol. 195 (48-49):

6661-6675.

- Bobach, T. and Farin, G. (2009). "Natural Neighbor extrapolation using ghost point." *J. Computer-Aided Design*. Vol: 41 (5): 350-365.
- Christos, D. A. (2009). "A multigrain Delaunay mesh generation method for multicore SMT- based architectures." *J. Parallel and distributed computing*. Vol 69 (7): 589-600.
- Cho, J.R. and Lee, H.W. (2007). "2-D frictionless dynamic contact analysis of large deformable bodies by Petrov-Galerkin natural element method." *J. Computer & Structures*. Vol. 85 (14-15): 4860-4871.
- Desai, C.S. and Christian, J.T. (1977). "Numerical Methods in Geotechnical Engineering." *McGraw-Hill*, New York.
- Gonzalez, D., Cueto, E., Chinesta, F., and Doblare, M. (2007). "A natural element updated Lagrangian strategy for free-surface fluid dynamics." *J. Computational Physics*. Vol. 223 (1): 127-150.
- Idelsohn, S.R., Onate, E., Calvo, N., and Del Pin, F. (2002). "Meshless Finite Element Ideas." *Fifth World Congress on Computational Mechanics*. Vienna, Austria.
- Jooyandeh, M., Mohades, A., and Mirzakhani, M. (2009). "Uncertain Voronoi diagram." *Information processing letters*, Vol 19 (13): 709-712.
- Lee, C., Kim, D., Shin, H., and Kim, S. (2008). "Trash removal algorithm for fast construction of the elliptic Gabriel graph using Delaunay triangulation." *J. Computer-Aided Design*. Vol 40 (8): 852-862.
- Liu, G.R., Wu, Y.L., and Ding, H. (2004). "Meshfree weak-strong (MWS) form method and its application to incompressible flow problems." *Int. J. Numer. Meth. Fluids*. Vol 46: 1025-1047.
- Liu, G.R. and Gu, Y.T. (2003). "A matrix triangularization algorithm for the polynomial point interpolation method." *J. Comput Appl. Mech. Engrg*. Vol. 192 (19): 2269-2295.
- Liu, G.R. (2002). "Introduction to Meshfree Methods and their programming." CRC Press.
- Liu, G.R. and Gu, Y.T. (2001). "A point interpolation method for two-dimensional solids." *Int. J. Numer. Meth. Engrg*. Vol 50: 937-951.
- Sukumar, N., Moran, B., and Belytschko, T. (1998). "The Natural Element Method in solid mechanics." *Int. J. Numer. Meth. Engrg*. Vol 43: 839-887.

Spherical Discrete Element Simulation of Seepage Flow with Particle-Fluid Interaction Using Coupled Open Source Software

Feng Chen¹, Eric. C. Drumm² and Georges Guiochon³

¹Geotechnical Engineer, HNTB Federal Division, Baton Rouge LA, 70802, USA, fchen@hntb.com

²Professor, Biosystems Engineering and Soil Science Department, University of Tennessee, Knoxville, TN, 37996-20103, USA, edrumm@utk.edu

³Distinguished Professor, Department of Chemistry, University of Tennessee, Knoxville, TN, 37996-1600, and Division of Chemical Sciences, Oak Ridge National Laboratory, Oak Ridge, TN, 37831-6120, USA, guiochon@ion.chem.utk.edu

ABSTRACT: This paper investigates the seepage flow through idealized particle assemblies comprised of spherical elements. Comparisons between an analytical solution and numerical approximation using the Discrete Element Method (DEM) with coupled hydromechanical interaction between the particles and the pore fluid are provided. In the coupled flow DEM, the fluid motion is treated at the macroscopic scale by solving the local averaged Navier-Stokes equation, while the particle interaction is treated at the microscopic scale. The numerical solution is compared with the classical analytical solution in terms of quantity of flow and the pore pressure distribution.

INTRODUCTION

The seepage flow through an assembly of saturated particles over a range of velocities or hydraulic gradients is a classic problem. In the widely adopted classical flow net solution (Lambe and Whitman 1969) or finite element solutions, e.g. MODFLOW (Harbaugh et al., 2000), these methods consider the granular media as a continuum and therefore microscopic inter-particle forces cannot be obtained. The discrete element method is an effective tool for simulating the mechanical behavior of granular soil particles, while computational fluid dynamics provides a rational method to describe the fluid flow. In this paper, coupled flow solutions are provided using a linked pair of open source codes, YADE-OpenDEM for the discrete element method (Kozicki and Donzé 2008), and OpenFOAM for the computational fluid dynamics (OpenCFD Ltd 2008).

THEORETICAL BACKGROUND

In the coupled fluid flow and particle interaction solution described here, the fluid motion is treated on a macroscopic scale, while the particle motion is described on the microscopic scale, as suggested by Anderson and Jackson (1967).

Equations of motion for the fluid - the averaged Navier-Stokes equation

The fluid domain is divided into cells as is common in the finite volume method. The pressure and the fluid velocity are treated as the locally averaged quantity over each fluid cell. The equation of continuity is given as:

$$\frac{\partial n}{\partial t} + \nabla(nU) = 0 \quad (1)$$

where n =porosity; U =fluid velocity; t =time. The momentum equation is given as follows:

$$\frac{\partial nU}{\partial t} + \nabla(nUU) - \nabla \cdot (\mu \nabla U) = -\frac{n}{\rho_f} \nabla p + f_p \quad (2)$$

where μ is the fluid viscosity, ρ_f is the density of fluid, f_p is the interaction force on the fluid per unit mass from the particle, p is fluid pressure.

Interaction term acting on fluid field from the particle

The interaction term representing the effect of a particle on the fluid, f_p , for the averaged Navier-Stokes equation (Anderson and Jackson 1967), is given by Ergun (1952):

$$f_p = \frac{\beta}{\rho_f} (\bar{U}_p - U) \quad (3)$$

where \bar{U}_p is the average particle velocity within a fluid cell, U is the fluid velocity and β is an empirical coefficient determined from Eq. (4):

$$\beta = \begin{cases} \mu(1-n)/d^2 n [150(1-n) + 1.75 Re], & \text{for } n \leq 0.8 \\ 0.75 C_D \mu (1-n) Re / (d^2 n^{2.7}), & \text{for } n > 0.8 \end{cases} \quad (4)$$

where d is the particle diameter, and the Reynolds number Re is defined as:

$$Re = \frac{|\bar{U}_p - U| \rho_f n d}{\mu} \quad (5)$$

and the drag coefficient C_D is:

$$C_D = \begin{cases} 24(1 + 0.15 Re^{0.867})/Re & \text{if } Re \leq 1000 \\ 0.43 & \text{if } Re > 1000 \end{cases} \quad (6)$$

Equations of motion for the particles:

For a particle in fluid, the equation of motion for a single particle is:

$$\dot{y} = (f_G + f_B + f_D + f_C) / m \quad (7)$$

where \dot{y} =acceleration of the particle; f_G =gravity force; f_B =buoyancy force; f_D =drag force; f_C =contact force; and m =mass of the particle. The inter-particle contact force f_C is obtained from the standard DEM approach as proposed by Cundall and Strack (1979). The drag force f_D is the interaction force acting on the particle from the fluid defined below.

Interaction drag force on the particle from the fluid

The drag force f_D is caused by the pressure gradient within the fluid cell and is obtained from the sum of the velocity difference between the particles and fluid, and may be written as:

$$f_D = \left\{ \frac{\beta}{1-n} (U - \bar{U}_p) + \nabla p \right\} V_p \quad (8)$$

where V_p is the volume of a single particle.

Coupling between YADE (DEM) and OpenFOAM (FVM) codes

Following the theory above, the particle phase is solved using the Discrete Element Method while the fluid phase is solved using the Finite Volume Method (FVM). The numerical solution was obtained by coupling two open source codes: the DEM code YADE (Kozicki and Donzé 2008) and the FVM computational fluid dynamics code OpenFOAM (OpenCFD Ltd 2008). In order to couple YADE and OpenFOAM, a customized YADE routine FluidDragForceEngine was written to wrap and incorporate the OpenFOAM fluid solver into the YADE main program as depicted in FIG. 1. The flow field (velocity, pressure) is first solved within the OpenFOAM solver; the FluidDragForceEngine then calculates the drag forces obtained from the flow field and adds the drag forces f_D to the YADE mechanical loop. Meanwhile, the drag forces exerted on the flow field are also incorporated to the average Navier-Stokes momentum equation (Eqs. (2)).

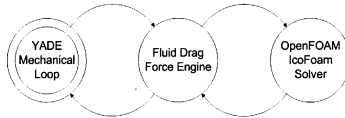


FIG. 1. Framework of YADE and OpenFOAM coupling.

2D SEEPAGE SHEET PILE PROBLEM DESCRIPTION

The classical sheet pile problem is investigated with the coupled DEM-CFD algorithm. The geometry of the sheet pile model is taken from Lambe and Whitman (1969) as depicted in **Error! Reference source not found.** The seepage under the sheet pile wall, pore water pressure, and pressure gradient in the subsoil can be obtained from the well established approach based on the flow net.

Analytical solution for the sheet pile model

The solution for the quantity of flow under the sheet pile wall and the hydraulic gradient at any portion of the flow domain can be obtained directly from the flow net, where the seepage or quantity of flow under sheet pile wall is:

$$\frac{Q}{L} = k_p h_L \frac{n_f}{n_d} \tag{9}$$

where k_p is the permeability coefficient, h_L is the head loss, and n_f/n_d is the shape factor from the graphical flow net. The exit gradient is:

$$i = \frac{\Delta h}{l} \tag{10}$$

where Δh is the total head loss across any pair of equipotential lines which is equal to H/n_d and l is the distance between the equipotential lines in the region of interest.

COUPLED DEM-CFD SHEET PILE MODEL

Scaling law for the sheet pile model

The computational time for a DEM solution can be significant for coupled flow problems with a large number of particles. Assuming the particle diameter $d=1\text{mm}$, the number of

soil particles in a 2-D model of the above problem is about 7.02×10^8 particles. An alternative approach is to adopt a reduced scale model of the prototype shown in FIG. 2 so that the DEM model can contain an acceptable number of particles, yet preserve the desired permeability. The dimension for the reduced scale sheet pile model chosen here is $1/N=1/660$ of the dimensions of the prototype as listed in Table 1. The scale model reduces the number of particles to 1800.

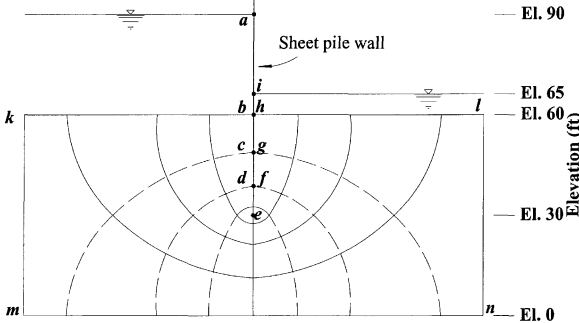


FIG. 2. Flow under sheet pile wall (Lambe and Whitman 1969).

Table 1. Scaled dimensions for the sheet pile prototype and the DEM/FVM model.

Length Reference source Error! not found.	Prototype (ft)	Prototype (m)	Model (m)
<i>km</i>	60	18.29	0.028
<i>mn</i>	130	39.62	0.060
<i>be</i>	30	9.14	0.014

In contrast to traditional scaled geotechnical centrifuge models (Taylor 2007), because the fluid flow in the soils are pressure driven, and the flow behavior is primarily determined by pressure (hydraulic) gradient instead of vertical stress within the soil, we can assume that the hydraulic gradient is the same in both the model and the prototype, and if the model and the prototype are composed of the same porous media, then:

$$k_{pp} = k_{pm} \nabla p_p = \nabla p_m \tag{11}$$

where ∇p_p is the pressure gradient in the prototype, and ∇p_m is the pressure gradient in the model. The gravity constant is kept the same for both model and prototype, and k_{pp} and k_{pm} is the permeability coefficient for the prototype and the model, respectively.

Coupled DEM-CFD sheet pile model

The coupled DEM-CFD model is created as shown in FIG. 3; the model shows the state of particles and fluid cells following the particle packing under a hydrostatic gravity field as described below, and each fluid cell contains around 23 particles. The sheet pile wall is placed between fluid cell 35, 29, 23 and 54, 60, 66, by creating two no-flow boundaries at *be* and *eh*. The soil and the fluid are considered incompressible, and it is also assumed that the soil can be represented by an assembly of particles. It can be regarded as a 2D plane strain problem with the thickness of the model taken as the diameter of the particle.

The particles that are slightly above the ground surface at points k and l are simply remnants of the initial hydrostatic packing process and could have been artificially restrained if desired. The boundary conditions for the flow under the sheet pile wall are as listed in Table 2.

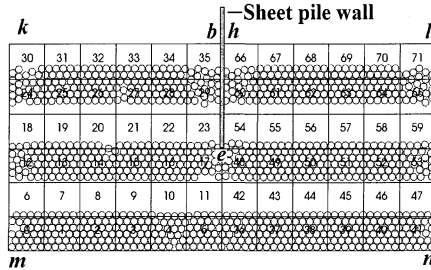


FIG. 3. Fluid mesh and initial particle packing for the 2-D sheet pile wall problem.

Table 2. Boundary conditions for the sheet pile model (FIG. 3).

Pressure boundary:		
Zero Gradient	km, mn, ml	
Fixed Value (Pa)	$kb: p=\rho_wgh$	$hl: p=0$
Velocity boundary:		
Zero Gradient	kb, hl	
Fixed Value (m/s)	$km, mn, ml: U=(0, 0)$	

Determine material properties of the sheet pile model

The basic physical and geometric properties of the sheet pile model are as listed in . The permeability coefficient is then derived from these basic parameters, using Ergun’s empirical equation (Ergun 1952) for a packed column of height H_{col} :

$$\frac{\Delta p}{H_{col}} = \frac{1-n}{dn^3} \left\{ 150 \frac{(1-n)\mu u^*}{d} + 1.75 \rho_w u^{*2} \right\} \tag{12}$$

where u^* is the superficial velocity and ρ_w is the density of water which now replaces the fluid density ρ_f in Eq. (2). The hydraulic gradient is:

$$i = \frac{\Delta h}{H_{col}} = \frac{\Delta p}{\rho_w g H_{col}} = \frac{1-n}{\rho_w g d n^3} \left\{ 150 \frac{(1-n)\mu u^*}{d} + 1.75 \rho_w u^{*2} \right\} \tag{13}$$

The permeability k_p can be obtained as:

$$k_p = \frac{u^*}{i} = \frac{\rho_w g u^*}{\frac{1-n}{dn^3} \left\{ 150 \frac{(1-n)\mu u^*}{d} + 1.75 \rho_w u^{*2} \right\}} = \frac{d^2 n^3 \rho_w g}{150 \mu (1-n)^2 + 1.75 d (1-n) \rho_w u^*} \tag{14}$$

Using the particle and fluid parameters listed in Table 3, the permeability coefficient is found to be $k_{p,avg}=0.0172\text{m/s}$ for the model (assume $u^* \approx 0$ and using average porosity $n_{avg}=0.437$ for the whole fluid domain).

Table 3. Physical and geometrical parameters for the 2D problem.

Parameter	Value	Unit
Solid (particle)		
Number, N_p	1800	
Radius, r	5.0×10^{-4}	m
Density, ρ_s	2650	kg/m ³
Contact stiffness, k_n	800	N/m
Friction angle	30	Degree
Fluid (Water at 20°C, 1atm)		
Density, ρ_w	1000	kg/m ³
Viscosity, μ	1.004×10^{-3}	Pa-s
Sheet pile configuration		
Width	0.060	m
Height	0.028	m
Thickness	1.0×10^{-3}	m
Fluid cell size $\Delta x \times \Delta y$	5.0×4.7	(10 ⁻³ m) ²
Gravity constant	9.81	m/s ²

SIMULATION PROCEDURE

Initial hydrostatic state

Before the boundary pressure conditions are applied, the particle assembly undergoes a settling procedure so that the hydrostatic state is approximately reached. The initial conditions are established in 2 steps: (1) The 1800 equal diameter particles are packed sequentially with no space or overlap with the water level above the topmost particle. (2) The particles then settle to the hydrostatic state under influence of gravity and buoyancy forces, i.e. the consolidation under gravity and buoyancy force is completed. The simulation will take the state after step (2) as the initial condition.

Applying the pressure gradient

Starting from the initial hydrostatic state above, a fluid pressure is then applied to the top left line kb of the sheet pile model while the top right line hl is fixed at $p=0$ so a pressure gradient is created within the saturated soil.

NUMERICAL SOLUTIONS FOR THE SHEET PILE PROBLEM

Starting from the initial condition as shown in **Error! Reference source not found.**, the coupled DEM-CFD solution will be discussed in terms of both the transient and the traditional steady state solutions.

Transient and steady state pressure distribution

FIG. 4 shows the computed contours of pore water pressure (which correspond to the equipotential lines in the flow net) at different solution times for an applied pressure in the model $\Delta p_m = 200 Pa$. This corresponds to an exit gradient $i_e = 0.48$ which is well below the critical value of $i_c = 1.0$. The computed pore water pressures are observed to change over time until the system reaches a steady state after 4×10^{-3} seconds (FIG. 4(d)). At this

solution time the equal potential lines are found to be in close agreement with the classical flow net solution as shown in FIG. 2.

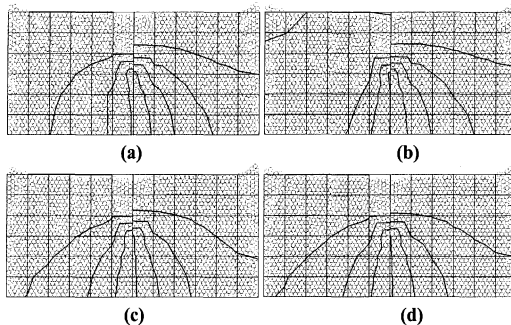


FIG. 4. Pressure contour development for applied pressure 200Pa at different time (a) $t=6 \times 10^{-4}s$, (b) $t=8 \times 10^{-4}s$, (c) $t=1.8 \times 10^{-3}s$, (d) $t=4 \times 10^{-3}s$.

The classical solution of quantity of flow per unit width through the prototype is:

$$q = \frac{Q}{L} = k_{p,avg} H \frac{n_r}{n_d} = 0.0172(0.0204) \frac{4}{8} = 1.75 \times 10^{-4} (m^3/s/m) \tag{15}$$

The DEM-CFD solution for quantity of flow is the sum of flux from fluid cells number 66-71 across the surface on the right side of the flow domain is $1.15 \times 10^{-4} (m^3/s/m)$, which agrees reasonably well with the analytical solution obtained with an average uniform porosity. The calculation details are shown in Table 4. In a similar manner, the sum of flux across the left side of flow domain (cells 30-35) can be obtained and is $1.07 \times 10^{-4} (m^3/s/m)$. The hydraulic gradient at the exit point is obtained from the flow net solution as $i_e=0.48$, which is well below the critical value of 1.0 corresponding to quick conditions.

Table 4. Quantity of flow under the model sheet pile wall using the DEM-CFD.

Cell ID	Computed porosity	Pressure (Pa)	U_x (m/s)	U_y (m/s)	$U_y^* = U_y \times \text{porosity}$ (m/s)
66	0.5770	1.5435	0.0006	0.0171	0.009879327
67	0.4434	1.1400	0.0003	0.0073	0.003236165
68	0.4434	0.9636	-0.0001	0.0062	0.002747864
69	0.4657	0.8225	0.0001	0.0057	0.00267446
70	0.4657	0.7069	0.0001	0.0049	0.002271956
71	0.4657	0.7340	0.0000	0.0048	0.002256888
				$Q/L =$	$1.15 \times 10^{-4} (m^3/s/m)$

U_y^* is the superficial velocity in the y direction

Contact force distribution

FIG. 5 shows the distribution of contact force between the particles, which indicates that the contact forces on the surface of the downstream side of the sheet pile are only slightly less than those at the upstream side, which is expected for the low value of the exit

gradient ($i_e=0.48$). If the pressure gradient is increased, the downstream contact forces will decrease, and the conditions leading to a quick condition may be investigated.

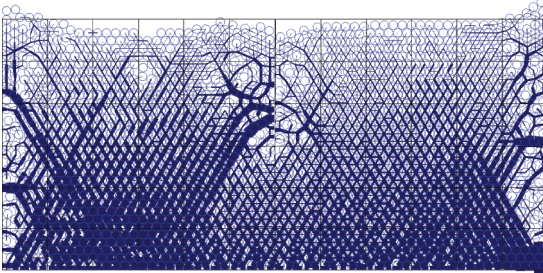


FIG. 5. Contact force plot between particles exit gradient $i=0.48$ (the broader the band the higher the contact forces).

CONCLUSIONS

A coupled DEM-CFD model was created for the classic fluid flow under sheet pile problem. In order to limit the number of particles, an equal pressure gradient scaling law was used to scale the problem domain of the model while maintaining the permeability of the prototype. The calculated steady state pressure contours and quantity of flow from the model reasonably matches the classical solution from the flow net. While not of practical significance, the DEM/finite volume method is also able to present the transient pressure development during the early stages of the pressure application. Because the DEM solution yields the inter-particle contact pressures, conditions leading to a quick condition may be investigated.

REFERENCES

- Anderson, T.B. and Jackson, R., (1967). "A fluid mechanical description of fluidized beds." *Industrial & Engineering Chemistry Fundamentals*, 6 (4): 527-539.
- Cundall, P.A. & Strack, O.D.L., (1979). "A discrete numerical model for granular assemblies." *Geotechnique*, 29: 47-65.
- Ergun, S. (1952). "Fluid flow through packed columns." *Chemical Engineering Progress*, 48 (2): 89-94.
- Harbaugh, A.W., Banta, E.R., Hill, M.C., and McDonald, M.G., (2000). *MODFLOW-2000*, the U.S. Geological Survey modular ground-water model -- *User guide to modularization concepts and the Ground-Water Flow Process: U.S. Geological Survey Open-File Report 00-92*, 121 p.
- Kozicki, J. and Donz , F.V. (2008). "A new open-source software developed for numerical simulations using discrete modeling methods." *Computer Methods in Applied Mechanics and Engineering*, 197: 4429-4443.
- OpenCFD Ltd. (2008). *The open source CFD toolbox, Programmer's Guide*, Version 1.4.1. Available at: <http://foam.sourceforge.net/doc/Guides-a4/ProgrammersGuide.pdf> [Accessed May 13, 2008].
- Lambe, T.W. and Whitman, R.V. (1969). *Soil mechanics*, New York: Wiley., pp 267-274.
- Taylor, R.N. (2007). *Geotechnical Centrifuge Technology*, Taylor & Francis., pp 20-26.

Seepage Failure and Erosion of Ground with Air Bubble Dynamics

Kenichi Maeda¹ and Hirotaka Sakai²

¹Associate Professor, Graduate School of Civil Engineering, Nagoya Institute of Technology, Gokiso-cho, Showa-ku, Nagoya, 466-8555 JAPAN; maeda.kenichi@nitech.ac.jp

²PhD. student, Graduate School of Civil Engineering, Nagoya Institute of Technology, Gokiso-cho, Showa-ku, Nagoya, 466-8555 JAPAN; cgt18503@stn.nitech.ac.jp

ABSTRACT: We report on the generation of air bubbles in a void and how this can affect seepage failure. In order to study this phenomenon, we conducted model tests with a new numerical simulation. During the tests we observed deformation-failure in sandy ground inundated with pore water that contained various values of dissolved oxygen. We investigated the process of seepage failure both with and without air bubbles, using PIV image analysis. It was found that the addition of air bubbles promoted damage to the ground even under low hydraulic gradients, and therefore we concluded that this local-progressive deformation was caused by the dynamics of air bubbles. We also succeeded in simulating these phenomena by a newly-developed Smoothing Particle Hydrodynamics (SPH) method that involves a process of generating air bubbles and enabling interactions among three phases (soil-liquid-gas)..

INTRODUCTION

Large flowage deformations and the seepage failure of ground “*pip*ing”, which induces erosion, are caused by the permeation of water through the granular ground layers. This plays an important role in the destabilization of ground during floods, liquefaction, erosion and so forth. In order to analyze these phenomena more precisely, it is necessary to model progressive seepage failure in the soil. Some reports have found that interactions between all three phases—solid, liquid and gas—play important roles. In particular, Kodaka & Asaoka (1994) could be the first instance in which the importance of the dynamics of air bubbles in geo-engineering was revealed. Furthermore, when the Tokai flooding disaster occurred in the Nagoya region on 11 September 2000, a man who witnessed the process of dike failure recounted his story in a newspaper; he claimed that, after a crack formed on the surface of the dike, white bubbles of water blew out of the crack, after which the dike gradually failed over a period of about three hours. In fact, this type of phenomenon has been frequently witnessed for generations. The blowing air bubbles that precede seepage failure are called “*frog blows bubbles*” by elderly people, while Terzaghi (1942) gives a definition of hydraulic failure without air bubbles.

In this study, we conducted model tests and developed a new numerical simulation method for seepage failure with air bubbles. The *smoothed particle hydrodynamics* (SPH) method (Gingold & Monaghan, 1977; Lucy, 1977), a completely mesh-free technique, was used to obtain the combined benefits of both the discrete and continuum methods. In this study (Maeda & Sakai, 2004; Maeda et al. 2006), we proposed SPH with a new method for calculating density, surface tension and multi-phases couplings. Our simulation results were also verified by comparisons with model test results.

MODEL TESTS WITH PIV

In our model tests, we observed the deformation-failure around sheet-pile in sand (Toyoura sand) ground submerged in two kinds of water (see Fig. 1(a)): water with low DO (dissolved oxygen) and water with high DO and over-saturated air (see Fig. 1(b)). In the latter, air bubbles were easily generated. Two types of tests were conducted, following Kodaka & Asaoka (1994): a “normal piping” test with lower DO and a “holding” test. In the normal piping test, a difference in water level, h , or head loss applied to the ground, was increased to a critical head loss, h_{cr} , in which piping occurred in the ground. In the holding test, applied head loss, h , was held until piping occurred. If piping did not occur even after much time had elapsed, h was increased again to generate piping. The velocity field of the ground was measured using particle image velocimetry (PIV) image analysis, and the strain rate fields were calculated.

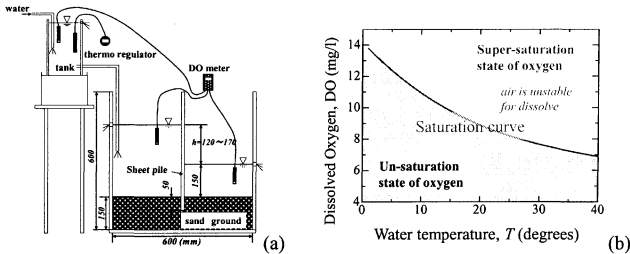


FIG. 1. Model test apparatus for seepage failure and DO (dissolved oxygen) saturation curve.

Figure 2(a) shows the typical deformation-failure behaviours around the sheet-pile for lower DO and higher DO cases respectively. Figure 3 shows the relative applied head loss, h/h_{cr} , indicating the resistance to piping with elapsed time after h was increased and/or held. In the lower DO case in the normal piping test, piping occurred at $h/h_{cr} = 1$, in accordance with the definition. However, in the higher DO case, even though h was less than h_{cr} , air bubbles were generated as shown in Fig. 2(b), and, consequently, failure occurred in the holding test. When the water level was increased after holding the smaller water level difference, h , for a long duration, the failure tended to occur even before the water level difference reached the critical level, h_{cr} (i.e. when $h/h_{cr} < 1$), which is a similar way of creep failure in a material under a constant loading condition that is less than its strength. This implies that air bubbles in the ground bring about

strength degradation. The relationship between air bubble generation and DO, and the influence of air bubbles on the ground were investigated in the following sections.

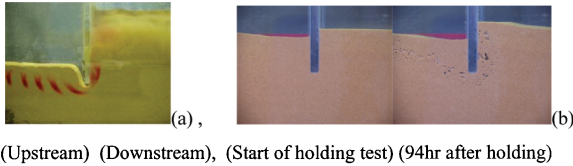


FIG. 2. Piping test: (a) seepage failure with water of lower DO and without air bubbles in normal piping test: increasing head loss of h to h_{cr} and (b) Deformed ground just prior to piping with water of higher DO in holding test: holding head loss $h = 0.8 \times h_{cr}$.

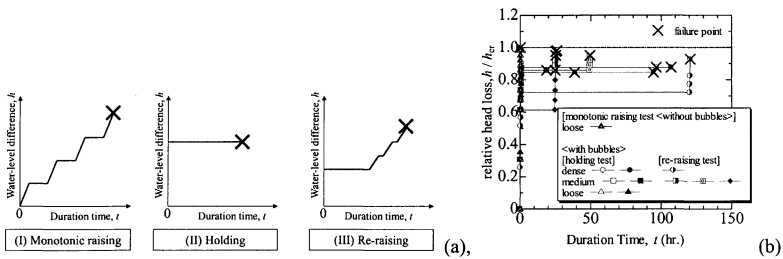


FIG. 3. Reduction of resistance to piping due to presence of air bubbles: (a) experimental conditions, (b) Decrease in resistance with time for various densities.

The change in the amount of air bubbles on the downstream side was calculated by image analysis and the change in the void ratio. Fig. 2(b) shows that as both amount of air bubbles and the void ratio, e , increase, the critical hydraulic gradient (resistance against the failure) of the ground, $i_{cr} = (G_s - 1) / (1 + e)$, decreases, where G_s is the soil particle specific weight. Otherwise, seepage distances around the sheet-pile, L , decrease due to scour in ground, as shown in Fig. 2(b). The hydraulic gradient, $i = (h/L)$, increases even through h is constant. Consequently, as the stability for piping, i_{cr}/i , decreases, the resistance to piping h/h_{cr} decreases as shown in Fig. 3. This is the air bubble effect.

NUMERICAL ANALYSIS: SPH

The SPH method is a particle-based Lagrangian method. It was originally developed by Gingold and Monaghan (1977) and Lucy (1977) in the field of astrophysics to solve motions of galaxies. The SPH method was not intended for application with actual soil grains but rather to treat “particles” as a granular mass (Fig. 4(a)), whose radius is h . Similarly, a water “particle” is a finite volume of water rather than a molecule. These particles can overlap. The spatial averaged value $\langle f(x) \rangle$ of a physical quantity $f(x)$ at centre point x of i -th particle is given by equation (1) using mass m_i and density ρ_i . The

physical quantity is interpolated using a smoothing function W in Fig. 4(a), where the effective distance of W was set to be $2h$ in this paper,

$$f_i = \langle f(\mathbf{x}_i) \rangle \cong \sum_{j=1}^N m_j \frac{f_j W_{ij}(\mathbf{r}_{ij}, h)}{\rho_j} \quad (1a), \quad 1 = \int W_{ij}(\mathbf{r}_{ij}, h) d\mathbf{r}_{ij} \quad (1b)$$

where $\mathbf{r}_{ij} = \mathbf{x}_i - \mathbf{x}_j$ and W_{ij} was defined by Eq.(1b). In this paper, the third-order B-spline function was employed as W_{ij} , and $r_{ij} = |\mathbf{r}_{ij}|$; the shape was similar to normal distribution.

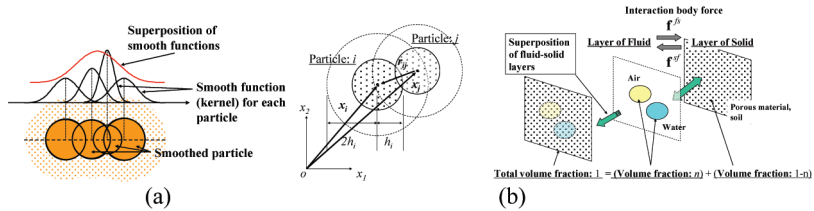


FIG. 4. SPH simulation procedures: (a) smoothed particle and smoothing function, (b) interaction force to coupling between solid-liquid-gas.

The density ρ_i of particle i is replaced with f_i . However, this original description shows large error in densities calculated around material interfaces. We remedied this point by means of the normalization and limited summation for a focused material a .

$$\rho_{i \in \text{Material } a} = \frac{\sum_{j=1 \in \text{Material } a}^N m_j W_{ij}}{\sum_{j=1 \in \text{Material } a}^N \left(\frac{m_j}{\rho_j} \right) W_{ij}} \quad (2)$$

The SPH description for a particle i in a motion equation can be explained as follows:

$$\frac{dv_i}{dt} = - \sum_{j=1}^N m_j \left(\frac{\sigma_j}{\rho_j^2} + \frac{\sigma_i}{\rho_i^2} + \Pi_{ij} \mathbf{I} \right) \cdot \nabla W_{ij} + \mathbf{f}_i \quad (3a), \quad \mathbf{f}^{sf} = -\mathbf{f}^{fs} = n \frac{\rho_f g}{k} (\mathbf{v}^s - \mathbf{v}^f) \quad (3b)$$

where σ and f are stress tensor and body force respectively. The matrix \mathbf{I} is the unit matrix, and Π_{ij} is the artificial viscosity.

For the purpose of coupling, the soil and the fluids of water and air were handled on different layers (see Fig.4(b)). The frictional body forces resulting from velocity differences between two phases, \mathbf{v}^s and \mathbf{v}^f , were calculated with Biot's mixture theory (Biot, 1941). The forces involved could be expressed by Eq. 3(b). Here, porosity n , permeability k , fluid density ρ_f and gravity acceleration g ($= 9.8 \text{ m/s}^2$) were included.

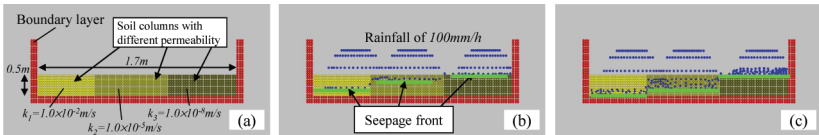


FIG. 5. The seepage front propagation induced by heavy rain fall by SPH simulation from (a) to (b) and (c), where the ground is divided into three vertical column with different permeability coefficients k of 1.0×10^{-2} , 1.0×10^{-5} and 1.0×10^{-8} m/s.

Figure 5 shows the simulated seepage behaviours with rainfalls of 100 mm/h under different permeabilities for water, where there was no air phase in the ground initially. It can be found that the seepage rate in the downward direction increases with permeability k . We also obtained a good correlation between the SPH solution and Terzaghi's theoretical one-dimensional solution (Maeda and Sakai, 2006). These indicate the coupling model in Eq. 3(b) is accurate. Figure 6 shows a soil-water coupling SPH model of the experiment shown in Fig.2(a) without air bubbles; water density is 1000 kg/m^3 , and the viscosity is $1.002 \times 10^{-3} \text{ N}\cdot\text{s/m}^2$. Air density is 1.207 kg/m^3 , and the viscosity is $1.810 \times 10^{-5} \text{ N}\cdot\text{s/m}^2$. The state equation of fluids and the constitutive law of granular material were employed (Maeda et al., 2006); surface tension was also introduced (Maeda et al. 2004). The elastic-perfect plastic-type model with internal friction angle and dilatancy angle was taken as the constitutive relation of soil, where elastic stiffness was described as a function of void ratio and mean effective stress (see Maeda et al., 2006). This model can successfully simulate characteristics of seepage failure not only during deformation but also after the failure events. We made comparisons between our test results and the simulation results for the pore water pressure and the velocity field, and they strongly validated this model. Figure 7 shows the dike with difference in water level on both sides after seepage had been induced in dike as shown in Fig.7(a). The proposed model could simulate a sequential failure.

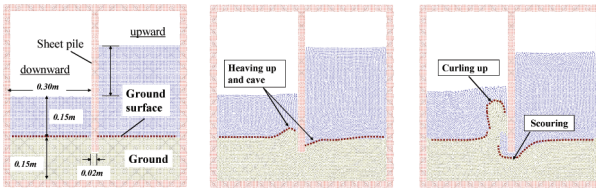


FIG. 6. Seepage failure coupling analysis around sheet-pile without air bubbles; ground with permeability k of $1.0 \times 10^{-5} \text{ m/s}$ when $h = h_{cr}$.

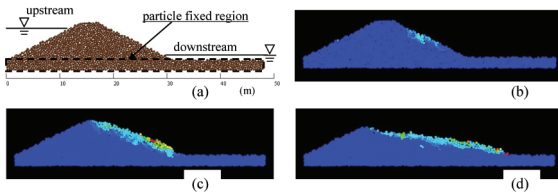


FIG. 7. Seepage failure analysis of dike where particle colour indicates its velocity (red is high; blue is low): (a) analysis configuration, (b) first local movement and erosion, (c) failure progression, (d) washed-out after collapse attached to the crest.

Figure 8 shows a three-phase coupling SPH prediction of the seepage failure with air bubbles at below 80% of the water height difference in Fig. 6. The air bubbles were forcibly replaced with another phase at the initial state. The local deformation and failure of granular ground are induced by rising air bubbles as well as experiments, even under a lower h than h_{cr} .

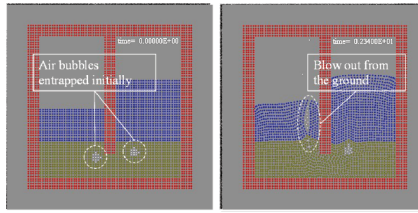


FIG. 8. Seepage failure analysis with air bubbles; generation of local failure occurs at local site even when $h = 0.8 \times h_{cr}$.

CONCLUSIONS

We investigated the effect of air bubbles generated in a void on seepage failure. We conducted model tests and developed an SPH simulation which could accommodate some modifications and three-phase coupling. In the model testing we observed the deformation-failure that occurred in sandy ground submerged by pore water with various values of dissolved oxygen. We found that the presence of air bubbles was linked to ground damage even under low hydraulic gradients and that the local-progressive deformation was induced by the dynamics of air bubbles. Moreover, we succeeded in simulating these phenomena by the newly-developed method. This study clearly validates and demonstrates the usefulness of SPH.

ACKNOWLEDGMENTS

The authors are grateful to the Japan Society for the Promotion of Science for its financial support with Grants-in-Aid-for Scientific Research (B) 20360210.

REFERENCES

- Biot, M. A. (1941). "General theory of three dimensional consolidation." *Journal of Applied Physics*, Vol.12: 152-164.
- Gingold, R.A. and Monaghan, J.J. (1977). "Smoothed particle hydrodynamics: theory and application to non-spherical stars." *Monthly Notices of the Royal Astronomical Society*, Vol.181: 375-389.
- Kodaka, T. and Asaoka, A. (1994). "Formation of air bubbles in sandy soil during seepage process." *Journal of JSCE*, Vol. 487 (III-26): pp.129-138. (in Japanese).
- Lucy, L. B. (1977). "A numerical approach to the testing of the fission hypothesis." *Astronomical Journal*, Vol.82: 1013-1024.
- Maeda, K., Sakai, H. and Sakai, M. (2006). "Development of seepage failure analysis method of ground with smoothed particle hydrodynamics." *Journal of Structural and earthquake engineering*, JSCE, Division A, Vol.23, No.2: 307-319.
- Maeda, K. and Sakai, M. (2004). "Development of seepage failure analysis procedure of granular ground with Smoothed Particle Hydrodynamics (SPH) method." *Journal of Applied Mechanics*, JSCE, Vol.7: 775-786.
- Sakai, H. and Maeda, K. (2007). "A study on seepage failure of sand ground with account for generation and development of air bubbles." *Proc. of 13th Asian Regional Conference on Soil Mechanics and Geotechnical Engineering*: 571-574.

A Proposed Calculation Method for Land Subsidence Caused by Groundwater Withdrawal in Jiangsu Province

Weihua Lv¹, Linchang Miao², and Chunlin Li³

¹Ph. D. Student, Institute of geotechnical engineering, Southeast University, Nanjing, China, 210096, lvweihua@yahoo.com.cn

²Professor, Institute of geotechnical engineering, Southeast University, Nanjing, China, 210096, lc.miao@seu.edu.cn

³Ph.D. Student, Institute of geotechnical engineering, Southeast University, Nanjing, China, 210096, lichunlin111@126.com

ABSTRACT: This paper proposed a coupled calculation model for land subsidence caused by groundwater exploitation, which can consider the variation of permeability of the confining aquifer during pumping. The coefficient of permeability of the confining aquifer can be calculated using water head decline. Coupling with the linear relation of water level decline and land subsidence, the subsidence is easy to compute. A case of Qingliang Primary School in Jiangsu province is conducted to verify the effectiveness, and the results indicated that the coupled calculation model could agree well with the measured data. Based on the coupled model, the water level decline and land subsidence can be predicted, which is important for making the groundwater exploitation plans.

INTRODUCTION

Prediction of land subsidence due to excessive groundwater pumping is important for protection of city buildings, tunnels and underground pipelines, which are suffering the geological hazard. As to calculation methods of land subsidence, they can be divided into two categories, namely, the two-step model method and the coupled model method. In the two-step method, the groundwater head decline is calculated firstly, and then the consolidation theory can be used to obtain the subsidence (Relif, 1969; Gambolati and Freeze, 1973; Gambolati, 1974; Helm, 1975; Gambolati, 1991; Xu, 1995; Li, 2000). The permeability and the void ratio in this method are both assumed constant, which might cause some error in the calculation.

The possible reason is the sand particle breakage was observed in compression test in which the pressure is almost equal to the earth pressure of the pumped aquifer. As to the second method, in the existing coupled models, a relative complex iteration process is necessary to consider the changing of void ratio and permeability. (Lewis, 1978; Bear, 1981; Shen, 2006; Luo, 2008). The deformation of the aquifer system is calculated at first, and then the void ratio and the permeability are back calculated and then reused to calculate the head decline. Many cycles are always needed to obtain the result, and the process is always complex. Therefore, this paper proposed a simplified calculation method to consider the variation of void ratio and permeability of the pumped aquifer. A case from Jiangsu province was analyzed to verify the effectiveness of the presented method.

COUPLED CALCULATION MODEL

Groundwater head decline calculation

In the proposed model, the void ratio, which acts the intermediate variable, is affected by the water level decline and the compaction of aquifer. Equation (1) is an empirical formula to calculate the permeability changing with the void ratio, which is developed based on a number of test data.

$$k/k_0 = (e/e_0)^3 \cdot (1 + e_0/e) \quad (1)$$

Where k_0 is the initial permeability coefficient, k is the permeability coefficient changing with the water head decline, and e_0 is the initial void ratio of the pumping aquifer, e is the void ratio changing with the pumping process. Theoretically, the volume of the pumped water should be equal to the void changing in the pumped aquifer. The water level decline can definitely cause the increasing of the effective stress. Equation (2) is a typical e - $\log p$ curve formula, which is commonly used in the geotechnical engineering.

$$c_c = (e_0 - e) / (\lg h - \lg h_0) \quad (2)$$

Where C_c is the compression index, e_0 and e are same as the variable in Equation (1), h and h_0 are the water head during pumping and the initial water head respectively. Combing Equation (1) and (2), the relation of void ratio and the water head during pumping can be obtained, which is the Equation (3). Then the coefficient of transmissibility T can be expressed as follows:

$$k = k_0 \left((e_0 - c_c \lg(h/h_0)) / e_0 \right)^3 (1 + e_0 / (e_0 - c_c \lg(h/h_0))) \quad (3)$$

In the groundwater dynamics theory, the coefficient of transmissibility T can be calculated using Equation (4):

$$T = kH \tag{4}$$

Where k is the permeability of the pumped aquifer, H is the thickness of the aquifer. Taking Equation (3) into Equation (4), one can get:

$$T = Hk_0 \left((e_0 - c_c \lg(h/h_0)) / e_0 \right)^3 (1 + e_0 / (e_0 - c_c \lg(h/h_0))) \tag{5}$$

Equation (5) apparently looks some complex, however, we found a simply relation between the water head decline and the coefficient of transmissibility, which can be represents as Equation (6):

$$T = Ah + B \tag{6}$$

Where A and B are two constants, and they can be determined using pumping test data. With a water head decline value, one can calculate a coefficient of transmissibility value through Equation (4). Then, drawing a curve of head decline versus coefficient of transmissibility using the test data, a liner tendency line could be obtained, thus A and B are both determined. Cooper-Jacob developed an equation which can be used to calculate water head decline, it is Equation (7) (Burbey, 2003).

$$h = 2.303Q \cdot \lg \left(\frac{(2.25tT)}{(r^2 S_s)} \right) / (4\pi T) \tag{7}$$

Where h is the water head decline, Q is the constant pumping rate, T is the coefficient of transmissibility of the aquifer, and S_s is the storage constant for aquifer. In Equation (7), the both sides have term h , which means we can calculate h using an iteration process, and the Newton Iteration Method was used to obtain h . During the calculation, we found the real result could be achieved only in 2 or 3 cycles.

Subsidence Calculation

Holzer (1981) pointed out that there is a linear relationship between the water head decline and the subsidence. The slope is the aquifer storage. Based on the water head decline determined in last section, one can easily obtain the subsidence.

EVALUATION

To evaluate the effectiveness of the proposed method, one case from Jiangsu province was conducted. Figure 1 is the water level, accumulated deformation and time curves of the second and the third confining aquifers in Qingliang primary school in Changzhou (Shi, 2006). Since 1995, the government has strengthened the management of groundwater exploitation. Especially after 2000, based on the proposal of the National People's Congress of Jiangsu province, Suzhou, Wuxi and Changzhou, were forced to stop pumping groundwater. Because of this policy, the water heads in the second and the third aquifers are starting coming back to the

1990's level.

Using Equation (7) and the parameters in Table 1, one can easily get the water head decline, and then base on the decline, the subsidence can be achieved. Figure 2 and 3 show the comparison of the measured data, the results by coupled model proposed in this study, and the uncoupled model. It demonstrates that the proposed method is more effective to predict the land subsidence.

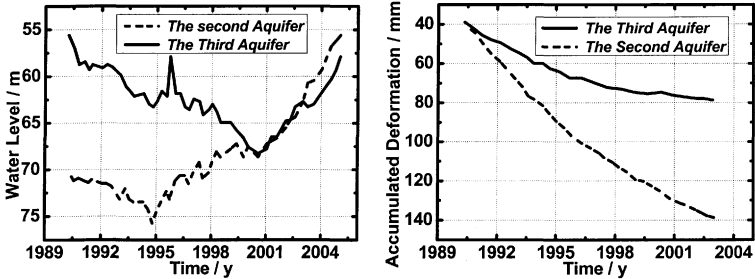


FIG. 1. Water level decline and deformation.

Table 1. Physical and mechanical parameters in Qingliang Primary School.

Layer Group	Water Content, w(%)	Bulk Density, $r(\text{kN/m}^3)$	Void Ratio, e	Compression Index, C_c	Cohesion, c(kPa)		Friction Angle, ϕ ($^\circ$)	
1	24.0	18.65	0.759	0.078	4.0		32.7	
2	25.2	18.80	0.762	0.088	18.0		28.1	
Layer Group	Pumpage, $q(\text{m}^3/\text{d})$	Initial Hydraulic Conductivity Coefficient, $T(\text{m}^2/\text{d})$	Distance From the Well, r(m)	Storage Coefficient, S_s	Thickness, H(m)	A	B	
1	2300	20.3	50	0.01899	92.66-109.99	-1.35	21	
2	2000	20.0		0.02556	118.5-144.78	E-3		

Note: 1. The second confining aquifer, green gray fine sand; 2. The third confining aquifer, sallow sand.

CONCLUSIONS

A coupled model based on Jacob's method was proposed considering the changing of void ratio and permeability of pumped aquifers. A formula, linking the permeability of the aquifer and the water head decline, was developed through the void ratio. With this formula, the permeability can be calculated with the water head

decreasing. Combing the linear relationship of the water head decline and the subsidence, the land subsidence can also be easily obtained. To verify the effectiveness of the presented method, a case from Jiangsu province was conducted. The whole process showed that the calculation results using the proposed model are more close to the observation data than the uncoupled model.

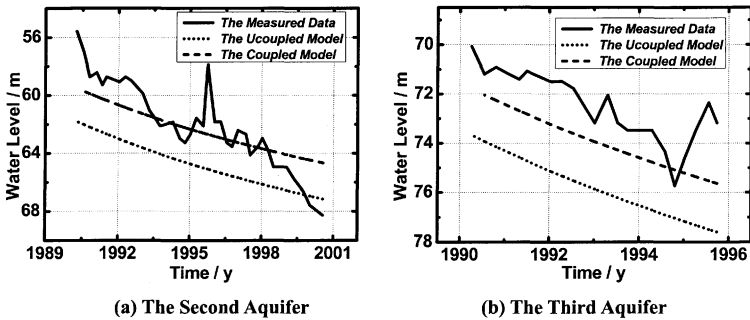


FIG. 2. Water level decline of two aquifers in Qingliang Primary School.

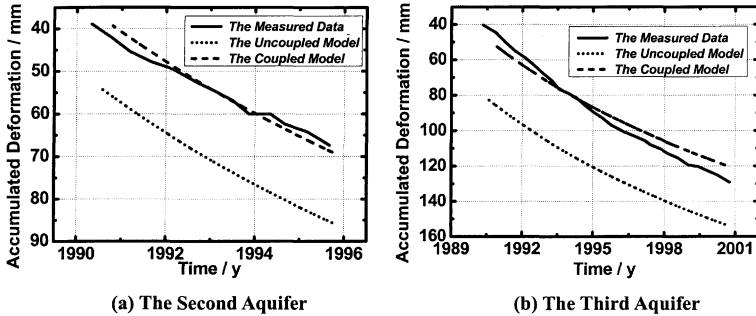


FIG. 3. Accumulated deformations of the aquifers in Qingliang Primary School.

ACKNOWLEDGEMENT

This paper is part of the project No. 50878051 which is supported by the National Natural Science Fund of China; and the project “Jiangsu Six Talent Fastigium Project” which is supported by the Jiangsu Provincial Government. The authors wish to express their gratitude for the support given to this work.

REFERENCES

- Bear, J., Corapcioglu, MY (1981). "Mathematical model for regional land subsidence due to pumping 2 integrated aquifer subsidence equations for vertical and horizontal displacements." *Water Resources Research* Vol 17, No 4, p 947-958.
- Burbey, T. J. (2003). "Use of time–subsidence data during pumping to characterize specific storage and hydraulic conductivity of semi-confining units." *Journal of Hydrology*, 3(22): 3-22.
- Gambolati, G., Freeze, R. A., (1973). "Mathematical simulation of the subsidence of Venice: 1. Theory." *Water Resources Research*, 9 (3): 721-733.
- Gambolati, G., Gatto, P., Freeze, R. A., (1974). "Mathematical simulation of the subsidence of Venice: 2. Results." *Water Resources Research*, 10 (3): 563-577.
- Gambolati, G., Ricceri, G., Bertoni, W., Brighenti, G., Vuillermin, E., (1991). "Mathematical simulation of the subsidence of Ravenna." *Water Resources Research*, 27 (11): 2899-2918.
- Helm, D. C., (1975). "One-dimensional simulation of aquifer system compaction near Pixley, California: 1. Constant parameters." *Water Resources Research*, 11 (3): 465-478.
- Holzer, T. L. (1981). "Preconsolidation stress of aquifer systems in areas of induced land subsidence." *Water Resource. Research*, 17(3), 693-704.
- Lewis, R. W., and Schrefler, B (1978). "A fully coupled consolidation model of the subsidence of Venice." *Water Resources Research*, 14(2):223-230.
- Li, Q. F., Fang, Z., Wang, H. M. (2000). "Calculation and prediction of model of extractive groundwater in Shanghai (in Chinese)." *Shanghai Geology*, 13 (2): 36-43.
- Luo, Z. J., Liu, J. B., Li, L. (2008). "Three-dimensional full coupling numerical simulation of groundwater dewatering and land-subsidence in quaternary loose sediments." *Chinese Journal of Geotechnical Engineering*. 30(2):193-198.
- Relif, F. S. (1969). "Analysis of borehole extensometer data from central California, in Land Subsidence." *Affaissement du sol*, 2:423-431.
- Shen, S.L., Xu, Y.S., and Hong, Z.S. (2006). "Estimation of land subsidence based on groundwater flow model." *Marine Georesource and Geotechnology*, Vol.24, 149-167.
- Shi, X. Q., Xue, Y. Q., Wu, J. C., Zhang, Y., Yu, J, Zhu, J. Q. (2006). "A study of soil deformation properties of the groundwater system in Changzhou area." *Hydrogeology and Engineering Geology*, 3:1-6.
- Xu, T. G. & J. A. M. Van der Gun (1995). "Predkting land subsidence with a constant-parameter coupled model for groundwater flow and aquitard compaction: the Markerwaard case." *Proc. International Symposium*, pp 369-379.

Geotechnical Characterization of the Simsima Limestone (Doha, Qatar)

Ioannis Fourniadis, PhD, DIC, MSc, FGS

Engineering Geologist, Arup Geotechnics, 13 Fitzroy Street, London, UK;
ioannis.fourniadis@arup.com

ABSTRACT: The Simsima Limestone is the main founding stratum in Doha, Qatar. The weathering pattern of the Simsima Limestone is complex, with unweathered rock often overlying more weathered rock, and the common presence of dissolution cavities secondarily infilled with uncemented material. To account for this variability, a weathering scheme has been developed that classifies the Simsima Limestone in terms of rock quality, taking into account the relative percentage of original limestone to secondary carbonate material; the degree of cementation of the secondary material; core recovery parameters; and intact rock strength. The rock quality zones are then related to engineering behaviour, especially as regards rock mass strength and stiffness. The classification of the Simsima Limestone into rock quality grades has been utilized in a number of recent geotechnical projects, where the improved classification of this complex material has the potential to lead to savings in terms of foundation design.

INTRODUCTION

The Qatar peninsula is geologically part of the Arabian Gulf Basin, which has been accumulating carbonate and evaporitic sediments since the Cambrian (Cavalier, 1970). The depth of the sedimentary succession overlying the basement in Qatar is estimated to be over 10km. The stratigraphy beneath Doha comprises a cover of Quaternary marine and sabkha deposits overlaying the Eocene Dammam and Rus formations. The Simsima Limestone member of the Upper Dammam Formation outcrops over 80% of the land surface of Qatar, including the Doha area, and, due to its thickness and geotechnical properties, has been the main founding stratum for many developments in the area.

GEOTECHNICAL VARIABILITY OF THE SIMSIMA LIMESTONE

The Simsima Limestone is an irregularly dolomitised, light grey to brown crystalline limestone, with local intercalations of chert and gray attapulgite (a type of swelling clay). Following its deposition in a shallow marine environment, sea levels dropped,

exposing the rocks to weathering during the Oligocene. Wet climatic conditions during the Pleistocene initiated the development of karst dissolution features of various sizes (from centimeters to tens of meters long) in the Simsima Limestone (Sadiq and Nasir, 2002). These karst features are often infilled by variably cemented fine-grained material (Figure 1).



FIG. 1. Simsima Limestone in exposure (10 km west of Doha city centre).

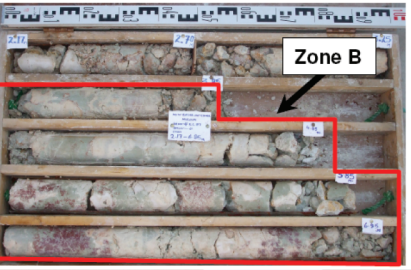
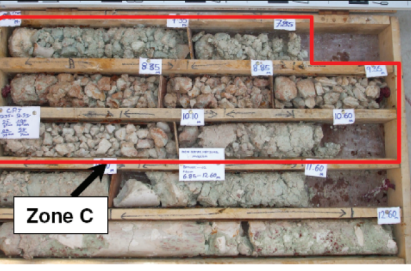
Arup Geotechnics has provided geotechnical advice for a number of prestigious projects in Doha, Qatar. A number of ground investigations associated with those projects have shown the Simsima Limestone to be a variable material with the potential for significant lateral and vertical differences in properties even over short distances. The engineering properties of the Simsima Limestone are largely influenced by the variable degree to which processes like dolomitization and karstic dissolution have acted on the rock mass. In the remainder of this paper, the term “weathering” is used to refer to the above rock altering processes.

An assessment of borehole logs and core photographs of high quality double- and triple-tube rotary core drilling indicates the weathering profile of the Simsima Limestone to often be complex, with highly weathered rock alternating with unaltered rock, or cavities secondarily infilled with weakly cemented carbonate and argillaceous material (Figure 2). This is a common feature of carbonate rocks encountered in arid environments, and is in contrast with typical profiles of ‘weathered’ over ‘unweathered’ rock encountered in more humid environments.

ROCK QUALITY ZONES FOR SIMSIMA LIMESTONE

The geotechnical properties of the Simsima Limestone largely depend on the relative percentage of original limestone to secondary material, and the degree of cementation of the secondary material: where the rock comprises a high percentage of weakly cemented secondary carbonate material, the rock mass generally exhibits lower strength and stiffness. To capture the different degrees of rock quality, or, weathering

in the rock mass, a weathering classification for the Simsima Limestone has been developed, which builds upon the classification scheme proposed by the Engineering Group of the Geological Society (London) (BS 5930, 1999).

Weathering Zone	Example core photograph	Example description
<p>A (fresh to moderately weathered rock)</p>	 <p>Moderately strong pinkish grey LIMESTONE with some vugs (5-50mm diameter, 5-15% by volume), grey staining and locally cemented with white moderately weak to moderately strong calcitic silty material.</p>	
<p>B (heavily weathered rock)</p>		<p>Moderately weak to moderately strong light grey fine grained crystalline weathered LIMESTONE. Closely spaced joints, heavy staining and occasional infilling of dark brown stiff clay and fine grained limestone gravel.</p>
<p>C (matrix-dominated with some corestones)</p>		<p>Recovered as non-intact gravel-sized limestone fragments in a calcitic sandy silt matrix.</p>

According to this approach, the rock mass is assumed to comprise two distinct materials, viz. rock and soil matrix. This is applicable to the case of the Simsima Limestone, where unaltered limestone contains variable amounts of weaker carbonate and argillaceous matrix material. The proportions of rock and matrix are estimated,

and used to classify the material into rock quality zones. Other criteria are considered, including core recovery, degree of cementation of infill material, and intact rock strength. These zones are then related to approximate engineering behaviour, in terms of rock mass strength and stiffness. Table 1 presents the three zones for the Simsim Limestone, along with the proportions of rock and matrix material, and typical engineering behaviour. In this table, fresh to moderately weathered material is identified as “rock”, while highly weathered material to residual soil is identified as “matrix”.

Table 1. Rock quality zones for the Simsim Limestone.

Simsim Limestone Rock Quality Zone	BS 5930:1999 Approach 3 Weathering Zone	Proportions of Rock/Matrix	Typical Engineering Behaviour
A	1 – 2	Rock: >90% Matrix: <10%	Behaves as rock. Apply rock mechanics principles to mass assessment.
B	3 – 4	Rock: 30 – 90% Matrix: 10 – 70%	Rock framework contributes to strength and stiffness; matrix controls permeability.
C	5	Rock <30% Matrix: >70%	Matrix controls strength, stiffness and permeability. Behaves as soil.

ESTIMATION OF ROCK MASS PARAMETERS

In estimating the strength and stiffness of the different rock quality zones, a rock mass classification approach has been adopted, as that allows empirical relationships to be used for assigning engineering parameters (Hoek et al. 1995). Rock mass parameters are obtained on the basis of the Geological Strength Index (GSI), as proposed by Hoek and Brown (1980). To arrive at the GSI for the three weathering zones, the zones are rated on the basis of the Rock Mass Rating (RMR) system for jointed rock masses (Bieniawski 1989), which takes into account RQD, intact rock unconfined compressive strength (UCS), fracture spacing and infill of the rock mass, and groundwater conditions. Table 2 presents the ratings assigned to the above parameters for each zone.

As regards the unconfined compressive strength, the variable nature of the Simsim Limestone rock mass means that a single strength value cannot accurately capture the variation in this material. Hence, a representative intact rock UCS has been estimated for material representative of the three main quality zones, on the basis of laboratory tests on recovered core (second column of Table 2).

Table 2. Rock mass rating for Simsim Limestone.

Simsima Rock Quality Grade	Intact rock UCS		RQD		Mean fracture spacing		Fracture conditions		RMR
	MPa	Rating	%	Rating	mm	Rating	Condition	Rating	$\Sigma R_{atn gs}$
A	12	2	50-75	13	>200	10	weathered	20	45
B	10	2	25-50	8	60-200	8	gouge<5mm	10	28
C	5	1	<25	3	<60	5	gouge>5mm	0	9

For the RMR values to be convertible to equivalent GSI, a value of 15 is assigned to the Groundwater rating and the Adjustment for Joint Orientation is set to zero (Hoek et al, 1995). The revised RMR ratings are then used to derive the GSI rating through the following relationship: $GSI = RMR_{99} - 5$, where GSI: Geological Strength Index; and RMR_{99} : revised Rock Mass Rating. The rock mass properties for the three rock quality zones are estimated on the basis of the GSI ratings, the intact unconfined compressive strength, the intact modulus and a material constant for the intact rock (Hoek et al, 1995). The rock mass deformation modulus, cohesion and angle of shearing resistance for the Simsim Limestone three weathering zones have been estimated in this manner (Table 3).

Table 3. Rock mass properties for Simsim Limestone.

Rock Quality Zone	GSI	Mass compressive strength (MPa)	Mass deformation modulus (MPa)	Cohesion (kPa)	Angle of shearing resistance (°)
A	55	2.4	2450	650	32
B	38	1.3	840	410	27
C	19	0.4	170	140	21

IMPLICATIONS FOR FOUNDATION DESIGN

As the cross-section in Figure 3 shows, the pattern of rock quality zones in the Simsim Limestone can be complex. This has implications for the design of deep foundations (e.g. bored cast-in-situ piles), where an approach that assigns a single value of compressive strength to the entire formation is not sufficient. Instead, an economic design can be achieved by zoning the founding material into rock quality grades as discussed above, and assigning different values of compressive strength and stiffness to each zone. The classification of the Simsim Limestone into rock quality grades has been utilized in a number of recent geotechnical projects, where the improved classification of this complex material has the potential to lead to savings in terms of foundation design.

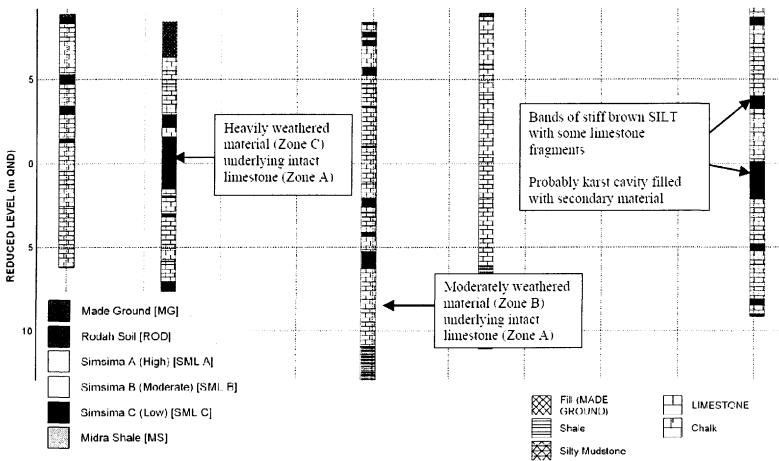


FIG. 3. Cross-section showing Simsima Limestone classification into weathering zones.

CONCLUSIONS

This study has presented a classification scheme of the Simsima Limestone into rock quality zones, utilising a rock mass characterisation approach. Values of compressive strength and stiffness have been derived for the three rock quality grades. It is suggested that a geotechnical classification of the Simsima Limestone in terms of rock quality zones can lead to a more rational and economic foundation design.

REFERENCES

- Bieniawski, Z.T. (1989). "Engineering Rock Mass Classifications." John Wiley, New York, 251pp.
- BS 5930 (1999) "Code of Practice for Site Investigations". British Standards Institution.
- Cavelier, C. (1970). "Geological Description of the Qatar Peninsula (explanation of the 1:100,000 Geological Maps of Qatar)." BRGM, Paris.
- Hoek, E. and Brown, E.T. (1980). "Underground Excavations in Rock." London: Instn Min. Metall.
- Hoek, E., Kaiser, P.K. and Bawden, W.F. (1995). "Support of Underground Excavations in Hard Rock." Balkema, Rotterdam.
- Sadiq, A.M. and Nasir, S.J. (2002). "Middle Pleistocene karst evolution in the State of Qatar, Arabian Gulf." *Journal of Cave and Karst Studies*, Vol. 64 (2): 132-139

Application of Microgravity Survey to Detect Underground Cavities in a Desert Karst Terrain

Hasan Kamal¹, A.M. ASCE, Ph.D., Mahmoud Taha² and Shaikha Al-Sanad³

¹Associate Research Scientist, Building and Energy Technologies Department, Kuwait Institute for Scientific Research, PO Box 24885 Safat, 13109 Kuwait, hkamal@kisir.edu.kw

²Research Associate, Building and Energy Technologies Department, Kuwait Institute for Scientific Research, PO Box 24885 Safat, 13109 Kuwait, mtaha@kisir.edu.kw

³Research Associate, Building and Energy Technologies Department, Kuwait Institute for Scientific Research, PO Box 24885 Safat, 13109 Kuwait, ssanad@kisir.edu.kw

ABSTRACT: Several sinkholes were detected in a residential area located close to the northeast coastal side of the Arabian Peninsula. The sinkholes occurred suddenly with different sizes and to a maximum of 31 m in depth. Comprehensive investigation studies were conducted for understanding the causes of the sinkhole occurrence in addition to recommend treatment measures. The results revealed that the geological profile is made of sandy overburden soil uncomfortably overlaying Karst limestone bedrock. The cause of the sinkholes was attributed to the dissolution of the limestone bedrock and the subsequent raveling of the overburden soil cover. Microgravity survey method was used in the geophysical investigation to detect subsurface cavities. The validity of the microgravity survey was confirmed after applying a drilling program. After 15 years, another microgravity survey was conducted in selected locations of the same residential area for the purpose of verifying the current underground status and assessing its development. In this paper, nature of the desert Karst terrain under study is described. The results of the two microgravity surveys are presented. The results confirmed the capability of the microgravity method to detect density anomalies and ground disturbances. The maps showed evolution of the anomalies in some locations within the studied area.

INTRODUCTION

A residential area was developed around 30 years ago in a desert terrain located in the northeast coastal side of the Arabian Peninsula, consisting approximately of 2500 housing units including community services. It is divided to six sectors, A1 to A6. After eight years of construction, four major ground subsidences occurred in the form of sinkholes (SH1 through SH4). The events caused destruction of property and threatened human lives. An immediate action was taken by the government to

evacuate and fence the affected area considering it as a high risk area.

After fifteen years, four new sinkholes were observed during recent investigation program. The first two sinkholes (SH5, SH6) occurred in the evacuated area delineated in Sector A1. Sinkhole SH7 occurred at the northeast corner of Sector A1, under the footing of high voltage tower. Sinkhole SH8 occurred in Sector A6. Figure 1 shows location and distribution of the occurred sinkholes. More information on the sinkholes including location, dimensions, and present condition is listed in Table 1.

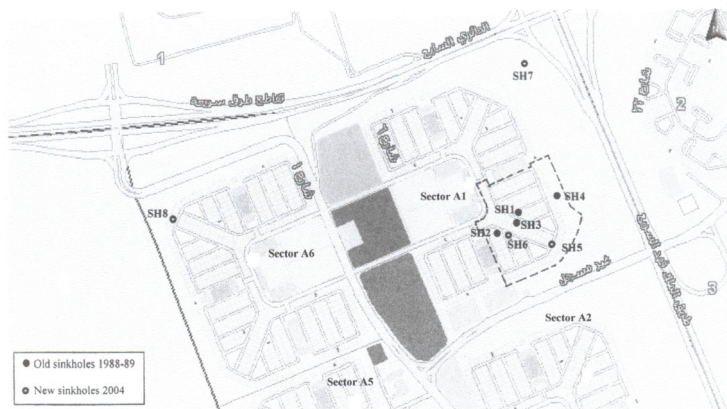


FIG. 1. Sinkhole location and distribution.

Table 1. Ground Subsidence Records

Sinkhole #	Location (Sector)	Date of occurrence	Diameter/length (m)	Width (m)	Depth (m)	
SH1	A1	April 1988	15.0	-	31.0	OLD
SH2	A1	April 1988	4.0	-	7.0	
SH3	A1	October 1988	7.0	-	9.0	
SH4	A1	June 1989	8.0	2.0	1.4	
SH5	A1	June 2004	4.8	2.6	0.83	NEW
SH6	A1	June 2004	1.5	-	0.54	
SH7	A1	June 2004	5.6	5.0	0.4	
SH8	A6	July 2004	7.0	-	6.0	

DESCRIPTION OF THE CONDUCTED INVESTIGATION PROGRAMS

Upon the occurrence of the sinkholes, several investigation programs were conducted with the direct association of Kuwait Institute for Scientific Research (KISR). The affected area is located at the northeastern edge of the Arabian Peninsula

and bordered by the Arabian Gulf in the East. It is characterized by a typical desert environment. The ground slopes gently from about 270 m above sea level in the extreme southwestern corner of the country towards the lowlands in the northeast.

As part of the investigation programs, geophysical survey was carried out to investigate the existence of underground cavities and their lateral extent. Three techniques were initially applied: resistivity, seismic cross-hole shooting and gravimetric measurements. The gravimetric testing (Microgravity method) was selected as it proved dependable and risk free, Figure 2. The survey results were represented in contour maps delineating anomalies varying from negative to positive values. The negative values interpreted as low density subsurface layers and the possibility of existence of cavities. As the contour numbers increase into the positive numbers, the possibility of cavities existence is reduced.



FIG. 2. Onsite measurement using gravimeter equipment.

The geotechnical investigation was carried out in the investigation program by drilling boreholes to depths reaching the limestone bedrock layer, up to the depth of 85 m. The geological profile of the area consists of 31 m to 39 m of overburden comprising of dense to very dense sand, which is underlain by limestone bedrock formation. The soil-rock interface contains dark chert nodules and sandstone. The groundwater table was around the soil-rock interface level. From the drilling records, the cavities were encountered at several depths at the limestone formation.

MICROGRAVITY SURVEY

Theoretical Concept

The principal of any gravity survey is to identify areas of contrasting density by surface measurements of the disturbance produced in the earth's gravitational field. The gravitational field is a function of: distance from the centre of the earth, centrifugal acceleration due to the earth's rotation, and distribution of the mass which is controlled by changes in the density of rocks in the earth. The theory of gravity is

formulated in Newton's law. This law states that a force (F) exerted on a mass (m_2) by a mass (m_1) is directly proportional to the product of the masses and is inversely proportional to the square of the distance between the centers of the masses. The unit is commonly called a gal. The survey method involves measuring the very small differences in gravitational force field, which are a function of the gravitational acceleration due to the sum of the attraction of the Earth's mass and the effects of its rotation. Full color residual anomaly maps are then produced, where the mass deficiencies indicated by negative residual anomalies.

Results of the First Microgravity Survey

The first microgravity survey was carried out in the area after the occurrence of the sinkholes in 1989. The survey covered the whole residential area, sectors A1 to A6. The microgravity survey produced contour maps delimiting the existence and extension of underground cavities, which were due to Karstic formations, in relation to known ground subsidence. Figure 3 shows the residual map for the whole affected area and the colors indicate the density level based on the anomaly value. Figure 4 indicates the extent and location of the underground cavities (voids). The sudden drop of the drilling heads during the drilling program proved the existence of the cavities. Accordingly, the highest risk area is determined to be around the first three sinkholes within sector A1.

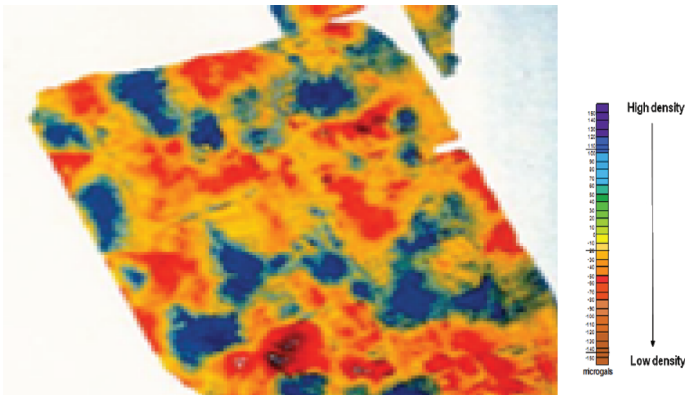


FIG. 3. Residual map for the whole residential area, first microgravity survey.

Results of the Second Microgravity Survey

After fifteen years, the second microgravity survey was carried out in the same evacuated area. The main purpose of the second survey was to confirm the existence and update the status and development of previous anomalies within the residential area. The survey emphasized on the highest risk area specified in the first survey

within sector A1 and other selected locations within the affected residential area. The residual map for sector A1 from the second survey is shown in Figure 5 which detects the extent and distribution of underground cavities. The existence and evolution of the anomalies from the first survey is confirmed.

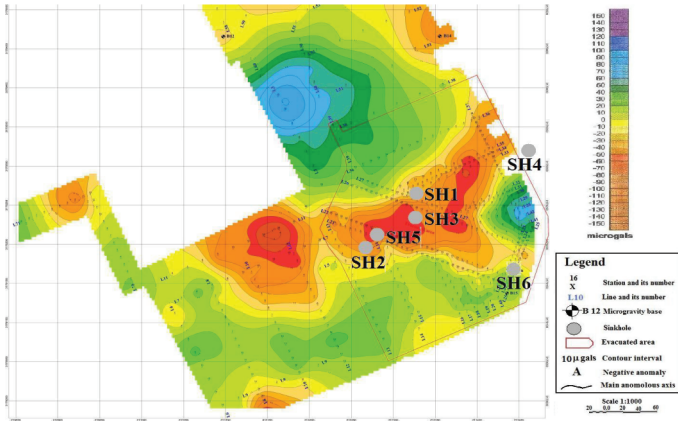


FIG. 4. Residual map for sector A1, first microgravity survey.

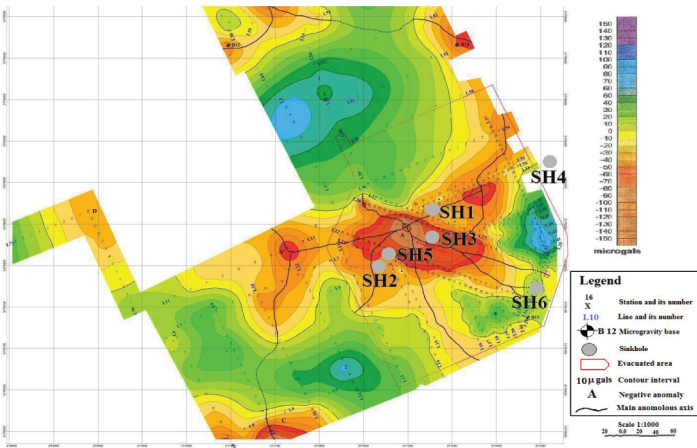


FIG. 5. Residual map for sector A1, second microgravity survey.

Comparison between the Microgravity Surveys

In order to assess the current condition of the underground cavities, its evolution and development, the results of the two previous surveys were compared for the residual

anomalies map. Residual maps represent the density variation within the clastic soil sediments and the underlying limestone bedrock in terms of low positive and negative anomalies depending upon the geological conditions. By comparing the two residual maps, the anomaly values indicate the evolving nature of the Karst cavities or loose sand lenses of some locations within the fenced zone in sector A1. It is clear from the colors that the anomaly values around SH3 and SH5 has increased and extended. Therefore, the risk is increased in this area while this area was not occupied. The information was sufficient for the decision makers to immediately treat the area.

CONCLUSIONS

To detect underground Karst cavities, two microgravity surveys were conducted in an affected residential area by ground surface subsidence. The time difference between the two surveys was fifteen years. The same method and professional experience are used for the purpose of accurate comparison. The microgravity method proved to be consistent and predictable for detecting Karst cavities existence, location, and extent.

The second survey detected the same general anomalies recognized in the first survey. Extension in size and amplitude of the anomalies were observed. The affected area is considered as an increasing risk of sinkhole development, although no residential activities conducted. To improve the quality of the microgravity survey, it is recommended to use fine grid of stations for accurate contouring of the anomalies. Results of the microgravity surveys were then used as a major factor for efficiently treating the affected residential area.

ACKNOWLEDGMENTS

The authors appreciate the support of the Public Authority of Housing Welfare (PAHW) and Kuwait Institute for Scientific Research (KISR) for this research project (EU23C).

REFERENCES

- Al-Rifaiy, I. (1990) "land subsidence in the Al-Dhahar residential area in Kuwait: a case history study", *Quarterly Journal of Engineering Geology*, London, Vol. 23, pp. 337-346.
- Burdon, D., and Al Sharhan, A. (1968) "The problem of paleokarstic Dammam limestone aquifer in Kuwait", *Journal of Hydrology*, Vol. 6, pp. 385-404.
- Kamal, H., Taha M. and Karam H. "Implementation of Treatment Measures for Sinkholes Occurrence in the State of Kuwait," *The Second International Conference on Problematic Soils*, CI-PREMIER CONFERENCES, Selangor, Malaysia, December 3-5 2006.
- Mukhopadhyaya, A., Al-Sulaimi, J., Al-Awadi, E., and Al-Ruwaih, F. (1996) "An overview of the tertiary geology and hydrology of the northern part of the Arabian gulf region with special reference to Kuwait", *Earth Science Review*, Vol. 40, pp. 259-295.

Author Index

Page number refers to the first page of paper

- Al-Sanad, Shaikha, 279
- Bai, Xiaohong, 118
Bai, Yan-Feng, 239
Benedetto, Andrea, 9
Brauchler, Ralf, 231
- Chandrasekhar, Biju, 216
Chen, Feng, 253
Chen, Hong-Shui, 95
Chen, Lei, 103
Chen, Li-Xia, 21
Chen, Wei, 95
Chi, Su-Yun, 1
- Drumm, Eric C., 253
Du, Juan, 31
Du, Yan-Jun, 103
- Ekkehard, Holzbecher, 194
- Fang, Peng-Fei, 95
Fourniadis, Ioannis, 273
Fujisawa, Kazunori, 71
- Gholizadeh, R., 245
Gomez, Jose, 51
Grabe, J., 159
Guiochon, Georges, 253
- Han, Pengju, 118
Han, Xiao-Rui, 210
Hanson, James L., 132
He, Qiang, 167
Hicher, P. Y., 126
Hsu, Shih-Meng, 1
Hu, Rui, 231
- Jardine, Philip M., 181
Jin, Fei, 103
Jun, Sang-Hyun, 224
- Kamal, Hasan, 279
Kim, Dong-Gun, 224
Ku, Cheng-Yu,
- Lee, Dong-Won, 224
Lei, Jin-Sheng, 15
Li, Chunlin, 267
Li, Lei, 146
Li, Yue, 15
Lin, Feng-Tsai, 79, 87
Lin, Wei-Chih, 79
Liu, Song-Yu, 103
Liu, X. F., 126
Lo, Hung-Chieh, 1
Lu, John C.-C., 79, 87
Lv, Weihua, 57, 267
- Ma, X., 159
Maeda, Kenichi, 261
Martin, Sauter, 194
Mazzella, Alessandro, 188
Mazzella, Antonio, 188
Miao, Linchang, 57, 267
Min, Fan-Lu, 210
Mishra, Rajat C., 216
Murakami, Akira, 71
- Naik, Ranjitsinh D., 216
Nishimura, Shin-ichi, 71
- O'Kelly, Brendan C., 111
- Parker, Jack C., 181

- Peng, Fangle, 63
Peng, Hui, 15
Phillips, Debra, 181
- Quille, Michael E., 111
- Rahardjo, Harianto, 202
- Saiyouri, N., 126
Sakai, Hirotaka, 261
Shahrokhbadi, S., 245
Singh, Jagjit, 132
Stephens, Adam, 132
Stone, Greg M., 132
- Taha, Mahmoud, 279
Tan, Yong, 63
Thomas, Hywel, 153
Toufigh, M. M., 245
- Vardon, Philip, 153
- Wang, Fei, 57
Wang, Hailin, 63
Wang, Yang, 21, 31
Wang, Zhe, 140
Watson, David B., 181
- Xiao, Daping, 202
- Xiao, Ming, 51
Xu, Sifa, 140
Xu, Zhenliang, 63
- Yang, Hong, 202
Yang, Jian-Min, 45
Yao, Zhi-Xiong, 239
Ye, Changyong, 39
Yesiller, Nazli, 132
Yin, Kunlong, 21, 31
Yoo, Nam-Jae, 224
- Zhang, Chun-Lei, 146
Zhang, Fan, 181
Zhang, Yan, 39
Zhao, Gan, 146
Zhao, Hao, 140
Zhao, Wei, 231
Zhao, Zhuo, 39
Zheng, Gang, 45
Zhong, Xiao-Chun, 210
Zhou, Jian, 239
Zhou, Jizhong, 167
Zhou, Li, 31
Zhu, Da-Peng, 15
Zhu, Wei, 146, 210
Zhu, Xiang-Rong, 95

Subject Index

Page number refers to the first page of paper

- Aquifers, 57, 231
- Artificial recharge, 216

- Bentonite, 132
- Biological processes, 153, 167
- Bridges, 39
- Bubbles, 261

- Caissons, 63
- Case studies, 9
- Cavitation, 279
- Cement, 103, 118
- Chemical properties, 153
- China, 15, 21, 31, 39, 45, 57, 210, 267
- Clays, 210, 224
- Closed form solutions, 79
- Coarse-grained soils, 202
- Computer aided simulation, 9, 194, 245, 253
- Concrete structures, 39
- Copper, 103
- Core walls, 132
- Corrosion, 118

- Data collection, 188
- Deformation, 57
- Design, 15
- Discrete elements, 253
- Displacement, 87
- Drainage, 224
- Drawdown, hydrology, 202
- Dredging, 146

- Embankments, 9, 71
- Experimentation, 118

- Failures, 261

- Field tests, 159
- Fills, 146, 181
- Filters, 210
- Finite element method, 15, 245
- Frost heave, 45

- Geographic information systems, 216
- Geotechnical engineering, 153, 188, 273
- Germany, 159
- Gravel, 210
- Groundwater depletion, 267
- Groundwater flow, 194
- Groundwater management, 181, 216
- Groundwater pollution, 167

- Half space, 79, 87
- Heat transfer, 79
- Heavy metals, 126, 167
- Homogeneity, 79
- Hydration, 146
- Hydraulic gradients, 239
- Hydraulic models, 194, 231
- Hydraulic pressure, 45

- Ireland, 111
- Isotropy, 79, 87

- Kaolin, 126
- Karst, 279

- Land subsidence, 267
- Landfills, 15, 140
- Landslides, 1, 21, 31
- Layered soils, 202
- Lead, 103, 111
- Levees, 51

- Limestone, 273
- Mapping, 216
- Mathematical models, 239
- Mechanical properties, 118
- Middle East, 273, 279
- Mining, 111
- Models, 71
- Municipal wastes, 95

- Nitrates, 167
- Numerical analysis, 224

- Parameters, 63, 231
- Particles, 253
- pH, 146
- Piles, 118
- Pollutants, 126
- Pore pressure, 253
- Porous media, 153
- Pumps, 57, 194

- Radiography, 231
- Railroad tracks, 9
- Rainfall, 1
- Recycling, 95
- Remote sensing, 216
- Renewable energy, 159
- Replacement, 132
- Reservoirs, 21
- Residential location, 279
- Risk management, 21

- Sampling, 188
- Seepage, 239, 245, 253, 261
- Shear strength, 51
- Simulation, 181

- Sinkholes, 279
- Slope stability, 9
- Slopes, 15, 140
- Slurries, 132
- Soft soils, 63
- Soil analysis, 45
- Soil compaction, 140, 126
- Soil deformation, 63, 71
- Soil erosion, 51, 71, 261
- Soil pollution, 103, 167
- Soil properties, 111
- Soil structures, 71
- Soils, 118
- Solid wastes, 95
- Statistics, 188
- Stochastic processes, 39
- Stress analysis, 45
- Surveys, 279

- Taiwan, 1
- Tensile strength, 140
- Thermal power, 159

- Uranium, 181

- Vegetation, 9

- Waste management, 95
- Water discharge, 224
- Water table, 202
- Water waves, 31
- Wells, 194

- Yangtze River, 210

- Zinc, 111